3D Printing of Engineered Cementitious Composites (3DP-ECC)

by

Wen Zhou

A dissertation submitted in partial fulfillment
of the requirements for the degree of
Doctor of Philosophy
(Civil Engineering)
in the University of Michigan
2023

Doctoral Committee:

Professor Victor C. Li, Chair
Professor SangHyun Lee
Associate Professor Jonathan Wesley McGee
Assistant Research Scientist He Zhu

Wen Zhou

wzhoucee@umich.edu

ORCID iD: 0000-0003-2344-7895

Dedication

To my beloved family and partner.

Unconditional love is real.

To women power,

which is real, too.

Acknowledgements

I started my PhD journey in 2020, a year that will forever be etched in my memory. It not only marked a brand-new stage in my personal life but stands as a testament to the collective memory of humanity. During this challenging period, I have been blessed with a truly unique experience, and it is with a grateful heart that I express my deepest appreciation to the individuals who have supported me along the way.

First and foremost, I would like to extend my utmost gratitude to my advisor, Prof. Victor C Li. The privilege of conducting my doctoral research under your guidance has been an extraordinary honor. Your boundless creativity, unwavering rigor, profound humility, and infinite patience have made you an exemplar for me. Numerous times, your encouragement and recognition provided me with the strength to overcome whatever obstacles I faced. Thank you for being not just my advisor, but also an inspiration in my career and life.

I also would like to extend my appreciation to my dissertation committee. To Prof. Wes McGee, thank you for leading me on the path of 3D printing research. I am grateful to Prof. Sanghyun Lee for his valuable advice on my work. And to Dr. He Zhu, your selfless help contributes to shaping and improving my research. Without the collective wisdom and expertise of my committee, this work would not have been possible.

I am deeply grateful to Prof. Yamei Zhang from Southeast University. Your support allowed me to set out my research in your lab when circumstances prevented me from being physically present at Michigan. I am truly grateful for the precious opportunity you provided during that time.

I cannot overlook the invaluable contributions of my lab mates and lab technicians. Your involvement has been pivotal, both in terms of experimental assistance and intellectual exchange. Thank you, Wei-Hsiu Hu, Mengjun Hou, Jan Pantolin, Steve Donajkowski, Justin Roelofs, and Ethan Kennedy, for those wonderful collaborations.

To my beloved parents, I am forever indebted to you. Your unconditional love, understanding, and support have made the impossible possible. Though you never hold your own PhD degrees, a part of my degree belongs to you.

Lastly, I would like to express my heartfelt appreciation to my partner and friends for the love, encouragement, and laughter that have sustained me throughout this journey. Thank you for your presence in my life.

Table of Contents

List of Tables

List of Figures

Abstract

3D concrete printing (3DCP) is revolutionizing construction practices. As a promising printing ink, ductile engineered cementitious composites (ECC) removes the dependence on steel reinforcement required for concrete structures. While ECC offers structural shape flexibility and 3DP promotes construction speed, there remain knowledge gaps that must be overcome to reach field readiness. This thesis builds a 3D printing ECC (3DP-ECC) knowledge system by experimental investigation and theoretical analysis, covering the design, control, and behavior of 3DP-ECC in its life cycle.

In the material production phase, material fresh properties were investigated. To quantify the buildability of printable ECC at the fresh stage, the time-dependent fresh properties of ECC were experimentally characterized. A quantitative methodology for evaluating buildability at both the material and structural scale was further proposed, with the influence of time progression and material-machine interaction taken into consideration.

During manufacturing, the impacts of print process parameters on 3DP-ECC were probed. To gain a deeper understanding of material-machine interaction in both fresh and hardened states, the inter-relations among material production control, micro-structure and macro-scale properties of 3DP-ECC were explored by varying the nozzle travelling speeds and nozzle standoff distances.

Moreover, to alleviate anisotropy of hardened 3DP-ECC, innovative printing patterns were designed and validated. Knitted and tilted filaments were designed to mimic the crossed-lamellar micro-structure of conch shells. The bio-inspired novel design rendered ECC's directional-dependent tensile resistance to three-dimensional space and introduced a complex interface system, effectively moderating anisotropy of 3DP-ECC.

In the use phase, the structural-scale behavior of printed elements was studied. Cavity walls with different infill patterns were printed and tested to examine the feasibility and performance of 3D printed ECC elements. Enhanced energy absorption ability and ductility compared to printed concrete walls were captured and valued.

Further, shrinkage and high carbon footprint concerns were mitigated by mix proportion optimization of printable ECC. The mix was designed to have both a lower carbon footprint than conventional concrete and early expansion capabilities to address shrinkage concerns. The designed printable ECC contributes to suppress environmental impact and prolongate service life by eliminating shrinkage-induced cracking.

This research seeks broad impact by filling the existing research gaps in 3DP-ECC and offering innovative solutions that can advance the field. The knowledge generated in this thesis offers critical insights into the future development and prospects of 3DP-ECC, ushering in the practical large-scale applications of 3DP of concrete structure that maximizes the unique advantages of 3D printing over conventional construction approaches.

Chapter 1. Introduction

1.1. Background, motivation, and objectives

3D printing of cementitious materials (3DCP) has revolutionized the traditional construction practices and brings new horizons for the development of the construction sector [1-3]. As an advanced additive manufacturing technology, 3DCP allows the printer to deposit cementitious materials layer by layer according to a predefined digital model, and automatically generate a printed concrete element [3].

Compared with the traditional construction method, 3DCP shows several distinct advantages. With automation procedure, 3D printing changes the traditional labor-intensive construction mode and economizes on labor. Further, the automated manufacturing process substantially promotes the efficiency of construction and shortens the construction period. In addition, the characteristics of additive manufacture remove the need for formwork required in traditional concrete casting and also significantly reduce the material waste in construction. The elimination of formwork enables 3DCP to produce geometrically complex elements or structures and realize the unification of both standardization and customization in manufacturing. Moreover, considering the immense environmental impact of the construction industry (accounting for approximately 38% of global greenhouse gas emissions and 40% of solid waste generation) [1, 4], the significance of reduction in material input and construction wastes is far from trivial. Since the consumption of formwork and generation of construction wastes are important sources of the carbon footprint produced in constructions, the application of 3DCP technology would bring about a radical change in suppressing the negative environmental impact in the construction industry [5]. Finally, 3DCP offers advantages in architectural shape complexity and surface texture, and in smart (thermal, self-cleaning) functionalities not practical in conventional construction approaches.

Although 3DCP has rendered concrete constructions broader possibilities, concrete has its inherent limitations as a building material, especially when it is applied in 3DCP process. Generally, concrete has relatively high compressive strength and disproportionate low tensile strength. Its

sudden fracture failure behavior under load is often characterized as brittle or quasi-brittle. To overcome this shortcoming, steel reinforcement is necessary in traditional concrete construction practice. Unfortunately, steel reinforcement is usually incompatible with 3DCP [6], which largely impedes the development and practical application of 3DCP technology, especially in large scale construction.

To solve the intrinsic conflict between the need of steel reinforcement and the practice of 3DCP, cementitious material with high ductility is considered as a potential choice and great substitute for printing ink, such as engineered cementitious composite (ECC). Engineered cementitious composite (ECC) exhibits strain-hardening characteristics and considerable tensile ductility, which distinguish ECC from conventional concrete and ordinary fiber reinforced concrete (FRC). For FRC loaded under uniaxial tension, deformation localization occurs at the first and only crack site, while overall load carrying capacity drops. This tension-softening behavior in FRC is valued for its more gradual loss of strength and its ability to limit the width of cracks by the bridging fibers (Figure 1.1(a)). Instead of tension-softening, ECC undergoes strain-hardening and continues to bear higher loads at increasing imposed strain, as shown in Figure 1.1(b). The growing tensile deformation in ECC is not localized but spreads to multiple microcracks covering an enlarging specimen volume. The multiple microcracking process represents a volumetric inelastic strain deformation analogous to plastic yielding of a ductile metal [7]. This self-reinforcing feature of ECC removes the dependence on steel reinforcement, making ECC an attractive ink for 3D printing [6].

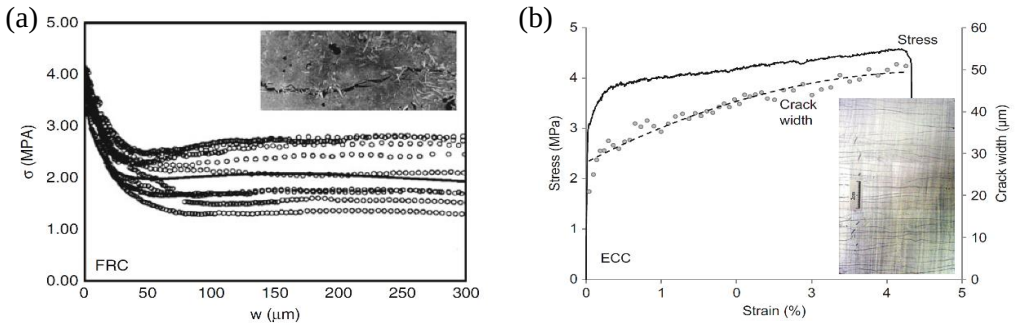

Figure 1.1: Characteristics of different mechanical responses: (a) Tension-softening in FRC. The tensile load continuously drops to zero as the crack width reaches about half the fiber length of 12 mm. (b) Tensile strain-hardening of a ECC (containing 2% volume fraction of PVA fibers). Load-bearing capacity is maintained under high strain of several percent, with width of multiple cracks limited to below 60 μm. [7]

To promote the development of 3D printing of ECC (3DP-ECC) technology, comprehensive and in-depth research are necessitated. The research of 3DP-ECC is not to simply reproduce the work of 3D concrete printing, but to establish an innovative knowledge base, since there exist several fundamental differences between ECC and conventional concrete:

(1) The introduction of fiber reinforcement adds additional variables when compared with conventional concrete and pure mortar, especially in 3D printing. For instance, one requirement raised by pumping of wet material is sufficient fluidity and lower viscosity. However, experiments have shown that matrix cohesion of ECC should be sufficient to facilitate uniform fiber dispersion [8]. Therefore, the rheological parameters of ECC need to be more delicately tuned to meet the potential conflicting rheological requirements raised by 3D printing. Another example is that the presence of fiber may accentuate the anisotropy of 3D printed elements in the hardened state, since fiber orientation poses substantial influence on the mechanical properties of ECC.

(2) The synergy of fiber, matrix and interface at the micro-scale determines the macroscopic performance of ECC in the hardened state [7]. For example, when evaluating the performance of 3DP-ECC, the orientation and morphology of the fibers play a pivotal role, while the pore structure and fracture toughness of the matrix and the interface also needs to be taken into consideration. The interrelations between 3DP processing parameters, composite microstructure, and composite performance further complicate the analysis of 3DP-ECC, but provide a platform for new knowledge generation.

(3) The most prominent advantage of ECC is its self-reinforcing feature, showing as strain hardening behavior under tension. Its excellent tensile performance, when evaluating the mechanical properties, is an important indicator, which is as critical as compressive and flexural properties (without steel reinforcement). While for ordinary concrete, the main foci are on the compressive and flexural properties (in the case with steel reinforcement).

Such differences create a knowledge gap and motivate research targeting at 3DP-ECC. To date, successful experiences have been gained in printing ECC components [9-11]. Li et al. [6] and Yu et al. [12] reported a stable twisted column with a height of 1.5 m and 150 layers printed, clear of structural collapse or material failure, as shown in Figure 1.2. Zhu et al. [13] also obtained hollow ECC cylinders with 17 layers. In the experiments by Figueiredo et al. [14], the printed ECC element eventually collapsed at the 14th layer. Various ECC mix designs (with different fiber

content, sand-to-binder ratios and water-to-binder ratios) were studied by Ogura et al. [15]. Mixtures with sufficient static yield stress and leading to no considerable deformation at the bottom layer was optimized for printing wall elements up to 120 mm high. Ivaniuk et al. [16] successfully created a sphere-like polyhedron with printed ECC modules.

Figure 1.2: 3DP-ECC twisted column with 150 layers in [6] and [12].

The current research foci on 3DP-ECC are mainly on feasibility study, mix design and basic mechanical properties. In the cases of 2% PVA fiber addition, 2-4 MPa direct tensile strength and 2-6% strain capacity were obtained along the printing direction [12, 17-18]. While in the other two directions perpendicular to nozzle movement direction, the tensile performance of 3DP-ECC was not comparable to the former [18-19]. Furthermore, substitute PVA fiber with PE fiber broadened the horizon of strain capacity of 3DP-ECC. With 1-2% PE fiber, 1-11.4% strain capacity was achieved along with a tensile strength of 4-5 MPa [13, 15, 20].

Although beneficial attempts have been made and preliminary research has progressed, there is still a long way to go before the establishment of a mature 3DP-ECC knowledge system. Several research fields remain to be covered, as summarized in Figure 1.3. From the beginning of the life cycle, the performance of 3DP-ECC in its fresh state determines the success of printing. Quantification and evaluation of the time-dependent rheology evolution of 3DP-ECC is required, since it is associated with the pumpability, extrudability, and buildability of 3D printing. Next, the

impact of different process parameters on the performance of printed ECC should be understood. After printing, the ECC will experience curing and hardening, and the mechanical properties after hardening need to be fully studied, with emphasis on the anisotropy of 3DP-ECC and the strengthening strategy of layer interface. Furthermore, given the long service life of infrastructures and buildings, the long-term performance of 3DP-ECC also requires more attention. For instance, shrinkage induced crack could undermine the integrity and service status of printed elements and therefore requires attention. In addition, on the basis of a preliminary understanding of 3DP-ECC, appropriate measures should be taken to mitigate the impact of high binder content on carbon footprint, which could be achieved by modifying the constituents and mix proportion of printable ECC.

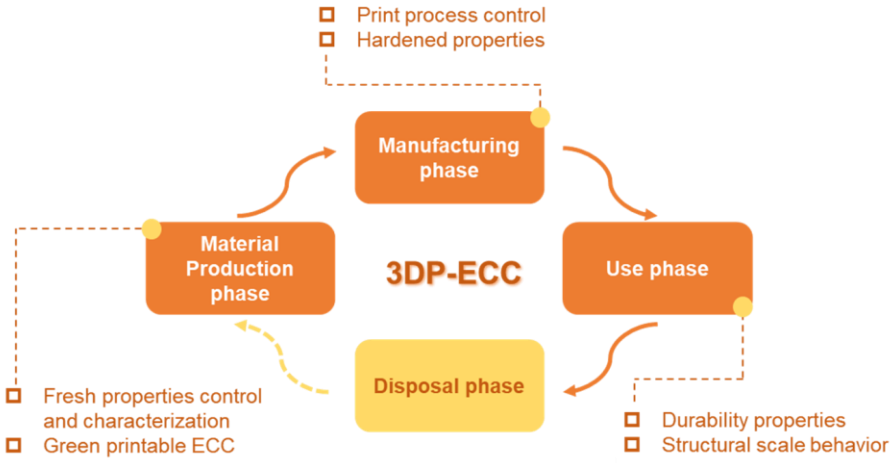

Figure 1.3: Life cycle of 3DP-ECC and required research foci.

To fill the research gap, the thesis research aims at overcoming the knowledge gap on machine-material interaction, investigating the behavior and characteristics of 3DP-ECC across each stage of its lifecycle, building a 3DP-ECC knowledge system through experimental investigation and theoretical analysis, and providing guidance for the current development and insights for future prospects of 3DP-ECC. The ultimate pursuit is to generate fundamental knowledge that supports 3DP-ECC as a future construction technology that is safe, efficient and environmentally sustainable.

1.2. Dissertation organization

The thread of this dissertation is developed in accordance with the research foci in different life cycle stages indicated in Figure 1.3.

Following this introductory chapter, Chapter 2 offers a comprehensive overview on technical approaches and material properties of 3DCP, spanning from an early age to hardened performance. Extrusion-based 3DCP is broken down into several stages and linked to corresponding evaluation indicators and material behaviors respectively. With the state-of-the-art research progress presented, the most pressing challenges and research priorities have also been identified, pointing to path forward for future research.

Chapter 3 sheds light on how to understand and quantify the buildability of printable ECC at the fresh stage. A quantitative methodology for evaluating the buildability of printable ECC at both the material and structural scale was proposed, with the influence of time progression and material-machine interaction taken into consideration.

To gain a deeper understanding of material-machine interaction in both fresh and hardened states, Chapter 4 probes into the inter-relations among material production control (printing parameters), micro-structure and macro-scale properties of 3DP-ECC. By varying the nozzle travelling speeds and nozzle standoff distances, the resulting micro-structure and mechanical performance of 3DP-ECC were characterized and analyzed.

Chapter 5 proposes a novel design method for alleviating anisotropy of 3DP-ECC. The methodology is to delay fracture and reduce anisotropy through the assignment of filament orientations in three dimensions space and the formation of complex interfaces system. At the same time, the direction-dependent mechanical properties and the crack kinking-trapping feature of ECC are also exploited. The two innovative printing patterns, knitted and tilted filaments, were printed and verified.

In Chapter 6, the performance of printed structural element is evaluated. Cavity walls with different infill patterns were printed and tested to examine the feasibility and performance of 3D printed ECC elements. Distinct failure modes were analyzed to understand the mechanical response of different structure patterns.

Chapter 7 explores the potential of developing a low-carbon and expansive printable ECC. The designed mix notably lowers the carbon footprint of printable ECC. Further, the shrinkage concern of printed cementitious material is addressed by the expansion developed at early age. The proposed printable ECC contributes to both suppress environmental impact and prolongate service life by eliminating shrinkage-induced cracking.

Chapter 8 is the concluding chapter, highlighting and summarizing the scientific findings and impacts to the research field. Limitations and future research priorities are also covered to guide future research.

Chapter 2. Literature Review

This chapter endeavors to provide a structured overview of the state-of-the-art research and major challenges pertaining to the 3D printing of cementitious materials, including conventional concrete, fiber-reinforced concrete, and ECC. By synthesizing relevant knowledge in a methodical manner, a comprehensive review of key aspects of 3DCP is presented, forming the foundation for a comprehensive understanding of the printing technology, material quality control, and finished product performance. In addition, unique material features of ECC are highlighted to illustrate the effectiveness and challenges in the combination of 3D printing and ECC.

2.1. 3D printing of cementitious materials

2.1.1 Methods and approaches

3DCP is an innovative technology undergoing explosive growth. In the stage from germination to maturity, many different approaches have been pioneered. Two of the most fundamental and most extensively applied are extrusion and particle-bed. Based on them, new methods have also been explored. In this thesis, extrusion-based 3D printing is emphasized and overviewed.

The most commonly used concrete additive manufacturing technology, employed in more than half of current 3DCP practices [3], is based on extrusion. Extrusion refers to the process of squeezing continuous filament of fresh mixture from a nozzle and depositing the material layer by layer per the established digital printing path. This technology was originally developed by Khoshnevis [21] as Contour Crafting in the 1990s. It was further improved and developed by subsequent researchers and gradually matured in technology. To date, extrusion has been extensively used in additive manufacturing of cementitious materials. Several typical showcases are shown in Figure 2.1.

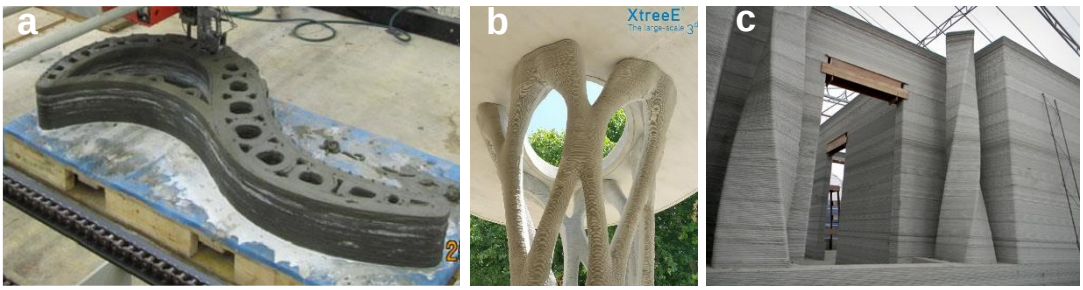

Figure 2.1: Showcases of extrusion-based 3DCP: (a) Printed concrete bench (University of Loughborough) [22]; (b) Printed concrete column (XtreeE) [23]; (c) Printed hotel suite (Total Kustom) [24].

Typically, there exist seven stages for extrusion process (Figure 2.2) [6]: (1) mixing; (2) pumping; (3) transporting; (4) extruding; (5) building; (6) curing; (7) hardened. As indicated above, most extrusion processes require the raw materials, including dry particles and water, to be mixed before printing. The cementitious mortar designed for extrusion usually contains a relatively high proportion of cement and an appropriate amount of fine aggregate, whose particle size is typically below 3 mm [3]. The fresh mixture is fed into an extrusion system through a pump. Inside the extrusion system, fluid mortar is transported in a hose and pumped to the nozzle. Except for pre-mixed material feeding, in-line printing systems has also been developed for mixing near the printing head [25-26].

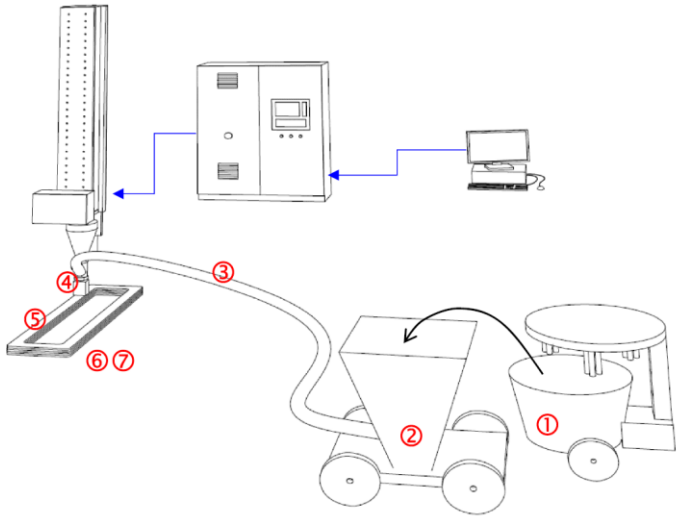

Figure 2.2: Schematic representation of 3DCP extrusion process [6].

Nozzles usually vary in shape and size in different printing instruments [27]. The shape of the nozzle can be round, oval and rectangular. Similarly, the size of nozzle varies drastically in different scenarios. The printed filament can be as fine as several millimeters, as in 3D Concrete Printing at Loughborough University [28-29]; in contrast, cross-sectional dimension can reach the order of tens of millimeters, even with a width of 150 mm, such as in CONPrint3D at Technical University of Dresden [30]. While the filament is forced out, the nozzle keeps moving cyclically according to the preset path determined by the computer program. Through continuous reciprocating cycles, the filaments of fresh mixture are superimposed on top of the previous layer, gradually building up the printing object. Nozzle opening, print speed, cycle time and the printing path in which the filaments are arranged are decisive parameters for the extruding process and also for the properties of the resulting element.

In general, extrusion offers all the common advantages of 3DCP technology, making it the most versatile and popular method. However, there are some limitations of extrusion-based method. First of all, due to the size limitation of the nozzle and the fluidity requirements of mortar extrusion, the filament lacks in its ability to depict very fine shape details. Therefore, the printed object of the extrusion method is susceptible to the low resolution, compared with particle-bed printing. Secondly, deformation of filament is usually inevitable due to the influence of the upper layer loading and its own weight, which also causes deviation between the finished product and its desired geometric shape. In addition, the printed concrete structure exhibits consistent properties along the printing direction, while exhibits anisotropy in the vertical direction on account of delamination. Specifically, for fiber-reinforced composites, anisotropy may be expected even within a printed layer, due to fiber orientation as influenced by the extrusion process. The anisotropy characteristic renders different material properties of printed elements from those of cast and challenges the structural performance.

A key prerequisite for the success of the extrusion process is that the rheological properties of cementitious material meet the printing requirements at different stages. To further enhance the correlation and mutual adaptation between printing operations and material properties, real-time monitoring and feedback are integrated into the 3DCP as an extension of extrusion technology. A team at ETH Zurich pioneered the Smart Dynamic Casting technology [31]. An extrusion formwork is installed on a 6-axis robotic arm, which precisely controls the speed and trajectory of

printing. During the entire printing process, the digital-controlled sensor system closely monitors the hydration process of mortar, measures its hardening dynamics, and then feeds the detected data back to the robot's drive system as operating parameters, thereby accurately passing chemical admixtures to control the hydration process and adjusting the movement speed of formwork. Smart Dynamic Casting combines slipforming with additive manufacturing technology, which inspires new development possibilities for 3DCP.

2.1.2 Fresh properties control

3DCP imposes complicated and subtle requirements on the properties of the printed materials. Especially at different stages of printing, sometimes the desired properties conflict with each other, such as the different requirements for mortar yield stress in the delivery and deposition phases. Considering the situation, the material performance at each stage should be evaluated separately, for example, from the perspectives of pumpability, extrudability and buildability, and finally strung together into a whole manufacturing chain. This requires the properties of the printing material to be delicately designed and harmoniously tuned to allow suitable rheological changes from mixing to filament placement and hardening.

On one hand, the initial fluidity of the mortar should be adequate to pump the fresh mixture into the extrusion system before printing. From this perspective, the yield stress and viscosity of the material should therefore be low enough to smoothly flow through the hose and simultaneously avoid clogging. On the other hand, the cementitious material should have an adequate rigidity to fully or partly bear its own weight once extruded with no further support by the nozzle (or formwork). To achieve this goal, the extruded material needs to exhibit sufficient yield stress and thixotropy. Subsequently, as the printed layers stacks on the top of each other, the increase of stiffness and strength of the lower layer should accelerate to provide sufficient shape retention ability and structural stability.

2.1.2.1 Flowability/Pumpability

Flowability/pumpability, the most elementary index to evaluate whether the cementitious material is feasible for printing, describes the ease and reliability with which material is moved through the

delivery system [29]. If the fresh mixture cannot be smoothly fed into the pump and delivered to the nozzle position, successful extrusion will be beyond the range of possibility. In order to assess the flowability/pumpability of the fresh mixture, two aspects must be considered simultaneously, the intrinsic rheological properties of the mixture and the frictional behavior between the mixture and the hose wall [32], whose impact on pumping will be discussed separately below.

The rheological behavior of the fresh mixture is most decisive for flowability/pumpability. Different from typical viscous fluids, the cementitious materials in the pumping pipe flows only when the applied stress is higher than its yield stress [33], which makes it more complicated in analyzing the flow behavior. In general, lower dynamic yield stress and plastic viscosity in rheology are favorable for better pumpability. Nonetheless, excessively low yield stress or plastic viscosity will increase the probability of segregation and lead to blockage inside the hose. Therefore, the value of viscosity and yield stress should be limited to a certain range, accompanied by a minimum design value [34].

Rheological properties are governed by mix proportion. Regarding mix design, particle gradation is a key factor. The rheology of mortar is remarkably affected by the particle size distribution of the raw materials [35-36]. Under appropriate proportion, some finer particles in the paste, such as fly ash (FA) and limestone powder, fill the voids formed between the coarser particles, acting like a lubricant, thereby reducing the internal friction inside the mortar and enhancing the fluidity [37]. Incorporating more fine particles also reduces the risk of segregation in the pumping process [38]. Generally, a reasonable gradation distribution and moderate proportion of fine-grounded mineral admixtures are beneficial to promote fluidity [36, 39-40]. This is mainly achieved with the addition of mineral admixtures.

The addition of FA has a profound effect on the rheological properties of concrete [41-44] that depends on FA content and size. Laskar et al. [45] reported that a low content of FA (replacing less than 30 wt.% of cement) led to a decrease in yield stress with FA content, since the spherical shape of FA reduces the friction among the angular particles due to “ball bearing effect”, while a higher replacement proportion (30%-50%) has witnessed an opposite effect due to potential adsorption of water reducer molecules by un-burnt carbons in FA. Likewise, Grzeszczyk and Lipowski [46] investigated pastes containing 60%-80% high-calcium FA. Higher yield stress and higher plastic viscosity were found compared with paste without FA. Grinding the FA to finer size

led to sharp viscosity reduction. With regard to the plastic viscosity, Beycioglu and Aruntas [47] pointed out that FA has a spherical geometry and a smooth surface, resulting in a decrease in water demand, hence decreased the viscosity and pose a positive effect on the fluidity of self-compacting concrete. However, Rahman et al. [48] found that FA remarkably increased the plastic viscosity of self-compacting concrete. An analogous conclusion was drawn by Laskar et al. [45] that an increase in plastic viscosity was observed at the 10% replacement rate. There may exist several reasons for these apparently contradictory conclusions on the effect of FA on paste rheology. One primary factor is the type of FA used. Different FA can significantly influence the rheology in different ways. Apart from types and amount of FA, influencing factors may also include the properties of other raw materials and the difficulty in isolating the influence of a single factor. In other word, the interactions between different components need to be taken into consideration.

The influence of other supplementary cementitious materials on the rheology has also been extensively studied and the conclusion are less controversial. In most cases, as the content of ground blast furnace slag (GBFS) increases, the plastic viscosity decreases due to the significant micro-filling effect, while the effect of GBFS on yield stress is uncertain [39, 41, 49-50]. Usually, the addition of silica fume contributes to higher dynamic yield stress and higher plastic viscosity [39, 45, 51-52], while its influence is highly related to the water-to-binder ratio and the different types of superplasticizer applied [35]. In addition, metakaolin and CSA cement are also used to tune the rheology of cementitious material [53-54].

In addition to supplementary cementitious materials, the use of chemical admixtures, like superplasticizer (SP) and viscosity modifying agent (VMA), can effectively modify the rheological properties of fresh mixture. It has been experimentally verified that SP decreases yield stress and plastic viscosity [37, 55]. In the premise of a same water-to-binder ratio, SP can substantially improve the fluidity of mixture without notably impairing its mechanical strength in hardened state. The working mechanism is to disperse the flocculated cement particles by adsorbing the SP molecules onto cement particles, thereby releasing the water trapped in between and improving the rheological behaviors [56]. Due to different molecular structures, the effectiveness of different types of SP in terms of rheology varies. For example, compared with the naphthalene sulphonate-based SP, the SP based on polycarboxylate reduces the plastic viscosity more efficiently, while its ability to lower yield stress is inferior [35]. In the case of VMA, incorporating VMA will facilitate

the increase of yield stress and plastic viscosity and reduce the fluidity [57-59]. Although VMA is effective in enhancing the fluidity and stability of fresh mixture, it should be noted that a higher pumping pressure is required for a more viscous mortar [60]. In addition, retarders, such as sodium gluconate (SG), tartaric acid (TA), citric acid (CA), are also applied to delay the hydration of cement, thereby adjusting the initial fluidity of the mixture and mitigating the workability loss over time [53, 61]. Similar to SP, the type of retarders has a significant effect on rheology modification [62].

The pumpability of ECC requires extra discussions since the fiber reinforcement adds additional variables to the rheological properties when compared with pure mortar. Experiments have shown that ECC mixtures with excessive fluidity led to fiber clumping and thereby suppressed the strain hardening characteristics of ECC, since matrix cohesion should be high enough to facilitate fiber dispersion [8]. To adjust the rheology of ECC to the optimal state, incorporating supplementary cementitious materials and chemical additives are effective means, similar to the case for mortar discussed previously. Partially replacing cement with FA serves to improve the rheological behavior of ECC [63]. It's worth noting, however, that high fly ash content cooperated with high fiber volume fractions may put the mixture at risk of separation and blockage of flow [64]. In regard to admixture, the dosage of SP is crucial to the flowability of fresh mixture of ECC [65-66], while an appropriate dosage of VMA also contributes to good fiber dispersion and enhances the performance of ECC mixtures [67]. Further, combinations of hydroxypropyl methylcellulose (HPMC) and Attapulgite nano-clay (ANC) [13] or melamine formaldehyde sulfonate (MFS) [68] has been verified to be effective in modifying the plastic viscosity and yield stress of ECC mixtures.

Except for rheological considerations, tribology of the material should be taken into consideration as well. Since the mortar flowing through the hose acts as a yield stress fluid, this directly leads to the fact that the mortar within a certain distance from the pipe wall is undergoing shearing, while there is an unsheared zone named “plug-flow” in the center of the pipe [69]. Furthermore, the suspended particles in the mortar will redistribute under the shear force in the outer area and migrate from the high shear rate areas to lower ones [70-71]. Therefore, a circular layer with unknown rheological properties and unknown shear thickness is formed in the hose, which hinders precise prediction of the flow performance of mortar.

During transport, the flowing mortar forms a low-viscosity lubrication layer at the hose wall [3], as shown in Figure 2.3. Studies showed that it is not the overall bulk rheology of the mortar but the properties of the lubrication layer that affect the pumpability and extrudability, i.e., pumping pressure and rate [72]. This poses a further challenge to the prediction of flow performance. It is true not only for ordinary mortar, but also for fiber-reinforced ECC [73]. However, it is worth noting that ECC tends to form a relatively thin lubricating layer during transport, according to [74]. The influence of this phenomenon on the pumpability of ECC requires further exploration.

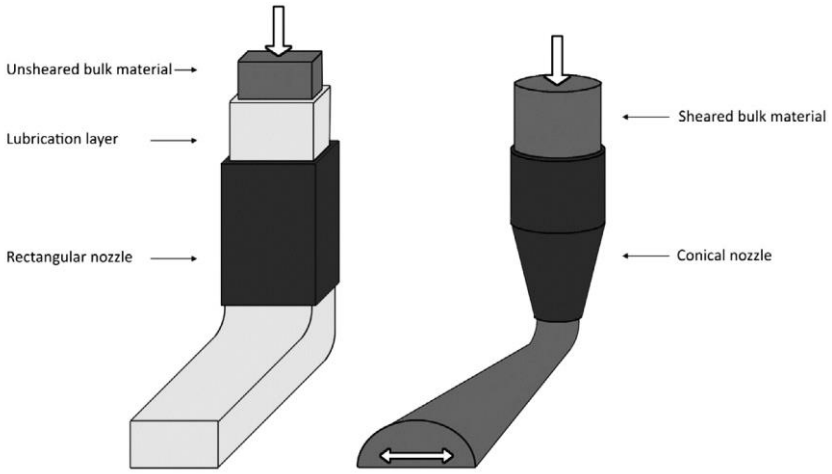

Figure 2.3: Laminar flow in a rectangular nozzle (left) and non-laminar flow in a conical nozzle (right) [72].

2.1.2.2 Extrudability

Extrudability depicts the ease, continuity and stability to extrude well-controlled filament through a nozzle. Extruded filament should meet several criteria to be considered qualified. The extrusion and deposition of the filament should be continuous, without any blockage, segregation or substantial cross-sectional deformation and with an acceptable degree of splitting/ tearing [29]. The quality of extrusion is affected by multiple factors, including the evolution of rheological properties, nozzle size, extrusion speed, etc.

The realization of extrudability is a trade-off of rheological properties. As discussed previously, the fresh mixture demands lower dynamic yield stress and plastic viscosity during pumping and transport to maintain sufficient fluidity under appropriate pumping pressure. However, the extruded filament needs to exhibit high static yield stress and plastic viscosity to maintain the

original cross-sectional geometry. For materials with low fluidity, mixture in the plug zone experiences almost no shear before arriving at the nozzle. Flocculation has already been initiated to provide initial yield stress, which can sometimes reach several thousand Pascals [75]. In this case, such extruded filament is rarely affected by gravity and the geometry of the filament can be well controlled, but at the cost of the extremely high pressure required for extrusion [33]. On the other hand, for materials with substantial fluidity, the material gradually builds up and grows in yield stress until the final shape is settled. During this transition process, the cross-section of filament is not stable and is vulnerable to deformation.

The competing rheological requirements for pumpability and buildability in 3DCP necessitate going beyond the scope of assessing the initial yield stress and viscosity, but instead rely on the control of the evolution of rheological properties over time during the printing process. To date, two approaches have been adopted to comply with the conflicting requirements [6]. One is to use thixotropic material which provides high yield strength and low viscosity after pumping, resulting in relatively high stiffness when extruded [76]. The thixotropic characteristic allows the material to be smoothly transported to the nozzle and maintain the desired cross-sectional geometry thereafter. The second approach is two-stage mixing. Fresh mixture with high fluidity is first pumped to the nozzle position, then accelerator or thixotropic agent is injected into the mixture shortly before deposition [33, 72, 77]. In this case, the desired shape retention ability is achieved within a few seconds after extrusion. Although this approach eliminates the requirement for inherent phase-change properties of the printable material, this further complicates the nozzle design in order to achieve the injection and dispersion of additives.

The size of the nozzle has a profound effect on extrudability. The ratio of maximum particle size to nozzle diameter is the most important indicator. If the particle size of the aggregate is not in an appropriate portion with the nozzle size, blockage and segregation can be induced, resulting in discontinuous filament. Malaeb et al. [78] reported that for aggregates with a maximum size up to 2 mm, optimal diameter for the nozzle is 20 mm. It was found that larger diameters would yield buildability issues, while smaller diameters cause segregation. Notwithstanding, for a similar aggregate size up to 2mm, Le et al. [22] succeeded in forcing the material smoothly through a 9 mm nozzle. The general correlation between nozzle size and particle size has not yet been established.

Another controlling factor of extrudability is the synchronization between movement speed of the nozzle and the flow rate of the extruded material. The flow rate should be accurately synced with the nozzle movement, otherwise the printed filament will exhibit discontinuity or inconsistency. However, it is difficult to reconcile the nozzle movement speed and the material extrusion speed. One method that has been proven effective is to dynamically adjust material flow rates through feedback. In the printing system designed by McGee et al. [64], a custom-built servo-driven progressive cavity (PC) pump is fed by a hopper mounted to a servo-driven peristaltic pump. The pressure sensor installed at the inlet of the PC pump provides the peristaltic pump feedback signal to maintain a constant inlet pressure when the flow rate changes. In addition, another in-line method has recently been proposed to quantify extrudability by measuring the electric power consumed during extrusion, i.e., unit extrusion energy. This innovative method establishes the connection between print head velocity and concrete pump discharge rate [79].

Compared with traditional cementitious material, a key consideration for ECC extrusion is fiber orientation. It is often assumed that the fibers in the extruded filament are aligned along the direction in which the printing nozzle moves. Nonetheless, Figueiredo et al. [19] revealed that the highly flexible fibers are mainly oriented diagonally in the printing plane and show a V-shape behind the nozzle rather than parallel to the printing path. The friction between fiber and the inner wall of nozzle and the lack of restriction at the nozzle outlet will cause deviation of fiber direction. Moreover, the orientation of fibers will also be affected by the ratio of fiber length to nozzle opening [6]. In [80], different ratios of fiber length to nozzle diameter have been extensively tested and optimized in fiber-reinforced concrete. By using a nozzle diameter (2 mm) that is smaller than the average fiber length (3-6 mm), the fibers can be highly aligned parallel to the printing path, thereby increasing the bending/tensile strength along a designated direction. Smooth extrusion and appropriate distribution of fibers are critical to the success of 3DP-ECC. They are not only related to the fresh properties of ECC, but also have a decisive influence on the hardening performance, which will be further discussed in the latter section.

2.1.2.3 Buildability

Buildability is defined as the ability of the printable material to build up without collapse or the resistance of deposited material to deformation under deadweight loading as the number of layers

increase, i.e., the shape retention ability of printed filament and component [29]. Lack of buildability severely undermines the stability and reliability of the printed element.

At the filament scale, the extruded filament must be able to withstand its own weight and the ever-increasing weight of the upper layers. The dominant form of this gravity-induced stress is shear stress, which imposes requirements on the yield stress of the wet materials [72]. The rate at which the yield stress increases with time, i.e. the structuration rate [81], is expected to scale with both the various length scales of the printed object and the extrusion length scales of the printing process [33]. Once the generated vertical stress in the filament exceeds its yield stress, the filament will deform or yield, resulting in variation in its cross-sectional shape or structural collapse.

Roussel [72] summarized the critical requirements for yield stress evolution during the deposition process (see Figure 2.4), considering potential failure of the underlying material due to gravity-induced stress. When a single layer of material is positioned, the magnitude of its self-weight stress should be around $\rho g h_0$, where h_0 is the layer thickness. As the layers stack up, the critical value of the yield stress is affected by the structure rising speed $\dot{H}$, where H represents the height of structure and $\dot{H}$ is its time derivative. Structure elevation demands a structuration rate $A_{thix} = \rho g \dot{H} / \sqrt{3}$ that scales with $\dot{H}$ [82]. Therefore, the minimum required yield stress is simply A_{thix} times the time t. Further, by the end of the duration, the stress level of the bottom material reaches $\rho g H / \sqrt{3}$. The yield stress of the wet material at each stage must be greater than the corresponding critical value demonstrated above to avoid failure at the material scale.

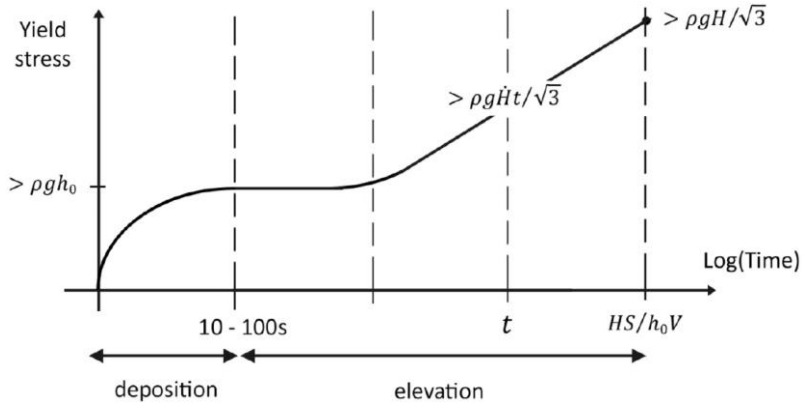

Figure 2.4: Yield stress evolution and target requirements, where S is the length of printing path, V is the nozzle velocity, and ρ is the printed material density [72].

Based on the comparison between the vertical stress acting on the initially deposited layer and the yield stress of the material, Perrot et al. [83] developed an analytical model for predicting the buildup rate as Equation 2.1.

$$\sigma_c(t) = \alpha_{geom} \cdot \left[\tau_{0,0} + A_{thix} \cdot t \right] \tag{2.1}$$

where $\sigma_c(t)$ is the critical failure stress which is compared with the gravity-induced stress, α_{geom} is a geometric factor of the printed structure and $\tau_{0,0}$ is the initial yield stress right after deposition. Through this model, it is possible to predict the failure height and the corresponding printing time, which further relates to the printing speed. However, this model mainly considers the failure at the material level, i.e., the deformation and collapse at the structure level are not considered.

In order to predict and analyze the mechanical properties of the overall structure, Suiker [84] suggested a mechanical model that considers elastic buckling failure and plastic collapse for straight wall structures. Roussel [72] proposed the analysis approach of critical height H_c, at which self-buckling is expected to occur in a slender printed structure, based on the elastic modulus requirement (Figure 2.5). More evaluation methods and models for predicting buildability are illustrated in Section 3.1.

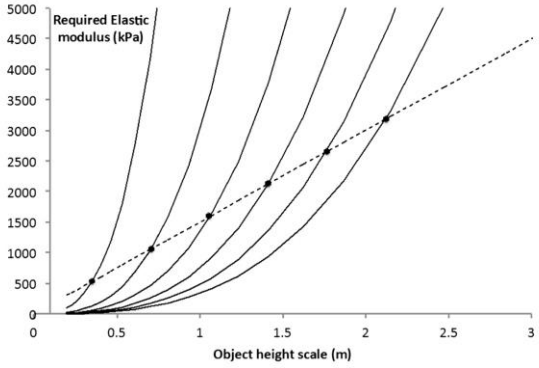

Figure 2.5: Required elastic Young modulus based on strength-based material failure (dotted line) and structural buckling (continuous lines) for layer widths of 5, 10, 15, 20, 25 and 30 cm and for a critical flow-onset shear strain of 2% [72].

Buildability is closely associated with layer cycle time. The printing path of extrusion must have a finite length to form successive layers. The time required for the nozzle moving from one point to the corresponding point of the next layer is then defined as layer cycle time [3]. The layer cycle time imposes influence on the buildup process from two contradictory perspectives. On one hand,

prior to deposition of the next layer, the extruded material should have a short rest time to build up internal structure, thereby maintaining its chemical activity to bond with the upper layer [82, 85-86]. Otherwise, cold joints are likely to form between the layers and weaken the interface. On the other hand, in the absence of agitation and shear stress, the yield stress of the wet material increases approximately linearly or exponentially with time [81, 83, 87-88]. If this dormant period is not long enough, sufficient shape stability cannot be developed, and the material may experience damage under gravity-induced loads. Moreover, if the horizontal printing speed is excessively increased in pursuit of a shorter layer cycle time, the existence of inertial stress in the extruded material cannot be neglected as conventionally. Therefore, rapid deposition may cause geometric defects in the extruded cross-section [3, 72]. To determine an optimal time interval for layer cycle, Yuan et al. [89] designed a device to monitor the change of layer deformation. Through simulation, the layer cycle time is correlated with and derived from the growth rate of static yield stress.

2.1.3 Hardened properties characterization

To be accepted as a reliable construction method, the extrusion of cementitious materials must lead to stable structural performance, while the material properties in the hardened stage dominate the structural performance of the printed component.

2.1.3.1 Layer adhesion

Layer interface is a weak link in the printed object, which can be attributed to multiple factors: 1) high interlayer porosity; 2) weak bond between adjacent layers caused by layer cycles and potential cold jointing; 3) lack of fiber bridging in fiber-reinforced cementitious material.

Layer adhesion is intensively affected by the cyclic printing process [90-91]. While the former layer of material undergoes rapid structural build-up after extrusion, it is gradually losing its ability to establish a tight bond with the next layer of wet material. Fast structuration, high thixotropy and long waiting time can cause so-called “cold joint”, and these factors are interconnected [86, 91-96]. Once the layer cycle time allows the thixotropy and structuration to take charge, the increased consistency of the previous layer will prevent the flow of latter layer from reinitiating a flow at the

surface and weak interface adhesion will be formed. Also, lack of contact between the adjacent layers can undermine the interfacial connection [97].

Moisture loss at the interface, which scales with layer cycle time, is also an important cause for weakened interlayer adhesion [94-96]. Without the protection of formwork, the outer surface of the wet material is exposed to external environment once extruded. After a dry region with thickness of a few hundreds of micrometers formed near the surface, free water on the surface that facilitates hydration and builds reliable bonding with the next layer becomes unavailable. In this case, Keita et al. [98] reported a 50% reduction in tensile splitting strength for uncovered specimens, compared with those where measures are taken to prevent dissipation. Similarly, the addition of accelerators will promote the early hydration, and thereby quickly consuming the free water at the interface, which will also hinder the generation of bond strength [99].

It has been shown that the length of layer cycle time has a significant impact on the interface. For example, affected by the layer cycling process, counting in structuration and water loss, the interfacial bond strength may be reduced by approximately 50% within tens of minutes [72], and even 77% in the extreme case where the layer cycle time is extended to 7 days [85]. However, some researchers have demonstrated that this effect may not be linear. Panda et al. [100] pointed out the existence of a critical time interval window. Within this time window, the degradation of interfacial strength is almost negligible; but once the time window is exceeded, reduction in bond strength is substantial.

For fiber-reinforced cementitious material, the interlayer situation is further complicated, since fiber orientation issues are involved. Affected by the extrusion process, random orientated fibers will be realigned as the fresh material flows through the nozzle. Therefore, majority of the fibers in the bulk material are distributed horizontally and are approximately parallel to or at a small angle to the direction of nozzle movement [80]. Intuitively, the fraction of fibers penetrating through the layer interface is minor, i.e., fiber bridging is scarce at the interface [101]. However, it has been proven experimentally that there are indeed a small amount of fibers bridging the cracks to slightly facilitate layer connection perpendicular to the print direction [6]. More research is needed on the horizontal layer interface of fiber-reinforced materials, seeking effective means to address the lack of interlayer fiber bridging.

Except for bridging effect, the addition of fibers may affect the interlayer bonding from another aspect, i.e., rheological properties. Usually in the case of mold-casting, the addition of various fibers can enhance the mechanical properties of concrete specimens, whereas in the case of 3D printing, fibers may have a negative impact on the filament bonding of the layered structure. It was found that the interlayer bond strength of polymeric fiber-reinforced geopolymers was 15%-23% lower than that of the control group without fibers. Polyvinyl alcohol (PVA), polypropylene (PP), and polyphenylene benzobisoxazole fibers were included in the experiment and reached a consistent conclusion [102-103]. This phenomenon is explained as the influence of fibers on the overall rheological properties. Compared with mixtures with no fiber, fiber-reinforced fresh materials yield relatively high stiffness in single layer cycle, thus impairing its ability to form a seamless interface with the previous layer. Considering the quality of the printed interface is affected by multiple factors, it may be possible to address this problem by properly tailoring the material properties.

In addition, Nerella et al. [93] found that even at a fixed interval of 1 day, the interface tensile strength of the mix with pozzolanic additives was reduced by less than 25%, while the one without pozzolanic additives experienced a reduction of 90%. This seems to show that interface performance is also highly related to material composition.

Through the above discussion, it has been shown that a wide range of process-dependent and material-dependent factors can affect the interfacial bond strength. However, going from one combination of systems and materials to another can yield considerably different outcomes. How to optimize the interlayer bonding still remains an urgent issue to be solved.

Various methods have been proposed. One attempt is to manually apply an adhesive agent to the interface. Cement paste [104], sulfur and black carbon-based polymers [105], and cellulose fiber reinforced cement [106], for example, are used as adhesive agents to be brushed on the surface of the newly printed layer. However, this method requires additional human labor and thus weakens the automation of the entire manufacturing process. Another method is to enhance interfacial bonding through mechanical interlock, for instance, integrating the tongue and groove technology into 3D printing to obtain a special grooved geometry (Figure 2.6) [6, 92], or modifying layer surface to make it rough enough to adhere to the next layer [107].

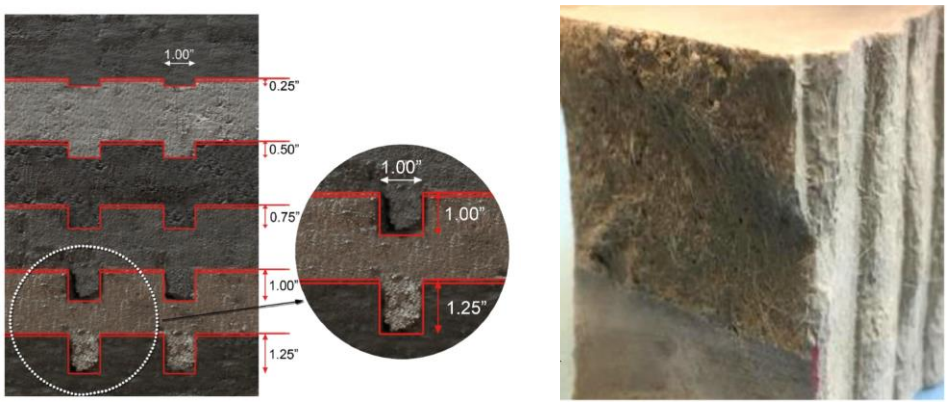

Figure 2.6: Grooved geometry of 3D printed conventional concrete (left) [92] and ECC (right) [6].

2.1.3.2 Anisotropy

Regarding the mechanical properties of 3DCP, the most notable feature is the widely reported anisotropy. This is determined by the nature of 3D printing manufacturing. Layering process will inevitably cause structural differences between the printing operation plane and its orthogonal direction (usually the vertical direction), which can be generally attributed to the property deviation of the interlayer surface from the bulk material. In order to assess the anisotropy of the printed object, mechanical properties are generally tested from three different loading directions, i.e., the longitudinal printing direction (Orientation III), the horizontal lateral direction perpendicular to printing direction (Orientation II) and the vertical direction orthogonal to the printing layer (Orientation I), as demonstrated in Figure 2.7.

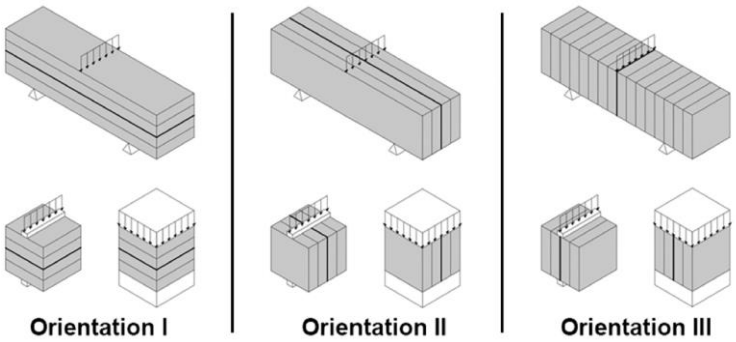

Figure 2.7: Directionally dependent mechanical testing respective to layer orientation [33].

The direction of printing and loading has a crucial influence on the tensile performance of the printed component. The out-of-plane (perpendicular to printing surface) tensile characteristic mainly presents as the interlayer bonding between successive filaments, which has been elaborated in the section of layer adhesion. While the in-plane tensile resistance can vary greatly in the cases with or without inner fiber reinforcement.

One of the greatest challenges of 3D printing is that conventional reinforcement is incompatible with extrusion process. As a quasi-brittle material, the tensile performance of concrete limits its structural application in different scenarios. To overcome this drawback, the potential of fiber-reinforced materials has been explored. It is widely acknowledged that the tensile properties of fiber-reinforced cementitious materials mainly depend on fiber distribution and pore size distribution. It is also the case for 3D printing. With the addition of fibers, the tensile properties in the in-plane direction are significantly improved due to the consistent fiber orientation (Figure 2.8) [19, 80, 108]. Moreover, the extrusion process improves the microstructure of matrix by forming uniform pores with narrower distribution, which also contributes to the excellent tensile performance [13].

Fiber addition has been seen to elevate the tensile strength of printed components. Panda et al. [109] used 0.25 wt.%-1.0 wt.% glass fiber to reinforce the geopolymer matrix and observed a significant improvement in tensile strength which scaled with the fiber content. Reinforced with 0.5 wt.% basalt fiber, concrete printed by Ma et al. [108] also showed a splitting tensile strength 10% higher than that of its cast equivalent.

Compared with tensile strength alone, tensile ductility of printed material is more of interest to structural design. This highlights the field of printed ECC. Zhu et al. [13] obtained printed ECC with a tensile strain capacity of more than 11% (with 2 vol.% polyethylene (PE) fibers) and verified that the tensile strain hardening characteristic of ECC along the printing direction was further enhanced compared with the cast equivalent. Superior strain-hardening characteristics of printed ECC in the longitudinal direction to that of mold-cast specimen are also reported by Yu and Leung [18], Ogura et al. [15], and Yu et al. [110] .

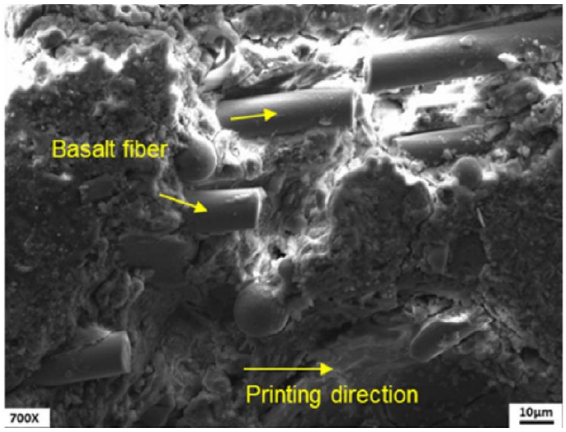

Figure 2.8: Fiber alignment at microscale [108].

Analogous to tensile strength enhancement, fiber reinforcement is also regarded as an effective means to overcome the shortcomings of insufficient flexural strength of printed components. With addition of fibers, flexural strength is mainly governed by the central bottom area of specimens where the maximum tensile stress occurs rather than the weak layer interface. Some studies suggested significantly enhancement of the flexural performance of printed components. Different types of fibers are involved, including PP fiber [85, 90, 102], PE fiber [13, 15, 101], PVA fiber [14, 19], glass fiber [109], carbon fiber [80] and basalt fiber [80, 108] and steel fiber [111].

Generally, the ultimate flexural strength and post-peak behavior of 3D printed fiber-reinforced materials in Orientation I is notably improved compared with traditional cast specimens, which is due to the advantages brought by uniform fiber orientation in printing. However, fiber type and fiber dosage imposes an important influence on the intensity of enhancement. For example, for PP fiber, only 0.25 vol.% dosage will greatly improve the flexural strength of 3D printed geopolymers by 17% to 34%, while 0.75 vol.% and 1.0 vol.% PP fibers could trigger flexure-hardening behavior [102]. Moreover, Le et al. [85] observed an increase of up to 45% in flexural strength, when a small amount of PP fibers is included. As for PE fiber-reinforced 3DP ECC, a 4%-9% increase was found compared with cast ECC with 1.0 vol.%-2.0 vol.% fiber dosage [13]. While in [101], a 30% increase corresponds to a 0.25% PE fiber content. Similar laws and deviations apply to other types of fibers as well. In sum, fibers have a positive effect on flexural performance, but to which extent the performance can be improved depends on the specific material composition, specimen type and printing setup.

Intuitively, the flexural performance in Orientation III shows substantial anisotropy. The flexural strength tested in this direction is lower than those in other directions. This is because the load is applied in the interface between filaments and the strength is highly dependent on the interlayer bond strength. Wolfs et al. [90] declared a flexural strength 14% lower than that in orientation I. The decrease by 14% is considerably smaller than the percentages up to 50% which were reported in [85] and [109]. Obviously, this deviation is closely related to the printing procedures and the resulting layer interface quality. With regarding to Orientation II, the flexural performance is usually between those in the other two directions [85, 108].

For compressive strength, the discrepancy is less dramatic. In Orientation III, compressive strength of 3D printed component is generally lower or comparable to that of its cast equivalent. The reduction in compressive strength can be explained as the interlayer voids introduced in the 3D printing process. It has been reported that the strength of hardened printed concrete may reach 80%-100% of cast [29]. While for materials with fiber, there is a wider range of deviations in the reported test results. Wolfs et al. [90] claimed that only 70% of cast strength was shown on printed components with polypropylene (PP) fibers. While ratios ranging from 70% to 95% were observed in [85]. Zhu et al. [13] found that the compressive strength loss of the 3DP ECC is up to 12%, varying with the fiber content. A similar conclusion is obtained by Yu and Leung [18]. Figueiredo et al. [14] reported that the compressive strength produced by the two manufacturing methods are very similar.

Less affected by anisotropy on the horizontal printing plane, the compressive strength in Orientation II is very close to that in Orientation III. This has been proven to be true for both conventional concrete and fiber-reinforced material by a number of studies [14, 85, 112].

Regarding the vertical direction, i.e., Orientation I, the influence of anisotropy seems uncertain, depending on material types. For printed conventional concrete, test results by Wolfs et al. [90] showed that anisotropy in compressive strength is almost negligible. While for fiber-reinforced geopolymer and ECC, the direction-dependent anisotropy is more pronounced. It was observed by Nematollahi et al. [112] that the compressive strength of the printed fiber-reinforced geopolymer in the vertical direction is considerably higher (up to 70%) than that in the horizontal plane, which can be attributed to the fact that the alignment of the fibers parallel to the extrusion direction help to bridge cracks formed under vertical compression. However, after the fiber content reaches 0.25

vol.%, further increase in fiber content downgrades the compressive strength in the vertical direction. The author concluded that the more air entrapped by the fibers leads to an increase in porosity and consequently a decrease in strength. However, in the experimental investigation by Figueiredo et al. [19], the vertical strength of ECC is 5%-17% higher compared with that in the horizontal direction. This ratio is significantly lower than the figure in the previous study. A contradictory conclusion was reached with an observed fact by Panda et al. [109] that the vertical strength (Orientation I) is lower than that in the printing direction (Orientation III) with glass fiber.

In fact, fiber introduction has both positive and negative effects on strength. On one hand, fiber incorporation leads to increased porosity and thereby a decreased strength; on the other hand, fiber can bridge the cracks and partially offset the negative effect of porosity [102]. Therefore, the final presentation of strength is the result of the combat of these two effects. Due to the limited research and the influence of multiple factors, including possible differences in material compositions, printing setup, and practical operations, a universal law in compression performance of printed components has not been established yet.

2.1.4 Durability concerns

Shrinkage and the associated cracking (Figure 2.9) pose construction concerns, particularly for 3D concrete printing (3DCP), as the elimination of formwork exposes the printed structure to the external environment at an early age, leading to excessive moisture loss and subsequent drying shrinkage and plastic shrinkage. Moreover, 3D printing typically involves the creation of thin-walled structures in the unit of filaments, resulting in a larger surface area-to-volume ratio that generally exceeds that of conventional structures. This further promotes early shrinkage. In addition, the absence of coarse aggregates and high binder content in printable cementitious materials exacerbate shrinkage concerns. Early shrinkage cracking can compromise the structure's mechanical properties and facilitate the ingress of corrosive agents, thereby raising concerns about structural integrity, safety, and durability.

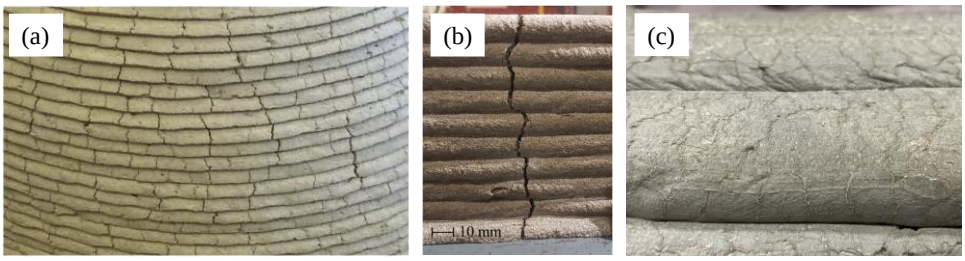

Figure 2.9: (a) Excessive cracks [113], (b) penetrating crack [114], and (c) surface cracks in 3D printed concrete/mortar elements.

Cracking in printed structures caused by shrinkage has been documented in real construction projects. For instance, in the printed Beckum House, located in Germany, cracks were observed and attributed to drying shrinkage induced by strong winds [115]. Similarly, in the reception center building on the Civic Square in Nanjing, China, cracks perpendicular to the print plane were noted on the facade elements, and the high cement content and the lack of coarse aggregate were presumed to be the cause [115].

Despite its significance, a standard procedure for measuring the shrinkage of printed components has yet to be established. Researchers have used different approaches to evaluate shrinkage. Le et al. [85] used mold-cast specimens cured in environments with varying humidity levels to probe the shrinkage behavior of printable materials. Similarly, Rahul et al. [116] evaluated the total and autogenous shrinkage of printable concrete with mold-cast samples and documented lower shrinkage with coarse aggregate included. Length comparator used in conventional shrinkage tests has also been applied to measure the free length change of hardened printed samples [117-118]. However, this approach is challenging for newly extruded fresh mixtures and omits the shrinkage before cement setting.

Non-contact measurements, such as laser measurement and digital image correlation (DIC) methods, have shown promise in monitoring printed components in both fresh and hardened states [2]. Federowicz et al. [119] attached steel reference points at both ends of a printed single filament, which allow for laser sensor measurement of free shrinkage. DIC system has also been adopted to capture surface displacements in printed single-layer or multi-layer elements and analyze shrinkage deformation and cracks by Moelich et al. [113, 120], Bertelsen et al. [121], Van Der Putten et al. [122], and Zhang and Xiao [123] (Figure 2.10).

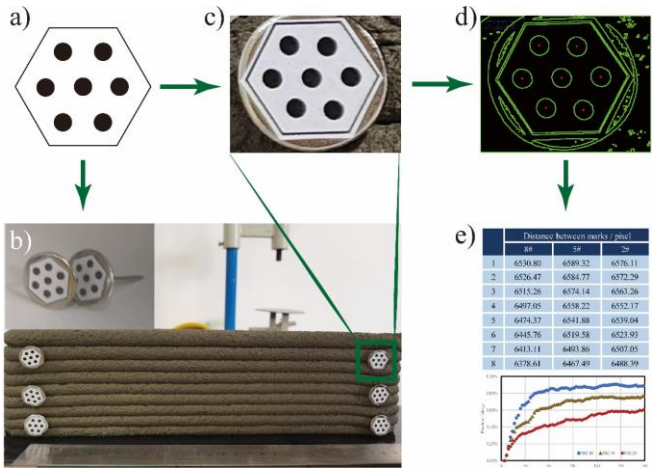

Figure 2.10: DIC system adopted in shrinkage test. (a) Black-white marker image; (b) Markers inserted into specimens; (c) Markers in photos found by feature pointes; (d) Wireframes of markers; (e) Distance measurement results. [123]

Various strategies have been developed to alleviate undesired shrinkage and shrinkage-induced cracking in mold-cast samples and 3D-printed elements [124]. Those have been proven effective include the addition of fibers [112, 117, 125-128], shrinkage reducing admixtures [119, 129], superabsorbent polymers [122, 130-132], and calcium sulfoaluminate cement [133-134]. Among them, fibers have been reported to efficiently alleviate plastic shrinkage and inhibit crack formation and propagation by bridging the cracks; shrinkage reducing admixtures (SRA) mitigate the issue of shrinkage by decreasing the surface tension of the pore solution, thereby impeding the evaporation of pore water; superabsorbent polymers (SAP) hold promise in reducing plastic shrinkage, drying shrinkage, and autogenous shrinkage by gradually releasing absorbed moisture into the cementitious matrix. It is important to note that the storage and release of water in SAP may affect the rheological properties of printable material during 3D printing, such as an increase in buildability [135-136]. As an alternative approach to mitigating shrinkage, incorporating calcium sulfoaluminate cement (CSA) generates a considerable quantity of ettringite during hydration, which exhibits expansive nature [137]. By partially substituting ordinary Portland cement (OPC) with CSA, the shrinkage of cementitious materials can be offset by this volume expansion. Nonetheless, the expansion magnitude of CSA is contingent on the amount of available gypsum and hydration water [138].

2.2. Engineered Cementitious Composites (ECC)

ECC is a type of fiber reinforced cementitious composite that addresses the fundamental weakness of conventional concrete, which lacks tensile deformation capacity. The most prominent and valued features of ECC are its high ductility and strain-hardening behavior [7]. ECC achieves ductility by systematic tuning of its microstructure to enable synergistic interactions between its fiber, matrix, and fiber/matrix interface features. As a result of deliberate engineering, the stress-strain curve of ECC is more similar to that of a metallic material, with a distinctive "yield" strength followed by tensile strain-hardening behavior. Hence, ECC is also known as Strain-Hardening Cementitious Composites (SHCC). During strain-hardening with multiple load-drops of varying magnitude, the stress-strain relationship can be approximated by a second linear branch with a lower slope than that during elastic deformation. The significant ductility of ECC arises due to the increasing number of closely spaced micro-cracks with crack widths typically less than 100 μm (Figure 2.11). The strain capacity is typically two orders of magnitude higher than that of normal concrete, which effectively contributes to enhance infrastructure resilience, durability, and sustainability by suppressing fracture failure.

Figure 2.11: ECC has high deformability while suppressing brittle fracture under (a) bending load and (b) direct tension. [7]

ECC has also shown exceptional durability in various exposure conditions, primarily due to the intrinsic tight crack width, which is independent of reinforcement details or structure size and

significantly reduces the effects of cracking-related deterioration mechanisms, making ECC structures more sustainable.

Moreover, the ductility of ECC plays a crucial role in extending the service life of structures. The project cost from a life-cycle perspective is effectively lowered due to reduced structural dimensions, elongated service life and reduced maintenance needs. Studies demonstrate that using ECC instead of conventional concrete in bridge decks and pavements projects can result in significant life-cycle cost savings up to 50% [139-142].

Field applications of ECC has been growing and validating the unique properties of ECC. ECC has found application in the domains of building, transportation, and water infrastructure, where specific mechanical and durability properties are exploited for each application. For instance, Glorio-Tower in Central Tokyo, Nabule Yokohama Tower in Yokohama, and Kitahama Tower in Osaka adopted ECC coupling beams in the building cores to enhance seismic resilience (Figure 2.12). Furthermore, an ECC link-slab was cast on-site on a bridge-deck in southern Michigan, which demonstrated robust service status even after more than a decade of use (Figure 2.13). In Shanghai, China, a special-shaped arch-shell with notable curvature was manufactured by spraying ECC into 3D printed mold and serves as a part of the Bamboo and Rattan Pavilion in the Flower Expo Garden in 2021 (Figure 2.14). The arch-shell works independently without any steel reinforcement and shows the excellent mechanical capacity of ECC structures. In addition to new structural applications, ECC has also been adopted as a desirable material for repairing or retrofitting various infrastructure types.

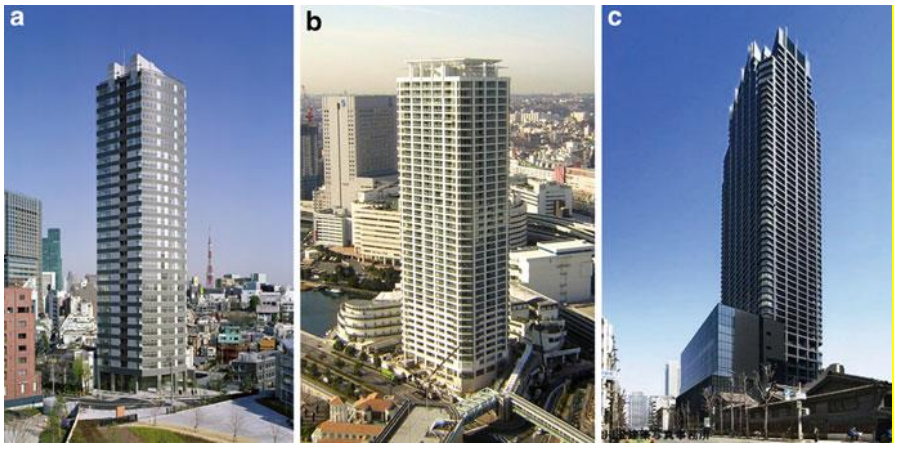

Figure 2.12: Buildings with ECC coupling beams: (a) 27 story Glorio-Tower, Tokyo, (b) 41 story Nabule Yokohama Tower, Tokyo, and (c) 60 story Kitahama Tower, Osaka. [7]

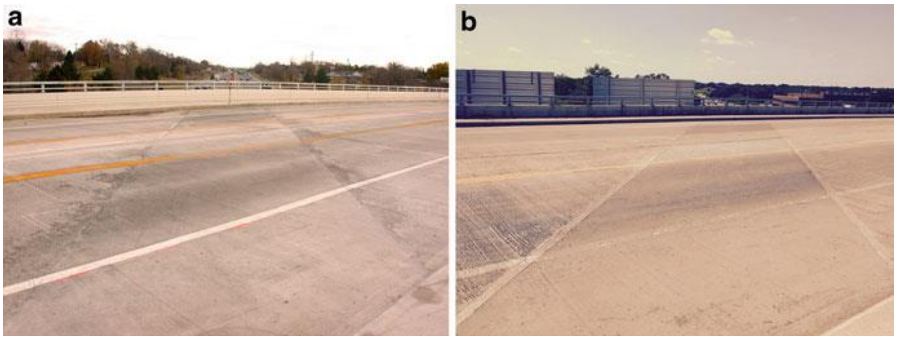

Figure 2.13: ECC link-slab (a) immediately after construction and opening to traffic in 2005 and (b) in 2015. [7]

Figure 2.14: Bamboo and Rattan Pavilion in the Flower Expo Garden, Shanghai, China. [143]

In recent years, various codes and specifications for ECC applications have been developed world-widely, providing testing and design guidelines for ECC structures, e.g., "Recommendations for Design and Construction of High Performance Fiber Reinforced Cement Composites with Multiple Fine Cracks (HPFRCC)" by Japan Society of Civil Engineers [144], "Strain Hardening Cement Composites: Structural Design and Performance" by RILEM [145], “JC/T 2461–2018 Standard Test Method for the Mechanical Properties of Ductile Fiber Reinforced Cementitious Composites” by Ministry of Industry and Information Technology in China [146], “T/CECS 1212-2022 Technical Specification for Strain-Hardening Cementitious Composites Structures” by China Association for Engineering Construction Standardization [147], etc. These documents provide valuable design guidance and shed light on appropriate adoption of ECC in reality.

2.3. Challenges and research priorities in 3D printing ECC (3DP-ECC)

3DCP has gained considerable attention both in academia and industry. Unlike traditional construction methods where components are cast in one go, 3DCP involves multiple steps, and various stages need to be smoothly linked. Many variables are therefore introduced into the printing process. In this regard, reliability of the technology and its final products has naturally become the most focal point of attention. For 3DP-ECC, similar challenges have been posed. To provide insights on proper quality control, major challenges are identified:

(1) Printability of cementitious material. Often conflicting requirements are imposed on the printing material during extrusion, especially in rheology and thixotropy. The composition, mix proportion, and workability of printable materials must be strictly controlled and harmonically tuned to meet the performance demands of different stages in the printing process.

(2) Compatibility between printable material and printing device. Precise coordination and synchronization are needed in the process of pumping, extruding, and building of cementitious materials. Therefore, printing systems capable of real-time monitoring and dynamic accommodation of the printing parameters to the material properties evolution are expected. Moreover, for ECC, the high content of fiber necessitates a more cautious selection of printing setups to achieve smooth extrusion.

(3) Reliability of the printed object. The ultimate goal of 3DP-ECC is to be widely recognized as a reliable automatic construction method that can be broadly applied to engineering practice. The prerequisite is that the printed component exhibits a solid service performance at least comparable to its cast equivalent. Structural stability and long-term performance are primary concerns.

To meet the above challenges and truly initiate a digital revolution in the construction industry, the following areas have been highlighted as the research focus and priorities for this thesis:

(1) Quantification of printing requirement. The existing evaluation indicators for fresh performance of 3DCP are mostly conceptual but lack quantitative means and criterion. For example, the assessment of buildability highly relies on visual inspection and empirical judgment. In this case, standard test methods, key indication parameters and allowable thresholds should be specified to establish a systematic quality control procedure for printable material.

(2) Alleviation of anisotropy. The inherent anisotropy of 3D printed objects has been demonstrated. The origin of the difference between printed and cast components can be mostly attributed to the presence of layer interface. Techniques to enhance the integrity of interfaces should be developed to promote overall structural performance.

(3) Implementation of structural-scale testing. Very limited studies on load testing at the structural level of printed structures have been present [148-149]. The need of better understanding structural integrity necessitates the implementation of structural testing, especially when steel reinforcement is eliminated, i.e., the case for ECC. This is critical for using strain-hardening ECC to overcome the incompatibility between steel reinforcement with the 3DP process for large scale structures.

(4) Reduction of carbon footprint. Considering the high binder content in printable cementitious materials, the resulting carbon emissions partially offset the positive environmental impact brought by 3D printing technology. Many beneficial explorations have been conducted, such as using low-carbon materials instead of traditional OPC. These preliminary explorations need to be followed up with more in-depth studies, to shoulder the responsibility for the entire human society while evolving the construction method.

Chapter 3. Fresh Properties Characterization of 3DP-ECC

3.1. Introduction

Buildability is generally characterized as the ability of the printable material to build up without significant deformation or collapse [72, 150-151]. Lack of buildability severely undermines the stability and reliability of the printed element. Generally, failures induced by insufficient buildability fall into two categories: local failure of material and overall collapse of structure [152] (Figure 3.1).

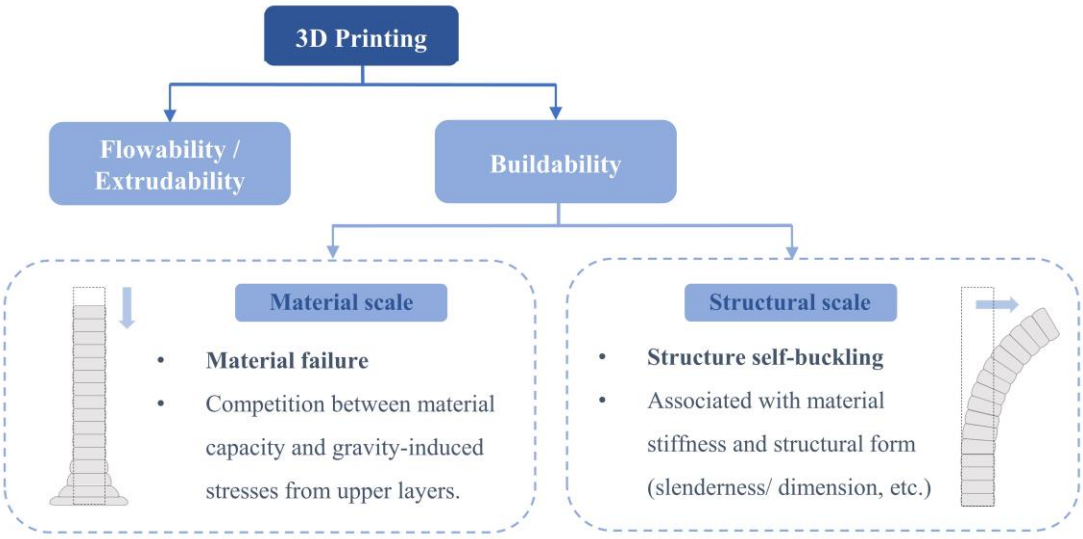

Figure 3.1: Failure modes during 3D printing.

At the material scale, the extruded filament must be able to withstand its self-weight and the increasing weight of the gradually built-up superstructure. Therefore, rapid increase of the strength and stiffness capacity are necessary once the filament is in place [33, 72, 81, 83]. Moderate and controllable deformation under loads facilitates the newly printed filament to joint with the previous layer in order to obtain sufficient layer adhesion [3]. Excessive deformation, however, will threaten the stability of the structure and results in overall failure. Once the generated vertical

stress in the filament exceeds its capacity, the filament will yield or deform significantly, resulting in variation in its cross-sectional shape and instability of the structure.

At the structural scale, even if the stress in a single layer is kept below the stress threshold, without causing any material failure, the cumulative strain and stress accounting for all the layers may impair the shape control and structural stability of the printed object, resulting in overall collapse of the element, especially when the printed structure is slender and vulnerable to self-buckling [3, 72, 75, 116, 153]. To evaluate the structural failure, Suiker [84] suggested mechanical models that considers elastic buckling failure for printed structures. Roussel [72] illustrated the requirements on the material elastic modulus based on the critical height H_c, at which self-buckling is expected to occur in a slender structure, as shown in Equation 3.1, to direct the design of materials.

$$H_c \approx \left(\frac{8EI}{\rho g A} \right)^{1/3} \tag{3.1}$$

where E is the elastic modulus of the fresh material, I is the moment of inertia, ρ is the density of printable material, g is the acceleration of gravity, and A is the horizontal rectangular cross-sectional area.

Various approaches have been proposed to experimentally evaluate buildability. The most straightforward one is to compare the maximum height or number of layers that can be stacked under the same print settings [22, 76, 151, 154-157]. Nonetheless, to visually inspect the buildability of material, printing is needed for each assessment. This evaluation method is suitable as an indicator for comparative and qualitative studies after printing without providing an effective prediction of buildability. Similarly, vertical strain or deformation of printed element also serves as an indirect evaluation index in post-hoc analysis [89, 158-159]. Another strategy is to predict the buildability of materials in the 3DP process ex ante by measuring material properties. Some of the commonly used material performance indicators include green strength [75, 160-165], yield stress [166-169], penetration resistance [168, 170] of wet material, etc. It is also suggested that cylinder stability test, which describes the deformation of a concrete cylinder after dynamic tamping or under static loading, can be applied to assess the shape stability of printed material [76]. Nonetheless, these indicators are mostly valued as references at discrete time points and assessed independently with printing parameters. Few studies have combined and interrelated the material evolution and structural buildup on a continuous timeline [16]. Furthermore, the majority of

previous studies focus on predicting the critical failure height/layer number. While another concern about 3D printed structure, that how to estimate and predict the deformation of printed structure when neither material nor structural failure happens, is barely addressed. Panda et al. [162] proposed an approach to estimate the deformation of printed structure based on material stiffness and geometrical parameters. However, the model assumed time-invariant material stiffness, which is only appropriate for evaluation of 3D printing finished within a short printing duration.

Furthermore, discrepancy in buildability of 3DP-ECC requires more attention. 3D printing of a twisted hollow ECC column up to 1.5 m high has been reported in [12]. In contrast, ECC elements were reported [13-14] to collapse at less than 17 layers during printing. In addition, 3DP-ECCs with enhanced buildability through optimizing static yield stress [15] and particle size distribution [11] supported the buildup of 120 mm and 210 mm high wall elements, respectively. Such discrepancy stems from the different printing mixture compositions, structural forms, printing setups and parameters. Multiple influencing factors and their interaction prohibit the establishment of a consistent methodology for evaluating the buildability of 3DP-ECC.

To fill the knowledge gap highlighted above, this chapter aims at providing a quantitative methodology for evaluating the buildability of printable ECC at both the material and structural scale. At the material scale, constant shear rate tests and incremental loading tests were conducted to assess the material capacity of fresh printable ECC. Further, the green strength of fresh ECC at different ages was characterized to derive a time-dependent strain-stress model, incorporating the influence of print settings (structure buildup rate). At the structural scale, the stiffness evolution of fresh ECC material was analyzed to facilitate the prediction of critical self-buckling height.

3.2. Materials and methods

3.2.1 Materials

The binders used includes ordinary Portland cement (Type I, Lafarge-Holcim) and fly ash (Class F, Boral Resources), the chemical compositions of which are listed in Table 3.1 [171]. Silica sand (F75, US Silica) was adopted as fine aggregate. Superplasticizer used in this research (ADVA 198) was a polycarboxylate-based high-range water reducer. Polyvinyl alcohol (PVA) fibers with a

length of 8 mm were employed as reinforcement of ECC. The properties of micro PVA fibers are listed in Table 3.2.

The mix proportions of printable PVA-ECC are shown in Table 3.3. The water-to-binder ratios and sand-to-binder ratio are 0.24 and 0.29, respectively. The dosage of PVA fiber is 1.5% by volume of the total composition. The bulk density of material is 1901 kg/m^3. For 3D printing, the fresh mixture of PVA-ECC was transferred directly from the mixer to the material hopper at the time of 20 min after water addition. The initial and final setting time of the printable ECC are 110 min and 515 min, respectively.

Table 3.1: Chemical compositions of OPC and FA (wt. %).

Material	CaO	Al_2O_3	SiO_2	SO_3	Fe_2O_3	MgO	Others
OPC	63.5	4.8	19.6	2.6	2.9	2.2	4.4
FA	17.4	19.8	39.4	1.9	11	3.7	6.8

Note: OPC: ordinary Portland cement; FA: fly ash.

Table 3.2: Properties of PVA fiber.

Length (mm)	Fiber diameter (μm)	Young's modulus (GPa)	Density (kg/m^3)	Surface oil content (wt. %)	Elongation (%)	Nominal Strength (MPa)
8	39	42.8	1300	1.2	6.0	1600

Table 3.3: Mix proportions of printable PVA-ECC (Unit: kg/m^3).

OPC	FA	Sand	Water	SP	PVA Fiber
605	678	372	308	1.8	19.5

Note: SP: superplasticizer.

3.2.2 Printing setups

The 3D printing system shown in Figure 3.2 consists of three main parts. Fresh ECC material is fed into the hopper, which is connected to a peristaltic pump system, and then transported through

a 15 ft hose to the printing tool. At the inlet position of the printing tool, a pressure sensor is mounted to detect the pressure fluctuation of material flow, and feed the signal back to the peristaltic pump to realize real-time monitoring and adjustment of the pressure. After pumping into the printing tool, fresh material is extruded from a nozzle by a built-in progressive cavity pump inside the tool. The precise positioning and controlling of the printing head are fulfilled by a 6-axis KUKA robot.

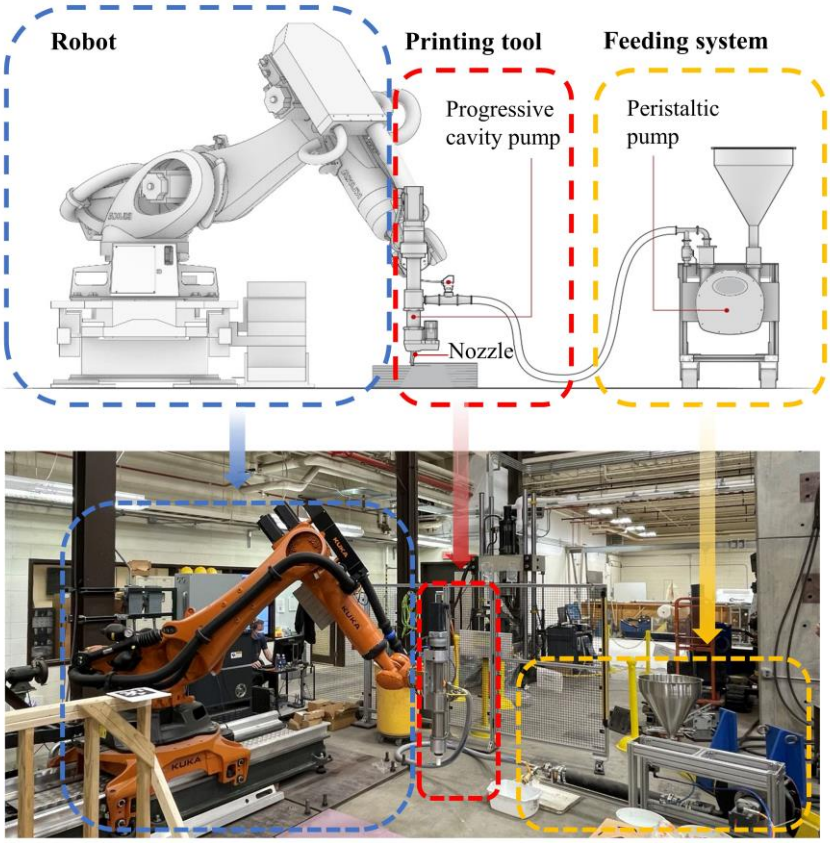

Figure 3.2: Printing setups at University of Michigan.

3.2.3 Constant shear rate test

Constant shear rate (CSR) test was conducted to assess the static yield stress evolution of printable ECC. The test applies a quasi-static rotational velocity (commonly 0.1-0.001 s^{-1} in previous studies [89, 166, 168-169]) to promote flow onset. A 4-blade vane rheometer (ICAR PLUS concrete rheometer, shown in Figure 3.3(a) was adopted for the test, with a vane radius of 63.5 mm, a vane height of 127 mm and a container radius of 143 mm. The test started at 20 min after water addition, and the testing protocol was shown in Figure 3.3(b): (1) pre-shear the fresh mixture at 0.5 s^{-1} for

60 s; (2) rest for 120 s; (3) shear at a constant rate of 0.01 s^{-1} for 60 s; (4) take out the vane, rest the material and repeat (1)-(3) every 20 min. The peak stress measured during each constant rate shear (flow onset) is recorded as the static yield stress of the material.

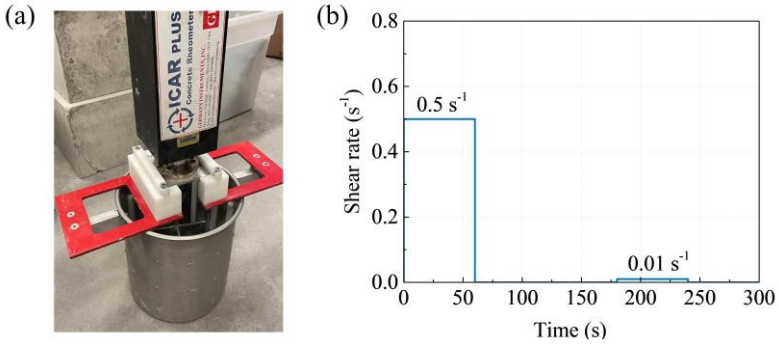

Figure 3.3: (a) Test apparatus and (b) test protocol of constant shear rate test.

3.2.4 Incremental loading test

The layer-by-layer deposition process during printing can be depicted by a stepwise loading process for the underlying material [16]. As each layer of material is deposited, the cumulative compressive load on the underlying material increases accordingly. For example, in this research, the thickness h_0 of each layer is 10 mm, and the corresponding increase in compressive stress can be calculated from Equation 3.2.

$$\Delta\sigma_0 = \rho g h_0 \tag{3.2}$$

where $\Delta\sigma_0$ represents the compressive stress increment, ρ is the density of fresh ECC material, g is the acceleration of gravity.

For the bottom material with a 50 mm by 50 mm horizontal area, each deposition results in a pressure increase of approximately 0.5 N. As the pressure rises, the stiffness and load-carrying capacity of the fresh material grows simultaneously. The strain and failure of the material under these two competing effects are thus of interest.

To simulate the evolution of the upper layer load, fresh ECC was fabricated into 50 mm× 50 mm× 30 mm samples for uniaxial compression test (Figure 3.4(a)). The sample geometry allows accurate measurement of strain, and is considered a fair simplification of the lowermost three-layers. The tests started at 20 min after water addition, as it is assumed that 20 minutes is a reasonable estimate for start time of printing, considering the time required for material preparation

and transport. The loading rate depends on the specific printing process simulated. During the process of 3DP, the vertical buildup rate of the structure is determined by the ratio of the nozzle travelling speed to the length of print path, and is constant for most cases, while the rate of stress accumulation is associated with the buildup rate through layer thickness. For instance, the structure buildup rate is 3 layers/min for a 0.5 m long straight wall printed at a nozzle travelling speed of 1.5 m/min, and the corresponding uniaxial loading rate is thus 1.5 N/min. Similarly, for a 10 layers/min buildup rate, the loading rate is approximately 5 N/min. The loading paths under different printing parameters are shown in Figure 3.4(b).

An INSTRON 5969 testing machine with a 50 kN loading cell was adopted for loading. Lubricant was applied to both loading plates before tests to alleviate the influence of friction. In this test, the geometrical changes of the sample were captured by a high-resolution camera and the strain was analyzed by ImageJ software. Material-scale failure is hereafter defined as fracture onset on the surface or the vertical strain of the sample reaching 40%.

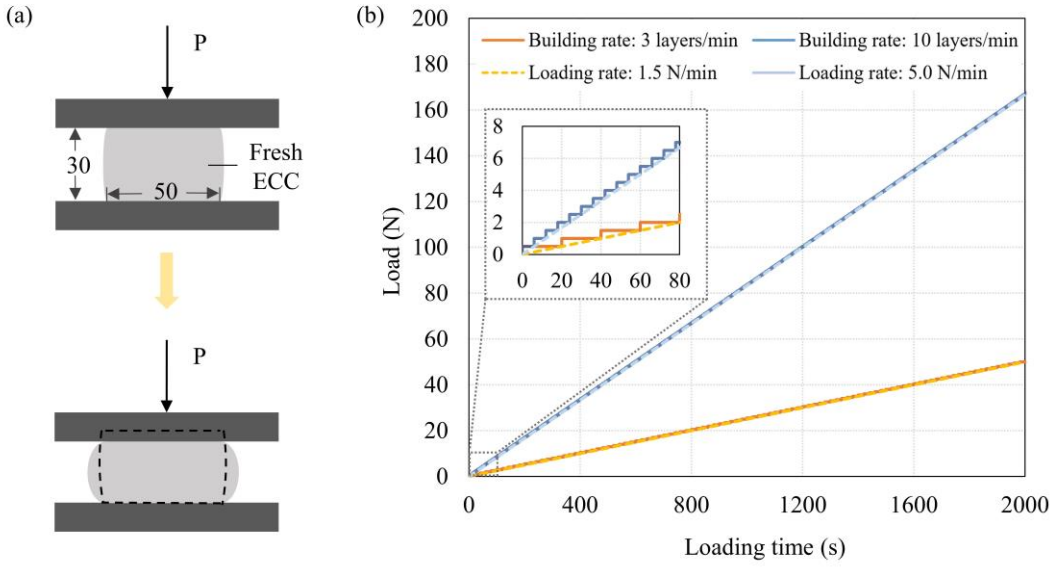

Figure 3.4: (a) Test setup (Unit: mm) and (b) loading paths of incremental loading test.

3.2.5 Green strength test

3D printing is a time-sensitive process. During printing, the components inside the material undergo interactive reactions and property evolution. The hydration process continuously

increases the strength and stiffness of the material over time, reducing its fluidity and enhancing the bearing capacity. At the same time, the external load conditions are also changing over time. The deposited material needs to withstand the gravity-induced load exerted by the accumulation of the upper material. These two processes, both progressing with time, are running simultaneously and competing with each other. If and when the bearing capacity of the material is reached and exceeded by external pressure, material failure will occur, which may lead to instability of the underlying layer and further result in overall failure of the structure. To predict the timing of material failure, it is critical to quantify the time dependent loading process and the green property development process, and to seek their intersection.

Green strength is an important indicator of material capacity, reflecting mechanical behavior of the material at a certain age. For a time-dependent process like 3DP, material behavior in a single time point is inadequate in depicting and predicting its mechanical response. Hence the green strength time-evolution should be quantified. In this case, fresh ECC specimens of 50 mm × 50 mm × 100 mm were fabricated and loaded under compression at the age of 20-100 min with an interval of 20 min (Figure 3.5(a)). The loading rate was kept at 8 mm/min to ensure tests completed within an average duration of 6 min in case of further strength increasement. Before loading, the surface of the specimen was sprayed with random black and white speckles to form a unique pattern. Changes in the image patterns during loading were recorded, and processed with Vic-2D software. The strain and displacement distribution could then be calculated and analyzed (Figure 3.5(b)).

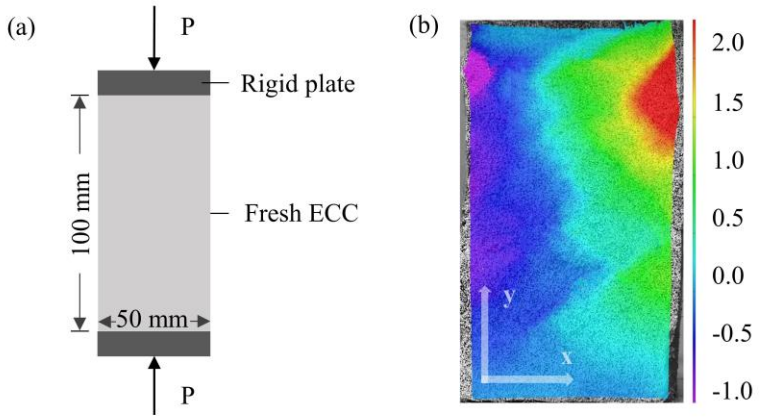

Figure 3.5: (a) Test setup of green strength test and (b) displacement field in x-direction when axial strain is at 10% (Unit: mm).

3.3. Material-scale analysis

3.3.1 Static yield stress evolution

The static yield stress growth of fresh ECC from 20 min to 60 min is summarized in Figure 3.6. Beyond 60 min, data is unavailable since the material became stiffer and raised the risk of reaching the torque limit of testing apparatus. Previous literatures has reported a wide range of initial static yield stress, i.e., from a few hundreds to thousands Pascal, for printable mixtures without fiber. The discrepancy mainly stems from different material status and testing protocols. Commonly, static yield stress within 20 min after water addition is below 5 kPa [83, 89, 162, 166, 169, 172]. Nonetheless, the yield stress of printable ECC reached approximately 6 kPa at 20 min age, and kept growing at a structuration rate (A_{thix}) of 122 Pa/min. Compared with printable cementitious materials without fiber, the high initial yield stress of ECC offers robust buildability and protects the material from plastic material failure.

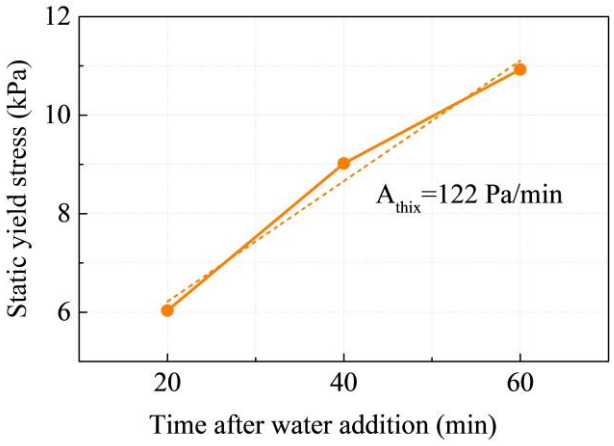

Figure 3.6: Static yield stress evolution of fresh printable ECC.

It has been widely acknowledged that fiber addition promotes the plastic viscosity and the yield stress of fresh cementitious materials within a certain range of dosage [173-176]. Fibers generally increase the surface area that needs to be wetted, thereby reducing the amount of free water to lubricate cement particles [177]. This is especially the case for synthetic fibers, e.g., PVA fibers, due to their low density and large amount. Besides, the intertwining of fibers may also promote resistance to flow and elevate yield stress [178]. The resulting high yield stress poses challenge to the pumping and extruding during 3D printing, yet is favorable to the rapid build-up of structure,

since the mechanical capacity of the material is enhanced. This desirable resistance of printable ECC is also confirmed by the incremental loading tests in later section, and distinguishes printable ECC from conventional mortars and pastes.

3.3.2 Incremental loading

The mechanical response of fresh ECC in the incremental loading tests is shown in Figure 3.7. As the tests were performed at different loading rates, the time scales represented by the two curves are different. The rate of material property evolution can be considered to be identical regardless of the loading path. However, for the 1.5 N/min loading, the slow rise in stress allows more time for the material to develop resistance. The rate of strain growth slowed down significantly when the strain developed to approximately 3%, at which point the test had been in progress for 16 minutes. While for a more rapid loading at 5 N/min, 3% strain was reached within 10 minutes. At 25 min after test initiation, the sample exhibited a vertical strain of 5%, and the corresponding compressive stress reached 50 kPa which approximates 250 layers (2.5 m) of material stacked on the sample.

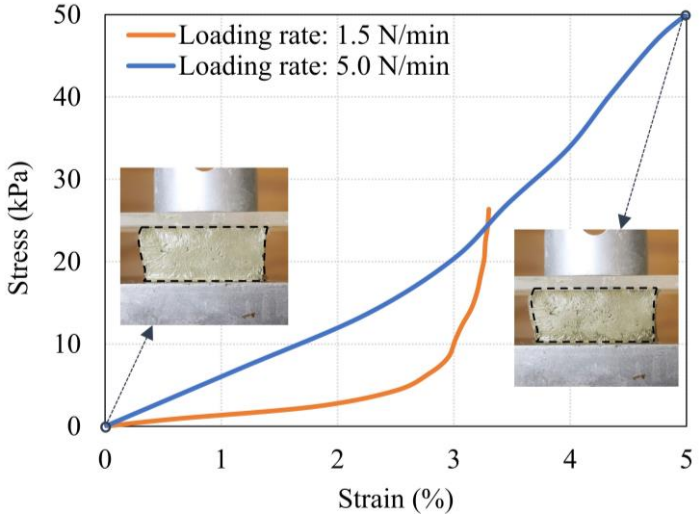

Figure 3.7: Mechanical response of fresh printable ECC in incremental loading tests.

Despite the relatively rapid buildup rate (10 layers/min) simulated, the printable ECC material experienced only 5% vertical strain in the test, and free of surface fracture, that is, the material showed no sign of failure. The reason why ECC material is effective against material-scale failure

lies in the higher growth rate of resistance compared with the external stress buildup. In the next section, the initial bearing capacity of the material (at 20 min after water addition) is also founded to be sufficient to withstand certain external loads. Therefore, both the high initial strength and the fast development of material capacity make printable ECC less vulnerable to material-scale failure.

3.3.3 Green strength development

Figure 3.8(a) plots the tested compressive stress-strain relationships from 20 min to 100 min after water addition. At all ages, stress increased approximately linearly with strain at the beginning stage of loading. After the strain level exceeded 15%, samples with younger ages (less than 60 min after water addition) maintained an approximate linear mechanical response, whilst the samples with a slightly older age (greater than or equal to 60 min) showed a gradual increase in stiffness. As the strain level went beyond 20%, shallow wrinkles and fine cracks began to appear on the surface. Further, when the strain exceeded 35%, the fresh material lost its dimensional stability, and was observed to present undesired fracture on the surface.

Stress data at the 10%, 20% and 30% strain level are extracted, plotted and connected separately in Figure 3.8(b) to create stress contours. Meanwhile, the compressive stress accumulated during printing is also mapped in the same figure. The slope of the stress accumulation line is determined by the structure buildup rate, i.e., ratio of printing speed to length of printing path. Two different structures were taken as examples - a 0.5 m long straight wall and a hollow cylinder with a diameter of 0.3 m, both printed at 1.2 m/min. The printing speed is identical to that adopted in actual printing and are determined based on the on-site material status and the synchronization among different devices.

It is found that the only intersection between the stress contours and the stress accumulation line is at the 10% strain level, which means, theoretically, the maximum strain the material could develop is slightly above 10%. According to the previous definition, 10% strain in material is not capable of inducing material failure. This result verifies the preliminary conclusion obtained in Section 3.1.1, that for printable ECC, the probability of material-scale damage is insignificant.

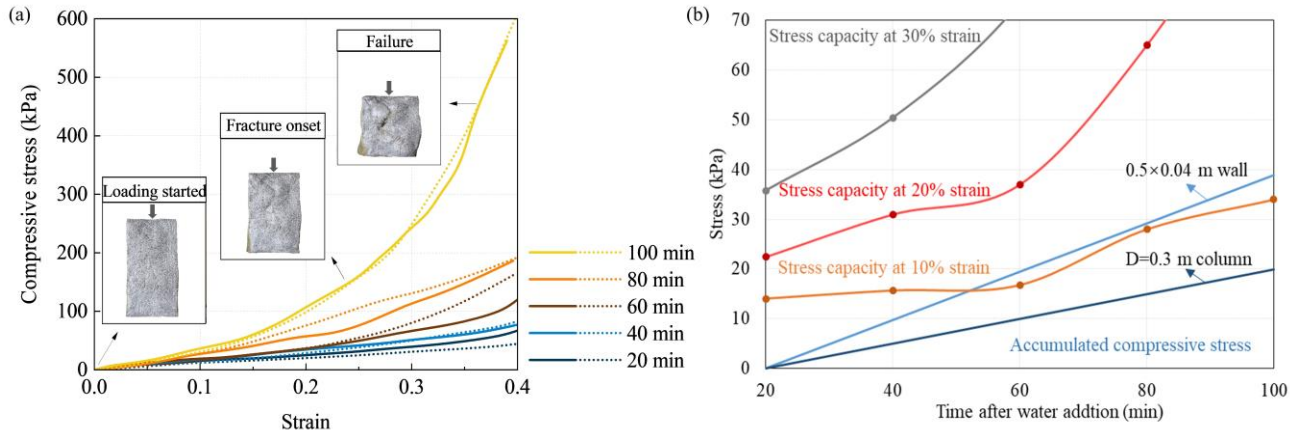

Figure 3.8: (a) Green stress capacity of printable ECC evolving with time and (b) its comparison with accumulated compressive stress.

3.3.4 Time-dependent strain-stress model

Although the reliability of printable ECC at the material scale is confirmed, the mechanical response and geometric changes of the material during printing are still of interest. On the premise that no structural collapse is induced by material failure, the emphasis of buildability evaluation should be put on the shape retention ability of the filaments. The geometric change in filament shape under load is of vital significance to the printed structure - the accumulation of deformation in each layer will ultimately affect the overall strain and structural stability of the finished product.

To evaluate the mechanical response of materials in this case, two key issues need to be addressed: (1) As aforementioned, the properties of the material and the external accumulated stress are two time-varying indices that are independent of each other. It is necessary to seek the law of their independent development, and further link the two together through the 3D printing process. (2) The 3D printed structure is created by stacking multiple layers of filaments, and the gravity-induced stress borne by each layer of material is nonlinear. In this case, the overall assessment of the structure needs to cover the individual behaviors of all filaments.

To address the first issue, a time-dependent mechanical model needs to be established. The time-dependent mechanical properties of the material have been obtained from green strength tests (Figure 3.9(a)). The next step is to visualize the time-related information implicit in the data. For this purpose, a 3D coordinate is created with strain (*x*-axis), time after water addition (*y*-axis) and stress (*z*-axis) being the axes. The original 2D stress-strain curves are marked in the new 3D

coordinate, arranged in chronological order along the *y*-axis (Figure 3.9(b)). Since the current data only represent the material behavior at discrete ages, the behavior on a continuous timeline needs to be reasonably inferred. Through interpolation, a continuous and smooth 3D surface is constructed, representing the time-dependent mechanical behavior of the deposited ECC material (Figure 3.9(c)).

Regarding structure buildup, a constant buildup rate (as is the case for the vast majority of printings) is assumed, the ratio of compressive stress growth to time development is thus invariable, denoted as $\sigma_c/\Delta t$. In Figure 3.8(b), this ratio represents the slope of the 2D stress accumulation line, while in Figure 3.9(d), it is the slope of the inclined plane in the 3D coordinate, since the pre-set printing program will not be disturbed by material property, i.e., the ratio is independent of the material strain represented by the *x*-axis. Different printing settings (including varying nozzle movement speeds, contour lengths, layer thicknesses, etc.) will generate specific buildup rates, which correspond to the inclined planes with varying slopes in the 3D coordinate system. Three inclined planes are inserted as examples in Figure 3.9(d), which correspond to three different $\Delta\sigma_c/\Delta t$ ratios, i.e., 2, 3, 4 kPa/min. It can be observed in Figure 3.9(d) that each plane has an intersection line with the generated surface. These intersection lines describe the early compressive stress-strain response of fresh ECC material at the specified buildup rates. By projecting the intersection line onto the stress-strain plane (*x*-*z* plane), a new strain-stress model is thus established (Figure 3.9(e)). It is worth noting that the time variable is no longer present in this model, however, the evolution of mechanical behavior induced by time progress is implicit in this 2D model. That is, the derived time-dependent stress-strain relationship is based on a certain time path and loading path, but the two variables of time and buildup rate are excluded from the simplified expression through the proposed modeling approach.

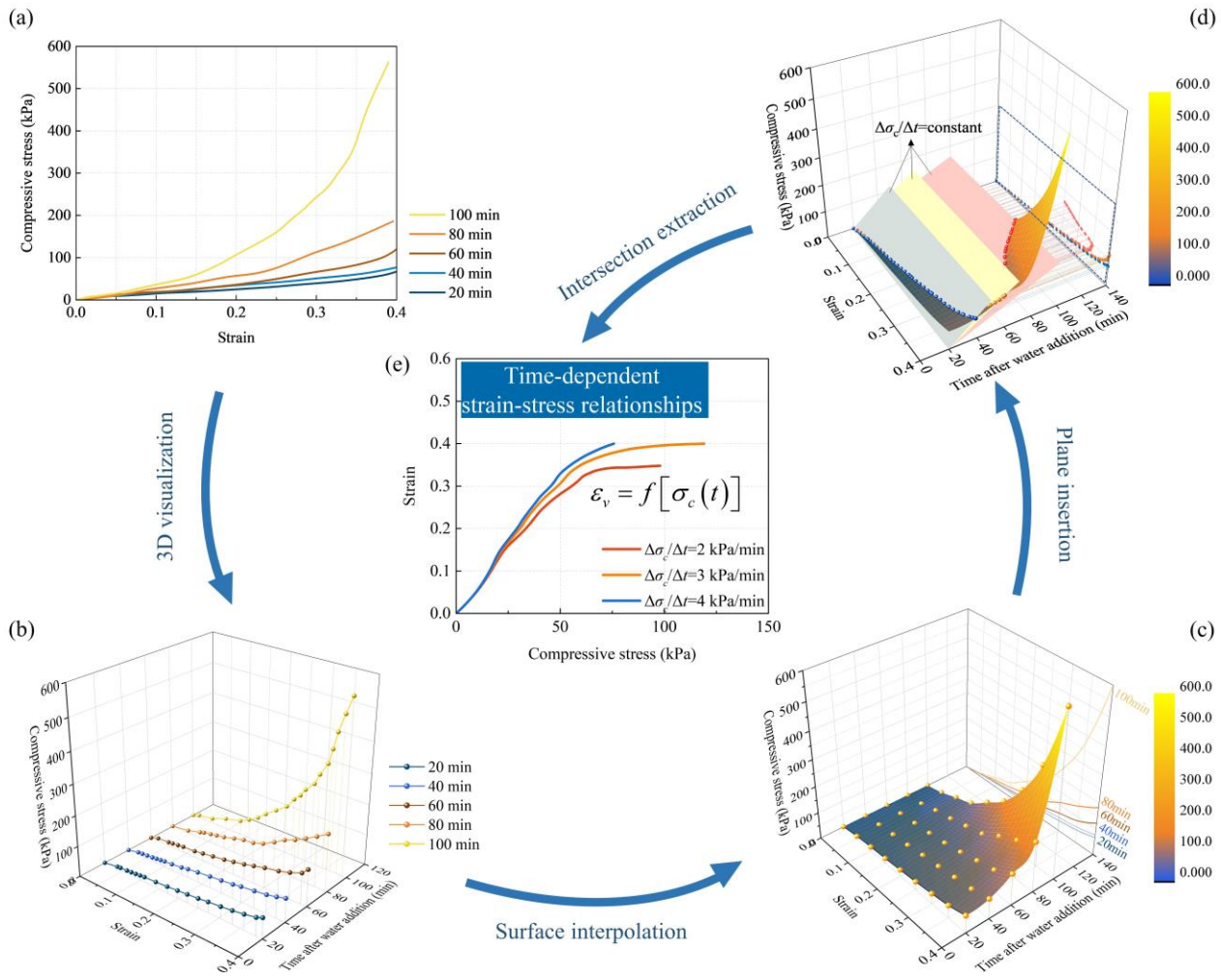

Figure 3.9: Methodology for developing the time-dependent strain-stress model.

The reason why the proposed model is a strain-stress model and not the other way around is that the focus is put on the strain response of the material while the stress progresses according to a known path pre-set by the printing program. In addition, the intersection line generated by the 2 kPa/min plane in Figure 3.9(d) contains a descending segment of the strain-stress curve. However, in consideration of material behavior, the descending branch does not have any practical and effective meaning. At the strain peak, ECC material has developed sufficient resistance to prevent further substantial deformation. As the stress further increases, the strain should therefore generate a plateau rather than a drop. With this consideration, the proposed strain-stress model excludes the descending segment.

The time-dependent strain-stress model proposed above provides the basis for material scale analysis, yet it is still at the scale of a single filament. Hence, further processing is required to integrate the behavior of multiple filament units into the behavior of the printed structure. In the strain-stress model, the material behavior in different layers is represented by discrete data points on the continuous curve. For simplification, the coordinate where the model sits is scaled as shown in Figure 3.10(a). The abscissa is modified from stress to the number of layers, which are linearly proportional with each other (Equation 3.3).

$$\sigma_H = \rho g H = N \cdot \Delta\sigma_0 = N \cdot \rho g h_0 \tag{3.3}$$

where N is the total number of layers for a printed structure with height H.

For a printed structure with N layers and height H, the bottom material corresponds to the strain ε_{N-1} in Figure 3.10(a). The vertical deformation of this layer can be determined by ε_{N-1} multiplied by h_0. Similarly, the vertical deformation of the overall structure can be written as the sum of each layer's deformations and thus can be approximated by the integral of the curve from 0 to N (Equation 3.4).

$$\Delta H = \left(\varepsilon_{N-1} + \varepsilon_{N-2} + \ldots + \varepsilon_1\right) h_0 = \sum_{n=1}^{N-1} \varepsilon_n h_0 \approx h_0 \int_0^N g\left(n\right) dn \tag{3.4}$$

where ε_i represents the vertical strain of the i th layer, $g(n)$ is the vertical strain as a function of layer number n.

Furthermore, with the abscissa reverted back to strain, the relationship between vertical deformation and the integral of strain-stress model is therefore obtained (Equation 3.5), as illustrated in Figure 3.10(b).

$$\Delta H \approx h_0 \int_0^{\sigma_H} f\left(\sigma_c\right) \cdot \frac{1}{\Delta\sigma_0} \cdot d\left(\Delta\sigma_0 \cdot n\right) = \frac{1}{\rho g} \int_0^{\sigma_H} f\left(\sigma_c\right) d\sigma_c \tag{3.5}$$

where $f(\sigma_c)$ is the vertical strain as a function of accumulated compressive stress, σ_H is the accumulated stress on the bottom material.

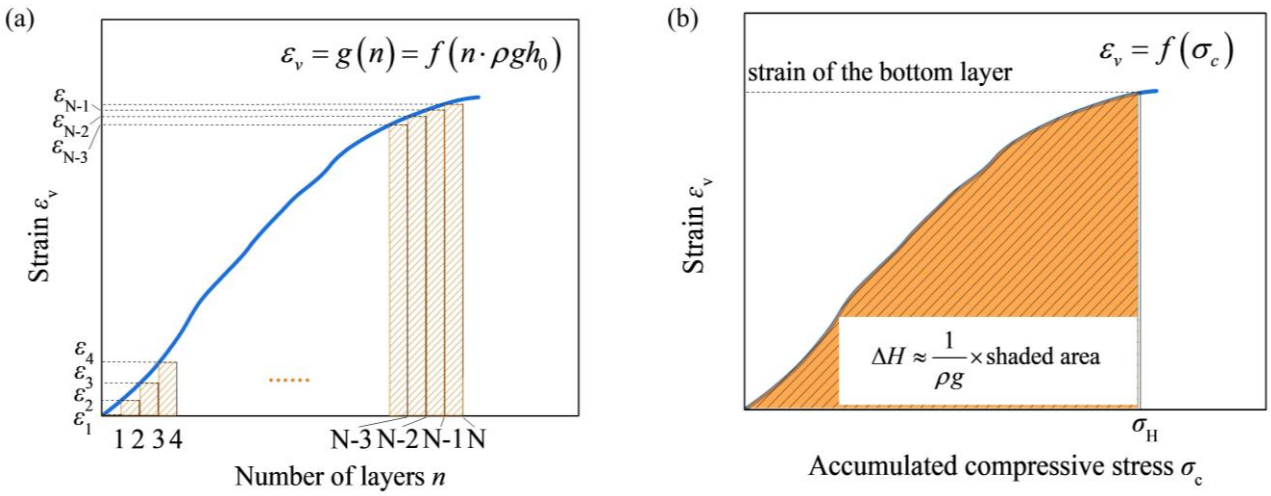

Figure 3.10: Derivation of accumulated vertical deformation of a multi-layered printed element.

To validate the proposed model, a straight wall with a length of 0.5 m was printed (Figure 3.11(b)). The wall thickness on the horizontal plane is the width of a single filament, which is approximately 40 mm. Before the structure underwent self-buckling, 22 layers were stacked, and a total height of 217 mm was observed. According to the printing settings of 10 mm layer thickness, the measured wall height reflected a vertical deformation of approximately 3 mm.

In this test, the printing nozzle traveled at a speed of 1.2 m/min, indicating a vertical stress growth rate of 0.47 kPa/min. An inclined plane corresponding to this slope is inserted into the 3D coordinate system in Figure 3.9(c) to obtain the intersection projection, that is, the time-dependent strain-stress model under this specific structure buildup rate (Figure 3.11(a)). The structural height of 22 layers implies a cumulative compressive stress σ_H of 4.29 kPa. Therefore, the strain-stress function is integrated from 0 to 4.29 kPa to obtain the prediction result of 2.2 mm. Hence, the predicted deformation correlates reasonably with the 3 mm experimental result.

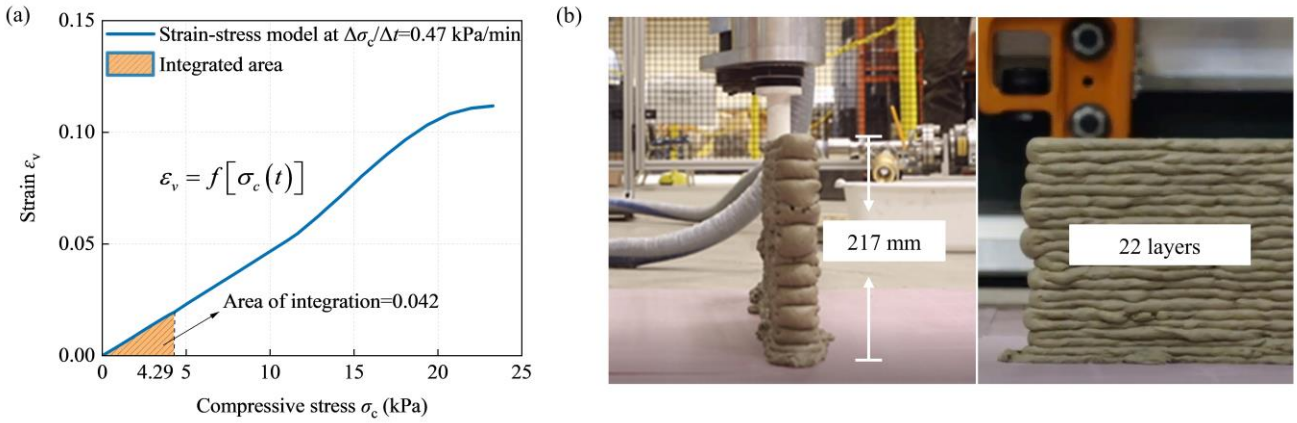

Figure 3.11: (a) Model prediction and (b) experimental verification of accumulated deformation of 3D printed structure.

In this proposed model, 3DP-ECC is emphasized as the printing ink of interest. Nonetheless, the approach is valuable as a universal modeling methodology. This means that the underlying logic of establishing time-dependent mechanical model as well as predicting structure deformation from laboratory material testing is also applicable to other types of 3D printed cementitious materials.

This model can demonstrate practical meanings in multiple scenarios: (1) by characterizing the material properties in the laboratory, it is possible to make an ex ante prediction of the structural deformation, which gives researchers and engineers the freedom to improve and optimize geometric control of the to-be-printed structure from the initial stage of material formulation; (2) the prediction given by the model can be used to modify and adjust the nozzle standoff distance during printing to avoid the structural instability problem caused by structure subsidence and constant nozzle elevation; (3) the time-dependent stress-strain constitutive relations could be incorporated into finite element analysis, providing theoretical basis and necessary material parameters for the early-age mechanical behavior analysis of the printed structure.

It is worth noting that further improvements can be applied to the model. First, the geometric dimension of the specimens in green strength tests was designed for compression tests and lateral support provided by adjacent material during printing is not taken into consideration for simplification. The unconfined uniaxial compressive test does not necessarily simulate the material dimensions and stress states in actual printing. Therefore, with the modeling approach not affected,

material characterization method can be modified to further approximate the actual stress state of the material in 3D printed structure. For example, confined uniaxial compressive tests with stacking layers [168] may be considered. In addition, this model does not take account of the influence of vertical stress applied by nozzle, which may be a concern for the cases where deposited filament is pressed by a lowered nozzle (e.g., using a down-flow circular nozzle with a lowered nozzle standoff distance). Further modification of the model prediction is needed when such printing setup is applied.

3.4. Structural-scale analysis

At the material scale, it has been elucidated that the excellent strength capacity of fresh ECC material effectively prevents collapse caused by material failure, indicating that for most cases, failure originated from structural instability will be the primary failure mode of 3DP-ECC.

Generally, self-buckling of a slender structure under its self-weight is controlled by its material property, structural form and dimensions. As in Equation 3.1, the critical height of a slender structure H_c is affected by material density ρ, stiffness E, second moment of inertia I and horizontal cross-sectional area A. Structural stability is difficult to be maintained under the self-weight when the height of the structure exceeds this threshold. This evaluation criterion has been suggested by Roussel [72] as a critical state for elastic buckling failure for 3DP structures. For conventional cast concrete structures, all the above parameters are fixed time-invariant values for a specific structure; for 3DP, however, the stiffness E is no longer a constant but a time-varying variable. The critical height of a printed structure at self-buckling is thus a function of time (Equation 3.6) and can be predicted by characterizing the stiffness evolution of the material.

$$H_c(t) \approx \left[\frac{8E(t)I}{\rho g A} \right]^{1/3} \tag{3.6}$$

To verify the above statement, two structures were designed and printed at 1.2 m/min – a 0.5 m straight wall (Figure 3.12(a)) and a 0.3 m diameter hollow cylinder (Figure 3.12(b)). For the straight wall, the critical height function can be simplified as in Equation 3.7 by plugging in the geometrical parameters using the second moment of area I for a rectangular cross-section.

$$H_c(t) \approx \left[\frac{2E(t)\delta^2}{3\rho g} \right]^{1/3} \tag{3.7}$$

where δ is the thickness of the wall.

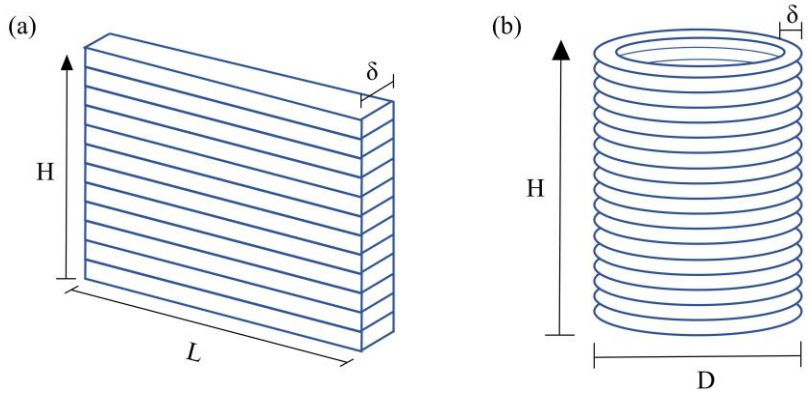

Figure 3.12: Schematic configuration of printed (a) straight wall and (b) hollow cylinder.

Stiffness evolution of the material can be extracted from the green strength test results (Figure 3.13(a)). Generally, the elastic modulus of a material is estimated from the linear elastic segment of the compressive stress-strain curve. According to ASTM C469/ C469M-14 [179], the modulus of elasticity is considered to be the tangential modulus before stress reaches 40% of the ultimate load. However, early-age ECC maintained a continuous increase in stress during compression, with no peak present. The approximately linear segments before 10% strain are adopted to derive the material stiffness at different ages [164] (Figure 3.13(b)). Assuming a linear development of stiffness (unit: kPa) with time (unit: min), an approximation of stiffness is fitted in Figure 3.13(c) (Equation 3.8).

$$E(t) \approx 2.65 \cdot t + 43 \tag{3.8}$$

Integrating Equation 3.7 and Equation 3.8, the $H_c(t)$ function for the straight wall is plotted in Figure 3.13(d). Under a fixed printing path and speed, structural height elevation as a function of time is also mapped onto the same coordinate. The two functions are found to intersect at t=23 min. At this time, the printed structural height catches up and exceeds the maximum allowable height that the material stiffness can support, leading to self-buckling of the structure post this point. Corresponding to the intersection point, a structural failure height of 0.18 m is predicted.

While in actual printing, the straight wall collapsed at a height of 0.217 m, as shown in Figure 3.13(e), which is in reasonable agreement with the prediction.

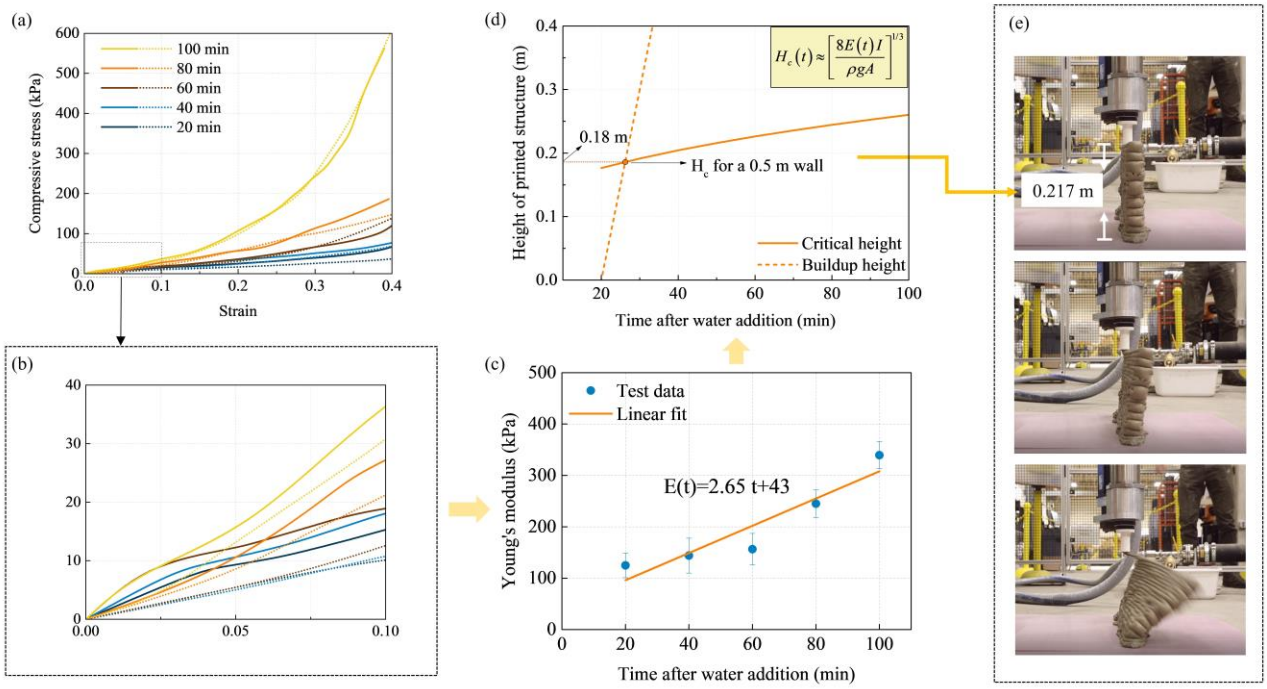

Figure 3.13: Methodology and validation for predicting self-buckling of printed ECC element.

Similarly, for the hollow cylinder in Figure 3.12(b), the critical height and buildup height can be derived as functions of time (Figure 3.14(a)) using the appropriate I for a circular cross-section. Unlike the previous case of straight wall, the two functions do not intersect within 100 min, meaning that structural self-buckling will not occur within this time range. Two primary reasons for the difference lie in: (1) under the same nozzle travel speed, the printing path length of the cylinder (0.942 m) is considerably longer than that of the straight wall (0.5 m), leading to slower structure height elevation; (2) the inherent geometric stability (represented by larger I/A value in Equation 3.6) of the cylindrical structure outperforms that of the straight wall. Self-buckling is thus less likely to occur. The cylinder was eventually printed to 49 layers and reached a height of 488.9 mm without any signs of structural instability (Figure 3.14(b)).

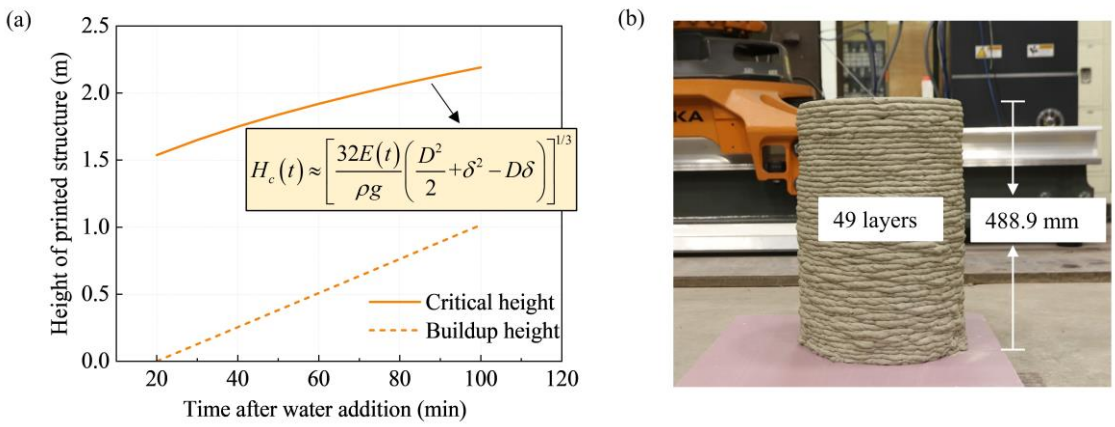

Figure 3.14: (a) Model prediction and (b) experimental verification of stability of a 3D printed hollow column.

From the above analysis, it can be concluded that at the structural scale, critical structural height for self-buckling can be predicted on the basis of material stiffness evolution. Laboratory characterization of materials can provide an assessment of structural stability, which in turn acts as feedback and presents specific and quantitative requirements on material tailoring. Furthermore, based on this evaluation approach, pre-mature self-bucking could be delayed or avoided by proper design of the structural geometry and the buildup rate. The understanding of the properties of printing materials sets clear boundaries for structural design of 3DP.

3.5. Summary and conclusions

This chapter developed a consistent and quantitative evaluation approach for buildability of 3DP-ECC, covering both the material and the structural scale. Instead of focusing only on material properties at certain ages, a methodology is proposed that recognizes evolving material behavior on a continuous timeline and that incorporates the information of designed printing. The influence of time progress is elaborated and embodied in the proposed time-dependent model.

Through experimental investigation and theoretical analysis, the following conclusions can be drawn:

(1) At the material scale, printable ECC material develops satisfying resistance to the accumulated vertical stress from upper layers at the early age. Constant shear rate test, incremental

loading test and green strength test demonstrate that the risk of material failure is low, at least for the material composition and processing approach used in the present research.

(2) Although material failure is not likely, geometric changes of the printed structure and mechanical response of the fresh material are of interest. A time-dependent strain-stress model of fresh ECC is proposed based on green strength development of the material. The proposed model makes reasonable prediction of structural deformation during deposition and lays the foundation for mechanical analysis of fresh extruded structure.

(3) At the structural scale, the critical height for self-buckling during printing can be predicted on the basis of stiffness evolution. Based on the evaluation approach, pre-mature self-bucking could be avoided by proper design of the structural geometry and the buildup rate (printing parameters), for a given material behavior evolution.

(4) The time-dependent fresh properties of printable material and the design parameters of 3DP (including structure design and printing parameters) are linked through time-related analyses. Buildability evaluations based on laboratory characterization of materials at both material and structural scales are therefore enabled.

(5) While the experimental work in the research reported here focuses on ECC material, the methodology proposed for buildability evaluation is applicable to 3D printing of concrete material in general. Hence this research contributes to the development of 3D printing of large scale civil and architectural structures.

Chapter 4. Effect of Process Parameters on 3DP-ECC

4.1. Introduction

The contribution of appropriate printing parameters to successful printing has long been recognized in the context of 3DP conventional concrete. The most decisive parameters include nozzle travelling speed, material extrusion rate, nozzle standoff distance, layer cycling time, nozzle shape and size, etc. [3, 64, 72, 82, 85, 94, 100]. These parameters pose substantial impacts on the extruding and stacking process in the early stage of 3DP life cycle and also on the properties of the resulting element. For instance, a controlling factor of extrudability is the synchronization between travelling speed of the nozzle and flow rate of the extruded material. The flow rate should be accurately sync up with the nozzle movement, otherwise the printed filament will exhibit discontinuity or inconsistency [64, 79]. Furthermore, the determination of travelling speed requires careful considerations. If the horizontal printing speed is excessively increased, the inertia induced stress in the extruded material cannot be neglected. Therefore, rapid deposition may cause geometric defects in the extruded cross-section [3, 72]. Another example is how nozzle standoff distance affects printing. It is suggested for 3DP concrete that a proper choice of nozzle standoff distance, i.e., the height of the nozzle above the upper surface of previous layer, can alleviate the problem of insufficient interface bonding [91]. Experiments have shown that reducing the standoff distance to approximately or slightly below the filament thickness suppresses the appearance of large voids at the interface [93, 180]. However, such pressing may cause uncontrolled geometric deviations and additional stress burdens to the underlying layer, even resulting in instability failures during the build-up process [181].

Despite the attention that process parameters received in the field of traditional 3DCP, no research on printing parameters of 3DP-ECC has been reported. However, such research is necessitated by the features of ECC. The rheology of ECC containing a relatively high content (up to 2% by volume) of microfibers with diameter less than 40 microns creates unique processing challenges, and sparks interest in the impact of printing processes on its self-reinforcing features. In addition,

interlayer properties of 3DP-ECC needs to be investigated to understand the influence of fiber bridging on the interface fracture resistance to loading.

To fill the research gap, this chapter aims at investigating the inter-relations among material production control (printing parameters), micro-structure and macro-scale properties of 3DP-ECC. As conceptually illustrated in Figure 4.1, with material constituents held constant, the adjustment of printing parameters is reflected by the variation in micro-structure of 3DP-ECC, which further poses influence on the material properties. In turn, the properties measured at macro-scale serve as feedbacks on the process control of 3DP-ECC. In this chapter, focus is placed on varying the nozzle travelling speeds and nozzle standoff distances. The resulting micro-structure of 3DP-ECC was observed through micro computed tomography scanners (μ-CT). Further, tensile performance and interlayer fracture performance of printed ECC were evaluated using uniaxial tensile tests and three-point bending tests.

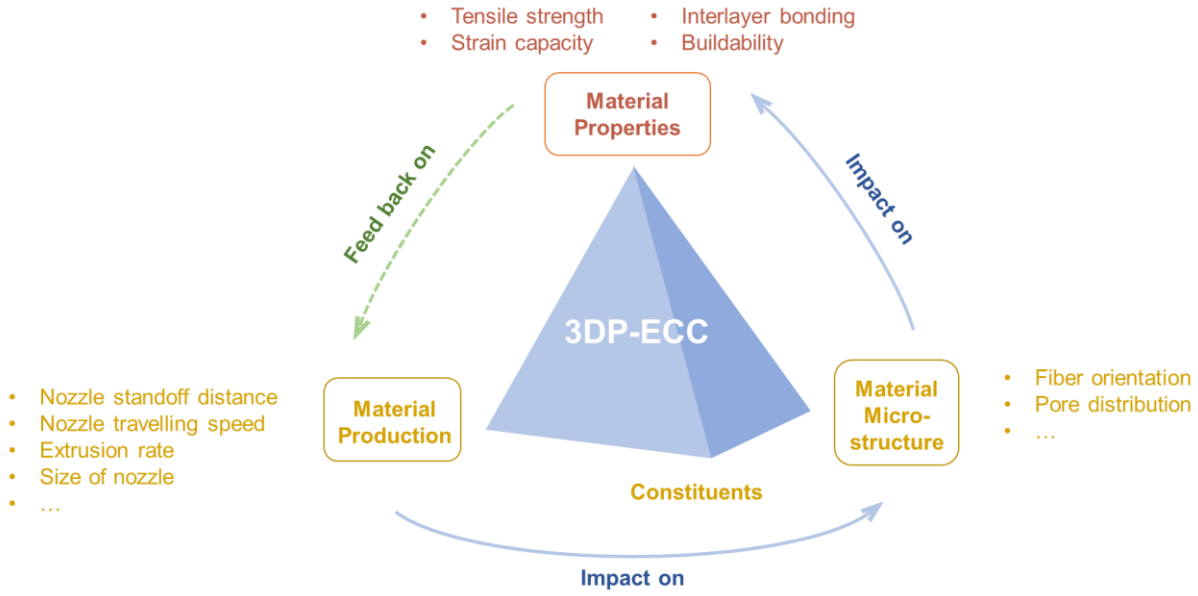

Figure 4.1: Failure modes during 3D printing.

4.2. Material and methods

4.2.1 Materials

The printing and testing in this chapter were conducted in the Southeast University in Nanjing, China. Therefore, the materials and devices adopted in this research were different from those in other chapters. The binders used includes ordinary Portland cement 42.5R, fly ash and silica fume, the chemical compositions of which are listed in Table 4.1. Silica sand with a particle size ranging from 100 μm to 200 μm was adopted for fine aggregate. Polyethylene (PE) fibers with a length of 12 mm were used as reinforcement of ECC. The properties of PE fibers are summarized in Table 4.2.

The two mix proportions of PE-ECC are listed in Table 4.3. Mix-1 was designed only for purpose of comparison regarding rheological properties, while Mix-2 was adopted for 3D printing in the following tests and casting of control (non-printed) specimens. The water-to-binder ratios of Mix-1 and Mix-2 are 0.22 and 0.24, respectively. The sand-to-binder ratio is 0.29 for both. The dosage of PE fiber is 1.5% by volume of the total composition. Using Mix-2 composition, mold-cast PE-ECC was tested. The cube compressive strength of cast ECC is 63.3 MPa with a 40 mm× 40 mm× 40 mm specimen. The flexural strength obtained from a 40 mm×40 mm×160 mm specimen is 14.8 MPa.

Table 4.1: Chemical compositions of binders (wt. %).

Binder	SiO_2	CaO	Al_2O_3	Fe_2O_3	MgO	SO_3	K_2O	TiO_2	L.O.I.
OPC	17.48	65.16	5.46	2.51	2.38	2.86	-	-	4.15
FA	41.12	6.05	37.00	5.56	0.88	1.08	0.71	1.38	2.89
SF	85.86	1.80	1.03	3.09	2.06	-	1.03	-	-

Note: OPC: ordinary Portland cement; FA: fly ash; SF: silica fume; L.O.I.: loss on ignition at 950°C.

Table 4.2: Properties of PE fibers.

Density (g/cm^3)	Diameter (μm)	Length (mm)	Tensile strength (GPa)	Elastic modulus (GPa)	Elongation at break (%)
0.97	24	23	3.0	116	1-3

Table 4.3: Mix proportions (ingredient-to-binder weight ratios) of PE-ECC.

	OPC	FA	SF	Sand	Water	SP	PE Fiber
Mix-1	0.47	0.44	0.09	0.29	0.22	0.0010	0.010
Mix-2	0.47	0.44	0.09	0.29	0.24	0.0018	0.010

Note: SP: superplasticizer; binder = OPC+FA+SF.

In preparation of the printing ink, all the dry ingredients, i.e., binders, sand and powdery SP, were premixed for 1 min first. Then 90% of the mixing water was added and agitated for 2 min to liquefy the dry materials. Fibers were divided into three equal portions and added to the mixture separately with an interval of 3 min's mixing each time. To promote the viscosity of the mortar before fiber addition and to enhance uniform fiber dispersion [182], the remaining water was held back until all the fibers were properly dispersed. The mixing speed was kept at 48 rpm during the mixing process. The fresh mixture of PE-ECC was transferred directly from the mixer to the material hopper of 3D printer at the time of 20 min after addition of the first batch of water.

4.2.2 Printing setups

The gantry-type 3D printer shown in Figure 4.2(a) has three degrees of freedom. Along the slide rails in three orthogonal directions, the hopper storing ECC can be moved to prescribed position with computer aid. ECC is extruded out of the hopper under the action of gravity and with the force applied by a built-in cavity pump. Connected to the hopper is a circular nozzle with a diameter of 20 mm for material to get through. The extrusion rate of material, i.e., the volume flow, is primarily determined by the rotating speed of the cavity pump. While the travelling speed of nozzle is independently controlled and adjusted by computer program.

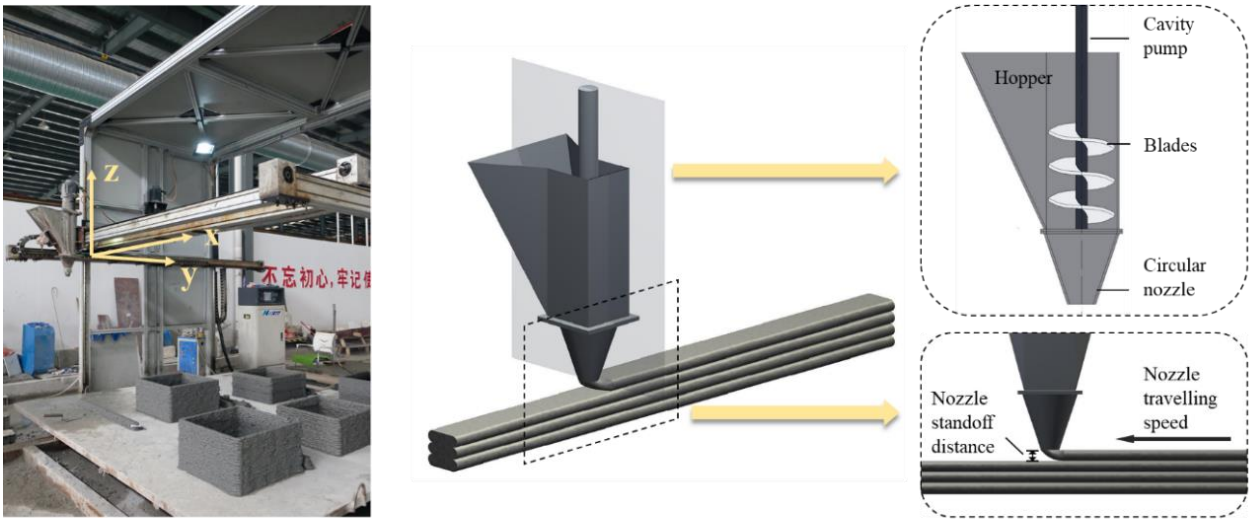

(a) Gantry printer (b) Schematic diagram of printing setup

Figure 4.2: Printing setups at Southeast University.

Two printing parameters posing substantial impact on printing process and quality, i.e., nozzle travelling speed and standoff distance, were chosen as the research foci. As schematically shown in Figure 4.2(b), nozzle travelling speed characterizes how fast the nozzle moves along the printing direction. It is essential to reconcile the travelling speed of the nozzle with the extrusion rate of material. Excessively rapid travelling relative to extrusion rate may cause geometric defects in the extruded cross-section [3, 72], while improperly slow deposition may accumulate redundant materials, impairing geometric integrity and structural stability. In addition, layer cycling time of printing will be stretched by slow printing, promoting so-called “cold joint”, where the deposited material loses its ability to establish a tight bond with the next layer of wet material [93]. To investigate how the synchronization between movement speed and extrusion rate is achieved, extrusion rate was held constant by fixing the rotating speed of pump to 90 rpm in this experiment, and travelling speed was modulated to have three grades, i.e., 7, 8, and 9 m/min, namely low, standard and high speed, respectively.

As a predetermined parameter in control system, nozzle standoff distance describes a fixed vertical height by which the nozzle is elevated after one layer of printing. It is worth noting that the standoff distance defined here is not always equal to the thickness of layer or the height difference between nozzle and the top surface of a previous layer. Rather, it stays unchanged during the whole printing process. Previous researches suggested that reducing the standoff distance to approximately or

below the filament thickness to suppresses the appearance of large voids at the interface [91, 93, 180]. In this experiment, the highest standoff distance, i.e., 14 mm, is slightly lower than the height of a single undisturbed filament at 16 mm.

The printing parameter matrix is summarized in Table 4.4. The ID of each group indicates the travelling speed and standoff distance. For instance, H12 represents high travelling speed (H) and standoff distance of 12 mm.

Table 4.4: Printing parameter matrix.

Group ID	Nozzle travelling speed (m/min)	Nozzle standoff distance (mm)
S10		10
S12	8	12
S14		14
H12	9	12
L12	7	12

Note: S: standard travelling speed; H: high travelling speed; L: low travelling speed.

4.2.3 Rheological test

Flowability of printing ink is crucial for extrusion. Proper flowability enhances the ease, continuity and stability to extrude well-controlled filament through a nozzle [29]. In this research, flow table test was conducted to assess the flowability of PE-ECC in fresh state as per ASTM C1437 [183]. The fresh mixture was filled into an inverted half cone with a bottom diameter of 100 mm and height of 60 mm. After removal of the cone, the table was raised and dropped 25 times. Then the diameter of the spread material was measured in two dimensions and the height reduction was regarded as slump, as shown in Figure 4.3. The flowability of material was tested from 20 min to 80 min after water addition at intervals of 20 min to depict the time-dependent evolution of rheology.

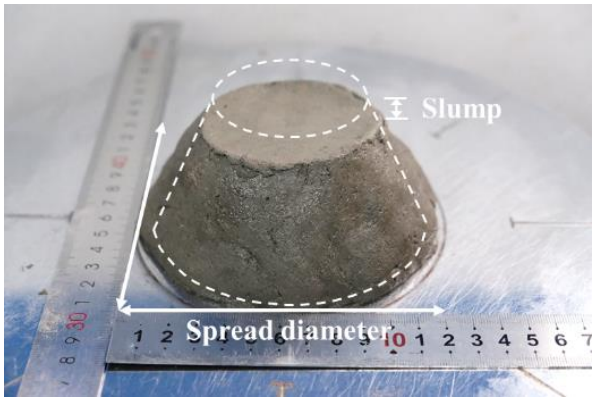

Figure 4.3: Measurements in flow table test Measurements in flow table test.

Buildability is generally characterized as the ability of the printable material to build up without significant deformation or collapse [72, 150]. The most straightforward approach to evaluate buildability is to compare the maximum height of printed element that can be built without failure under the same print settings [151]. Nonetheless, PE-ECC in this research exhibits remarkable resistance to material failure during structure buildup and satisfying structural stability with the geometries specified in this research. In this case, without failure of printed elements, resistance of the deposited material to deformation under increasing deadweight loading is considered as an appropriate indicator of buildability evaluation. This shape retention ability can be quantified by monitoring the geometrical changes of the printed filament and structure [22, 170]. At the scale of an integrated printed object, average vertical strain is considered as an evaluation index [170]; while at the scale of single filament, variation of filament thickness can serve as a measure. In this experiment, a box-shape element stacking to approximately 300 mm high was printed for each group. The height of the whole element and each layer were measured at four edges separately and arrived at an average value.

4.2.4 Mechanical tests

Uniaxial tensile test and interfacial fracture test were conducted to charaterize the mechanical performance of specimens. In addition, micro-scale features of printed and cast ECC were probed.

To prepare specimens for tensile test, a beam-like element with three parallel filaments per layer and five layers stacked was printed for each group and cured for 28 days. Dog-bone specimens

[184] were then extracted directly from the beam-like element by saw cutting, as shown in Figure 4.4(a). Meanwhile, control specimens were prepared by mold casting and shared the same mix proportion with the printed ones. The geometry of dog-bone specimen is designed to promote dense micro-cracking in the narrow gauge region (80 mm in length). The specimens were uniaxially loaded at a fixed loading rate of 0.4 mm/min whilst two linear variable displacement transducers (LVDTs) measured the average tensile strain in the gauge region. Pin end shown in Figure 4.4(b) helped to minimize misalignment and undesired moment during loading.

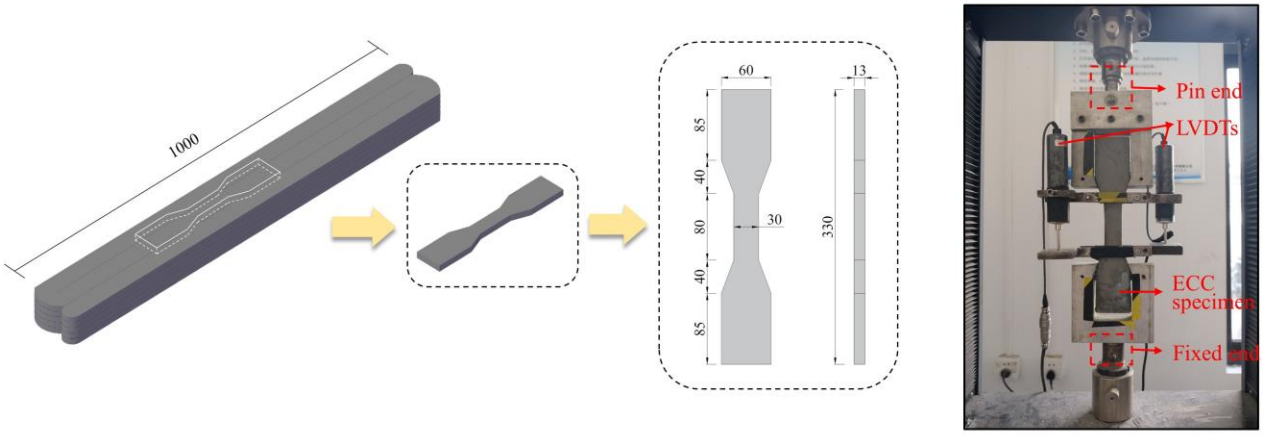

(a) Specimen configuration (b) Test setup

Figure 4.4: Tensile specimen and test setup (Unit: mm).

Layer interface is usually a weak link in 3DP due to potential high interlayer porosity and cold joint, therefore inducing inferior mechanical performance at the interface than that in the bulk material. For ECC, this is especially the case, since the lack of fiber bridging at the interface accentuates the anisotropy. Characterizing layer adhesion of 3DP-ECC is hence of paramount significance. Considering the failure of the interface is governed by crack propagation, three-point bending tests of notched specimens are appropriate for capturing interlayer bonding characteristics.

The specimens of interfacial fracture tests, with a dimension of 200 mm× 40 mm× 20 mm [185], were cut from the top portion of the printed box-shape elements at an age of 28 days, as shown in Figure 4.5(a). For each group, the specimens were notched either at the position of interface (namely inter-layer) or in the middle of a layer (namely intra-layer). The height of notch is 40% of the beam depth, i.e., 16 mm. The setup for three-point bending test is shown in Figure 4.5(b). The loading above the notch was applied at a rate of 0.05 kN/s until specimen failure.

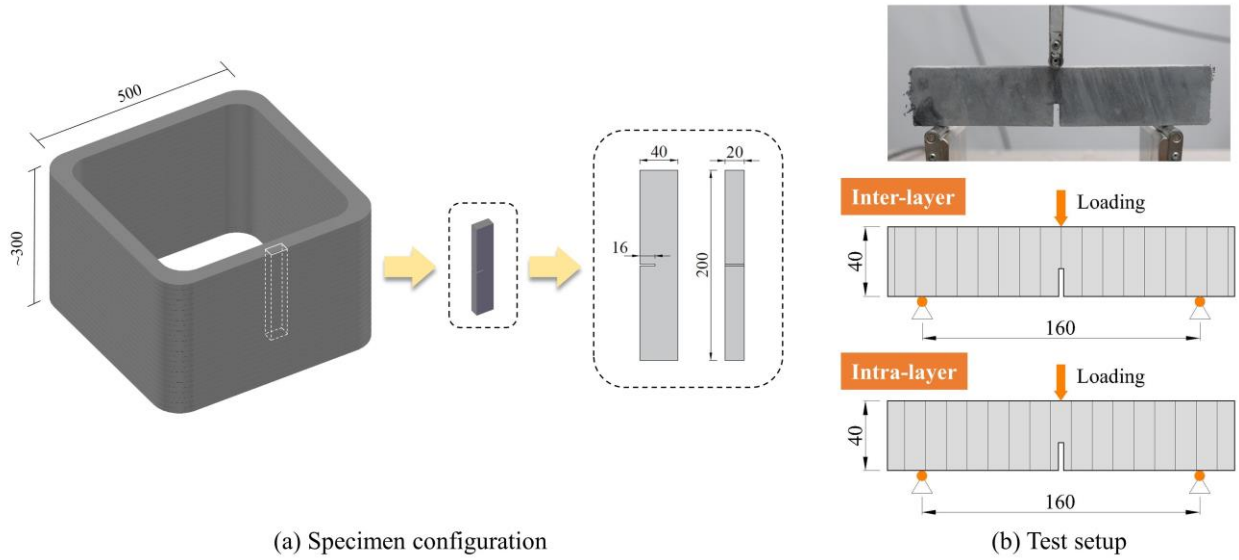

Figure 4.5: Interfacial fracture specimen and test setup (Unit: mm).

It is widely acknowledged that the mechanical properties of ECC at macro scale is dominated by its micro-structure, including features of fiber orientation and pore size and distribution [13, 67], which is also applicable to 3DP-ECC. Changes in printing parameters can be expected to introduce variations to the micro-structure of ECC. Micro computed tomography scanner (μ-CT) was applied to observe the micro-structure of 3DP-ECC. μ-CT sliced and scanned the 3DP-ECC sample. By combining the sliced images, the 3D model of pores and dense bulk material was reconstructed and visualized in the software Dragonfly. Additionally, the feature and distribution of pores were captured and analyzed.

4.3. Rheological properties

4.3.1 Flowability and extrudability

Figure 4.6(a) plots the test data of flowability from 20 min to 80 min after water addition. Fresh mixture of Mix-2 outperformed that of Mix-1 in terms of spread diameter, indicating superior flowability. At a nozzle travelling speed of 8 m/min and a pump rotation rate of 90 rpm, the extrudability of Mix-1 appeared unsatisfactory. As shown in Figure 4.6(b), the relatively lower flowability of Mix-1 mixture resulted in difficulties in extrusion and deposition, leading to

apparent surface cracks and undesired voids in printed filaments. Such defects in manufacturing could raise the risks of undermined structural integrity and inconsistent mechanical performance. In contrast, Mix-2 yielded continuous and intact filaments within open time. Ample fluidity assisted in the smooth extrusion of fresh ECC.

Considering the intrinsic conflict between sufficient flowability and desired buildability, the material must be harmoniously tuned to control its rheological properties. For a printing setup with cavity pump directly forcing the material out of a hopper, ECC Mix-2 is appropriate to enable successful extrusion whilst demonstrating shape retention ability.

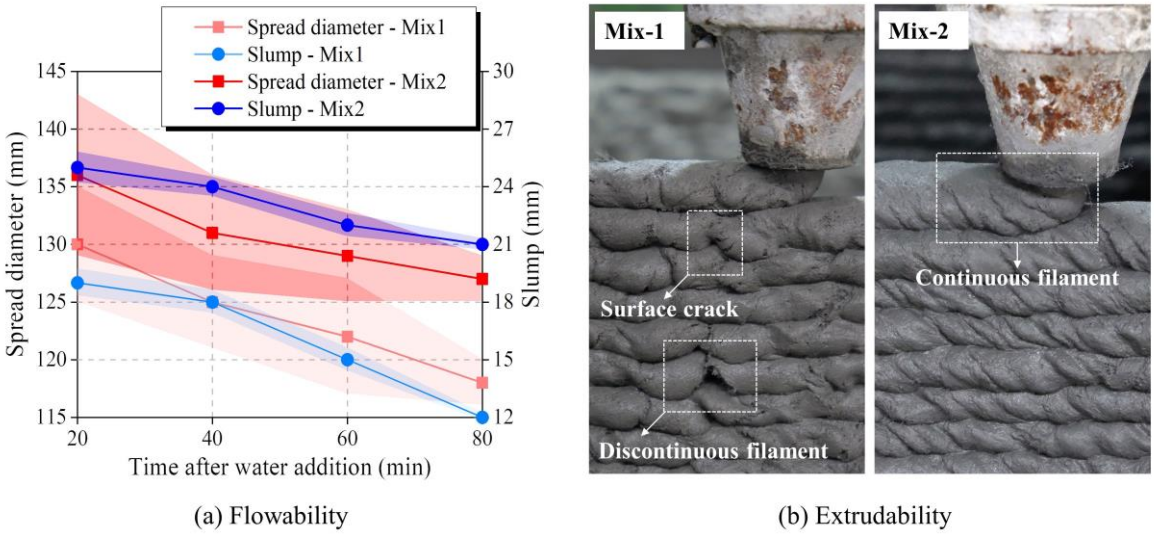

(a) Flowability (b) Extrudability

Figure 4.6: Rheological properties of fresh printable ECC. The variability of measured spread diameter and slump is indicated by the shaded area in the plot.

4.3.2 Effect of printing parameter on buildability

Intuitively, buildability describes the ability of the printed structure to be built up without failure. In the present research, buildability of 3DP-ECC was demonstrated by five groups of box-shape elements (Figure 4.7) printed without any local buckling, overall collapse, excessive deformation or sensible eccentricity. More specifically, buildability can be quantified and evaluated by defining shape retention ability. Under the increasing load from upper layers and potential pressure applied by the nozzle, the filament deposited first inevitably undergoes a change in its cross-sectional shape. The magnitude of this geometrical change can be used to characterize buildability in 3DP and is especially straightforward for comparative research.

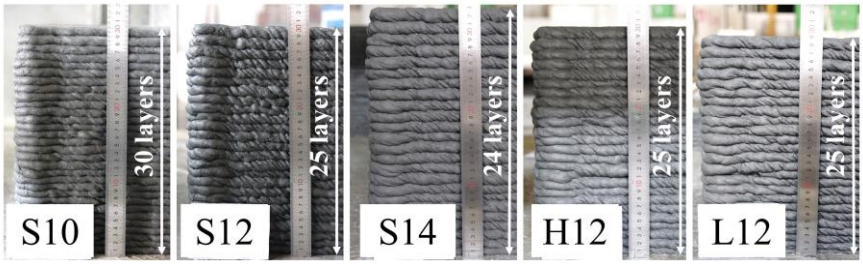

Figure 4.7: Side views of the printed box elements.

To capture the geometrical change at both the element-level and filament-level, the heights of the entire printed component (Table 4.5) and each layer were recorded. To enhance the comparability, the total height of all elements was controlled to around 300 mm during printing, except for S14 group with notably thicker layers. Without gravity-induced deformation, the designed height of every element is supposed to be the product of layer number and nozzle standoff distance. Hence, the average vertical strain (Equation 4.1) of the printed elements can be calculated as one indicator of overall deformation. It should be noted that the influence of the top (h_1) and bottom (h_n) layer is removed to mitigate the interference caused by leveling and measurement errors.

$$\varepsilon_v = 1 - \frac{(H - h_1 - h_n)}{(n-2)\, h_0} \tag{4.1}$$

where ε_v represents the average vertical strain overlooking the top and bottom layer, n is the number of layers, h_0 is the prescribed nozzle standoff distance, H is the total height of the printed element, h_1 and h_n are the measured thickness of the top and bottom layer, respectively.

Generally, the average vertical strain scales with nozzle standoff distance (Figure 4.8). As aforementioned, the nozzle standoff distance is slightly lower than the thickness of an undisturbed filament and therefore poses restriction on the vertical height of filament during extrusion. When fresh mixture leaves the outlet of the nozzle, a vertical pressure generated by the nozzle is exerted on the upper surface of the filament. Consequently, the fresh ECC filament is vertically compacted, decreasing in height and expanding laterally. This tendency increases as the standoff distance is lowered. A flatter cross-section of filament is then shaped. In this case, the load transfer between two adjacent layers occurs on a larger and flatter contact surface, thereby mitigating the effect of the gravity-induced pressure on causing further deformation of the filament. This “pre-loading” by nozzle in fact consumes part of the deformation capacity of the material in advance, so that

upon completion of deposition, the filament retains little deformability but gains better shape retention ability. As a result, printing with a lower nozzle standoff distance improves the buildability of 3DP-ECC by yielding a less significant vertical strain.

Table 4.5: Geometrical dimensions of the printed box elements.

Group ID	Number of layers n	Height H (mm)	Ave. layer height $\bar{h}$ (mm)	Ave. filament width $\bar{w}$ (mm)
S10	30	302	9.96	42.0
S12	25	300	11.91	39.0
S14	24	332	13.77	37.0
H12	25	300	11.91	36.5
L12	25	294	11.87	40.0

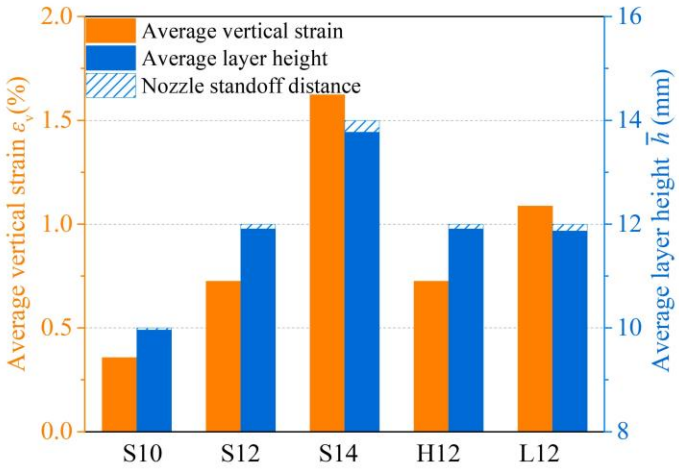

Figure 4.8: Average vertical strain of the printed elements as influenced by nozzle standoff distance and nozzle travel speed.

Slightly higher travelling speed does not have a significant effect on the overall vertical strain, whereas the low printing speed shows a negative impact on buildability of 3DP-ECC. With slow movement of nozzle, redundant material accumulates behind the nozzle, reflected as a higher average filament width compared with the standard group. Excessive materials threaten the stability of geometrical dimensions, since it is difficult to control the position of material accumulation and the direction of material movement under compression. As a result, the layered

materials may not stack neatly with control but skew among layers. This increases the vertical deformation and also impairs the dimensional precision and geometric stability of the printed object.

In addition to overall vertical strain of the object, variation in layer thicknesses can serve as an indicator of buildability as well. Deviation of layer thickness implies relative deformation among non-uniform layers. Compared with normalized average deformation, the deviation of layer thickness depicts more details about the vertical deformation distribution among different layers. As shown in Figure 4.9, the standard deviations follow a similar trend with average vertical strain. The variation in layer thickness is enlarged with the increase of nozzle standoff distance, indicating more notable difference in deformation between the upper and lower materials. As an indirect shape index, the standard deviation of layer thickness is deemed as an auxiliary evaluation method and a supplement to the average vertical strain index.

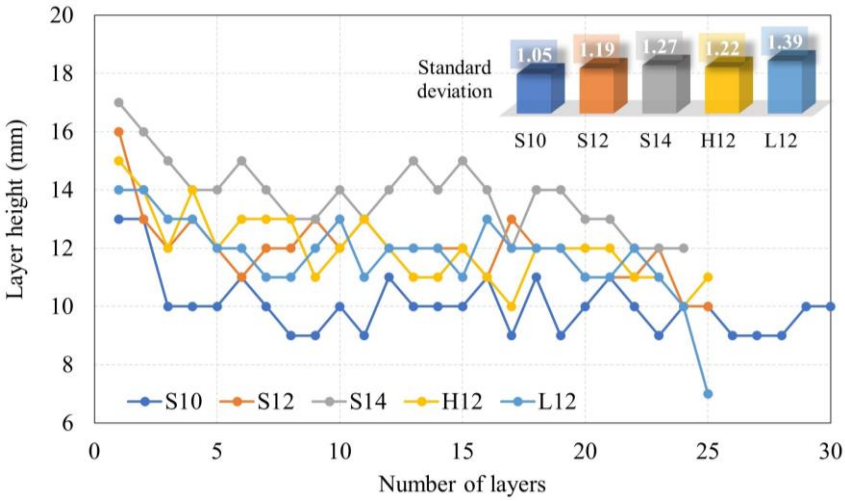

Figure 4.9: Deviation of layer thickness from initial thickness (layer no. 1) during the printing process as more layers are built-up.

4.4. Mechanical properties and micro-structures

4.4.1 Tensile performance

By exhibiting strain-hardening behavior under tension, cast ECC offers unparalleled tensile performance in the field of cementitious materials. Although processed with an entirely different technology, 3DP-ECC is expected to exhibit similar ductility. Superior tensile performance in

3DP-ECC has been captured in previous studies [12-13, 15, 18]. Nonetheless, printing device and process parameters can pose dramatic influence.

In the current study, 3D printing process was observed to weaken the tensile performance of PE-ECC. As can be seen in Figure 4.10 and 4.11, the cast specimens outperformed printed ECC in terms of multiple cracking ability, tensile strength and strain capacity. Both factors of fiber and matrix are responsible for the performance reduction in printing.

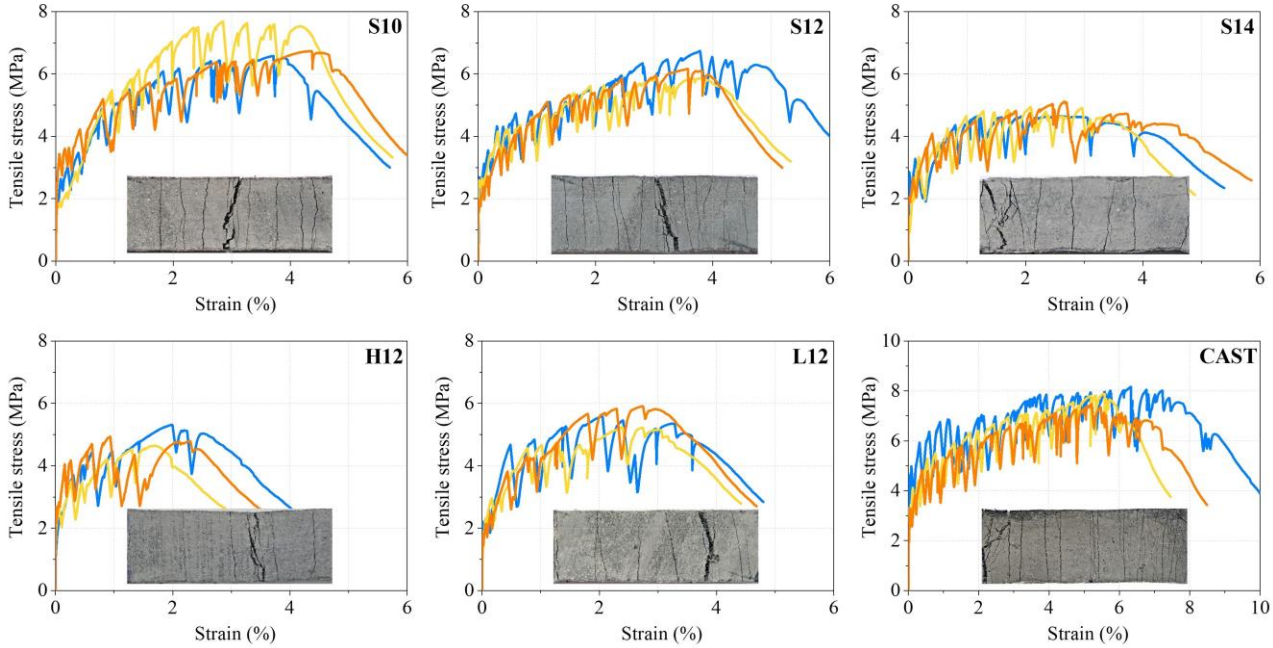

Figure 4.10: Tensile stress-strain curves of 3DP ECC and corresponding damage pattern after uniaxial tensile tests, compared to the cast specimen.

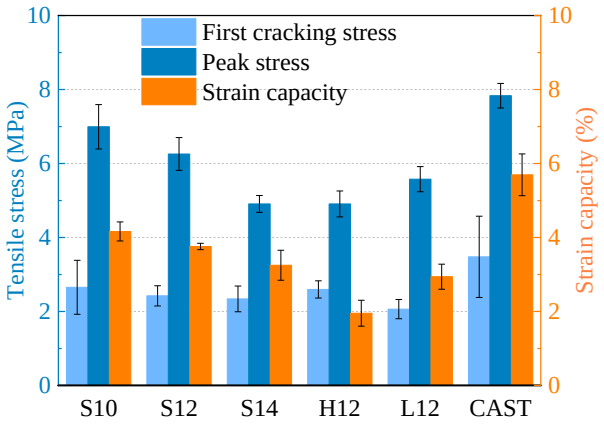

Figure 4.11: Tensile performance of the printed and cast ECC.

The observed discrepancy in tensile performance between cast and 3D printed specimens stems from the disturbance of fibers by the progressive cavity pump before extrusion. When the blades of the pump rotate, fresh ECC is continuously sheared in the hopper and extruded out of the nozzle in a twisted form. In this process, the thin synthetic fibers are vulnerable to curling considering their flexibility. The crack-bridging ability of fibers are therefore not fully exploited in resisting tension. Moreover, the orientation inside the twisted filament also appears to be not fully aligned with the printing direction. As shown in Figure 4.12, fibers in the cast specimens are randomly distributed and orientated. However, fiber in printed ECC has a certain trend of orientation. The filament of S12 exhibits a fiber orientation that is approximately 45 degrees oblique to the printing direction, which significantly weakens their tension resistant efficiency in the print direction. An even more obvious in-plane angle is observed in the L12 group. Due to the accumulation of redundant materials, the fibers are nearly orthogonal to the nozzle movement direction. This explains the less than desired tensile performance observed at low printing speed.

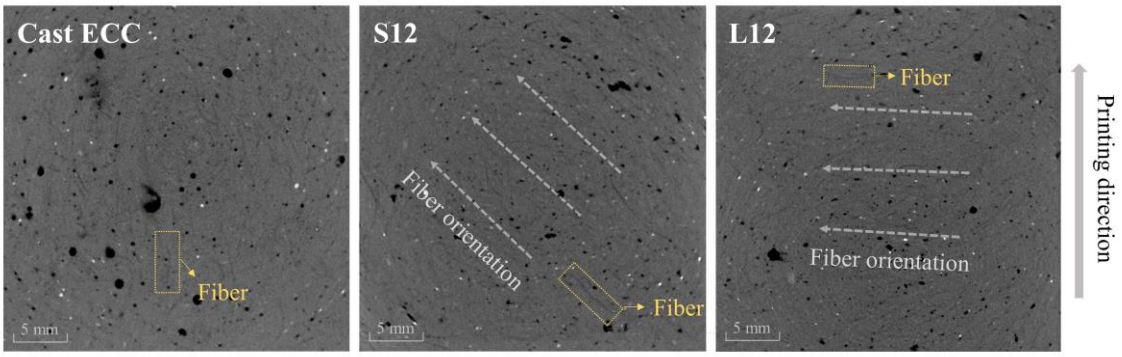

Figure 4.12: Fiber orientation in μ-CT scanning images for cast versus 3D printed (S12 and L12) specimens.

Pore structure also influences the tensile performance. In this study, porosity was measured by the software Dragonfly. It is generally expected that the print process results in a lower porosity than its cast counterpart since the extrusion pressure should compact the material [15, 85]. However, this turned out not to be the case. Porosity by volume of the cast sample, as shown in Figure 4.13(a), is between those of S12 and S10 group. Nevertheless, the strength of the matrix as reflected by the initial cracking strength, is not only affected by porosity, but is strongly influenced by the pore size distribution. Compared with 3DP-ECC, cast ECC possesses a higher proportion of finer pores

(Figure 4.13(b)), indicating a more refined micro-pore structure. Therefore, cast ECC showed a higher initial cracking strength under tension due to its denser matrix.

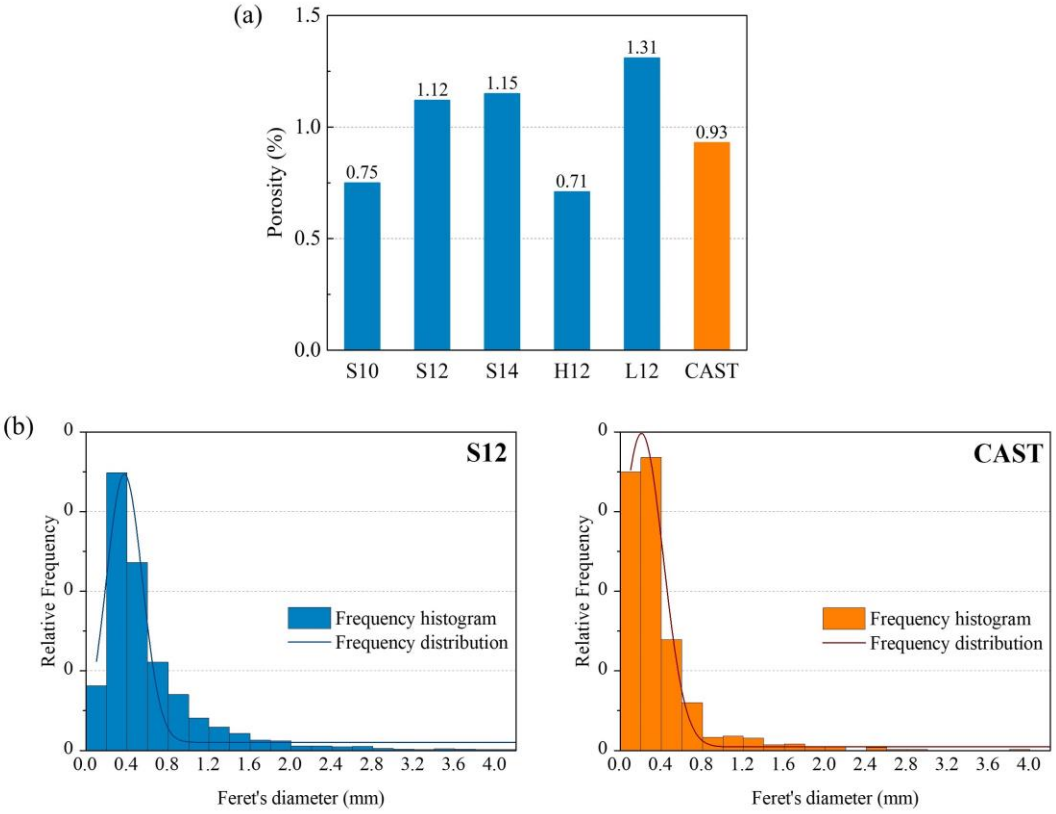

Figure 4.13: (a) Porosities and (b) pore size distribution of the printed and cast ECC.

The standoff distance of nozzle imposes notable influence to the tensile performance of 3DP-ECC. Enhanced tensile performance is seen accompanied by a lower standoff distance. This improvement can be viewed from two aspects: fiber and matrix. At a lower standoff distance, the additional compressive stress applied by the nozzle flattened the fiber and increased its alignment in the horizontal plane. That is, the out-of-plane angle of the fiber is reduced. In this case, the tensile capacity in the print direction is improved due to more efficient fiber orientation. On the other hand, due to the additional stress by the nozzle, the material undergoes a secondary compaction after deposition, and the pore structure is slightly affected. Lower standoff distance yields denser matrix with lesser porosity, as indicated in Figure 4.13(a). It can also be seen from Figure 4.11 that the initial cracking stress of ECC scales inversely with nozzle standoff distance in general, confirming the reduction of porosity and toughening of matrix. Taken the effects of

fiber and matrix together, reducing the nozzle standoff distance from 14 mm to 10 mm increased the strain capacity of the same mixture by approximately 30%, while the tensile strength was enhanced by up to 39%.

Regarding nozzle travelling speed, moderate printing speed, i.e., the S12 group, showed superior tensile capacity than both H12 and L12 groups, indicating printing speed may be optimized to yield optimal tensile performance. One underlying issue associated with low printing speed is the potential accumulation of excessive materials. With limited space for deposited material, the newly-extruded redundant material will compress the former, having fibers more likely aligned orthogonal to printing direction (Figure 4.12). For high-speed printing, despite the compactness of the matrix (Figure 4.13(a)), the tensile performance demonstrated in the tests cannot be kept on par with the S12 group. One possible explanation is that the extruded filaments of H12 are thinner than standard ones because of the relatively small material volume flow. As a consequence, H12 also experienced a relatively smaller vertical secondary compaction caused by the additional stress of the nozzle. Greater out-of-plane angles of fibers are therefore formed, leading to a weakening of the tensile performance.

4.4.2 Interfacial bonding

Interfacial bonding of 3DP-ECC originates from two major sources. One part of layer adhesion is generated in the contacting area of wet cementitious materials, and closely associated with layer cycling time. It is natural to expect that printing speed imposes notable influence on the formation of cold joint. In this research, however, the maximum difference in single-layer printing time was restrained to less than 4 seconds due to the limited contour length. Therefore, printing speed is not considered to be a main factor affecting matrix adhesion. The other portion of interfacial bonding comes from fibers bridging the interface when it is torn apart. When an upper layer of material is deposited, the self-weight will press it into the underlying layer, with part of the fibers penetrating through the interface and yielding inter-layer fracture resistance.

The superimposed influence of these two sources shapes the typical interfacial fracture curve as a dual-peak curve (Figure 4.14). During the three-point bending, load first increased almost linearly with displacement until the fracture toughness of the matrix was exhausted. The brittle fracture of the cement matrix caused a rapid post-peak drop of load. Nonetheless, the load would not plummet

to zero as in the failure of brittle cementitious materials. Due to the existence of fibers, stress redistributes after the matrix fractures, and fibers bridging the fractured surface play a crucial role in bearing the load. In this case, the load capacity rose halfway until it reached another peak or a plateau, and allowed further development of large deflection. The second ascending branch characterizes the fiber bridging ability of ECC, and the enhancement in overall fracture resistance capacity is remarkable. Compared with the brittle fracture of traditional cementitious materials, the ductile failure exhibited by ECC substantially delays the occurrence of failure and minimizes the hazard caused by catastrophic failure.

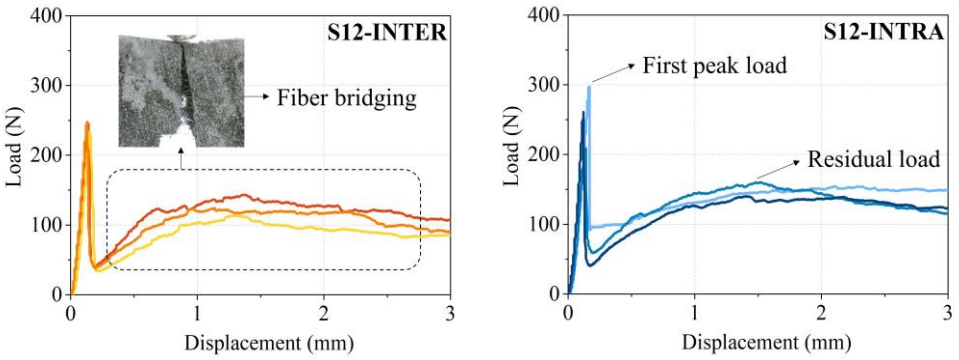

Figure 4.14: Ductile inter- and intra-layer failure demonstrated by 3DP-ECC.

Fiber is the main factor responsible for the difference of fracture resistance between inter- and intra-layer samples. As shown in Figure 4.15, fiber bridging inside the printed layer is generally more pronounced, attributed to the advantage in fiber quantity. As a result, the fracture resistance of intra-layer samples is mostly superior to that of inter-layer ones (Figure 4.16). Nonetheless, due to the significant cross-sectional deformation of the filament in the S14 group, as will be detailly discussed in later paragraph, the interface of the wet material is strongly bonded, and the unevenness of the interface may increase. This promotes the fracture resistance at the interface, but also causes potential difficulties in accurately positioning the interface when notching, which may explain why the inter-layer samples of S14 group exhibit higher residual loads than those of intra-layer ones (Figure 4.16).

Compared with fiber, matrix is not the dominant factor accounting for the difference. Through μ-CT scanning, pore distribution along layer stacking direction was observed. It turned out that the porosity in inter-layer area does not show prominent differences with intra-layer ones (Figure 4.17).

More air voids are introduced to the interior of bulk material due to the agitation of pump than the interface. The pore distribution also confirms that having the nozzle standoff distance slightly lower than the natural filament height can effectively suppress the appearance of interlayer voids, since it is natural to anticipate air voids entrained between the layers to form large voids [97].

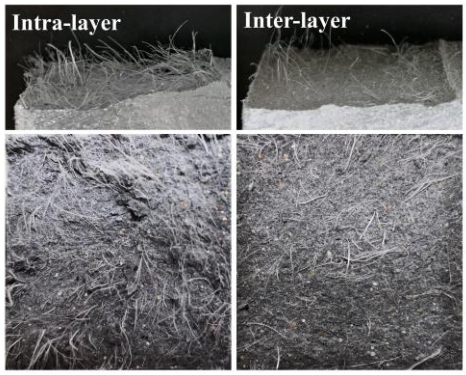

Figure 4.15: Fracture surfaces of intra- and inter-layer samples.

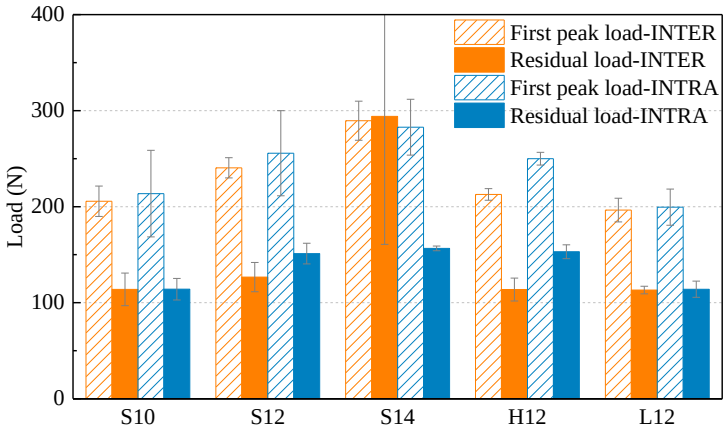

Figure 4.16: Fracture resistance capacity of 3DP-ECC.

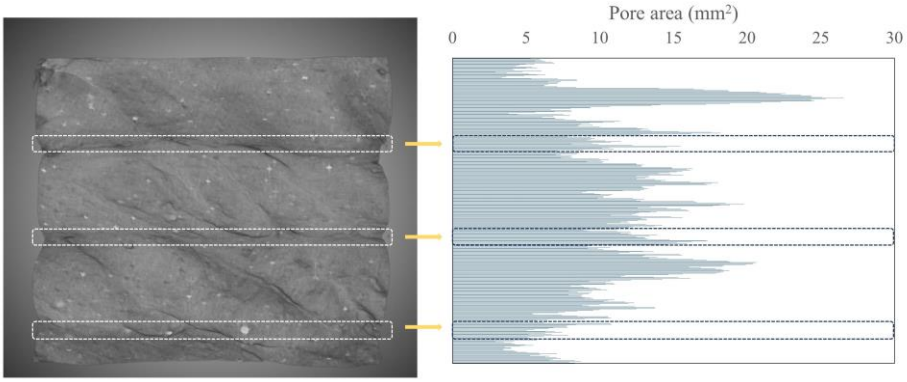

Figure 4.17: Pore distribution along vertical direction (the boxed areas layer to layer represent interfaces).

As presented in Figure 4.16, both inter-layer and intra-layer fracture resistance capacity scales with nozzle standoff distance. This remarkable trend is related to the amount of fibers bridging adjacent layers, which is further associated with the deformation of the contacting region. Greater nozzle standoff distance (e.g., S14) generally leads to more significant cross-sectional deformation. Since the original shape is barely disturbed by the additional pressure applied by the nozzle, the filament is able to maintain its cross-sectional geometry similar to the nozzle shape (circular) when extruded. Nonetheless, due to the inevitable dead-weight loading from the upper layers, the material is vertically squeezed to experience geometrical change, and the contacting area of adjacent layers is expanded, as illustrated in Figure 4.18. During this deformation process, the fibers near surface penetrate into the cement matrix of the adjacent layer, contributing to interfacial fracture resistance. Interlayer bonding is therefore strengthened. In contrast, a lower nozzle standoff distance generates a less rounded cross-section when extruded. Synchronous deformation between the two layers is relatively imperceptible. In addition, more fibers are flattened and aligned along the horizontal plane, meaning less fibers penetrate the interface, and contributing to weaker interfacial fracture resistance.

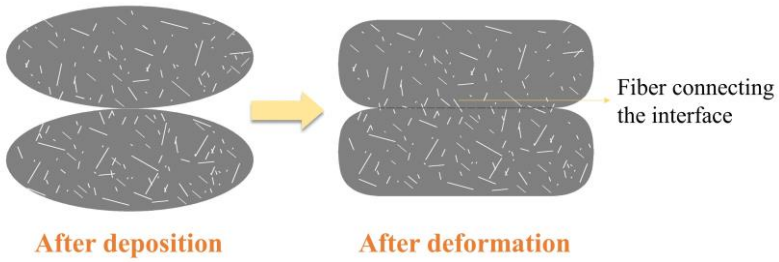

Figure 4.18: Geometrical change in filament cross-sections after filament deposition.

It is worth noting that for different nozzle standoff distances, the in-plane tensile performance and interfacial bonding always show opposite trends, as shown in Figure 4.11 and Figure 4.16. This is because the nozzle height and the additional vertical stress primarily determine the shape and remaining deformability of the filament. Lower nozzle height means more preloading, more horizontal fiber orientation, which brings about excellent in-plane tensile characteristics but yields weaker interfacial bonding.

Variation in printing speed, at least within the range in the current study, does not significantly alter the interfacial fracture resistance, as confirmed by the similar residual loads of the INTER groups of S12, H12 and L12 in Figure 4.16.

4.5. Summary and conclusions

This chapter experimentally investigates the influence of two printing parameters – nozzle travel velocity (print speed) and nozzle standoff distance – on the microstructure and mechanical performance of 3DP-ECC. The following conclusions can be drawn:

(1) In order to capture geometrical changes at both the element-level and filament-level, average vertical strain and variation in layer thickness are suggested to be adopted as quantitative indicators for evaluating buildability of 3DP-ECC. Experimental evidence showed that the buildability of 3DP-ECC scales inversely with nozzle standoff distance and could be undermined by slow printing.

(2) The tensile performance of 3DP-ECC was weakened by printing when compared to its cast equivalent, indicated by 10% and 26% reductions in tensile strength and strain capacity, respectively. The primary reason is disturbed fiber orientation inside the twisted filament and different pore distribution.

(3) The tensile properties of 3DP-ECC were enhanced by lower standoff distance and moderate printing speed. Nozzle standoff distance mainly poses effect by altering the out-of-plane angle of fibers and the micro-pore structure of matrix, while printing speed also exerts influence on the in-plane orientation and out-of-plane angle of fibers.

(4) Inter-layer bonding of 3DP-ECC was found to be strengthened by greater nozzle standoff distance. More fibers take effect in connecting adjacent layers when significant cross-sectional deformation happens along with greater nozzle standoff distance. Nonetheless, different printing speed does not notably alter the bridging effect of inter-layer fibers.

Printing parameters and material properties are important indicators that are intrinsically linked in 3DP practice. In this chapter, significant trend in material performance caused by different printing parameters have been captured. However, the same change of printing parameters can lead to trade-offs for different properties. For example, reduction of nozzle standoff distance can

considerably improve the tensile performance of 3DP-ECC, but simultaneously impair the interfacial fracture resistance. Therefore, a cautious selection of printing parameters is warranted.

In summary, this research portrays the interaction between printing parameters and material properties as a cornerstone for optimal 3DP process. Through comprehensive and in-depth research, the performance of 3DP-ECC can be enhanced and optimized by careful adjustments of the printing parameters. Correspondingly, the properties of the finished product can also be used as feedbacks to provide valuable information and guidance for the optimization of printing parameters. In this manner, additive manufacturing of ECC when fitted with real-time sensing capability (for example, of printed layer thickness), can create a closed-loop 3DP process control (for example of standoff distance).

Chapter 5. Path Design Method Addressing Anisotropy Concern of 3DP-ECC

5.1. Introduction

3DP allows the automatic generation of a layered element. The layering process inevitably introduces interfaces into the 3DP structure and causes property deviation of the interlayer surface from the bulk material. During the deposition and stacking of filaments, air voids could be entrapped between adjacent filaments and successive layers, undermining the interfacial properties [85]. Further, while the former layer of material undergoes rapid structuration after extrusion, it is gradually losing its ability to establish a tight bond with the next layer of wet material. Fast structuration, high thixotropy, long cycling time, and moisture loss at the surface may result in cold joints at the position of interfaces and threaten the integrity of manufactured objects [86, 91-96]. Consequently, anisotropic mechanical properties are inadvertently introduced into the laminated structure owing to the existence of interfaces between printed layers.

Anisotropy in 3D printed objects was widely reported - their directionally dependent mechanical properties vary significantly with the loading orientations [33, 108, 186]. In flexural, tensile, and compressive tests, loadings from the three different orientations in Figure 2.7 yield different results. Generally, the flexural and tensile properties obtained from Orientation I are the most favorable. In contrast, Orientation III exhibits inferior bending and tensile performance. When tensile forces act directly on the interfacial planes, i.e., the weak link in the structure, crack propagation and ultimate failure tend to occur at the interface position before the bearing capacity of the bulk material is exhausted [187]. In terms of compressive strength, the effect of anisotropy seems less prevalent [90, 109].

For 3D printed fiber-reinforced cementitious material, the situation is further complicated. Fiber reinforcement is regarded as an effective means to promote the flexural and tensile performance of the printed components. Previous studies reported significant enhancement of flexural performance with various types of fibers, including PP fiber [85, 90, 102], PE fiber [13, 15, 101], PVA fiber [14, 19], glass fiber [109], carbon fiber [80], basalt fiber [80, 108] and steel fiber [111].

For example, 0.25 vol.% PP fiber was reported to improve the flexural strength of 3D printed geopolymers by up to 34%, while 0.75 vol.% and 1.0 vol.% PP fibers could trigger flexure-hardening behavior [102]. Le et al. [85] observed an increase in flexural strength of up to 45% when a small amount of PP fibers was included.

With the addition of fibers and the extrusion process of 3DP, the tensile and flexural properties in the in-plane direction (Orientation I) are significantly improved due to more consistent fiber orientation [19, 80, 108], even surpassing the performance of the cast specimens. With 2.0 vol. % PE fiber, a 14% increase was observed in the tensile strain capacity of 3DP-ECC compared with cast ECC [13]. Yu et al. [12] and Xu et al. [9] also suggested higher tensile strengths and strain capacities of 3DP-ECC. With aligned fibers reinforcing the matrix along the printing direction, anisotropy is expected even within a single filament and exaggerated in the whole picture of the printed structure.

Intuitively, specimen loaded in Orientation III shows inferior flexural and tensile performance compared with the other two directions, as the resistance capacity in Orientation III highly depends on the interlayer bonding characteristics. In addition to the aforementioned factors, the lack of fiber bridging at the interface is another primary concern in fiber-reinforced cementitious material [101]. Previous studies showed up to 74% drop in flexural strength of printed fiber-reinforced cementitious material when switching the loading orientation from Orientation I to Orientation III [90, 187-188]. Regarding Orientation II, the flexural performance is usually between those in the other two directions [108]. Some test results on the mechanical properties of 3DP synthetic fiber-reinforced cementitious materials in previous literature are summarized in Table 5.1.

The anisotropy characteristic renders different material behaviors of printed elements from those of cast concrete and challenges the structural performance. Various methods have been proposed to meet the anisotropic challenge. One attempt is to apply adhesive agents to the interface. Cement paste [104], sulfur and black carbon-based polymers [105], and cellulose fiber-reinforced cement [106], for example, are used as adhesive agents to be brushed on the surface of the newly printed layer. However, this method either requires additional human labor and thus negates the automation of the entire manufacturing process or demands extra preparation and extrusion of the agents, undermining the efficiency of manufacturing. Another technique is to enhance interfacial bonding through mechanical interlock, for instance, by integrating the tongue and groove

technology into 3D printing to obtain a grooved geometry [6, 92] or modifying the layer surface to make it rough enough to adhere to the next layer [107]. In addition, inserting reinforcement in the vertical direction is also a popular strategy. Steel wire mesh [189], straight steel bar or fiber [190-191], and staple/U-nail [192-193] have been embedded perpendicular to the printing plane to provide interlayer reinforcements. These beneficial attempts offer a means of enhancing the mechanical performance in Orientation III with external reinforcements. Nonetheless, for fiber-reinforced cementitious ink, e.g., ECC, it may be more concise and effective to utilize the inherent internal reinforcement and directional-dependent features to alleviate the anisotropy.

Taking advantage of 3DP's feature of enabling complex paths and the orientation-dependent properties of fiber-reinforced composites, anisotropy could be alleviated without introducing any external reinforcements. As elucidated before, the tensile and flexural behavior of 3DP fiber-reinforced materials is most favorable in one direction (commonly the direction of filament generation). Through the delicate design of 3D spatial paths, filaments are deposited in different orientations, thus allocating tensile/flexural resistance capacity to multiple directions. In addition, 3D spatial path design alters the simple and unitary orientation of interfaces, complicating the weakest path along which cracks propagate along, thereby delaying the occurrence of failure.

The design of the 3D spatial patterns is inspired by the natural crossed-lamellar structure of conch shells. As shown in Figure 5.1, conch shell possesses three orders of lamellas in its natural structure. The interwoven interfaces created by the laminate structures in multiple orientations empower the conch shell with high ductility in bending tests despite the brittle nature of its compositions. Mimicking this biological nature, bio-inspired printing patterns can be designed, aiming at higher flexural strength and ductility of the printed structures. As a promising printing ink, ECC exhibits robust tensile ductility and strain-hardening behavior, especially in Orientation I [6-7, 11-15, 171]. To endow 3DP-ECC with appropriate spatial orientations, knitted and tilted structures were designed and printed. Flexural tests from various orientations were conducted to probe the anisotropic characteristics of these innovative structures.

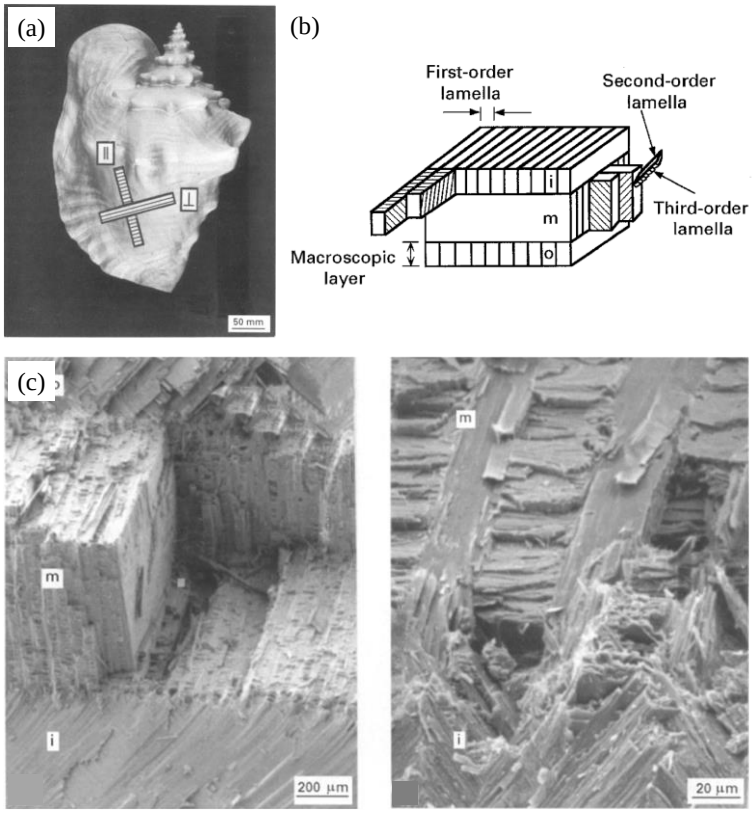

Figure 5.1: (a) A strombus gigas conch shell, (b) the schematic drawing of its crossed-lamellar structure, and (c) the fracture surfaces under four-point bending. [194]

Table 5.1: Studies on anisotropic properties of 3D printed cementitious materials.

Authors	Binders	Aggregates	Admixtures	w/b	Fiber type	Fiber length (mm)	Fiber content	Orientation	Flexural strength (MPa)	Tensile strength (MPa)	Tensile strain capacity (%)	Compressive strength (MPa)
Le et al. (2012) [85]	OPC, FA, SF	silica sand	SP, retarder, accelerator	0.26	PP	12	1.2 kg/m^3	I	12-17 (11)			84-102 (107)
								II	13 (11)			77-95 (107)
Nematollahi et al. (2018) [112]	FA	silica sand	CMC	0.38	PP	6	0.75 vol.%	I	6.1			25.9
								II	6.5			13
								III				17.7
							1.0 vol.%	I	7.5			18.2
								II	7.5			15.4
								III				14.5
Wolfs et al. (2019) [90]	OPC, LP	silica sand	rheology modifiers	0.495	PP		Little	I	4.29 (4.28)	3.68 (4.11) (SP)		28.51 (42.3)
								II	4.7 (4.28)	3.72 (4.11) (SP)		29.19 (42.3)
								III	3.68 (4.28)	3.55 (4.11) (SP)		29.19 (42.3)
Figueiredo et al. (2020) [19]	OPC, BFS, LP	-	SP, VMA	0.20	PVA	8	2.0 vol.%	I	7.2-7.5	2.4	0.26	44.09
								II		2.41	0.31	41.93
	OPC, FA, LP	silica sand	SP, VMA	0.28				I	3.4-3.9	1.64	0.15	17.66
								II		1.65	0.24	15.02
Ding et al. (2020) [101]	OPC	silica sand	SP, HPMC	0.35	PE	6&12	1.0 wt.% (in total)	I	9.53 (10.05)			
								II	8.88 (10.05)			
							1.4 wt.% (in total)	I	10.29 (15.09)			
								II	11.54 (15.09)			

Table 5.1 Continued. Studies on mechanical properties of 3D printed cementitious materials.

Authors	Binders	Aggregates	Admixtures	w/b	Fiber type	Fiber length (mm)	Fiber content	Orientation	Flexural strength (MPa)	Tensile strength (MPa)	Tensile strain capacity (%)	Compressive strength (MPa)
Yu et al. (2021) [110]	OPC, FA	silica sand	SP, HPMC	0.24	PVA	8	2.0 vol.%	I		3.38 (3.36)	3.09 (3.00)	28-31 (31.2)
								III				21-24 (31.2)
Zhu et al. (2021) [20]	OPC, FA, SF, SAC	silica sand	SP, HPMC	0.26	PE	6&12	2.0 vol.% (in total)	I	6.28 (4.95)			
								II	4.83 (4.95)			
Ye et al. (2021) [195]	OPC, FA, SF	silica sand	SP	0.26	PE	18	2.0 vol.%	I	14.5 (15.1)	4.67 (6.81)	7.50 (9.81)	45.8 (38.8)
								II	14.4 (15.1)			40.4 (38.8)
								III				40.2 (38.8)
Ding et al. (2021) [196]	OPC	silica sand	SP, HPMC	0.35	PE	6&12	1.4 wt.% (in total)	I	12.3 (13.9)			
								II	13.6 (13.9)			
Aslani et al. (2022) [10]	OPC, FA, SF	silica sand, crumb rubber	SP	0.27	PVA	12	1.75 vol.% of binder	I	9.2 (3.5)			33.5 (32.5)
								III				34.5 (32.5)
Sun et al. (2022) [188]	SAC, SF, mineral powder	silica sand	SP, retarder	0.16	PVA	9	1.2 vol.%	I	13.9 (13.0)			75 (81)
								II	13.5 (13.0)			70 (81)
								III	8.3 (13.0)			66 (81)

Note: Figures inside the parenthesis are the corresponding data of the mold-cast specimens; SP: splitting tensile strength; OPC: ordinary Portland cement; FA: fly ash; SF: silica fume; SAC: sulfoaluminate cement; LP: limestone powder; SP: superplasticizer; VMA: viscosity modifying agent; HPMC: hydroxypropyl methylcellulose; NC: nanoclay; CMC: sodium carboxymethyl cellulose; PP: polypropylene; PE: polyethylene; PVA: polyvinyl alcohol; HDPE: high-density polyethylene.

5.2. Material and methods

5.2.1 Materials

The mix proportion of printable PVA-ECC is shown in Table 5.2. The chemical compositions and properties of binders and PVA fibers used can be found in Table 3.1 and Table 3.2. The water-to-binder ratio and sand-to-binder ratio are 0.25 and 0.26, respectively. The dosage of PVA fiber is 2.0% by volume of the total composition. The bulk density of the material is 1959 kg/m^3. Tensile properties of cast PVA-ECC at the age of 28 days were shown in Figure 5.2. For 3D printing, the fresh mixture of PVA-ECC was transferred directly from the mixer to the material hopper 20 minutes after water addition.

Table 5.2: Mix proportions of printable PVA-ECC (Unit: kg/m^3).

OPC	FA	Sand	Water	SP	PVA Fiber
497	781	332	320	2.5	26

Note: SP: superplasticizer.

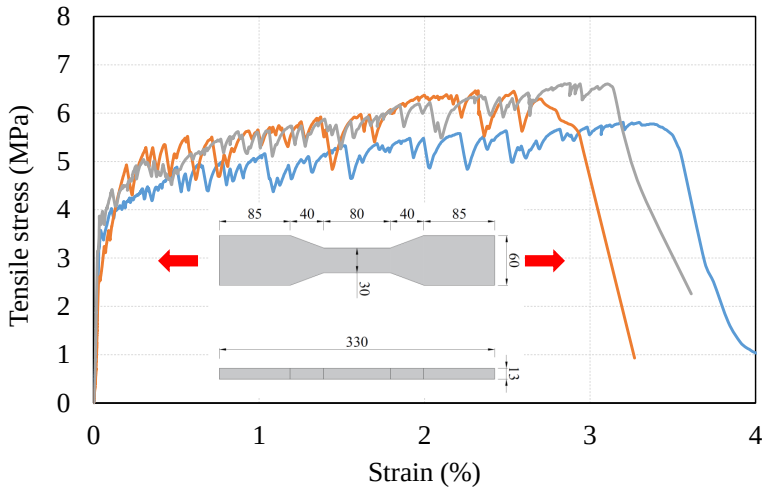

Figure 5.2: Tensile properties of cast ECC under direct tensile tests.

5.2.2 Printing patterns

Details in the printing setups can be found in subsection 3.2.2. Three different printing patterns are introduced and depicted in this sub-section: parallel filaments, knitted filaments and tilted filaments.

5.2.2.1 Parallel filaments

Parallel filaments are the most common pattern of 3D printed structures in practice. Parallel filaments are usually deposited in a fixed sequence layer by layer, as shown in Figure 5.3(a). Each layer is deposited on the print plane (x-y plane) and then advances to the next layer, building up structure height in the vertical direction (z-axis). A Rhino model of parallel filaments path adopted in this research is shown in Figure 5.3(b). The fillets at the end of filaments are designed to avoid sharp corners and help the tool align smoothly.

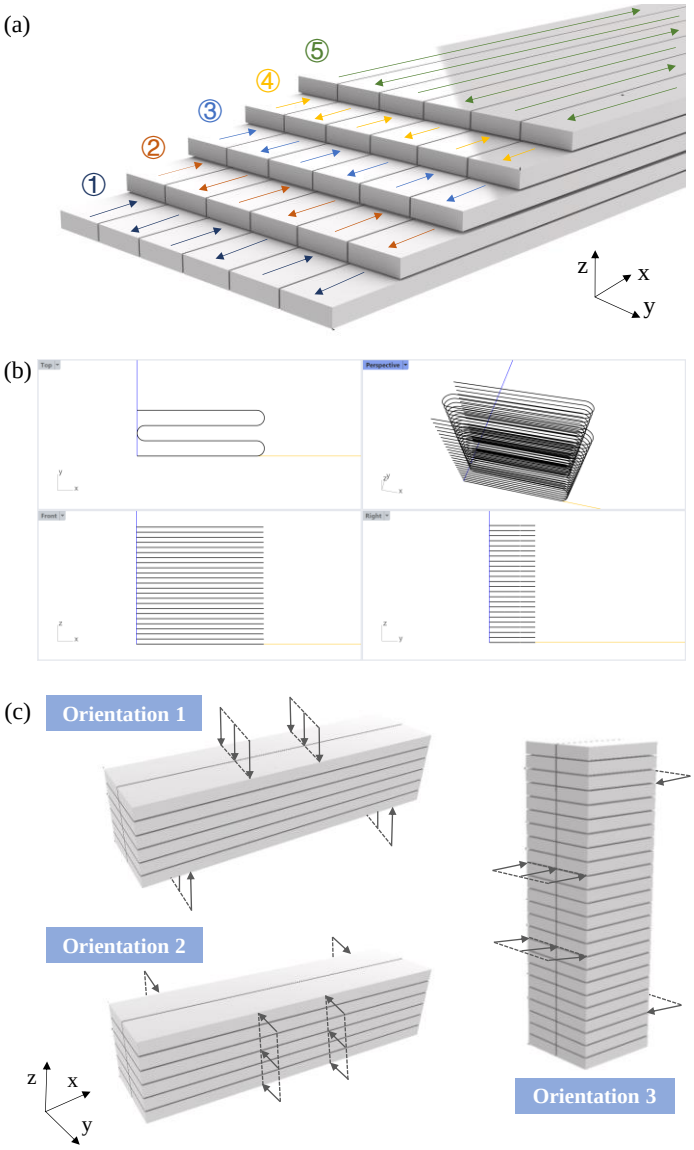

Figure 5.3: (a) Schematic diagram, (b) Rhino model, and (c) different loading scenarios for parallel filaments (Interfaces are exaggerated in the schematic diagrams to show the positions).

This printing pattern is valued for being straightforward to design and requires only three degrees of freedom for a 3D printer. However, the presence of anisotropy is a primary concern for parallel filaments. As printing is restricted in the x-y plane, layer interfaces along the z-direction are prone to insufficient bonding and potential cold joints. This issue requires particular attention for fiber-reinforced cementitious materials, e.g., ECC. Due to fiber alignment along the printing direction (x-axis) led by extrusion, fibers' effect of bridging cracks in the x-y plane and in the z-direction shows a dramatic discrepancy. Four-point bending tests were conducted in three different loading scenarios (Figure 5.3(c)) to quantify the anisotropy of parallel ECC filaments. The test setup is detailed in subsection 5.2.3.

5.2.2.2 Knitting filaments

Knitting filaments describes a printing pattern mimicking the crossed-lamellar micro-structure of conch shells. The printing process for this pattern is schematically depicted in Figure 5.4(a). For step ①, two parallel filaments are deposited along the x-axis on the printing base, and another single filament is placed on top of the first layer. Following this, in step ②, stair-wise filaments are generated back and forth in the y-z plane until the previous filaments are fully covered. Then another "layer" of parallel filament is extruded, as in step ③, on the upper surface of the "stair steps". Parallel filaments and stair-wise filaments are deposited alternatively on top of each other, creating an interwoven 3D pattern of ECC filaments. A Rhino print path design corresponding to knitting pattern is presented in Figure 5.4(b). Figure 5.4(c) shows four-point bending tests in three different loading orientations.

Compared with the traditional parallel pattern, the most prominent features of knitting design are:

(1) Knitting transcends the regular practice of single-layer printing in the two-dimensional plane (x-y plane) and unidirectional stacking in the third dimension. It expands both the single filament path and the overall structure construction to an actual three-dimensional space. This three-dimensional space design renders the direction-dependent mechanical properties of ECC (excellent tensile ductility in the printing direction) to the element out of the conventional printing plane (x-y plane). It is an attempt to homogenize material performance at the structural level through architectural design.

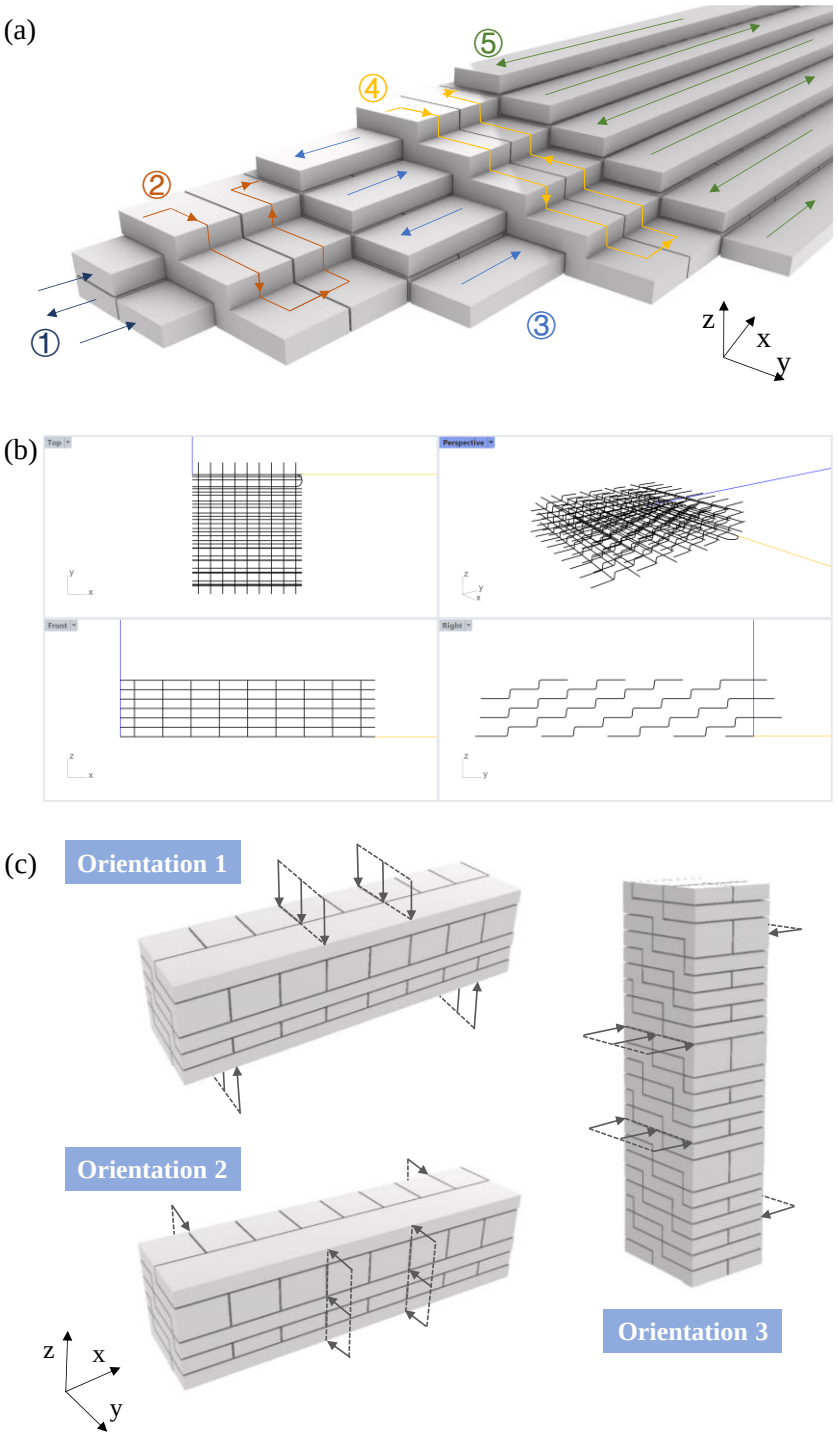

Figure 5.4: (a) Schematic diagram, (b) Rhino model, and (c) different loading scenarios for knitted filaments (Interfaces are exaggerated in the schematic diagrams to show the positions).

(2) Compared with parallel filaments, the knitting process introduces a more complex three-dimensional interface system, which converts interface from the original weakness into a structural strengthening method: The interface is generally considered relatively brittle. Even with highly ductile ECC materials printed, the interface can produce a brittle or quasi-brittle mechanical response due to the lack of fiber connections. However, the complex staggered interfaces in the conch shells enable brittle materials to yield excellent fracture toughness by forcing the crack front to twist as it propagates. Therefore, in the structural design of 3DP-ECC, intentionally creating tortuous and rugged interfaces could induce the development of multiple cracks, promotes energy dissipation, and delays crack penetration.

5.2.2.3 Tilting filaments

Alternating deposition of cross-ply structure (0° and 90° filaments, sometimes also including 45° filaments) is a common practice to moderate the in-plane anisotropy of 3DP. However, this design generally does not contribute to performance improvement in the vertical direction (z-axis). Therefore, a tilted pattern was proposed. Filaments at 0° (along the x-axis) and 90° (along the y-axis) are deposited in layers; nevertheless, instead of printing on the conventional x-y plane, the deposition occurs on the top surface of an inclined base, which was printed first at an angle to the x-y plane, as shown in Figure 5.5(a). The base is shaped by stacking several layers of filaments along the x-axis to form an inclined surface (step ①). A layer of parallel filaments is then placed along the x-direction with the same inclination as the base (step ②), followed by a next layer of parallel filaments along the y-z plane (step ③). Repeat steps ② and ③ until the desired dimension and shape are achieved. A Rhino model for tilted pattern and three different loading orientations are illustrated in Figure 5.5(b) and Figure 5.5(c), respectively. The printed structures in this research were tilted by 27 degrees.

The underlying logic of tilting design is analogous to that of knitting: to endow the printed structure with tensile/bending resistance in the y- and z-directions, and to bring in a more advanced interface system. By simply tilting a basic printing pattern at an angle, the interfaces are elongated in length and could contribute to delay fracture, although it does not produce zig-zag interfaces as in knitting.

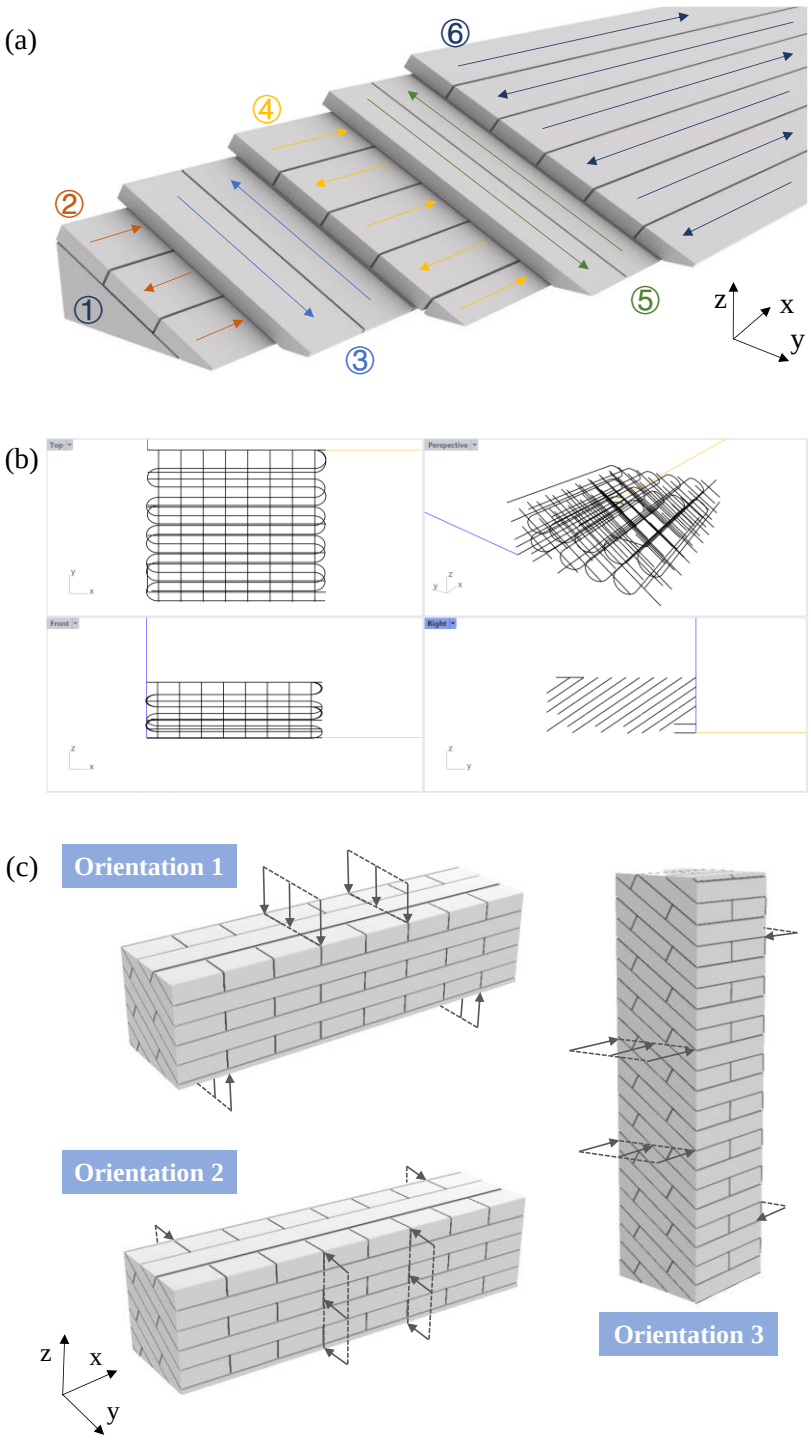

Figure 5.5: (a) Schematic diagram, (b) Rhino model, and (c) different loading scenarios for tilted filaments (Interfaces are exaggerated in the schematic diagrams to show the positions).

5.2.3 Four-point bending test

The test system (Figure 5.6(a)) consists of three main parts: (1) loading setup, (2) motion capture system, and (3) digital image correlation (DIC) system. The four-point bending tests were carried out on an MTS 810 machine, as shown in Figure 5.6(b). ECC specimens are 200 mm in length, 50 mm in width, and 50 mm in depth. The three loading spans are 50mm, 60mm, and 50mm, respectively, due to the limitations of the experimental equipment (Figure 5.6(c)). The loading rate is 0.2 mm/min. Four kinematic markers are attached to the specimen to locate the position of specific points on the surface. The absolute position changes of the markers are captured by an NDI Optotrak motion capture system shown in Figure 5.6(d) to derive the mid-span deflection of the specimen. In addition, a high-resolution camera and a lighting system are placed in front of the specimen, to monitor the morphological and positional changes of the random black and white speckles on the specimen surface for DIC analysis.

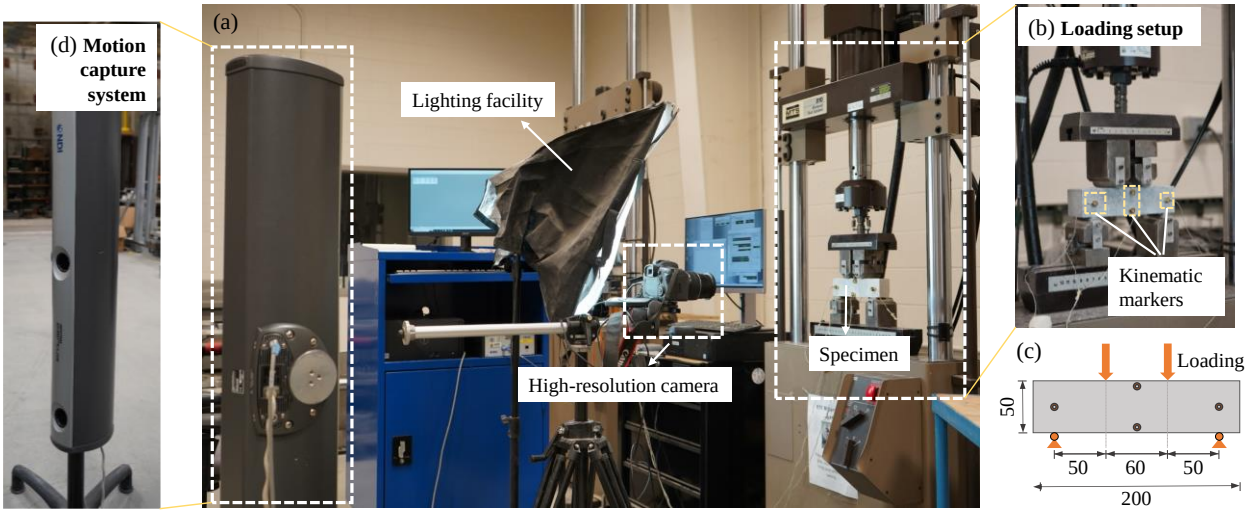

Figure 5.6: Test setups.

5.3. Flexural performance

5.3.1 Parallel filaments

Figure 5.7(a) illustrates the four-point bending test results for parallel filaments and cast ECC specimens. The relationships between flexural stress and mid-span deflection are shown. The flexural stress is calculated according to Equation 5.1, and the mid-span deflection is derived from the relative position change of the four markers shown in Figure 5.6(b).

$$\sigma = \frac{3F(L-L_i)}{2bd^2} \tag{5.1}$$

where F is the load; L is the length of the support span, i.e., 160 mm in this research; L_i is the inner span, i.e., 60 mm; b and d are the width and depth of the specimen, respectively.

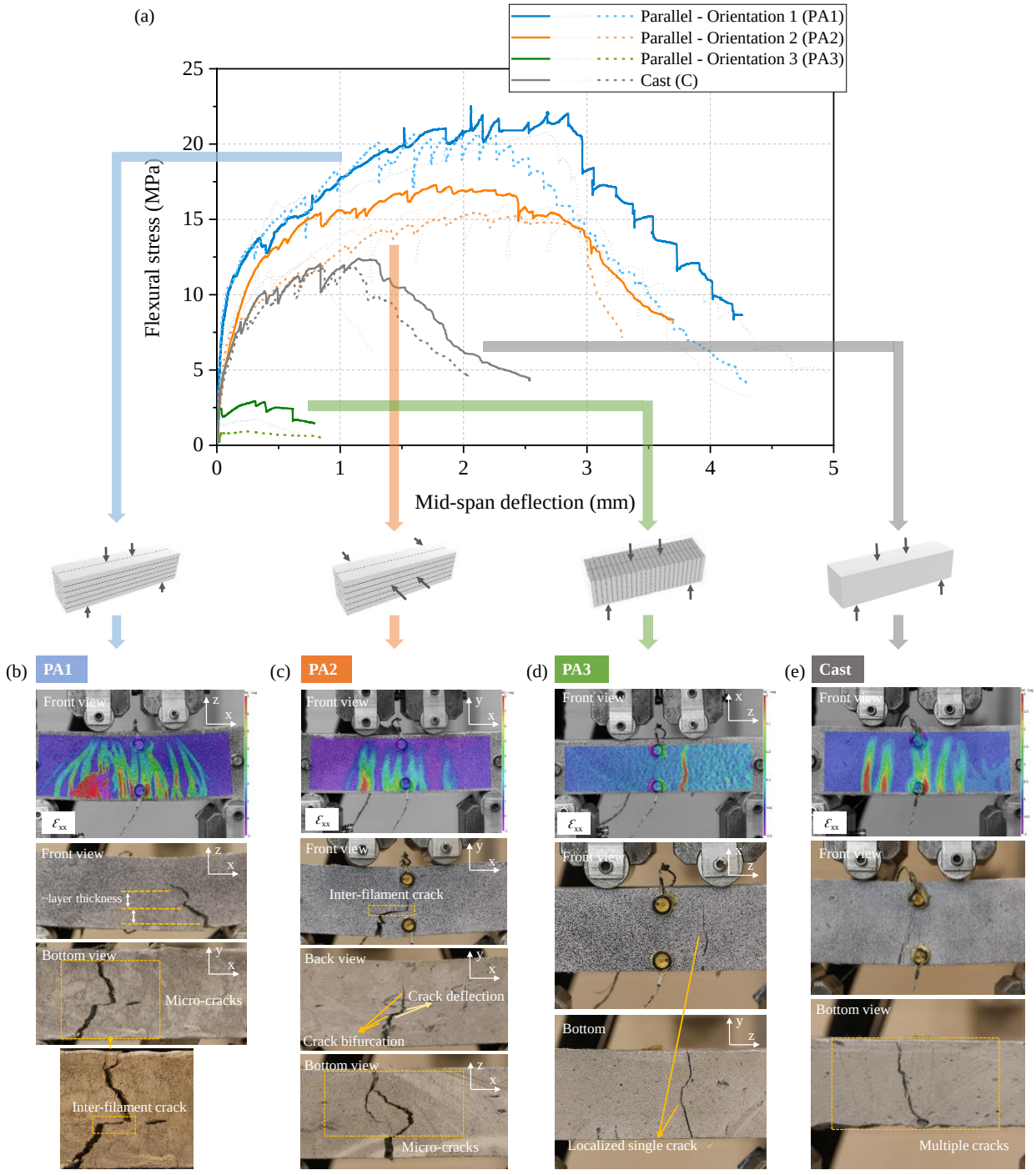

Figure 5.7: Flexural performance of parallel ECC filaments and cast ECC in four-point bending tests.

Parallel filaments loaded in Orientation 1 (abbreviated as PA1) showed excellent flexural performance in both flexural strength and mid-span deflection. The PA1 group exhibited unparalleled flexural resistance, with an average flexural strength exceeding 21 MPa. Robust strain-hardening behavior was observed. The fluctuation of load originates from the successive development of multiple micro-cracks. As each new micro-crack develops, the brittle cementitious matrix is unable to bear the stress, resulting in a slight stress drop. Nonetheless, as the stress redistributes between fibers and matrix, the load-bearing capacity of the specimen is elevated to a higher level than the original stress peak. The strain hardening continues until stress concentration occurs on one crack plane with the lowest load capacity, causing the crack opening to gradually grow until fracture. This process is analogous to the plastic yielding in ductile metal and empowers ECC with the unique "metallic" tensile ductility [7].

The failure mode of PA1 also validated the remarkable mechanical response. In the initial loading stage, instead of showing tensile strain concentration at a single location and developing a localized crack, smeared strain showed up at the tensioned region of the PA1 specimen. In Figure 5.7(b), the DIC-analyzed image illustrates the distribution of horizontal tensile strain (ε_{xx}). It should be noted that the subscript of ε_{xx} stands for the horizontal direction in the analyzed image, not the printing direction of 3DP. Smeared tensile strain (the red regions) indicates multiple cracking sites. As confirmed in the bottom view image, dense micro-cracks were captured.

The flexural performance of PA1 remarkably outperformed that of cast ECC, with higher flexural strength and more ductile response. Moreover, the PA1 group also showed a substantially different failure mode from cast ECC. PA1 group generated denser micro-cracks in the tension region, and the main fracture crack was tortuous along the height of the specimens (Figure 5.7(b)); in contrast, cast ECC showed fewer cracks on the bottom and bunches of straight cracks on the front (Figure 5.7(e)). There are three primary sources of these differences:

(1) Fiber alignment in 3DP-ECC. It has been reported in 3D extrusion that the fibers tend to align along the printing direction, i.e., the direction of nozzle movement [19]. It is the same case for 3DP-ECC in this research. As shown in Figure 5.8, the PVA fibers exhibited a strong orientation tendency along the x-direction in the filaments. Compared to cast ECC with random fiber distribution, consistency in fiber orientation results in a more robust tensile and flexural resistance,

inducing denser micro-cracks in the tension region (see Figure 5.7(b) and 5.7(e)). This makes PA1 a more favorable orientation, as fibers exhibit the best crack bridging capacity in the x-direction.

Figure 5.8: Fiber alignment observed in 3DP-ECC.

(2) Crack bifurcation and deflection in a laminate structure. The stacked parallel ECC filaments resemble the layered structure of laminate composites and therefore share a similar crack propagation pattern. In four-point bending tests, the tension region at the bottom layer/filaments is subjected to the highest tensile strain and therefore is the location where cracks initiate. After the load-bearing capacity of the bottom filaments is exhausted, the cracks penetrate through the layer and are deflected into the interface/interlaminar region, creating an interface delamination crack. As can be appreciated in Figure 5.9(a), after the crack ① penetrated the lowermost layer, the crack tip developed in two different directions along the interface, crack ② and ③. Nonetheless, deflected cracks do not persist along the interface. Since the maximum bending stress in the experiment is located at the mid-span and decreases along the span, the driving force for the interfacial crack propagation gradually reduces [197]. Under the loading circumstance, the ratio of driving forces (energy release rate) and resistance (crack extension resistance or fracture roughness) of the crack tip could vary in two directions, that is, along the interface or into the adjacent layer. When the ratio in the latter scenario surpasses the former, the crack tip tends to kink out into the upper layer/filament [198]. This crack bifurcation depends on the local driving forces and local material characteristics (R) of both the interface and the filament matrix near the interfacial area. In Figure 5.9(a), crack ③ was kinked into crack site ⑤ after advancing for approximately 12 mm (Figure 5.9(b)), and the main crack continued to develop along the interface for another 10 mm and then kinked into crack site ⑥ (Figure 5.9(a) and Figure 5.9(c)).

The deflection and bifurcation processes occurred successively during the test, as shown in Figure 5.9(a). For example, after crack ④ cut through the filament, the crack was further deflected to a horizontal crack ⑦ (Figure 5.9 (a) and Figure 5.9(d)). Repeated crack deflections were also captured in the front view of Figure 5.8(b). The spacing between each reorientation of crack is approximately the layer thickness, confirming that the distortion of cracks occurred at the interlayer position. Furthermore, a zigzag fracture crack was observed on the bottom view in Figure 5.7(b), illustrating that the crack kinking occurred not only on the x-z plane and at inter-layer interfaces, but in the interior of the specimen and at the inter-filament interfaces. Both crack deflection and bifurcation promote energy dissipation and reduce the overall rate of crack development, thereby enhancing the damage tolerance of the printed parallel ECC filaments.

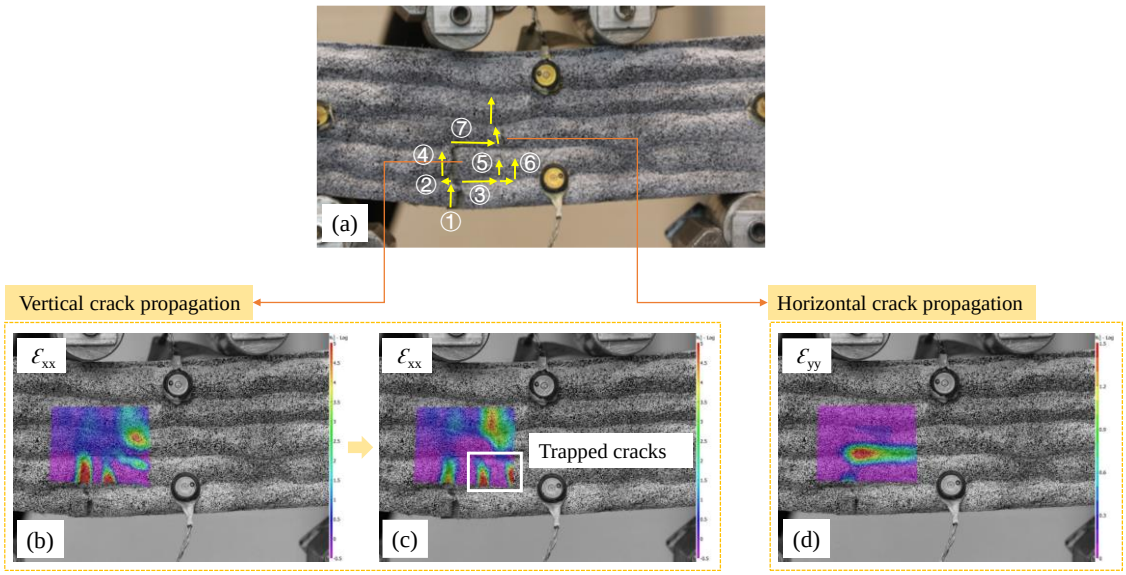

Figure 5.9: Crack kinking and trapping in 3DP-ECC.

(3) Crack trapping feature of ECC. As kinked out from the interface, the crack tip experiences a low initial toughness in the matrix and attempts to keep growing into the upper filament. In the case of brittle bulk material, the filament would be penetrated through and fractured at the cracking site. Conversely, if the bulk material has a rising fracture resistance, i.e., exhibits an R-curve characteristic [198], the resistance which the kinked crack tip encounters rapidly catches up with the driving force due to fiber bridging, then the advance of the crack can be stopped. In this case,

the kinked cracks are trapped in the filament. Cracks ⑤ and ⑥ in Figure 5.9 (a) evidenced the crack kinking-trapping mechanism in 3DP-ECC. Both cracks were kinked out from the interfacial crack ③ to the filament matrix, showing concentrated tensile strain at the cracking sites in Figure 5.9(c), then trapped by fiber bridging inside the filament with no further propagation along either vertical or horizontal directions. The crack kinking-trapping mechanism of 3DP-ECC facilitates energy consumption and yields a more ductile mechanical response.

Under the synergistic effect of the above factors, the flexural performance of PA1 notably exceeded those of the other groups in Figure 5.7(a). In addition to the highest flexural strength, PA1 also exhibited remarkable energy absorption capacity. The area under the stress-deflection curve of the PA1 group is approximately 3-4 times that of the cast ECC. The excellent energy absorption capacity removes the dependence on steel reinforcement, enabling robust structural integrity and reliability through the combination of 3DP technology and ductile ECC materials.

Parallel filaments loaded in Orientation 2 (PA2) possessed a slightly lower flexural strength than PA1 while exhibited a similar failure mode. In the tensioned zone of the specimen, dense micro-cracks were developed (bottom view in Figure 5.7(c)), as the fiber alignment still imparts a reliable crack bridging ability in the x-direction under the loading scenario of PA2. The relative reduction in flexural strength in PA2 is attributed to the slight difference in crack propagation modes. As illustrated before, cracks in PA1 were deflected at the interlayer positions, while in PA2, similar deflections occurred on the inter-filament surfaces (see the front view and back view in Figure 5.7(c)). Due to the geometrical difference in filament width and height, PA2 contains fewer interfaces in the x-y plane, indicating less chance of crack deflection and bifurcation and impairing the energy dissipation capability. Nonetheless, extensive deflection and distortion of cracks were captured in the interior of the specimen due to the existence of layer interfaces in the x-z plane (bottom view in Figure 5.7(c)). Although the overall flexural performance was slightly inferior to PA1, the mechanical response of PA2 was notably improved when compared to cast ECC, attributed to the influences of the three factors demonstrated above.

Despite the excellent flexural properties of parallel filaments in Orientation 1 and 2, the performance in Orientation 3 (PA3) showed a dramatic drop. Due to the fiber alignment along the x-direction, layer interfaces have insufficient fiber bridging and thus become the most vulnerable positions when parallel to the loading direction. Once a crack is initiated in the tensioned matrix,

the lack of fiber bridging cannot stop the crack or bear a higher load during the crack propagation and eventually develops into a localized fracture crack. Consequently, different from the smeared multiple tensile cracks of PA1 and PA2, deformation localization into a single fracture was observed in the tension zone of PA3, as shown in the DIC-analyzed image in Figure 5.7(d). The interfacial failure inhibited the strain-hardening behavior of ECC material and induced drastic reductions, i.e., up to 91%, in strength and deflection compared with PA1. This is the primary concern about anisotropy in 3DP - the mechanical properties in Orientation 3 acutely deviate from the other two directions, raising doubts about the integrity and reliability of 3D printed structures in complex stress states and real application scenarios.

The impressive flexural performances of parallel filaments in Orientations 1 and 2 verified that 3D printing technology improves ECC performance at the structural scale through fiber alignment and laminate structural form. However, in Orientation 3, the emergence of anisotropy poses challenges to structural integrity. This apprehension gave rise to the attempts to mitigate anisotropy through the delicate design of innovative structural forms, i.e., knitted and tilted filaments, as depicted in the following subsections.

5.3.2 Knitted filaments

The four-point bending test results for knitted filaments and cast ECC specimens are summarized in Figure 5.10(a). Compared with parallel filaments, knitted filaments loaded in Orientation 1 (KN1) and Orientation 2 (KN2) showed inferior flexural strength and mid-span deflection. This is due to the fact that the parallel filaments align all fibers to the x-direction to the greatest extent, maximizing the performance in PA1 and PA2 loading cases. Unlike parallel printing, knitting alters the orientation of some filaments in the architected structure, diverting part of the fiber alignment from the x-direction to other directions. Due to the presence of filaments deposited along the y- and z-directions, the proportion of fibers arranged along the x-direction is reduced, thus impairing the flexural properties of KN1 and KN2. Despite the weakened performance, KN1 outperformed its cast counterpart in flexural properties, while KN2 exhibited comparable performance with cast ECC. Therefore, knitted filaments loaded in Orientation 1 and 2 are able to meet the requirements of the same application scenarios as cast ECC.

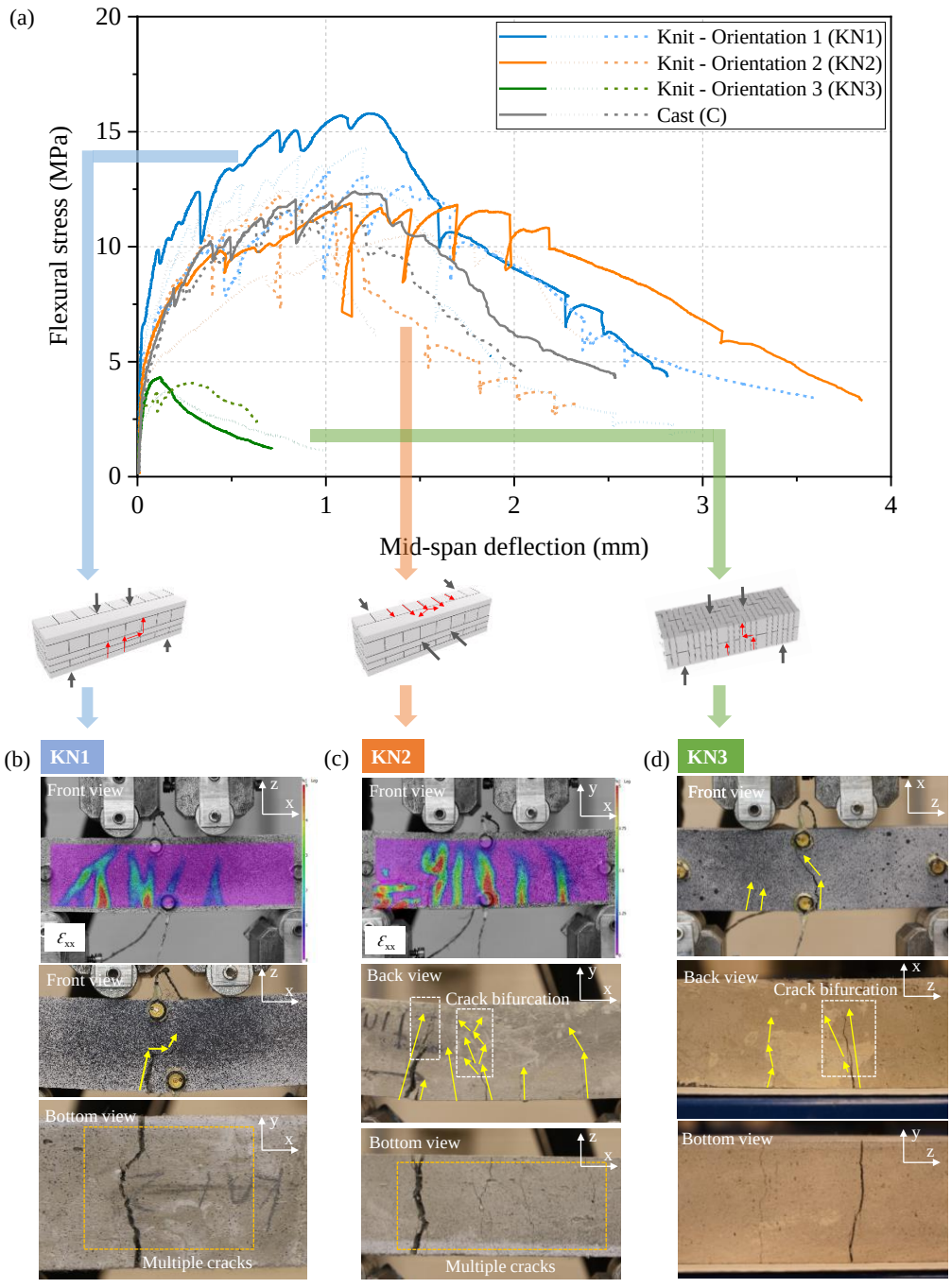

Figure 5.10: Flexural performance of knitted ECC filaments in four-point bending tests.

Knitting creates a different failure pattern than cast ECC and parallel filaments. Generally, in the four-point bending tests, tensile cracks were initiated at multiple locations on the bottom of all PA1, PA2, KN1, and KN2 specimens. In the PA1 group, cracking arises in the bulk material of

the continuous filaments, whose properties are homogenous along the x-direction. The cracks thereby have a uniform probability to develop at random positions along the entire tension zone, thus forming dense cracks that are closely spaced. In KN1, however, there is a priority in the crack initiation location. As seen in the bottom view in Figure 5.10(b), spacing between main cracks was approximately 30 mm, i.e., the width of a single filament, verifying that cracks tend to develop at the inter-filament interfaces between adjacent y-direction filaments. This tendency restrains the initial crack development, limits the energy-releasing rate, and weakens the overall ductility compared with the parallel filaments.

The bottom cracks progressed along interfaces in the loading direction. Further deflection and bifurcation occurred when they were deflected into the x-direction filament. This phenomenon is more pronounced in KN2. As shown in Figure 5.10(c), the bottom cracks fully developed along the inter-filament interfaces and advanced for some distance in the y-direction. When reaching the intersection of filaments, the cracks entered the continuous x-direction filament. Cracks experienced successive bifurcations and extended toward surrounding areas. A dendritic cracking pattern was thus shaped. Deflection and bifurcation of cracks, as previously elucidated, promote energy dissipation and delay failure to achieve excellent ductility in PA2. The ultimate fracture surface (Figure 5.11) also confirmed that the deliberate design of a complex interface system promotes a more tortuous fracture path of the printed ECC structure. Since the width of the filament is three times the height, x-direction filaments account for a larger proportion in the x-y plane than in the x-z plane, as shown in the cracking schematic diagrams. Thus, KN2 is generally more conducive to crack bifurcation within the filament, yielding greater mid-span deflections and superior ductility.

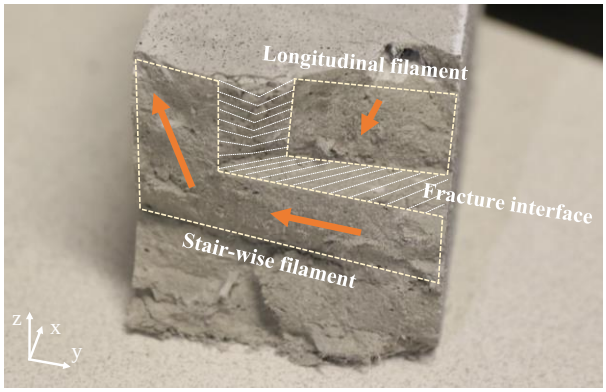

Figure 5.11: Fracture surface of knitted ECC (the specimen was loaded to complete fracture).

In Orientation 3 (KN3), improved flexural properties over parallel filaments (PA3) were presented. Regarding the cracking mode, bottom cracks had the same tendency to initiate at the interlayer interfaces. However, the number of cracks developed was not as numerous as in KN1 and KN2 (Figure 5.10(d)). During the upward progression, one main crack was deflected into a diagonal direction when encountering the interlayer interface (front view in Figure 5.10(d)). While in the back view, the orientation of the same crack was less inclined, indicating there was crack distortion inside the specimen. Furthermore, bifurcated crack was captured in the back view and bottom view. Overall, no significant enhancement in mid-span deflection was seen in KN3, compared to PA3. However, non-singular cracks and crack deflection and bifurcation contribute significantly to strength. Up to 116% increase in flexural strength in Orientation 3 was observed when knitting pattern was applied.

In general, knitting filaments creates a unique flexural failure mode and allows for deliberate performance tuning of 3DP-ECC. The flexural strengths of knitted filaments in Orientation 1 and 2 were inferior to those of parallel filaments; however, the rich cracking patterns coupled with the filament's tensile resistance induced comparable or even superior performance to cast ECC. It was observed in both KN1 and KN2 that cracks commonly started at the inter-filament positions, and then were interrupted by the continuous filaments midway. Cracks were forced to zigzag into the interior of the filament and bifurcated successively, forming more crack tips and a more complex crack network. During this process, the strain-hardening behavior of the specimen is guaranteed, and fracture failure is delayed.

5.3.3 Tilted filaments

The four-point bending test results for tilted filaments and cast ECC specimens are summarized in Figure 5.12(a). The flexural strengths of tilted filaments in Orientation 1 and 2 fell between those of parallel filaments and knitted filaments, while still prominently higher than the cast counterparts.

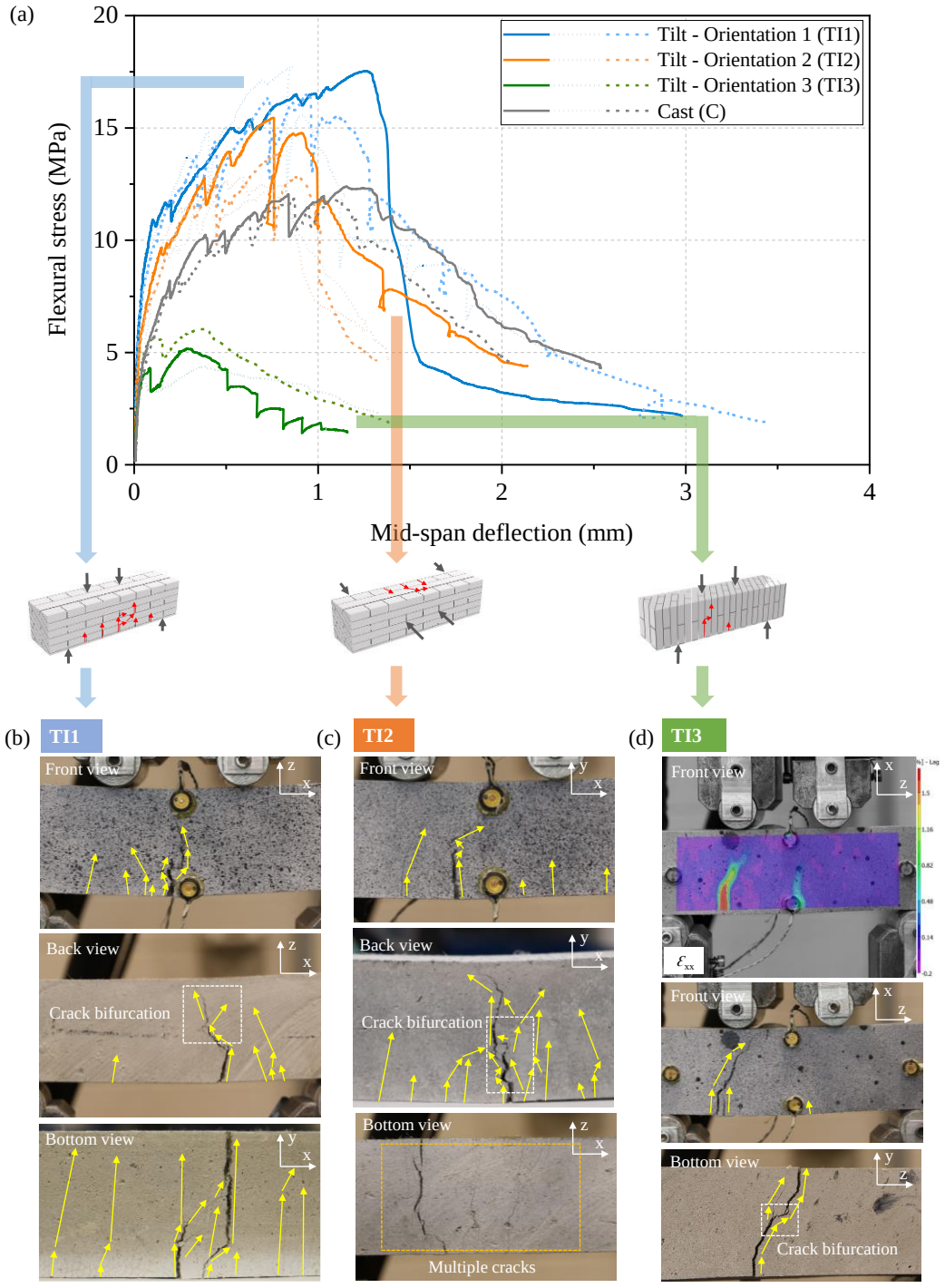

Figure 5.12: Flexural performance of tilted ECC filaments in four-point bending tests.

Regarding the fracture mode, it was found that the crack patterns of TI1 and TI2 were analogous to those of KN1 and KN2. Multiple tensile cracks arose from the tension zone at the bottom of the

specimen. Since both short filament segments (parallel to the y-z plane) and continuous longitudinal filaments (along the x-direction) are included in the bottom region, deflection and branching were observed at the bottom cracks (bottom views in Figure 5.12(b) and Figure 5.12(c)). As the cracks progressed upward along the loading direction, deflection was observed at the intersection of the interfaces with different orientations. Cracks were prone to branching after being kinked into longitudinal filaments, resulting in an expanded crack distribution (front and back views in Figure 5.12(b) and Figure 5.12(c)).

Compared with KN1 and KN2, the interface system of tilted filament is relatively plain, including inclined inter-layer and inter-filament ones orthogonal to each other. This means it may be easier for a crack to penetrate and cause damage through the flat interface than through a complex zig-zag interface. As a result, despite the higher flexural strength, TI1 and TI2 possessed relatively lower mid-span deflections than knitted filaments. The ductility of TI1 was comparable to that of cast ECC, while the mid-span deflection of TI2 specimens was slightly weakened.

In Orientation 3 (TI3), a remarkable superiority of tilted filaments was demonstrated - TI3 showed a drastic boost in flexural strength compared to PA3. As seen in the bottom view of Figure 5.12(d), the tensile cracks started approximately along the direction of the inclined layer interface. However, unlike PA3, which split rapidly from a simple straight crack, TI3 experienced crack deflection and bifurcation. This indicates that the crack advance inside the specimen did not completely follow the flat layer interface. Instead, twisting and turning of cracks in the interior took place. In addition, the crack was deflected from the layer interface into the inter-filament one in the middle of the upward progress and turned diagonally into a filament. Corresponding to this crack deflection is a slight stress drop on the stress-deflection curve, followed by a re-uplift, which symbolizes the redistribution of stress and the increase in bearing capacity due to interior fiber bridging. Consequently, the peak stress of TI3 reached 279% of PA3. A stress softening segment was observed thereafter, with progressive crack opening and failure of fiber bridging.

Generally, the failure modes of tilted filaments were similar to those of knitted filaments, benefiting from crack deflection and bifurcation. Furthermore, substantial increases in flexural strength compared to knitted filaments and cast ECC were witnessed. The main contributing factor is the designed interface system. Nonetheless, the ductility of TI1 and TI2 were comparable to or slightly weaker than that of cast ECC.

5.4. Discussion on anisotropy

The flexural strengths and mid-span deflections of the three printing patterns and cast ECC are presented in Figure 5.13. In Orientation 1 and 2, the flexural strength of most printed specimens surpassed their cast counterparts, except for KN2 which possessed a slightly lower strength than the reference. The most favorable PA1 was observed with an average flexural strength of 21.6 MPa, revealing a 73% increase compared to cast ECC. For PA2, the increasing percentage was 35%. In addition, KN1 and TI1 also achieved 118% and 142% of the cast strength. Regarding mid-span deflection, PA1 and PA2 exceeded the cast equivalent by 155% and 93%, respectively. For KN1 and KN2, this increase was 20% and 45%. Tilted filaments showed comparable deflection to cast ECC in Orientation 1, while amounted to 70% of cast ECC in Orientation 2. Additionally, in Orientation 1 and 2, knitted and tilted filaments established their respective advantages in strength and ductility. The difference in path design made knitted filaments more ductile, while tilted filaments resulted in higher bearing capacity. In general, the flexural performance of various 3DP-ECCs in Orientation 1 and 2 has transcended or at least is comparable to the integral cast ECC. This means that under those two load scenarios, 3DP-ECC can meet the same structural requirements as cast ECC and provide more reliable capacity.

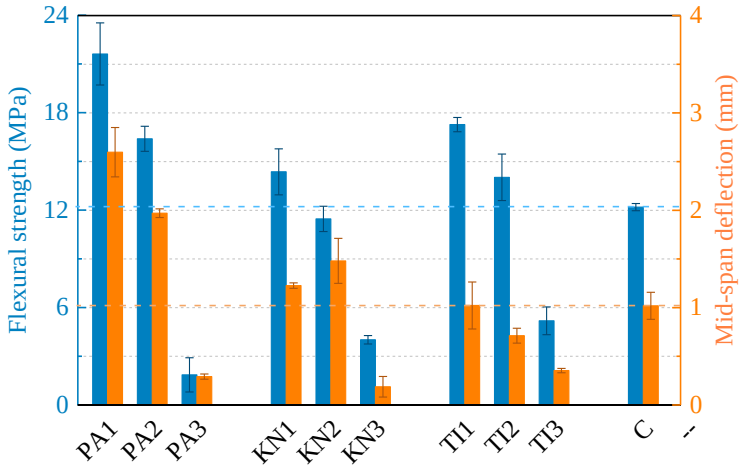

Figure 5.13: Flexural strengths and mid-span deflections of printed and cast ECC.

In Orientation 3, remarkable enhancements of flexural strength were obtained by knitting and tilting filaments. An up-to-179% increase was observed in TI3, and the strength of KN3 also exceeded that of PA3 by 116%. It is worth noting that, despite the high strength of KN3, the

corresponding deflection is reduced compared to PA3, and a strain-softening behavior was captured. For TI3, nonetheless, the increases in strength and deflection occurred simultaneously. As illustrated in the previous subsection, the flexural stress elevated again after the stress drop caused by initial cracking, delaying the overall failure of the specimens.

The preeminent strength of printed ECC compared to cast one can be attributed to the fiber alignment and the kinking-trapping mechanism of ECC. The former renders filaments with the maximum tensile resistance in the printing direction. In the cases of knitted and tilted structures, the fiber bridging capacity is further allocated to different orientations, as shown in Figure 5.14. While the latter takes advantage of the interfaces and ECC's material features to capture and trap cracks during their progression, thereby effectively enhancing the mechanical response of the structure.

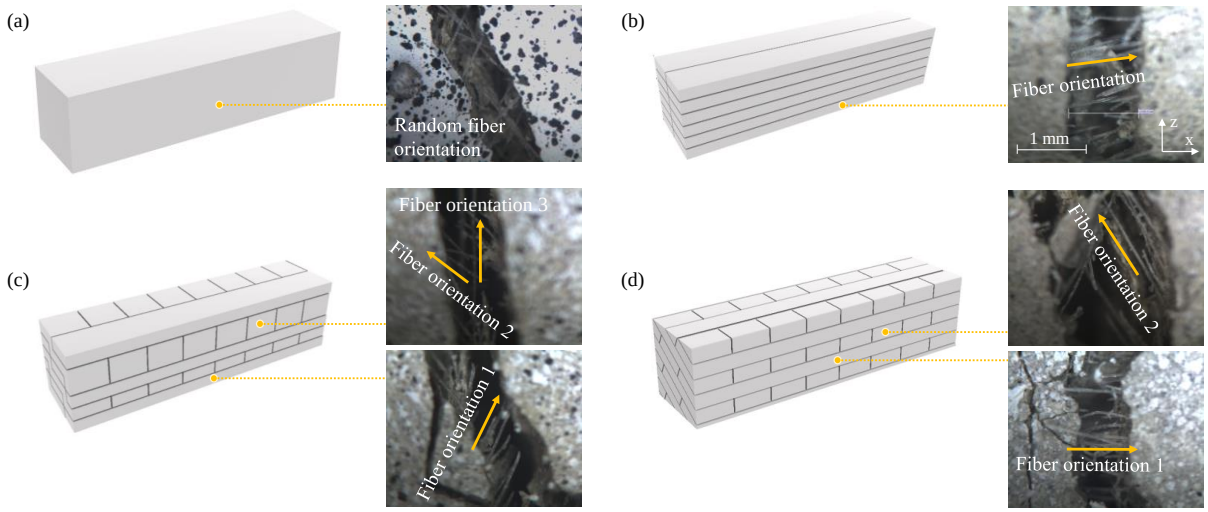

Figure 5.14: Microscopic illustration of fiber alignment in (a) cast ECC, (b) parallel filaments, (c) knitted filaments and (d) tilted filaments.

Regarding anisotropy, the ratios of the strengths in Orientation 2 (f_2) and Orientation 3 (f_3) relative to Orientation 1 (f_1) are presented in Figure 5.15. For all three different printing patterns, f_2/f_1 values are approximately 0.8, showing that strength difference in these two directions is not the primary concern regarding anisotropy. Knitting and tilting slightly improve the ratio with a limited margin. For f_3/f_1, however, there is a notable improvement with knitting and tilting. In this research, f_3 is merely 8.6% of f_1 in conventional parallel printing, causing concerning anisotropy. While in

the case of knitted and tilted filaments, the f_3/f_1 ratio is promoted to 28% and 30%, respectively, demonstrating an effective alleviation of anisotropy. This improvement originates from the architectured structural forms with tortuous interfaces.

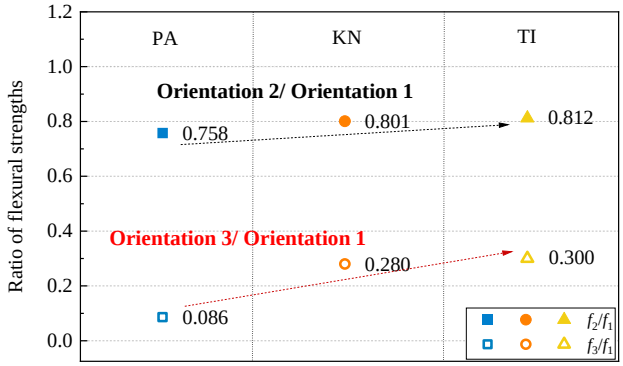

Figure 5.15: Ratios of flexural strengths in different loading orientations.

It is worth noting that the mechanical properties of the printed structures are also substantially affected by multiple factors, e.g., printing setup, material compositions, structural geometry, printing parameters, etc. Therefore, the effect of knitting and tilting filaments on mitigating anisotropy is not limited to increasing the f_3/f_1 ratio to 30%. In an optimized printing scenario, the reference value of f_3/f_1 in parallel filaments can exceed the ratio in this study, and the effectiveness of knitting and tilting will be further improved to achieve better homogenization of the 3DP-ECC structure.

Anisotropy alleviation has been confirmed with the proposed innovative printing patterns. However, more improvements can be made to further address the anisotropy issue. Given the excellent mechanical performance of 3DP-ECC in Orientation 1 and 2, there is still a gap between Orientation 3 and the other two in terms of strength and ductility. From the perspective of fracture mode, the designed patterns have the potential to induce more tensile cracks under Orientation 3 loading. The pattern design should be further refined and optimized to obtain more desirable cracking modes and stimulate higher structural bearing capacity and ductility.

5.5. Summary and conclusions

This chapter developed two innovative printing patterns, knitted and tilted filaments, for 3DP-ECC. Both filaments were printed and saw-cut for four-point bending tests. In addition, conventional parallel filaments and cast ECC were used as references. Through experimental investigation and analysis, the following conclusions can be drawn:

(1) Knitted and tilted filaments were designed to mimic the crossed-lamellar micro-structure of conch shells. The three-dimensional space design rendered ECC's directional-dependent tensile/flexural resistance to the element out of the conventional printing plane (x-y plane). Moreover, the patterns introduced a more complex three-dimensional interface system, which converted the original structural weakness into a structural strengthening method.

(2) In four-point bending tests, parallel filaments loaded in Orientation 1 and 2 showed excellent flexural properties and robust strain-hardening behavior, notably outperforming the cast counterparts. The advancement was attributed to three primary sources: (1) fiber alignment in extruded ECC filaments; (2) crack bifurcation and deflection in the laminate structure; and (3) crack trapping feature of ECC.

(3) Due to the unitary orientation of interfaces and lack of fiber bridging, the flexural performance of parallel filaments in Orientation 3 showed a dramatic drop compared with the other two orientations. The interfacial single-crack failure inhibited the strain-hardening behavior of ECC material and induced drastic reductions, i.e., up to 91%, in flexural strength. The emergence of anisotropy poses great challenges to structural integrity.

(4) Knitted and tilted filaments showed superior or comparable bending performance to cast ECC in Orientations 1 and 2. Furthermore, knitting and tilting filaments create a unique flexural failure mode and allow for deliberate performance tuning of 3DP-ECC. In four-point bending tests, multiple tensile cracks arose from the tensioned zone at the bottom and progressed in the loading direction. Further deflection and bifurcation occurred when the cracks encountered filament intersections, promoting sufficient energy dissipation and delaying failure to achieve desirable ductility.

(5) In Orientation 3, remarkable enhancements of flexural strength were obtained by knitting and tilting filaments, compared to parallel filaments. An up-to-179% increase was observed in tilted

filaments, and the strength of knitted filaments also exceeded that of parallel filaments by 116%. The ratio of the strength in Orientation 3 (f_3) relative to Orientation 1 (f_1) was increased from 8.6% to 30%, indicating effective alleviation of anisotropy in 3DP-ECC. This improvement primarily originates from the architected structural forms with tortuous interfaces in knitted and tilted filaments.

The strength of this method in alleviating anisotropy lies in that no external reinforcements are necessary, and the automated construction process is not interrupted. 3DP technology's flexibility in enabling more design freedoms is maximally exploited, and ECC's excellent material features are taken advantage of. Furthermore, by building complex interface systems, the proposed patterns convert interfaces from vulnerable weak links in a structure into an effective means to strengthen the printed structure and delay failure. With feasibility of these alleviation methods verified, more effective and efficient structural forms can be created following this inherent logic in future research.

Chapter 6. Structural-Scale Behavior of 3DP-ECC Wall

6.1. Introduction

The advancement of 3DP technology has opened up new possibilities in the construction industry. One of the key factors in promoting the application of this technology is to understand and verify the structural performance of 3D-printed structural elements. Structural-scale tests provide essential data on the mechanical properties and behavior of the printed elements in replacement of the conventional cast elements. Understanding the behavior of the printed elements and especially the failure mode under different loads and environmental conditions can inform the design of structures, enhance the quality of 3D-printed concrete structures, and facilitate the development of new applications and solutions. As such, this research topic is crucial to realize the full potential of 3D concrete printing technology and to meet the demands of the construction industry for faster, safer, and more sustainable construction methods.

Beams, walls, and columns represent fundamental elements of a structure, warranting extensive research attention. Investigations have been conducted on 3DP beams, encompassing a range of beam types, such as steel-reinforced concrete beams [199] and fiber-reinforced cementitious beams. For instance, Asprone et al. [200] conducted a three-point bending test on a 3-meter 3D-printed reinforced concrete beam, which consisted of segmented sections assembled with steel reinforcement. The ultimate failure of the beam was induced by shear damage at the segment interfaces and steel-concrete anchoring failure. Zhu et al. [20] explored the bending behavior of 3D-printed ECC beams with different infill patterns through three-point bending. The tested beams demonstrated a ductile failure mode, achieving a comparable bearing capacity to that of a reinforced concrete beam with a 1.51% reinforcing ratio. Additionally, the filament orientation of the infill pattern exhibited a significant influence on the beam's bending performance. Moreover, to verify the feasibility of a 3DP bicycle bridge project, a downscaled reinforced concrete bridge (beam part without columns) underwent a four-point bending test in Eindhoven [201-202]. Notably, failure cracks originated from the interface region before propagating into the bulk area. Following this, Ahmed et al. [203] also performed a four-point bending test on a girder spanning 5.875 m, to

validate the structural performance of another 3DP concrete bridge. The girder consisted of multiple printed segments interconnected with prestressed steel rebars. It is noteworthy, however, that while the whole bridge structure incorporated four pairs of columns, they were designed as reinforced concrete elements cast in situ rather than printed.

Despite the obvious need, current research on the behavior of printed wall/column, the other type of fundamental structural element highlighting compression bearing capacity, is scarce. Daungwilailuk et al. [149] manufactured concrete walls with two different patterns, i.e., a flat wall with an inner truss and a diamond wall, and conducted uniaxial compression tests. Printing patterns were found to notably influence the failure mode and ultimate mechanical capacities of the printed concrete walls. The diamond wall showed a tendency of tensile strain concentration in the area of pits and therefore vulnerable to splitting and spalling, while the flat wall was enhanced by the inner truss. Han et al. [148] performed uniaxial compressive tests on large-scale 3D-printed concrete walls (up to 2.4 m high) with and without horizontal steel reinforcement and with varying ratios of height to thickness. The appearance of horizontal steel was reported to undermine the mechanical capacity of printed concrete walls. In addition, brittle failure was witnessed in all concrete walls with sudden collapse and vertical cracks penetrating through the height. In addition, Bos et al. [202] tested a 3DP concrete cavity wall with insulation material inside under uniaxial compression. Nonetheless, the tested wall had been preloaded in three-point bending before compressive test and was not loaded to failure. Therefore, the mechanical behavior of the printed wall was not fully captured.

In this research, cavity walls are 3D printed using the ECC material developed in Chapter 5, and placed under uniaxial compression load till failure. The inclusion of cavity configurations in the wall design serves the purpose of augmenting their thermal or acoustic insulation properties. These cavities can be subsequently filled with insulating materials to further enhance their capabilities. However, this study does not delve into the investigation of the filling materials or the insulating effect. Rather, the primary focus is directed towards guaranteeing the structural performance while reserving cavity space. The objective of this study is to comprehend the compressive behavior of the printed ECC wall as a representative structural component. Through an analysis of its mechanical response mechanism, it is aimed to identify the similarities and distinctions from

extensively studied conventional cast elements, thus providing a knowledge base for future structural applications.

6.2. Material and methods

6.2.1 Materials

The mix proportion of printable PVA-ECC used in this study is identical to that shown in Table 5.2. The chemical compositions and properties of binders and PVA fibers used can be found in Table 3.1 and Table 3.2. For 3D printing, the fresh mixture of PVA-ECC was transferred directly from the mixer to the material hopper 20 minutes after water addition. After printing, all specimens were cured in a 22 ± 2℃, 16 ± 5% RH environment for 28 days.

6.2.2 Patterns of cavity walls

Three distinct wall patterns have been designed and printed, as shown in Figure 6.1. The Hollow walls group consists of walls with dimensions of 400 mm length, 100 mm width, and 312 mm height, creating a structure with 24 layers. A single filament, with a designed geometry of 20 mm in width and 13 mm in height, is deposited for each layer. The TrussA and TrussB groups have the same contour geometries as the Hollow group but possess different infill patterns. The TrussA group has four trusses to infill the wall's inner cavity area, while the TrussB group adopts six trusses. All truss filaments have the same dimensions as the exterior filaments and are printed continuously with the exterior walls.

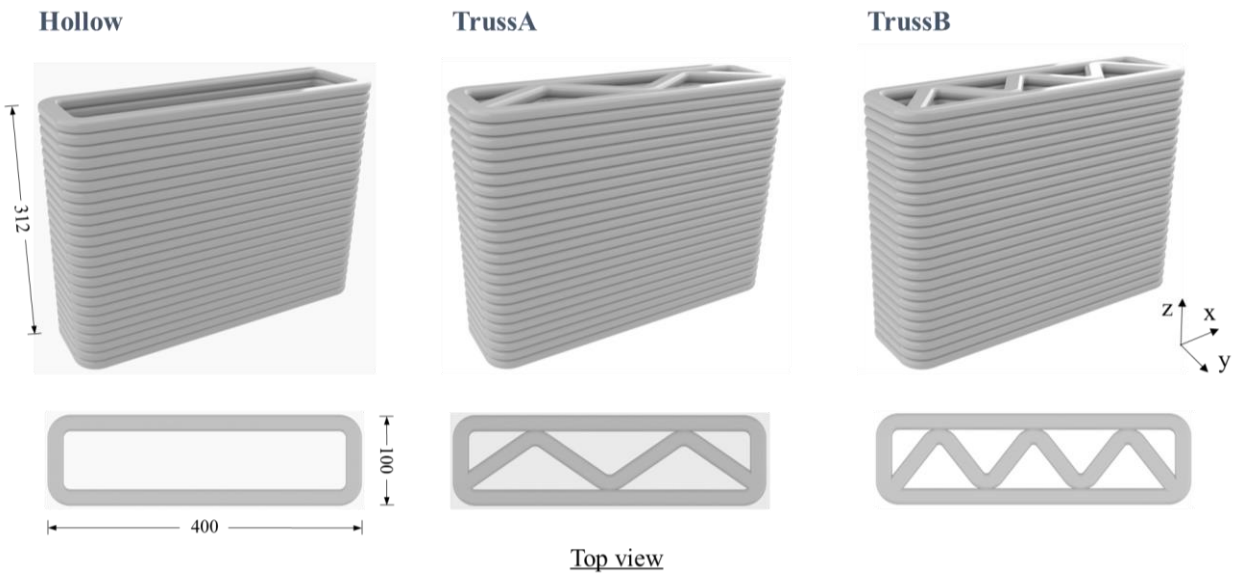

Figure 6.1: Schematic diagrams and top views of different printing patterns. (Interfaces are exaggerated in the schematic diagrams to show the positions.)

6.2.3 Compressive test

The mechanical behavior of the printed walls under compression was investigated through uniaxial compression tests. Prior to testing, all specimens were leveled with gypsum cement on the upper surface to ensure complete contact with the loading beam, as illustrated in Figure 6.2(b). The Instron 1336 machine (Figure 6.2(a)) was used to carry out the tests under a monotonic displacement-control loading rate of 0.01 mm/s. To measure the displacement and deformation of the ECC wall during compression, 13 kinematic markers were affixed to the wall specimens at specific locations as shown in Figure 6.2(c). The Optotrak motion capture system recorded the changes in marker positions, which were then collected by a data acquisition system. The vertical and out-of-plane deflections at various positions could be determined and analyzed from the marker position data. In addition, random black and white speckles were spray-painted on the front surface of ECC wall. Their unique patterns were captured by a high-resolution camera for subsequent digital image correlation (DIC) analysis.

In addition, the compressive strength of cast ECC was evaluated through compression tests of 50 mm cubic specimens as a reference. The test was performed on a Forney compression machine with a monotonic loading rate of 0.6 kN/s.

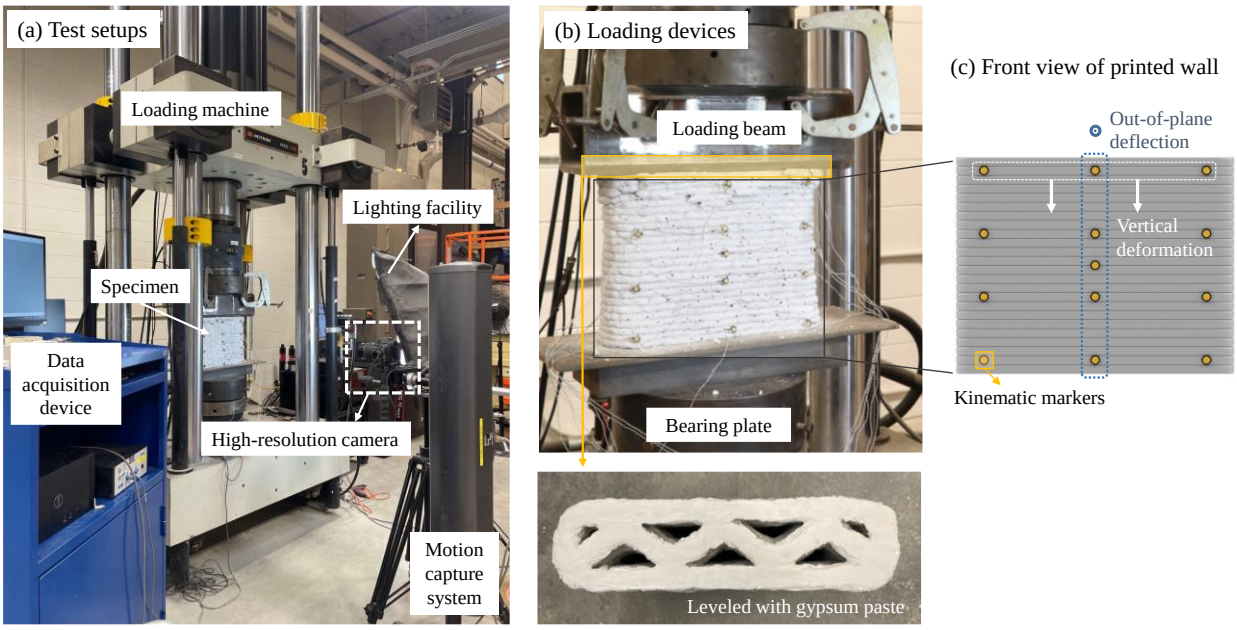

Figure 6.2: Compressive test setup for printed ECC walls.

6.3. Results and discussion

6.3.1 Failure mode

The crack and damage patterns observed in the Hollow wall group are depicted in Figure 6.3. Figure 6.3(a) presents the results of DIC analysis at the initial stage of loading and cracking. The color map represents the horizontal (x-direction) strain observed in the front view of the specimen. The top layers of the wall exhibit a dispersed field of tensile strain. The tensile strain concentration area extends diagonally from the top left and right ends of the specimen towards the central section, suggesting the potential directions of primary crack initiation. However, in the final failure mode (Figure 6.3(b)), it is evident that the main cracks exhibited a more horizontal inclination than indicated in the strain analysis diagram. During loading, several cracks initially propagated through the top filaments before extending into the horizontal interface. These cracks subsequently underwent zigzag deflection and kinking, penetrating through multiple layers and developing obliquely towards the central area of the specimen. Additionally, a dense distribution of micro-cracks was observed within the fracture region, as depicted in the close-up image in Figure 6.3(b). This failure mode can be attributed to various factors, including end effects of loading, inherent

material properties of ECC, multiple interfaces introduced by 3D printing, etc. The influence of the above factors will be elucidated below in detail.

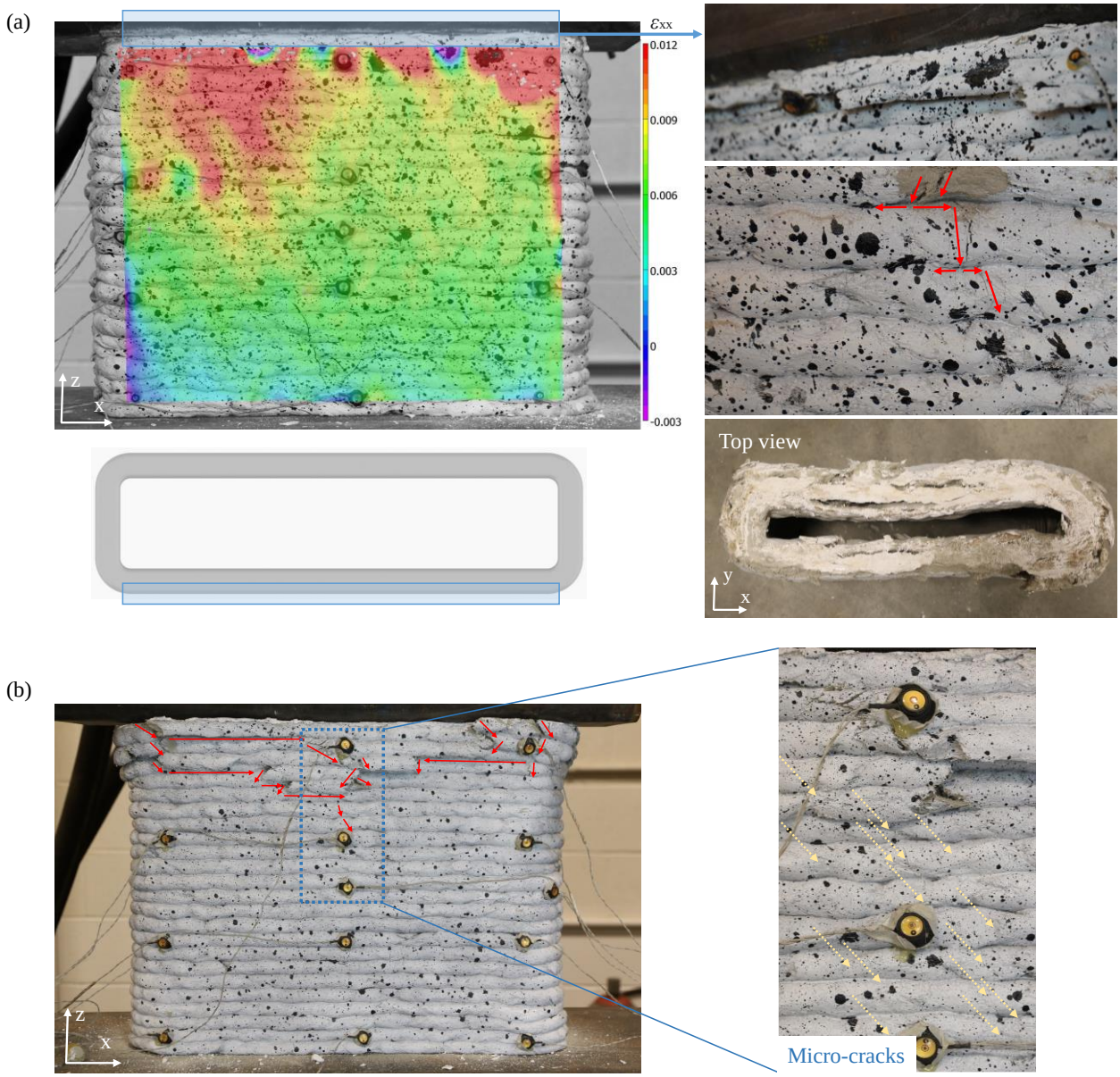

Figure 6.3: (a) Horizontal strain field and crack pattern and (b) failure mode of Hollow wall under compression.

The influence of the end effect, i.e., the friction between the loading beam and the specimen surface, significantly affects the failure mode of the printed wall. In the case of normal concrete subjected to uniaxial compressive loading, disregarding end friction typically results in a failure

pattern characterized by vertical columnar splitting. This occurs as micro-cracks or voids in the specimen give rise to subparallel wing cracks along the loading direction under pressure. With load progressively increasing, these wing cracks gradually propagate and interact, eventually resulting in a splitting failure [204]. However, the presence of end friction, particularly in specimens with small height-to-width ratios, leads to the formation of single- or double-cone failure in cylindrical or prismatic concrete specimens. This arises from the mismatch between the loading plate/beam and the specimen in Poisson's ratio and stiffness, leading to frictional lateral constraints exerted by the loading plate on the loading surfaces of the specimen, i.e., the lateral deformation of the specimen is confined. At this stage, the loading area of the specimen experiences multi-axial compression instead of uniaxial compression. The effect of the constraint gradually diminishes with distance from the loading surfaces of the specimen, resulting in the bulging and peeling off of the concrete at the mid-height.

Likewise, in the experimental setup employed in this study, the friction between the loading beam and the printed wall cannot be disregarded. This end friction is manifested in the observed strain concentration position in Figure 6.3(a). In contrast to the vertical direction, the strain concentration region prone to cracking exhibits an inclined propagation direction. This deviation arises from the weakening restraint exerted by the end plate.

3D extrusion enables the creation of a laminate structure, introducing multiple interfaces that significantly influence the failure mode of the specimen. DIC analysis revealed a horizontal inclination angle of approximately 45-60 degrees for the strain concentration region in the initial loading stage. However, the actual main crack angle (indicated by the red arrows in Figure 6.3(b)) did not exceed 30 degrees, as interfaces interfered with crack propagation. Once a vertical crack penetrates through the top filament, two potential paths for crack tip progression emerge: penetration into the matrix of the subsequent layer or propagation along the horizontal interface. The criterion for crack propagation is governed by the relative magnitude of the crack driving force (energy release rate) and the fracture resistance (crack extension resistance or fracture toughness) at the crack tip. Initially, the crack was deflected into the interfacial region, forming an interface delamination crack. However, the interface crack was not persistent. When the driving force-to-resistance ratio of the lower-layer filament surpassed that of the interface, the crack underwent kinking and entered the matrix of the bulk filament. At this stage, the crack faced two potential

scenarios: propagating through the filament or being trapped within it. Fibers play a crucial role here by trapping and ceasing crack propagation. Upon the crack tip entering the matrix, the bridging effect of fibers swiftly rose the fracture resistance of the material, a phenomenon known as the R-curve behavior [204]. Consequently, not all cracks successfully penetrated to the subsequent layer; some got trapped within the bulk material. The mechanisms of crack deflection, kinking, bifurcation, and trapping have been extensively elucidated in Subsection 5.3.1.

The observed failure mode of the printed ECC wall in this study arose from the combined influence of ECC's material features and the presence of interfaces. As a comparison, a printed concrete wall with a similar aspect ratio in [149] also showed deflected and kinked cracks, however, the primary inclined or vertical cracks generally penetrating through multiple layers and reach the lower part of the printed wall without being trapped or stopped (Figure 6.4), which is notably different with ECC walls. In addition, fiber bridging eliminated the common catastrophic failure of conventional concrete [148]; instead, the printed ECC wall exhibited slight filament fractures under compression and stayed intact with over 20 mm vertical deformation.

Figure 6.4: Crack pattern of a printed hollow concrete wall under compression (adapted from [149])

The cracking and failure modes of the TrussA group are summarized in Figures 6.5. The introduction of inner trusses brought about a change in the cracking pattern of the printed ECC

wall. As depicted in Figure 6.5(a), the DIC analysis in the initial loading stage revealed three distinct strain concentration regions on the top filaments, corresponding to the three connecting/supporting locations where the interior trusses intersect with the exterior walls. In the experimental observations, micro-cracks first developed at the three contacting locations in the top layer. Subsequently, several main cracks gradually propagated from these locations, resulting in filament fracture. Ultimately, local filament spalling occurred within the strain concentration area (Figure 6.5(b)). From the top view image, it is shown that spalling does not entail the complete detachment of the outer wall but rather the peeling of fragmented sections that cracked along the width of the filament. Cracking and tearing of filaments in the transverse direction were observed in all three sets of tests. This behavior arises from the highly consistent fiber orientation within the 3D extruded filaments, which predominantly aligns with the printing direction (mainly the x-direction). Consequently, the filaments possess greater tensile strain capacity in the printing direction, while their resistance to tensile cracking in the perpendicular direction (y-direction) is diminished. When the truss filaments experience cracking and lateral expansion, an outward force is exerted on the exterior wall, resulting in strain concentration at the contact area. This leads to the emergence of a distinctive failure mode specific to walls with trusses, which differs from that observed in the hollow wall configuration.

It is also noteworthy that the corners, serving as the juncture between the truss and the exterior wall, coincide with the starting and ending points of the print paths. These locations inherently represent weak links within the structure. Coupled with the effect of the truss, the vulnerability in these regions for fracture initiation is accented.

Similarly, TrussB group depicted in Figure 6.6 manifested an analogous cracking pattern. In the initial stages of the experiment, the contact region of the truss and the exterior wall exhibited strain concentration and cracking onset. The cracks originating at the lateral corners propagated downward and developed obliquely, penetrating the horizontal interfaces and filaments. Upon ultimate failure, the front and rear exterior walls of the structure deviated significantly from the specimen, yet did not detach from the main body.

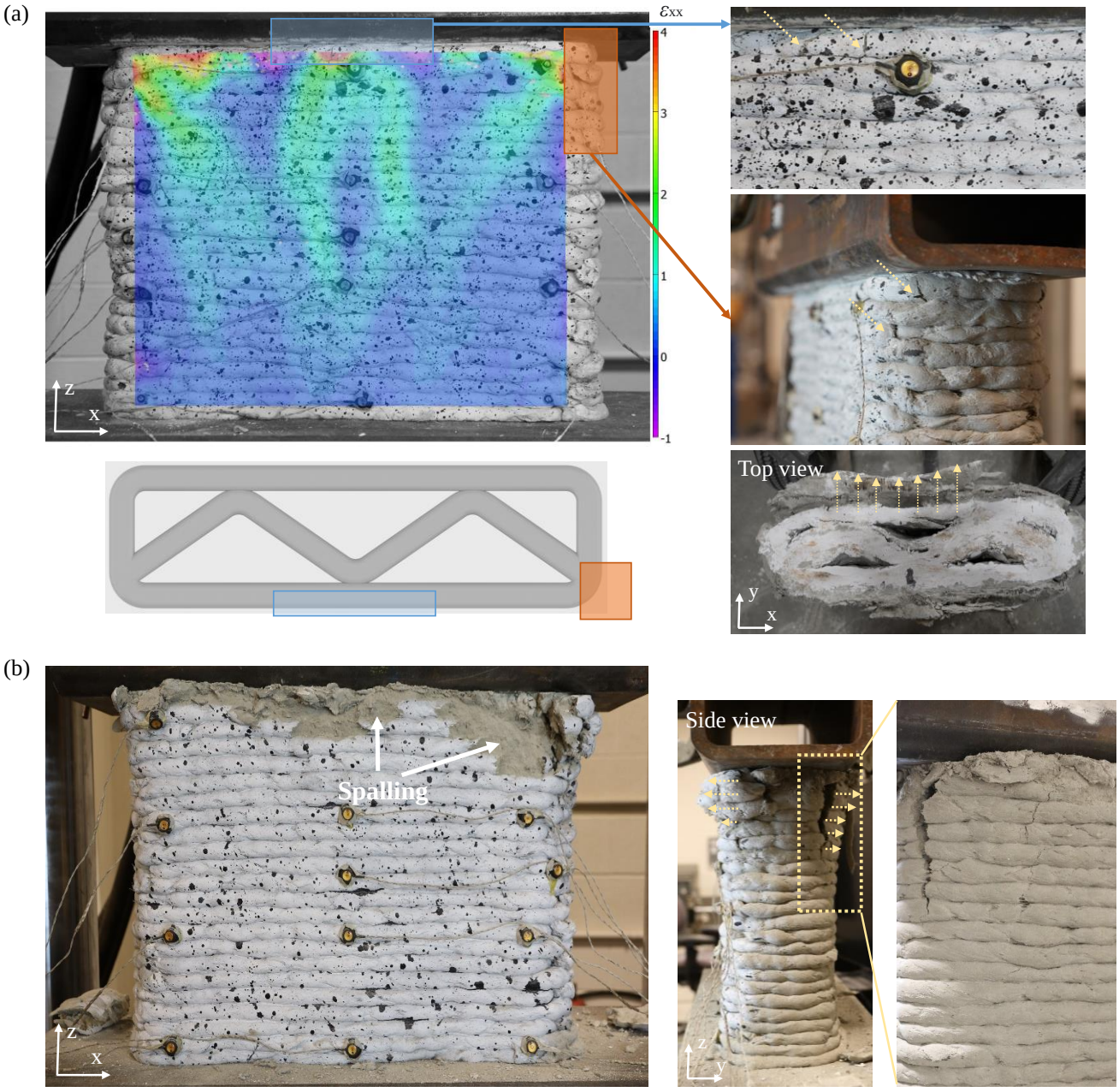

Figure 6.5: (a) Horizontal strain field and crack pattern and (b) failure mode of TrussA wall under compression.

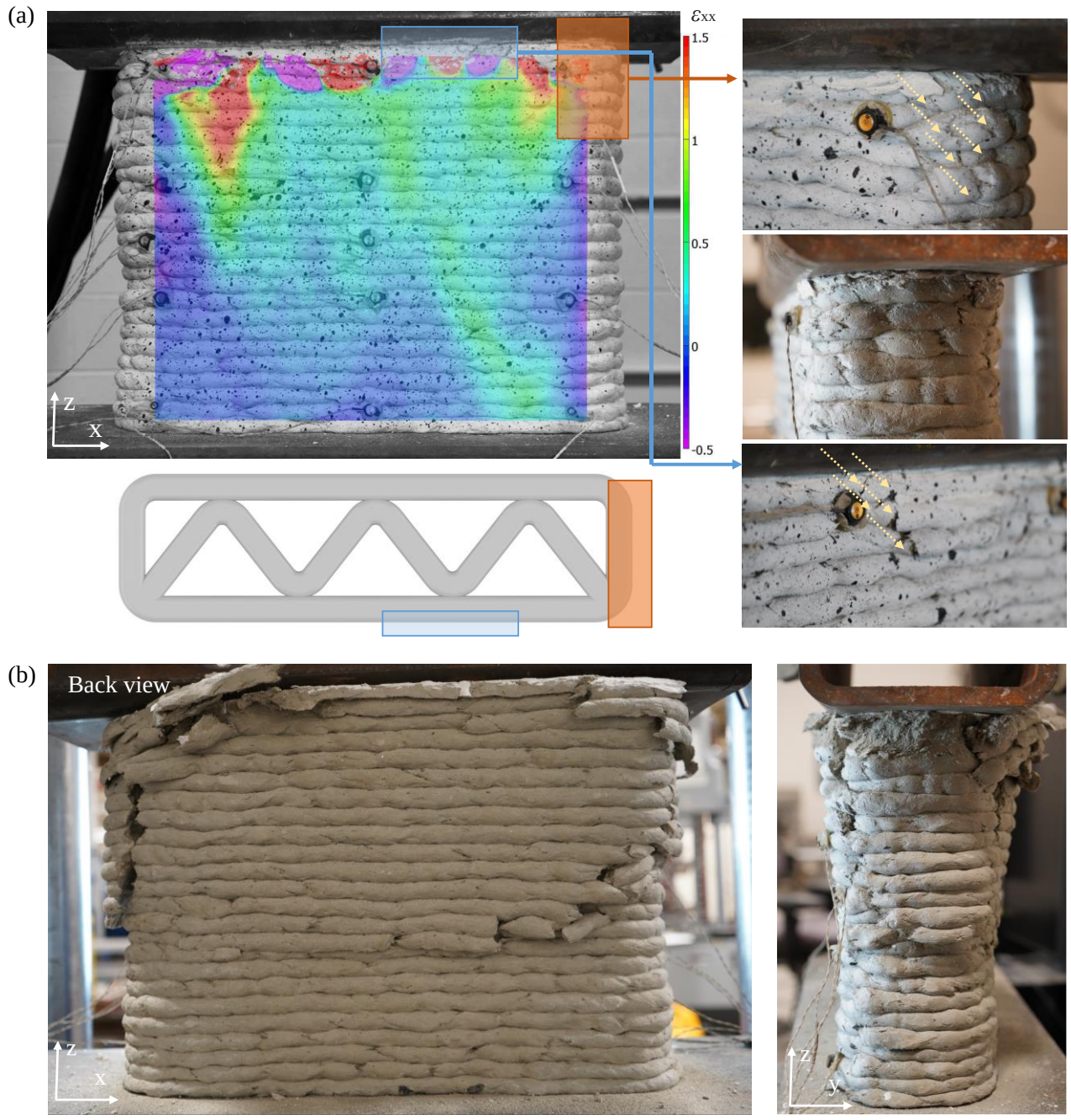

Figure 6.6: (a) Horizontal strain field and crack pattern and (b) failure mode of TrussB wall under compression.

Summarizing the failure modes of the three groups, it is evident that the presence of trusses significantly impacts the failure characteristics of the printed ECC walls. One aspect of this influence is exemplified by different out-of-plane deflections, as schematically shown in Figure

6.7. The Hollow group exhibited the least out-of-plane deflection. Correspondingly, only partial breakage and bulging of the upper filaments were observed in the exterior walls. In contrast, both the TrussA and the TrussB groups displayed considerably higher levels of out-of-plane deflections. This can be attributed to the lateral expansion and deformation of the interior trusses, which exert tensile forces on the exterior walls. Owing to the inherent nature of 3DP ECC, the continuous filaments in the long edge possess greater tensile resistance, while the corners are relatively vulnerable. Consequently, micro-cracks and minor filament breakage or tearing predominantly occur in the middle section of the outer wall, whereas significant damage cracks tend to develop at the corners. Considering these combined effects, the printed wall with trusses is more susceptible to breakage and deflection at the corners, resulting in increased out-of-plane deformation. Moreover, as the density of trusses increases (as seen in TrussB relative to TrussA), the magnitude of out-of-plane deformation is further amplified.

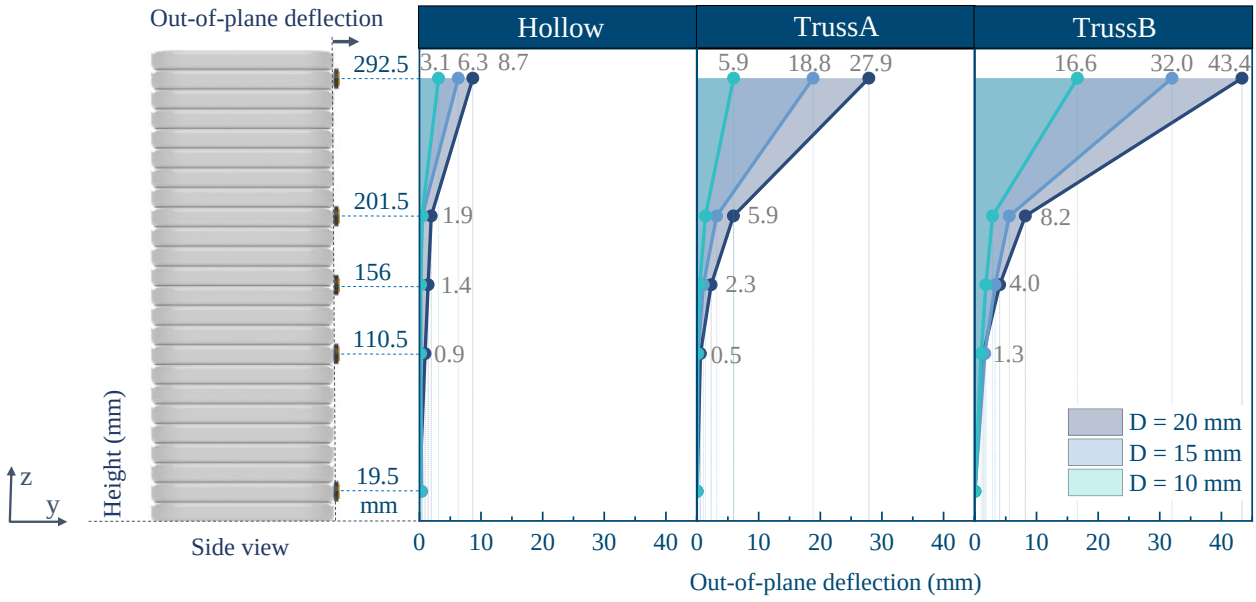

Figure 6.7: Out-of-plane deflection mode. D is the vertical deformation of the printed wall under compression.

Nonetheless, it should be noted that the vertical deformations corresponding to maximum loads for all three groups fall within the 4-6 mm range. Consequently, the vertical deformations (D = 10/15/20 mm) indicated in Figure 6.7 surpass the deformation at peak, that is, the figure

exclusively displays out-of-plane deflections during the post-load-peak stage. Prior to reaching the maximum load, the deflections of all ECC walls were insignificant and therefore disregarded in the analysis. Thus, the difference in out-of-plane deflections did not pose a notable influence on the peak strength of the printed wall.

6.3.2 Mechanical behavior

As elucidated in the previous section, the compressive failure mechanism of conventional concrete without fibers (disregarding end friction effect) manifests as the formation and interaction of vertical wing cracks leading to splitting failure. Due to the brittle nature of concrete, this failure mode tends to be explosive and catastrophic, accompanied by a sharp drop in load post peak and negligible residual bearing capacity. In contrast, ECC demonstrates a remarkable ability to mitigate damage with the incorporation of fibers. Before reaching the peak stress, the presence of fibers enhances the compressive performance of ECC by enhancing the sliding resistance of pre-existing micro-cracks and reducing the growth rate of wing cracks. These are attributed to the bridging effect of fibers, which require extra energy for debonding and pull-out of fibers, thereby heightening overall resistance. Consequently, cracks within ECC are stabilized, leading to a ductile mechanical response. Prior to the peak, the stress-strain curve of ECC exhibits a more gradual ascent in comparison to conventional concrete. Following the peak, the stress does not experience a sharp decline as observed in concrete but retains a residual load-bearing capacity of approximately 50% of the peak value [7].

In this study, the typical compressive force-displacement curves of printed ECC walls are presented in Figure 6.8. The load demonstrated an approximately linear increase to 80% of the peak, followed by a gentle nonlinear/inelastic rise to the peak value. Subsequently, a plateau was reached after a moderate decline in load. The residual capacity of the plateau retained 60%-75% of the peak value. For the TrussB group, a gradual decrease in load was captured after the plateau stage. In this phase, the bridging capacity of the fibers gradually diminished as cracks opened wider, and partial failure and spalling of the exterior wall occurred. While the Hollow and the TrussA groups stayed in the plateau and retained 62% and 73% of the peak load, respectively, when vertical deformation reached 20 mm. This ductile behavior also endows printed ECC walls with a remarkable energy absorption capacity, as evidenced by the area between the curve and the

displacement axis. For similar 3D-printed concrete walls documented in literature [148-149], the force-displacement curve often lacks the post-peak stage, as it cannot be captured due to a complete collapse of the structure.

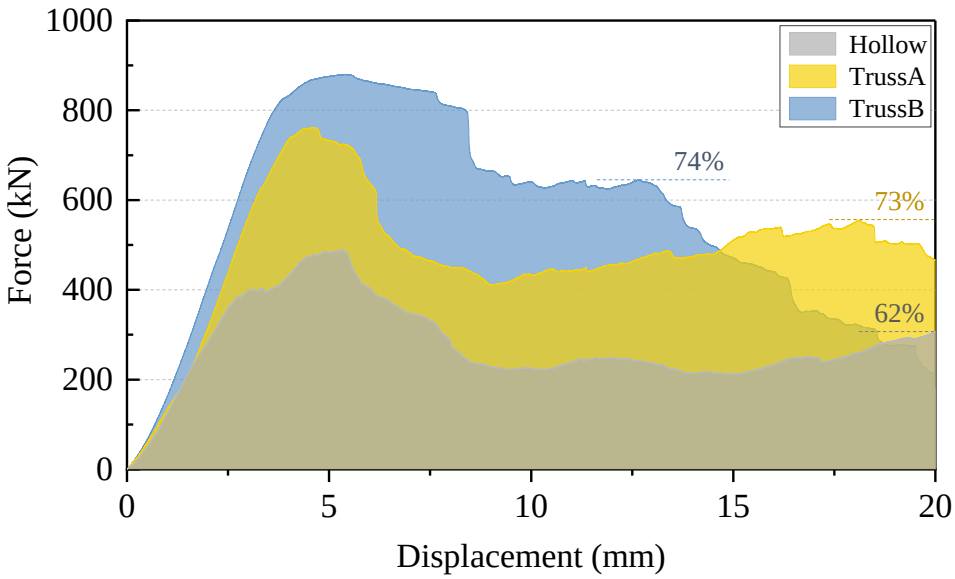

Figure 6.8: Force-displacement curves of printed ECC walls under compression.

The remarkably ductile mechanical response exhibited by the printed ECC wall highlights its promising advantage in resilience. Upon reaching the peak load, the printed ECC demonstrated a moderate level of damage, e.g., partial filament cracking, in contrast to the catastrophic brittle failure typically observed in conventional concrete. The ultimate damage, wherein the exterior wall exhibits notable fracture and deflection, occurs within a vertical deformation range of 10-20 mm, which surpasses twice the peak deformation. Consequently, the structure exhibits robust damage tolerance and effectively delayed failure.

Furthermore, the specimen maintained its structural integrity beyond the elastic stage, as previously elucidated. During the subsequent plastic deformation phase, the printed ECC wall further retained a substantial residual bearing capacity (up to 73% of the peak load), in contrast to conventional concrete wall which experiences almost complete functionality loss. These suggest that the functional and structural degradation of printed ECC components remains limited, even in the presence of significant plastic deformation. Owing to the delayed onset of failure and the

preservation of functionality, printed ECC component requires minimal repairs and shows the potential to facilitate rapid post-event recovery following major disaster events.

Figure 6.9 presents the maximum load-bearing capacity and compressive strength of various printed ECC walls. The compressive strength of printed ECC wall was derived from the force born by unit horizontal solid material area, not including the hollow area. The reference group consists of cast cubic specimens, serving solely to show the material characteristics of the printable ECC, as the size and fabrication process of the cast group differ from those of the printed walls.

In comparison to the Hollow group, both truss-incorporated groups exhibited higher compressive strength, indicating the beneficial impact of truss on element capacity. Specifically, the TrussB group witnessed a remarkable 34% increase in compressive strength. However, it is important to highlight that, as previously mentioned, the inclusion of trusses also complicates the ultimate failure mode of the printed wall, leading to pronounced out-of-plane deflection and fracture of exterior walls after peak load. Hence, the reinforcement provided by trusses necessitates a tradeoff between enhanced load-bearing capacity and the resultant failure mode.

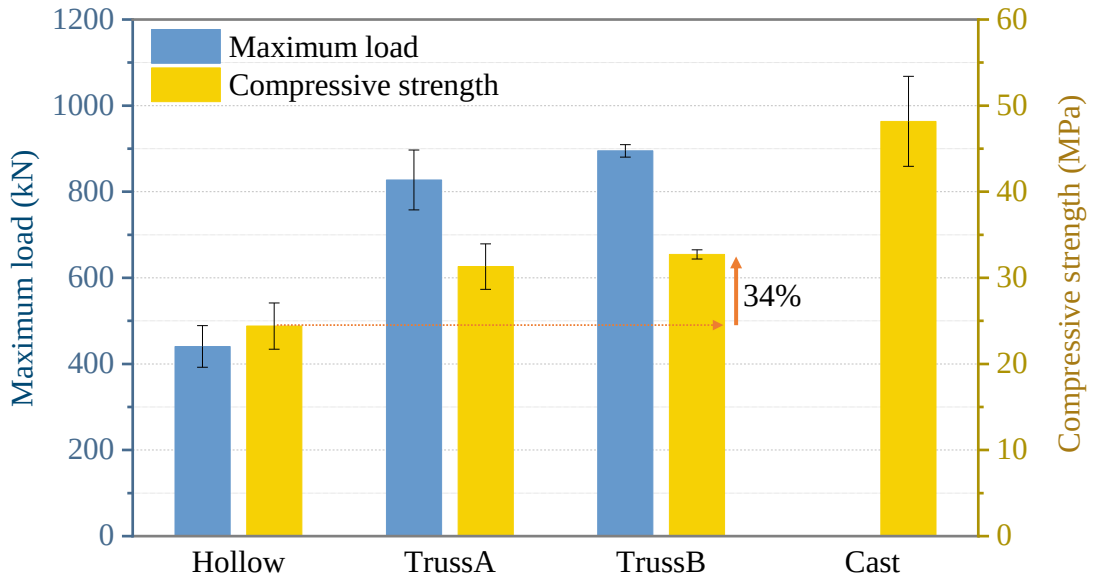

Figure 6.9: Compressive capacities of printed ECC walls.

6.4. Summary and conclusions

This chapter centers on the mechanical behavior of 3D printed ECC walls at the structural scale. Compressive tests were conducted to investigate the failure mode and mechanical performance of printed walls employing various infill patterns. The following primary conclusions can be drawn:

(1) Compression tests revealed distinctive crack and failure patterns in 3D printed ECC walls. Various factors influenced these failure modes, including the end effects of loading, the inherent material properties of ECC, the presence of multiple interfaces introduced by 3D printing, and the design of the printing path.

(2) Incorporation of inner trusses notably altered the failure mode. DIC analysis showed that the strain concentration regions on the top layer filaments aligned with the intersection locations between interior trusses and exterior walls. This phenomenon arose due to the cracking and lateral expansion of the truss filaments, which exerted outward forces on the exterior walls.

(3) Ductile mechanical response and enhanced energy absorption capacity were captured in 3DP-ECC walls, highlighting its promising resilience advantage. For printed ECC walls, a plateau was reached after a moderate post-peak decline in load, with 60%-75% of the peak capacity retained.

(4) While 3D printed ECC walls with trusses exhibited enhanced compressive capacity, the introduction of trusses also resulted in greater out-of-plane deflections of the exterior walls. Therefore, caution must be exercised when employing trusses as a means of structural reinforcement.

In addition to validating the viability of 3DP-ECC walls as high-ductility compression members, this study also offers valuable insights into the influence of interfaces on the mechanical response in 3DP-ECC elements. The introduction of interfaces through additive manufacturing process impacts the element's performance from various perspectives. Instinctively, interfaces represent vulnerable weak links in a structure and are prone to premature failure. Even in fiber-reinforced printing materials like ECC, the interface's load-bearing capacity is not as reliable due to the relatively weaker fiber bridging effect compared to the bulk filament.

However, the findings from Chapter 5 and this chapter highlight the positive influence of interfaces on the behavior of 3DP-ECC. For instance, in Chapter 5, the intricate 3D interface system helps mitigate the anisotropy of 3DP-ECC’s flexural performance. This is achieved by the repetitive and

alternating development of cracks along the interface and within the bulk material, combined with ECC's inherent crack-trapping ability. In this chapter, compression-induced cracks exhibit a propensity to propagate downwards through the structure, nonetheless, this tendency is disrupted by the presence of interfaces. The alternating crack propagation along the horizontal interfaces effectively confines the damage to the upper portion of the structure. Combined with ECC's exceptional ductility, the printed structure is protected from top-to-bottom splitting damage. Generally, the role of interfaces in the behavior of 3DP-ECC structure is dialectical, necessitating careful consideration of interfaces in structural design and performance analysis.

Moreover, the resilient response exhibited by the printed ECC components, as observed in this investigation, holds promising implications for the utilization of 3DP-ECC. The remarkable ductility and strain hardening ability of printed ECC beams are intuitively comprehensible. Previous research [20] has demonstrated that by testing beams in a favorable direction. In that case, the inherent advantages of 3DP-ECC can be maximized, particularly its superior tensile and flexural resistance originating from fiber alignment. This study further substantiates that printed ECC wall/column also retains a notable resilience response when subjected to compressive loading. Such a response aligns with the structural requirements for delayed failure and the preservation of functionality, thereby enhancing overall structural safety. Consequently, the application prospects of 3DP-ECC as a safe and efficient construction method are further validated.

Chapter 7. Low-Carbon, Early-Age-Shrinkage-Resistant Printable ECC

7.1. Introduction

The concern regarding shrinkage in conventional ECC arises due to its higher free shrinkage values, which can surpass two to three times that of ordinary concrete [205]. This can be attributed to the absence of coarse aggregates in ECC, which are known to limit cement shrinkage internally. As a result, ECCs containing higher binder content and no coarse aggregate exhibit greater shrinkage. However, it is worth noting that the absence of coarse aggregates and the high binder content are common in most printable cementitious materials as well. Moreover, due to ECC's inherent multiple cracking ability, ECC can limit crack width much lower than that of concrete in restrained shrinkage scenarios [206-207]. Additionally, the inclusion of fiber has been verified to effectively alleviate plastic shrinkage and suppress cracks, which is interpreted as the effect of fibers in bridging the cracks and preventing them from developing [125].

As elucidated before, the elimination of formwork, absence of coarse aggregate and high binder content have also posed challenges to the structural integrity and durability of 3D printed cementitious elements. To enhance and optimize printable ECC for increased application potential, this study aims to design and develop an enhanced printable ECC material with the following features: (1) appropriate printability and open time, (2) consistent expansion behavior to mitigate the cracking risk in printed structures, (3) environmental friendliness, with reduced carbon footprint and embodied energy, and (4) mechanical properties comparable to those of ordinary printable and cast-in-place ECC. Two types of ECC mixes with LC3 (Limestone Calcined Clay Cement) and CSA incorporated were designed and validated to accomplish these objectives. Printability tests, mechanical tests, shrinkage tests, and greenness analyses were carried out.

7.2. Material and methods

7.2.1 Materials

The binders used to prepare printable ECC includes Portland-limestone cement (PLC), calcium sulphoaluminate cement, metakaolin, limestone powder, fly ash (Class F), and silica fume, the oxide compositions of which are listed in Table 7.1 [171]. In this research, LC3 cement based ECC has been employed as a reference. LC3 cement refers to a composite material comprising Portland cement, metakaolin, and limestone powder blended in a proportionate weight ratio. Crumb rubber (40–80 mesh) was added to induce micro-cracking and enhance the ductility of printable ECC. Silica sand (F75) was adopted as fine aggregate. Polyvinyl alcohol (PVA) fibers with a length of 8 mm were employed as reinforcement of ECC. The properties of the micro PVA fibers can be found in Table 3.2.

The mix proportions of printable ECCs are shown in Table 7.2. The water-to-binder ratio and sand-to-binder ratio are 0.20 and 0.37, respectively. The dosage of PVA fiber is 2.0% by volume of the total composition. The bulk density of both mixes is 1996 kg/m^3.

For 3D printing, the fresh mixture was transferred directly from the mixer to the material hopper 15 minutes after water addition. Details in the printing setups can be found in subsection 3.2.2.

Table 7.1: Chemical compositions of binders determined by X-ray fluorescence method (wt. %).

Binder	CaO	Al_2O_3	SiO_2	Fe_2O_3	MgO	SO_3
PLC	63.6	5.3	19.3	3.3	2.2	3.0
CSA	46.2	10.1	7	0.7	1.1	33.1
MK	0.0	46.6	50.8	0.5	0.0	0.1
LS	54.8	-	0.2	-	0.6	-
FA	17.4	19.8	39.4	11	3.7	1.9

Note: PLC: Portland-limestone cement; CSA: calcium sulphoaluminate cement; MK: metakaolin; LS: limestone powder; FA: fly ash.

Table 7.2: Mix proportions of printable ECCs (Unit: kg/m^3).

Group ID	PLC	CSA	MK	LS	FA	SF	CR	Sand	Water	SP	Fiber
LC3-ECC	223	-	71	51	841	30	30	466	253	4.0	26
CSA-ECC	91	132	71	51	841	30	30	466	253	4.0	26

Note: SF: silica fume; CR: crumb rubber; SP: superplasticizer.

7.2.2 Printability evaluation

The time-evolving rheological properties of printing material play a critical role in 3D printing processes [72]. Successful printing requires a balance between the flowability and buildability of fresh cementitious materials. On the one hand, the fresh mixture must possess adequate flowability to facilitate smooth extrusion while avoiding clogging. On the other hand, the material must provide sufficient rigidity to support its own weight and the additional deadweight loads resulting from the extrusion of additional layers. Achieving this goal necessitates careful design and harmonization of the printing ink's properties to enable appropriate rheological changes from mixing to filament placement and hardening while retaining sufficient shape retention and stability of the extruded material.

Flow table tests were conducted to assess the flowability of the ECC mixture in a fresh state as per ASTM C1437 [208]. The prepared mixture was filled into an inverted half cone with a bottom diameter of 100 mm and height of 60 mm. After removal of the cone, the table was raised and dropped 25 times. Subsequently, the spread diameter of the material was documented, as shown in Figure 7.1(a). The test was repeated from 20 min to 120 min after water addition or until initial setting, at intervals of 20 min.

The shape retention ability of fresh ECC was evaluated by placing a 1 kg mass block onto the top of half-cone-shaped materials, and the resulting vertical deformation before and after 1 min loading was recorded, as illustrated in Figure 7.1(b).

In addition, the initial and final setting times of fresh mixtures were also determined per ASTM C403/C403M-16 [209].

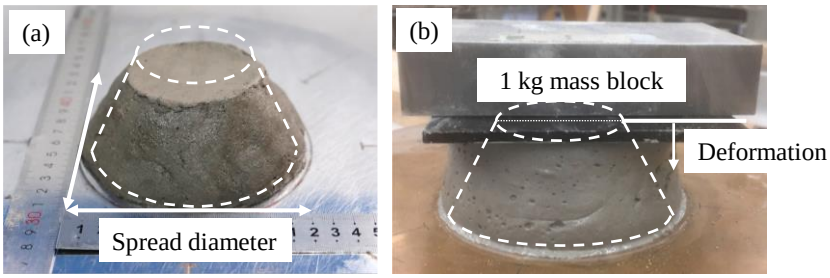

Figure 7.1: Measurements in (a) flow table test and (b) shape retention test.

7.2.3 Shrinkage monitoring

7.2.3.1. Shrinkage measurement for cast ECC

The free length change of cast ECC was determined as per ASTM C490/C490M–17 [210]. 25 mm × 25 mm × 300 mm prism specimens were cast and air-cured until set. At final setting, the specimens were de-molded, and the deformation measurement with a length comparator started after that. For the LC3-ECC and the reference group of CSA-ECC specimens, curing occurred in a 20 ± 3°C, 40 ± 5% RH environment after demolding. According to Zhu et al. [211], wet curing with water was effective in maintaining expansion over time for CSA-ECC. Hence, another group of CSA-ECC specimens was kept under 20 ± 3°C, 95 ± 5% RH condition for wet curing in the first three days, followed by curing in the same environment as the reference group.

7.2.3.2. Shrinkage measurement for printed ECC

Measuring free deformation in printed ECC using traditional methods can be challenging for the following reasons: (1) The geometry of 3D printed specimens typically fails to achieve the same level of accuracy as cast specimens. Consequently, non-standard specimens pose significant challenges to shrinkage measurement using conventional apparatus. (2) Unlike cast pieces, printed items do not require setting and hardening in the mold, and they are exposed to external environments at an earlier age, i.e., right after deposition. These lead to a need for earlier onset of shrinkage measurement, thereby complicating the entire process.

Therefore, a non-contact measuring system was employed, as shown in Figure 7.2. The measuring process involves first depositing filaments on a lubricant-coated plastic film and stacking them

into 10 layers to form an ECC short wall with dimensions of approximately 400 mm in length, 30 mm in width, and 100 mm in height. The lubricant was applied to suppress the restraint on length change exerted by the friction between the bottom layer and the printing surface. Within 30 minutes of printing, kinetic markers were pressed into the designated layer position along with thumbtacks. The markers were placed on the 2nd, 5th, 8th, and 10th layers (from bottom to top) with a 300 mm length between two markers on each layer (Figure 7.2(a)(b)). Optotrak camera was placed opposite the specimen to monitor changes in the makers' spatial positions, allowing for the length changes of the filaments over time to be captured.

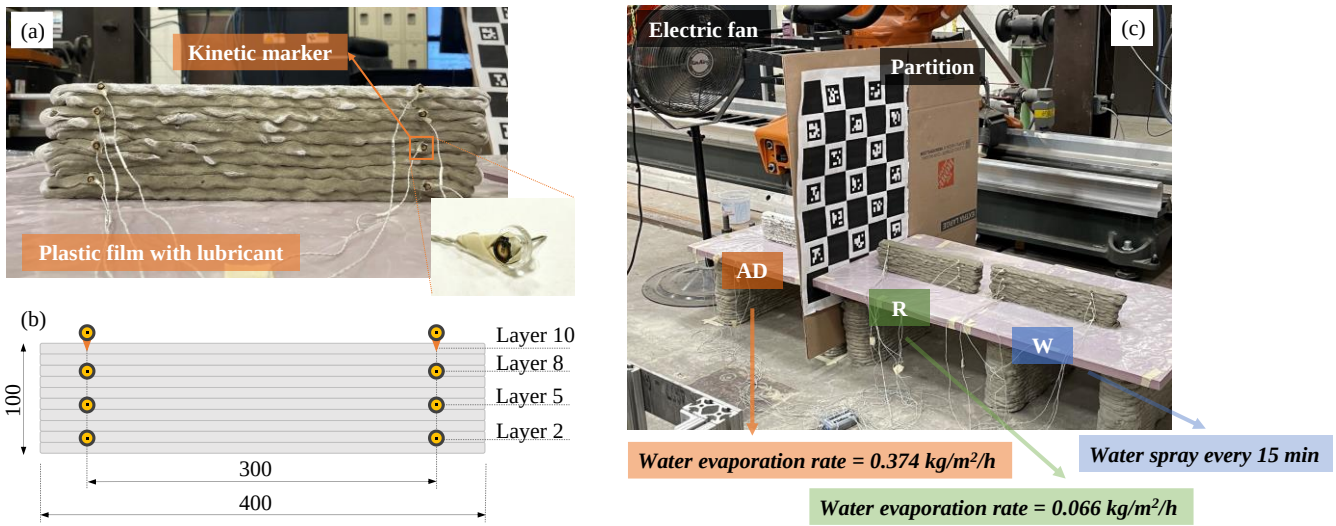

Figure 7.2: (a) Shrinkage monitoring setup, (b) schematic diagram (unit: mm), and (c) simulated environmental conditions for printed ECC.

Shrinkage monitoring was initiated at the 30-minute mark, with three different ambient environmental conditions being simulated simultaneously, as illustrated in Figure 7.2(c). The condition in which an electric fan was used to stimulate airflow and accelerate water evaporation in the printed ECC was referred to as accelerated drying (AD). Under this condition, a surface water evaporation rate of 0.374 kg/m^2/h was measured by monitoring the weigh change in a pan of water placed next to the printed element. The corresponding evaporation rate for the reference group was 0.066 kg/m^2/h. The environmental condition corresponding to the reference group (abbreviated as R) was the room condition, which was isolated from the AD group by a partition to prevent the influence of accelerated airflow. The temperature in the room was maintained at 20

± 3°C, with relative humidity (RH) of 16 ± 5°C %. The other group was the wet condition (abbreviated as W) or the water spray condition, which was applied only to the CSA-ECC group. This condition involved spraying water onto the specimen's surface every 15 minutes to keep the surface moist. All environmental condition simulations lasted for 3 hours, after which all printed ECCs were cured under room conditions and monitored for shrinkage.

7.2.4 Mechanical properties characterization

7.2.4.1. Uniaxial tensile and compressive tests

After curing in air at 20 ± 3°C and 40 ± 5% RH, the cast ECC was subjected to uniaxial tensile tests at ages 3 d, 7 d, and 28 d. The dimensions of dog-bone specimens adopted in uniaxial tensile tests are shown in Figure 7.3. The geometry is designed to concentrate the micro-cracks in the gauge region (80 mm in length). The specimens were uniaxially loaded at a fixed loading rate of 0.5 mm/min while two linear variable displacement transducers (LVDTs) measured the average tensile strain in the gauge region. For uniaxial compressive tests, 50 mm cubic specimens were manufactured and tested at a monotonic loading rate of 0.6 kN/s.

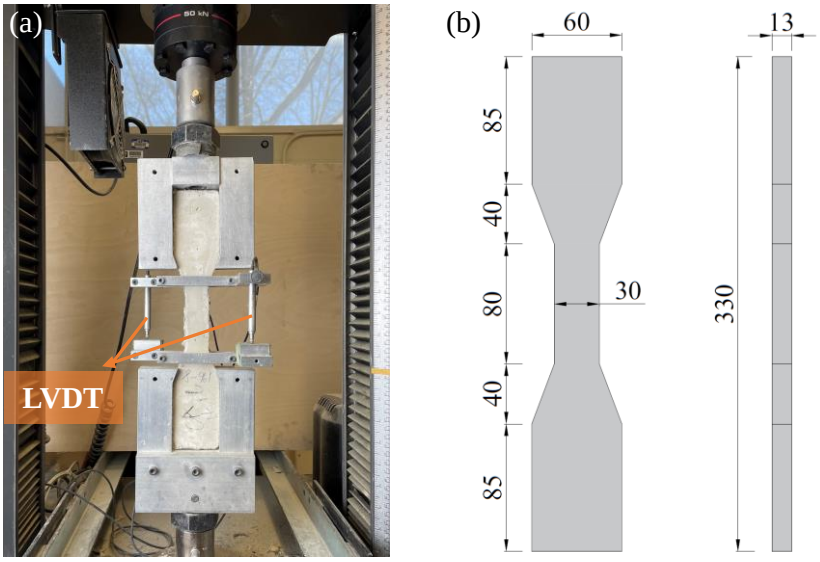

Figure 7.3: (a) Uniaxial tensile test setups and (b) geometries of the dog-bone specimen (unit: mm).

7.2.4.2. Four-point bending tests

Printed and cast ECC beam specimens with a length of 240 mm, a width of 75 mm, and a depth of 35 mm were tested at 28 d. The four-point bending tests were performed on an MTS 810 machine. The loading rate was set at 0.2 mm/min. Kinematic markers were affixed to the specimen to determine the position of specific points on the surface, as depicted in Figure 7.4. Optotrak motion capture system from NDI was used to capture the absolute position changes of the markers to obtain the mid-span deflection of the specimen. Mid-span deflection was derived from the relative position change of the three markers shown in Figure 7.4(b).

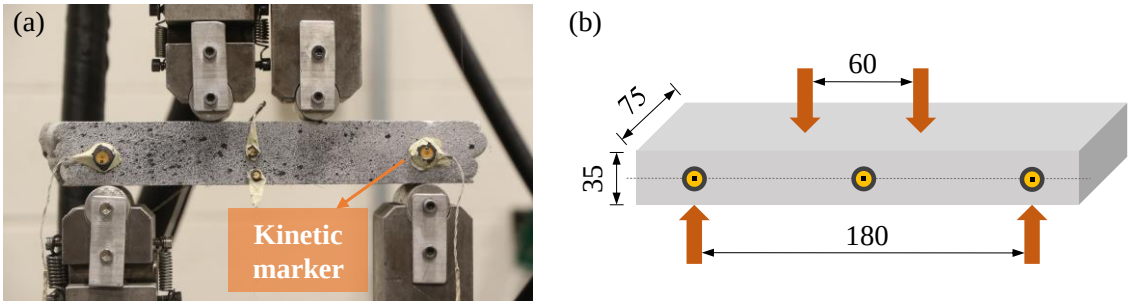

Figure 7.4: (a) Four-point bending test setups and (b) geometries of the specimen (unit: mm).

7.2.5 Carbon sequestration

In the pursuit of making a further impact on the environment in addition to optimizing ECC formulation, the possibility of carbon sequestration has been explored. After printing, the ECC beam was allowed to harden and cure for 20 hours in air before being placed in a carbonation chamber. The chamber was filled with bone-dry carbon dioxide gas with a purity of 99.8% and pressurized to 5 bars. After 24 hours of carbonation curing, the specimens were cured in air under 20 ± 3°C and 40 ± 5% RH for a period of 26 days, as illustrated in Figure 7.5.

In addition, both carbonated and uncarbonated ECC samples underwent thermogravimetric analysis (TGA) to quantify their CO_2 sequestration capacity. ECC specimens were sliced and grounded into fine powder samples. The weight change of samples was recorded as the temperature increased from room temperature to 1100°C, with $CaCO_3$ decomposition taking place between 550 – 950°C. The amount of CO_2 released was determined by measuring the mass loss in this temperature range, and CO_2 uptake was then calculated accordingly.

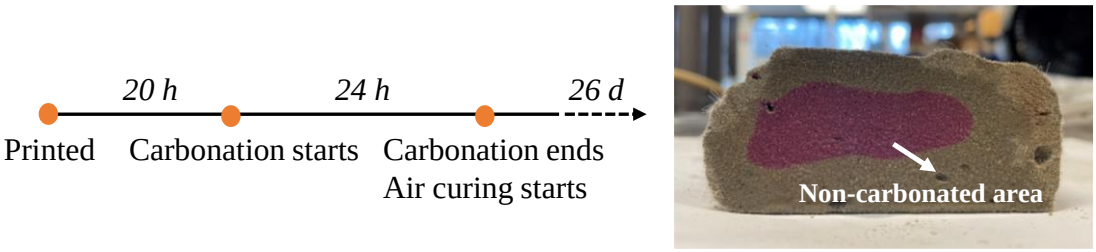

Figure 7.5: Procedure of ECC carbon sequestration.

7.3. Printability

Figure 7.6 plots the test data of flow table tests and shape retention tests from 20 min to 120 min after water addition. The flow test for the CSA-ECC group was conducted for a duration of 60 minutes. The test was terminated before the fresh mixture reached its initial setting state and became excessively stiff at 65 min. As a result, no further flow measurements were taken beyond this point.

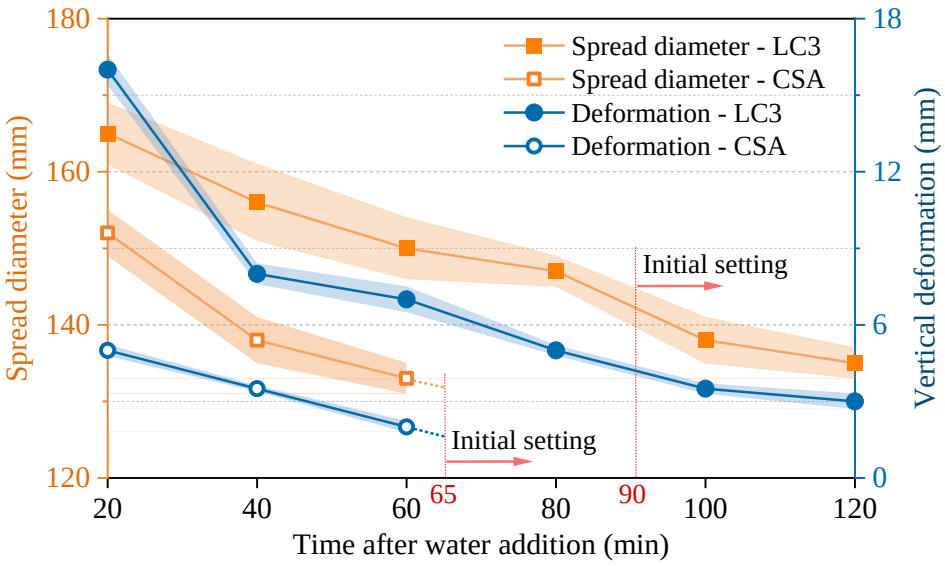

Figure 7.6: Spread diameter and shape retention test results. (The shaded area in the plot indicates the variability of measurements.)

20 min after adding water, the LC3-ECC group exhibited an initial spread diameter of approximately 165 cm, slightly surpassing the 152 cm value of the CSA-ECC group. The addition of CSA to the mixture reduced its fluidity but simultaneously decreased vertical deformation and

enhanced shape retention at 20 min. As time progressed, the spread diameter and vertical deformation of the two groups of fresh mixtures declined accordingly as the fresh mixtures experience hydration and flocculation.

At the 65-minute mark, the CSA-ECC mixture underwent initial setting, which limits the printable time window (or open time) to about 60 min, beyond which the mixture can no longer be extruded. In contrast, LC3-ECC demonstrated an initial setting after 90 min from water addition, which allows its open time to extend to 80 min, as evidenced by a spread diameter of 147 cm, indicating sufficient fluidity. Regarding the final setting, CSA-ECC and LC3-ECC exhibited a final setting time of 135 min and 305 min, respectively. These results suggest that the addition of CSA considerably accelerated the process of ECC hardening and shortened the open time. However, the open time of CSA-ECC of 60 minutes is considered sufficient, given that the open time of printable materials reported in previous literature typically ranges from 35 to 150 min [3, 22, 180, 212-214].

Considering the intrinsic conflict between sufficient flowability and desired buildability, the printable material must be harmoniously tuned to control its rheological properties. Previous research has shown that printable ECC has robust resistance to material yielding failure, making the shape retention ability of the fresh mixture an essential indicator for evaluating buildability [215]. In this study, introducing CSA into the printable ECC mix effectively enhanced the shape retention ability, despite a slightly reduced open time compared to LC3-ECC. As such, the designed CSA-ECC material is considered promising for 3D printing due to its robust deformation resistance and sufficient printable time window.

7.4. Shrinkage behavior

7.4.1 Free length change of cast ECC

Figure 7.7 depicts the shrinkage and expansion behavior of the mold-cast material over 28 days. In the case of air-cured LC3-ECC, sustained shrinkage was observed, which progressed monotonically in 28 days. The free length change measured 850 με on the initial day after demolding, and the growth rate gradually decelerated over time thereafter, eventually plateauing after a week. After the 28-day monitoring period, the average shrinkage of LC3-ECC stabilized at approximately 1730 με.

LC3-based ECC tends to display lower shrinkage compared to OPC-based ECC [216]. A crucial contributing factor is the variance in pore size. Coarser pores in LC3-based ECC alleviate the capillary tensile stress, mitigating water loss from mesopores, which is a principal driver of drying shrinkage. Nonetheless, literature reports on this matter are inconclusive [217-220], possibly contingent on the material compositions, substitutions ratio, pore system, etc.

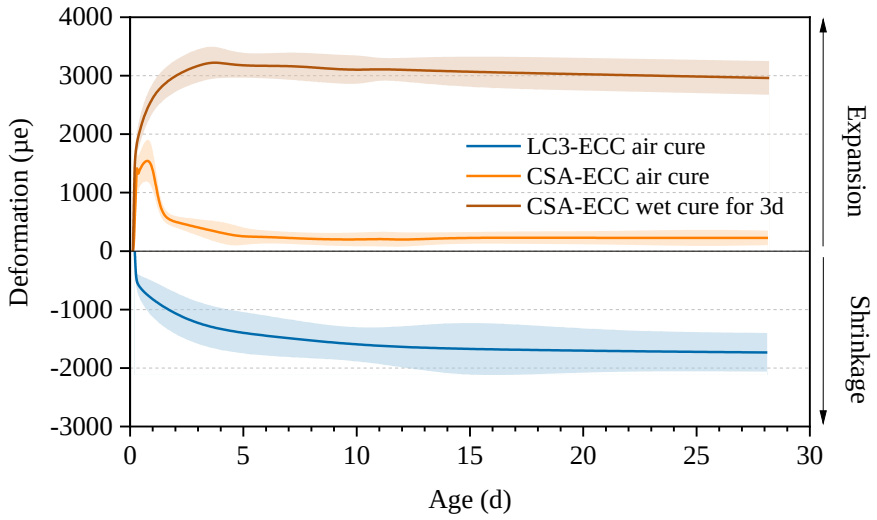

Figure 7.7: Free length changes of cast LC-ECC and CSA-ECC (The shaded area in the plot indicates the variability of measurements.)

CSA-ECC underwent two different curing conditions. The first, air curing after demolding, was identical to the LC3-ECC group. Owing to the presence of CSA cement, the length of the CSA-ECC specimen continued to expand during the first day instead of shrinking and reached 1710 με. The underlying mechanism of CSA cement expansion is usually linked to ettringite formation and its expansive nature [137-138]. Following the peak value, the amount of expansion gradually decreased within two to five days and eventually stabilized at 225 με.

Another curing condition for CSA-ECC involves wet curing during the first three days after demolding, with the relative humidity of the environment maintained at 95% ± 5%, followed by air curing. Under such condition, the peak expansion of CSA-ECC surged to 3230 με. In this study, the wet-cured CSA-ECC reached maximum expansion at approximately 3 days, corresponding to the generation period of ettringite in CSA hydration reported in prior research [216]. During subsequent air curing, the length of the CSA-ECC specimen underwent a marginal decrease, and

expansion remained stable at 2960 με after 28 days, with an expansion loss of only 8%. This suggests that wet curing and water replenishment during the early stage of hydration effectively improved the expansion performance of CSA-ECC. As previously stated, the expansion of CSA-ECC is attributed to the generation of ettringite, one of the primary hydration products of CSA. The existence of sufficient calcium sulfate and water during the early hydration stage are essential prerequisites for ettringite formation. Equation 7.1 shows the chemical reaction in CSA hydration process that forms ettringite [221-222]. Existing research showed that CSA cement requires a maximum of 30% water for complete hydration [223]. In this study, the water-to-binder ratio was kept at 0.20 and relatively low. Therefore, supplementary free water pronouncedly enhances the hydration degree of CSA and promotes expansion.

$$C_4A_3\bar{S} + 2C\bar{S}H_2 + 34H \rightarrow C_3A \cdot 3C\bar{S} \cdot 32H + 2AH_3 \quad (7.1)$$

where $\mathrm{C} = \mathrm{CaO}$, $\mathrm{A} = \mathrm{Al_2}O_3$, $\bar{S} = SO_3$, $\mathrm{H} = \mathrm{H_2O}$.

7.4.2 Shrinkage of printed ECC

The changes in the length of printed LC3-ECC walls during the early-age state (0.5 h-3.5 h after extrusion) and the first 28 d are depicted in Figure 7.8. As illustrated in Figure 7.8(a), notable shrinkage of LC3-ECC under room conditions (LC3-ECC R group) occurred within the first 3h of observation. With the exception of the second layer (L2), which was close to the printing surface and may be restrained by friction, the remaining three layers (L5, L8, L10) all experienced shrinkage of approximately 1500 με within 3 h. This value considerably surpasses the deformation measurement of mold-cast LC3-ECC, which shows less than 500 με in the first 3 h of measurement and attains 1500 με in 7 d. Multiple reasons contribute to this discrepancy. Firstly, printed ECC has a larger specific surface area and drier curing conditions than mold-cast ECC, resulting in more considerable shrinkage. Additionally, the deformation monitoring of printed ECC started after 30 min of extrusion, within an hour following the addition of water, and before the printed material was hardened. In contrast, the length measurement of cast LC3-ECC began after the final setting (5 h after water addition). Consequently, the deformation of cast ECC during the first few hours was omitted.

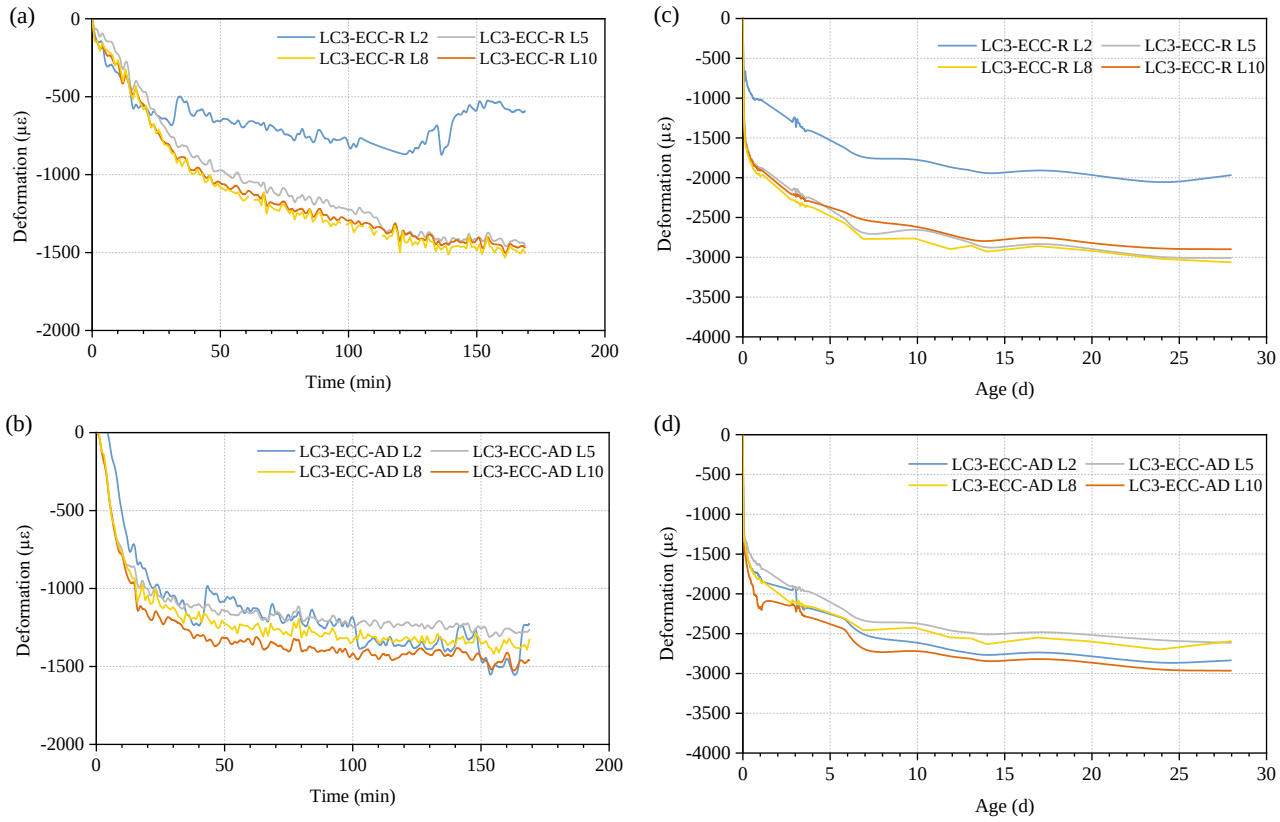

Figure 7.8: Length changes of printed LC3-ECC short walls in (a)(b) 3 hours and (c)(d) 28 days after printing.

The shrinkage of printed LC3-ECC in the accelerated drying (AD) environment followed a pattern analogous to that of the control group (R), with a similar average shrinkage in 3 h (Figure 7.8(b)). However, a notable difference was observed in the slope of deformation growth, which was significantly greater in the AD group than in the R group, indicating a faster rate of shrinkage development. The drier ambient environment resulting from AD accelerates the loss of surface moisture and hastens shrinkage development. Nevertheless, this effect was primarily concentrated during the early stage. After the first 3 h, when the drying condition was terminated, the shrinkage development of both groups became increasingly consistent. At 28 days after printing, the LC3-ECC AD group attained an average shrinkage value of approximately 2700 με, which did not significantly exceed that of the LC3-ECC R group (Figure 7.8(c)(d)). Furthermore, since the electric fan for blowing air is nearer to the upper surface of the printed short wall in the AD group

and the 10th layer has the largest exposed area, the shrinkage value of L10 is higher than those of other layers. In the R group, the shrinkage gradient among layers is less pronounced.

The printed CSA-ECC wall was initially cured under three distinct environmental conditions. In contrast to mold-cast CSA-ECC, printed CSA-ECC did not exhibit expansive behavior under room condition. Instead, an average shrinkage value of 750 με was attained within 3 hours, as depicted in Figure 7.9(a). This is attributed to excessive water loss at an early age which refrained the formation of ettringite. Nevertheless, its shrinkage value was significantly reduced compared with the LC3-ECC R group. In the CSA-ECC AD group, more rapid shrinkage development and higher shrinkage magnitude were observed (Figure 7.9(b)). Analogous to LC3-ECC, the shrinkage difference between various layers was more evident in the AD environment. As demonstrated in Figure 7.9(d)(e), both groups of CSA-ECCs experienced sustained shrinkage during the first few hours. While during the period from a few hours to 2 days, the shrinkage value began to be gradually offset, indicating that CSA cement was still generating expansive hydration products at this time. The shrinkage regained dominance after 2 d and progressively increased until stable. At 28 days, the deformation of the CSA-ECC R group exhibited an average shrinkage of approximately 850 με, whereas that of the CSA-ECC AD group reached 1170 με. A primary conclusion can be drawn that the effect of early excessive water loss on CSA-ECC is more pronounced than that on LC3-ECC, not only altering the shrinkage progression rate in early age but affecting the ultimate shrinkage magnitude - 3 hours of accelerated drying augmented the shrinkage value by 38%.

In the case of CSA-ECC, an additional curing method is employed to assess its deformation behavior. During the first 3 h of monitoring, water was sprayed every 15 min onto the surface of the printed walls to investigate the influence of water supplementation on the deformation response of CSA-ECC. The CSA-ECC W group fluctuated between expansion and shrinkage within the first 40 min. Beyond this time, a consistent expansion growth was witnessed and an expansion value of 800 με was captured by the end of the 3 h. Expansion continued to increase for several hours before surface water evaporated, after which shrinkage began to dominate, resulting in a brief decline in expansive deformation between 5 h and 15 h. Subsequently, the expansion value rose again, reaching a second peak at 1.5 d to 2 d, and gradually diminished thereafter to a plateau of 550 με. It was revealed that merely 3-hour wet curing is sufficient to efficiently stimulate the

expansive capacity of CSA-ECC, with the subsequent 28-day expansion loss controlled to less than 50%.

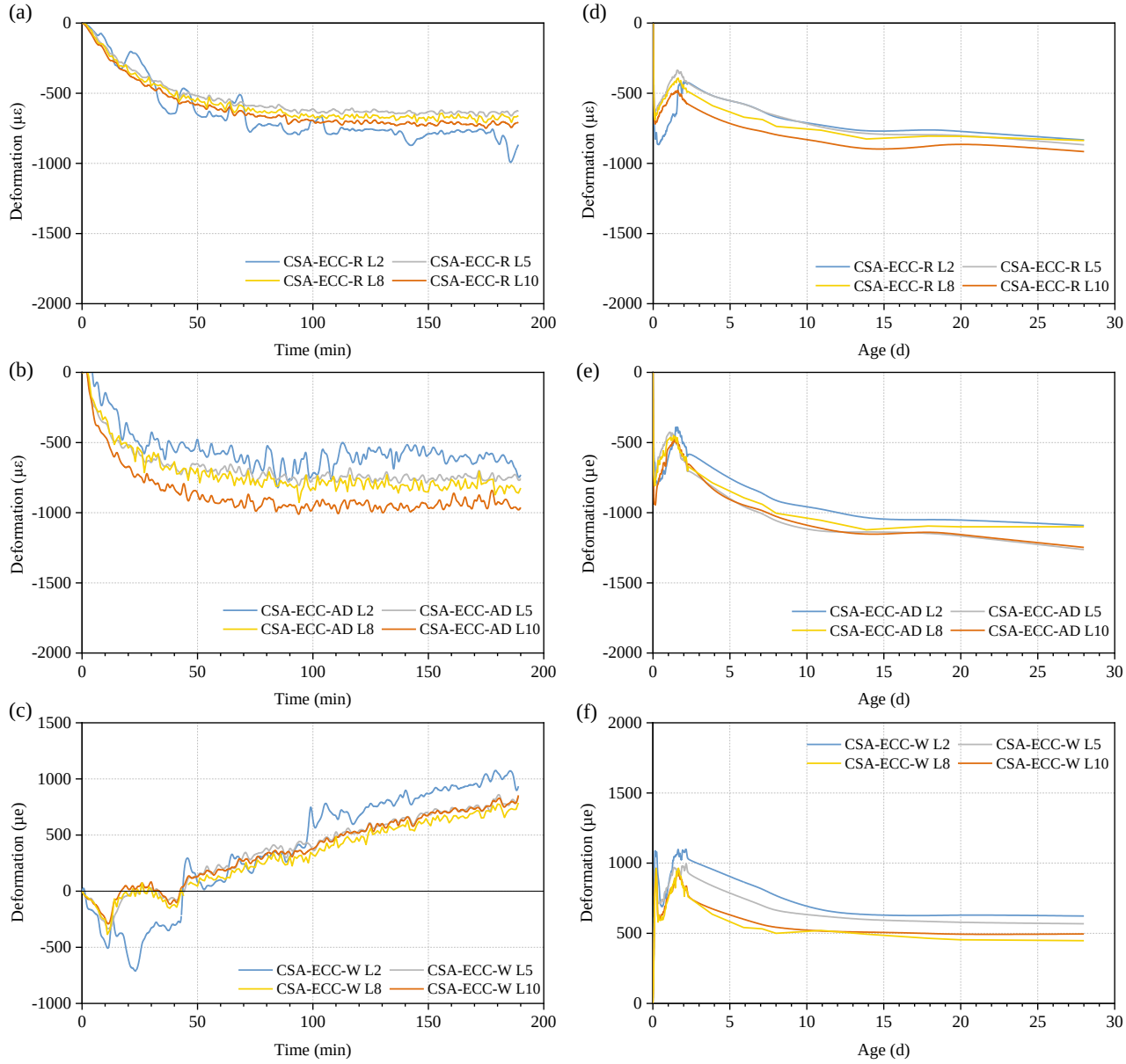

Figure 7.9: Length changes of printed CSA-ECC short walls in (a-c) 3 hours and (d-f) 28 days after printing.

The investigation into the deformation behavior of CSA-ECC in different environments is informative for its practical application in 3D printing. Suppose the printed elements are placed in a dry outdoor environment without additional treatment, the expansion potential of CSA may not

be realized, thus reducing the benefits of using CSA-ECC. Therefore, the use of printable CSA-ECC needs to be accompanied by appropriate post-processing measures, such as water spraying or covering with a wet cloth, to maximize its advantages. Previous literature [216] indicated that ettringite formation occurs within 3 days, and [224] further demonstrated that most of the heat generated during hydration occurs between 2 and 12 hours after the onset of hydration. The wet curing time of 3 hours employed in this study is considerably shorter than the peak period of CSA hydration. It is thereby conceivable that CSA-ECC could exhibit a more satisfactory expansion effect given prolongated wet curing is provided. Further investigation and research are needed to identify the optimized curing methods regarding this issue.

7.5. Mechanical performance

7.5.1 Tensile and compressive properties

Figure 7.10 summarizes the uniaxial tensile properties of LC3-ECC and CSA-ECC at 3 d, 7 d, and 28 d. Overall, the tensile properties of the two are comparable; nevertheless, slight differences exist in the early stages. CSA-ECC exhibited 15% higher tensile strength at 3 d than LC3-ECC, owing to the higher early strength provided by CSA [225]. The hydration products of CSA cement densify the ECC matrix, resulting in higher initial cracking strength and tensile strength, and also a decrease in the early strain capacity of CSA-ECC, as depicted in Figure 7.10(c). As the curing progresses, the strength of ECC continued to increase, whereas the strain capacity showed a downward trend. At 28 d, the strength and strain of both groups were comparable, with CSA exhibiting a marginal 8% higher strength. Figure 7.10(a)(b) illustrate the typical failure modes of both materials, with the average crack width before failure being less than 50 μm.

Concerning compressive strength, cast CSA-ECC showed a slightly higher strength compared to LC3-ECC after 28 d, with both exceeding 30 MPa, as shown in Figure 7.11. Moreover, the strength of 3D-printed LC3-ECC and CSA-ECC surpassed that of their casted counterparts, due to the alignment of fibers in the printing direction that bridge the transverse cracks [112].

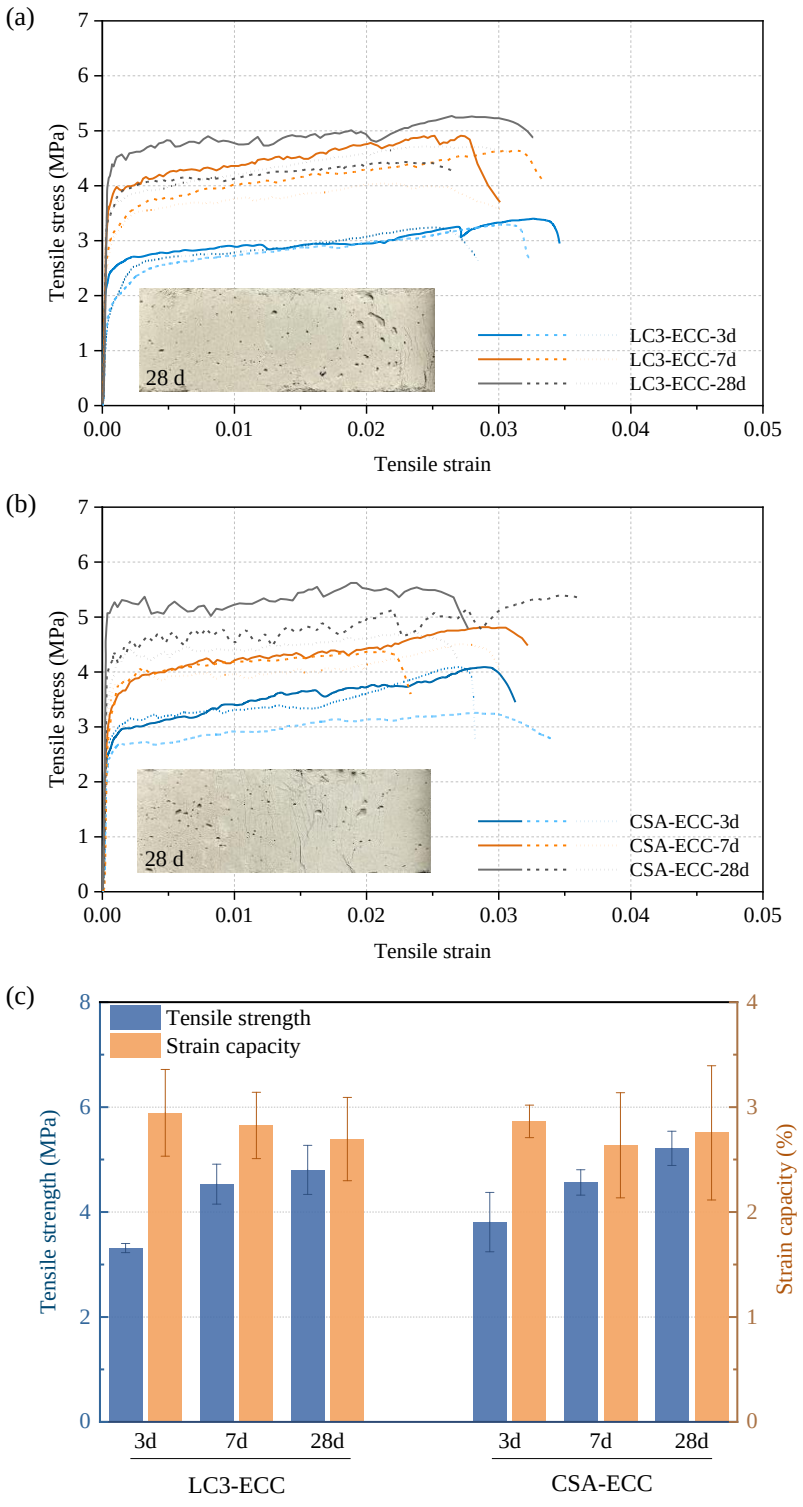

Figure 7.10: Tensile performance of LC3-ECC and CSA-ECC at different ages.

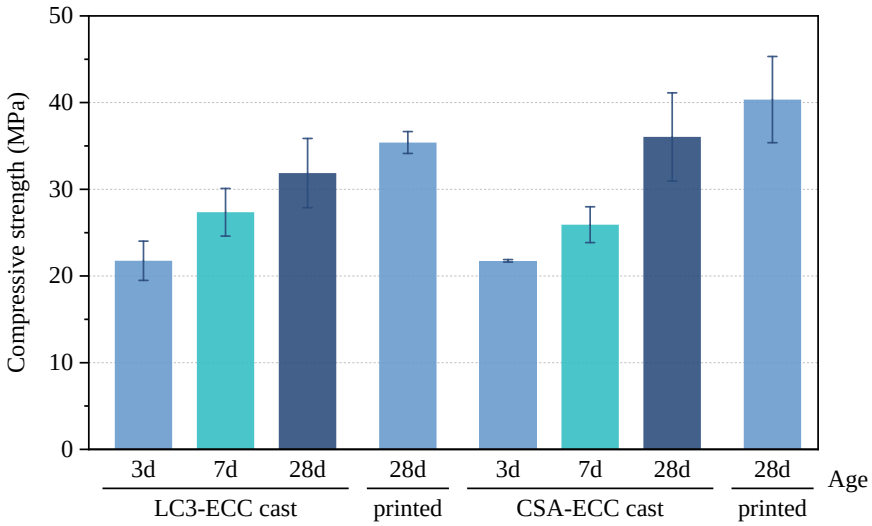

Figure 7.11: Compressive strength of the cast and printed LC3-ECC and CSA-ECC at different ages.

7.5.2 Flexural performance

Figure 7.12 and Figure 7.13 illustrate four-point bending test results for ECC specimens. The relationships between flexural stress and mid-span deflection are shown, where the flexural stress is calculated according to Equation 7.2, and the mid-span deflection is derived from the relative position change of the markers in Figure 7.12.

$$\sigma = \frac{FL}{bd^2} \tag{7.2}$$

where F is the load; L is the length of the support span, i.e., 180 mm in this research; b and d are the width and depth of the specimen, respectively.

Figure 7.12 presents the flexural properties of printed and cast ECC, with the printed ECC cured in air. The cast LC3-ECC reached an ultimate flexural strength of approximately 10 MPa, while the printed LC3-ECC showed a remarkable increase in strength, as well as a gain in the corresponding mid-span deflection, as depicted in Figure 7.12(a). This indicates that the extrusion process of 3D printing enhances the flexural properties of ECC, a finding that aligns with previous research. The extrusion process tends to align fibers in the printing direction [19], thus improving tensile and bending resistance by enhancing the bridging ability of fibers in this loading direction [12, 226]. The printed LC3-ECC specimen generated denser micro-cracks in the bottom tension

region, and the major fracture crack followed a zig-zag structure as it deflected upwards (Figure 7.12(c)), due to the layered structure formed by printing [197]. Furthermore, the ECC material has an intrinsic crack kinking-trapping mechanism that captures and stops cracks deflected at the interface, thereby delaying the fracture process and improving the energy dissipation capacity of the specimen [227]. The same is true for CSA-ECC, with the printed specimens outperforming the cast counterparts in bending resistance, as illustrated in Figure 7.12(b). The cast and printed CSA-ECC showed comparable average flexural strength to LC3-ECC.

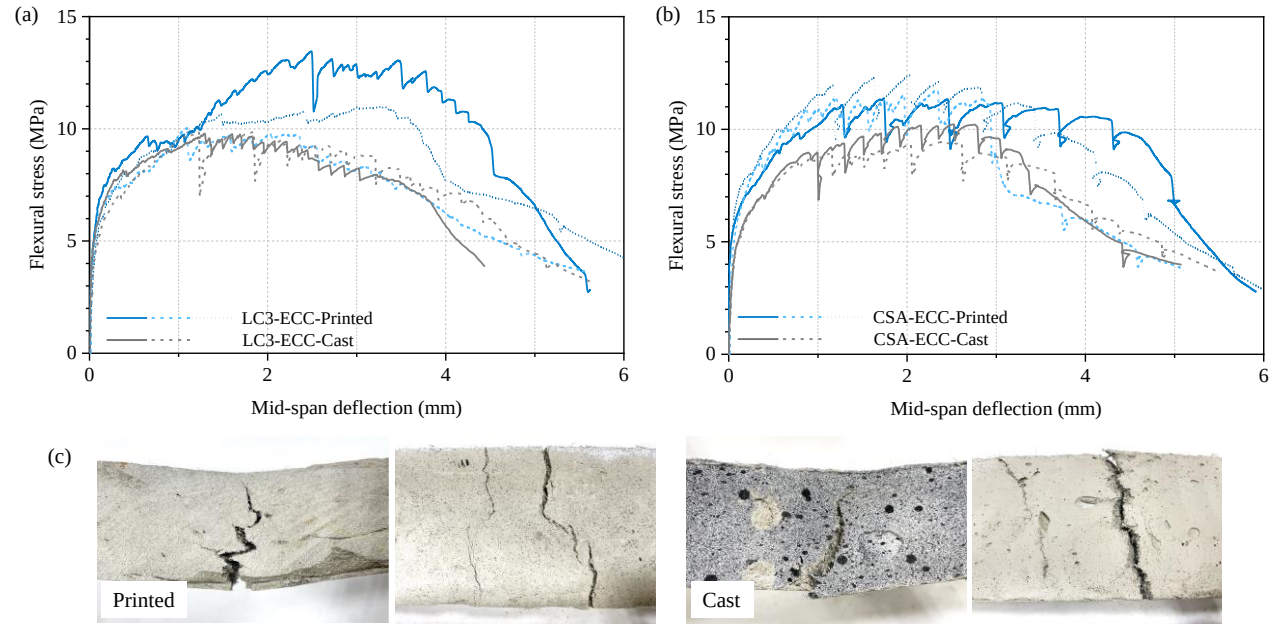

Figure 7.12: (a)(b) Flexural properties and (c) fracture modes of printed and cast ECCs.

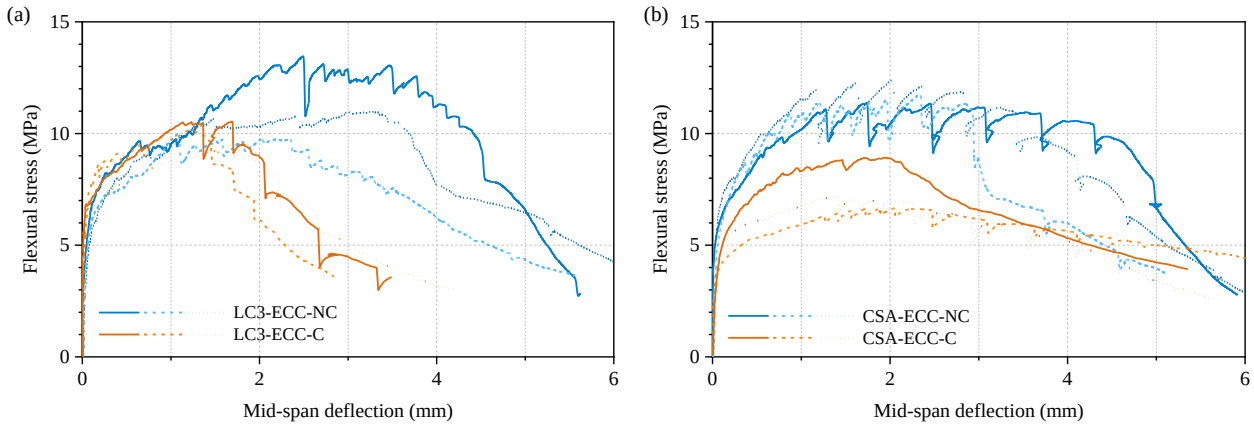

Figure 7.13: Flexural properties of printed ECCs with and without carbonation curing.

The comparison of the four-point bending results of printed ECC with and without carbonation curing is presented in Figure 7.13. Both LC3-ECC and CSA-ECC experienced a significant loss of strength and mid-span deflection after subjected to carbonation. LC3-ECC exhibited an average decrease of 15% in its ultimate strength, whereas CSA-ECC experienced a more pronounced decline of 35%. The reduction in mid-span deflection also led to a compromise in the energy absorption capacity of the specimens. Although carbonation can mitigate the negative impact of printing materials on the environment, as discussed in the following subsection, it has an adverse effect on the mechanical properties of printed ECC. It is also worth noting that carbonation may hinder the expansion ability of CSA-ECC, as expansive ettringite can be decomposed by carbonation [228-229]. The effectiveness of CSA in resisting early shrinkage can thus be hindered. Hence, it is suggested to apply carbonation curing to printed ECC with caution to ensure the mechanical performance of materials and structures.

7.6. Material greenness

The carbon footprint and embodied energy of LC3-ECC and CSA-ECC were analyzed and quantified, as illustrated in Table 7.3 and Figure 7.14. Reference groups, comprising a classic mix of ECC, i.e., M45 ECC [230], and concrete [231], were used for comparative purposes. It was found that, M45 ECC had a significantly higher carbon footprint compared to concrete, reaching 600 kg/m^3 and equivalent to 160% of concrete. The main carbon footprint source was Portland cement, accounting for 81% of the total carbon. In LC3-ECC, incorporating limestone and metakaolin reduced the carbon emission caused by cement to 42% of its original value. The 60% substitution of PLC by CSA in CSA-ECC further enhanced this positive environmental impact, resulting in a 70% carbon emission reduction in cement portion compared to M45. Besides the amount of cement used, the changes in the binder composition system were also reflected in the high ratio of FA. The proposed weight ratios of FA to LC3 exceed 2.4, effectively reducing carbon emissions while maintaining excellent mechanical properties. Taking all components into account, LC3-ECC has an overall 15% reduction in carbon footprint relative to the concrete reference, while CSA-ECC achieved a remarkable reduction of 31%. This implies that CSA-ECC offers a greater environmental advantage than ordinary concrete.

Table 7.3: The embodied energy and carbon footprint of ECC ingredients.

	PLC [a]	CSA [b]	MK [c]	LS [d]	FA [e]	SF [e]	CR [e]	Sand [e]	PVA [a]	SP [a]
Energy (GJ/ton)	5.0	2.2	3.48	0.62	0	0.036	4	0.067	101	35
CO_2 (kg/ton)	811	360	330	12.2	0	14	200	23.3	3400	1667

[a] The energy and carbon footprint of PLC were estimated as the sum of 90% OPC [232] and 10% limestone addition.

[b] The energy and carbon footprint of CSA are assumed to be 40% of OPC [233].

[c] Data from [234-235].

[d] Data from [236-237].

[e] Data from [238].

Furthermore, considering the reduction in structural dimensions that ECC can bring due to its excellent mechanical properties, the volume consumption of ECC required to meet the same application scenario is significantly lower than that of concrete. This will greatly reduce the overall carbon and energy footprint of the structure. A recent joint-less pavement project in the University of Michigan has indicated that ECC can reduce the thickness of pavement to half of that of conventional concrete pavement, demonstrating a 50% material consumption reduction, while maintaining reliable functions without steel reinforcement. In previous engineering applications in Japan, up to 50% volume reductions has also been witnessed in ECC tunnel linings compared with conventional concrete linings [7, 239].

In addition, carbon dioxide curing was employed in this study to promote carbon sequestration further. After 24 hours of curing, the carbon dioxide captured exceeded 10% of cement mass, which is reflected in the negative axis of the carbon emission in Figure 7.14. This offset can reduce the overall carbon footprint of CSA-ECC to 59% of the concrete reference, while LC3-ECC reaches 75% of concrete. This development is inspiring for achieving global environmental targets for reducing carbon emissions and highlights the material upgrade compared to conventional printable cementitious materials (which usually have a high cement content).

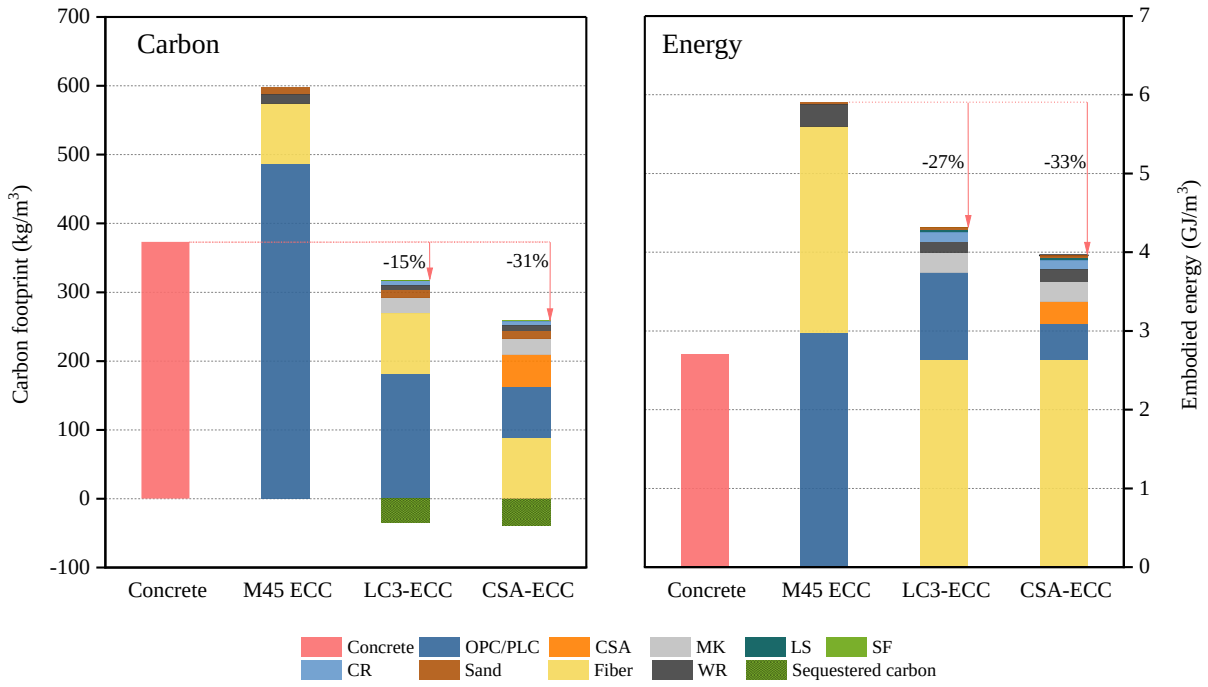

Figure 7.14: Carbon and energy analysis of LC3-ECC and CSA-ECC with reference groups.

Optimizing and upgrading the binder system has reduced the overall embodied energy of LC3-ECC and CSA-ECC to 73% and 67% of M45, respectively. Nonetheless, the energy per unit of ECC remains higher than that of concrete. It was noted that PVA fiber contributes a significant portion, accounting for about 44% of the energy, in addition to cement. Replacing PVA fibers with PP fibers or other green fibers can effectively reduce the overall embodied energy of ECC [240], to achieve a more energy-efficient product. Further research is needed to improve the energy efficiency of ECC. However, it should be noted that even if PVA fibers with higher unit energy are used, this calculation of energy in Figure 7.14 is still on the standpoint of material scale. The reduction in material consumption that ECC can achieve is sufficient to offset its high unit energy consumption, viewed from the structural or element perspective. For instance, as mentioned previously, the use of ECC can reduce pavement volume by up to 50%, which means that for a pavement with the same function, the overall energy consumption of LC3-ECC and CSA-ECC is comparable to, or even lower than, that of the concrete pavement.

In this study, two ECC formulations were proposed and verified to effectively reduce the environmental impact compared to traditional cementitious materials. This is particularly valuable

for printable materials without coarse aggregates. Additionally, the exceptional material and structural properties of ECC warrant the reduction in structure and element size and in material consumption. These benefits further enhance the contributions of proposed ECCs to mitigating environmental stress and pose more profound effects.

7.7. Printing showcase

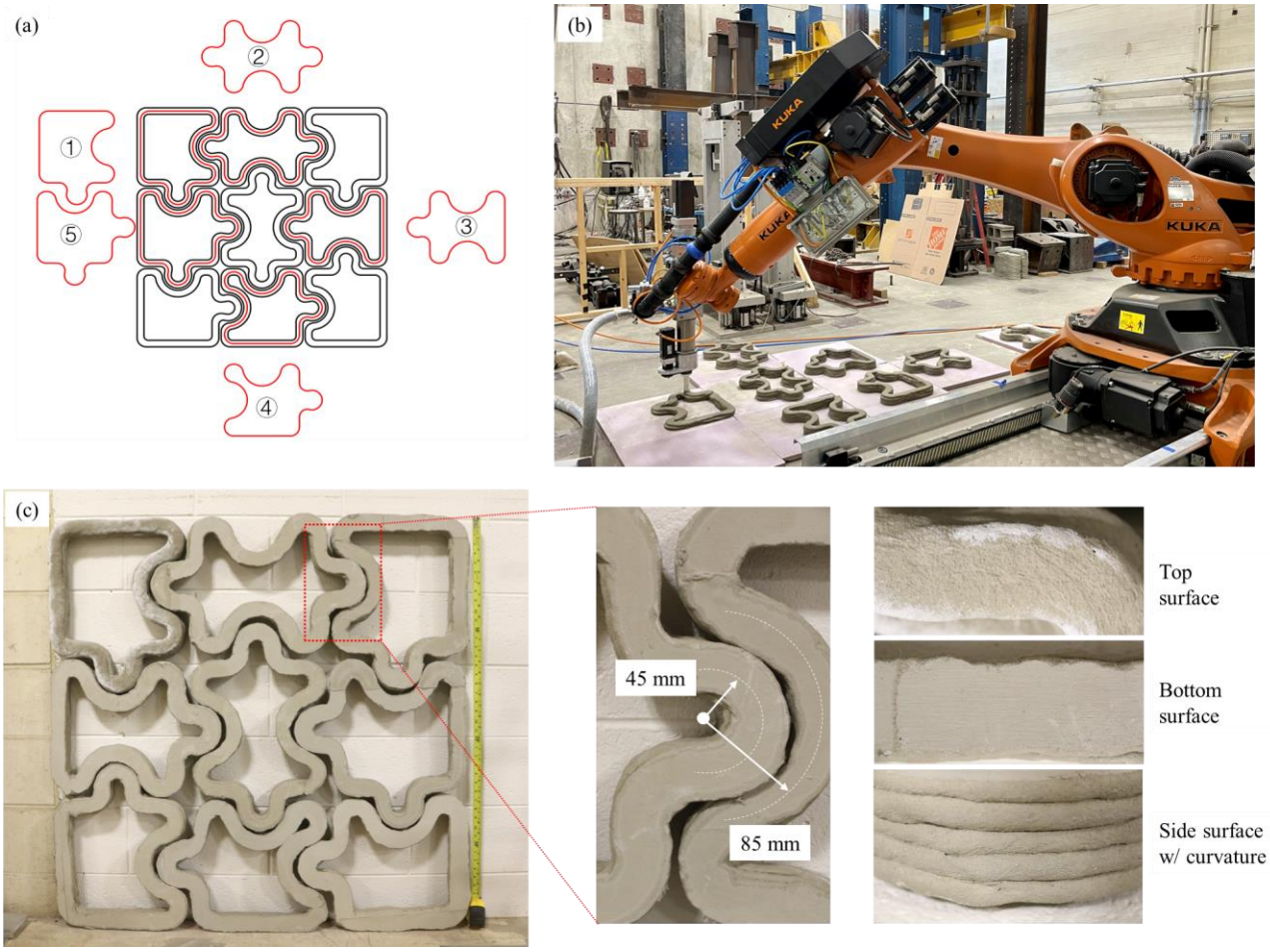

Figure 7.15: (a) Puzzle-inspired printing pattern design; (b) printed pieces; (c) self-interlocked ECC pieces and close-up looks

To demonstrate the feasibility of printing shrinkage-resistant low-carbon ECC, a showcase component was designed and printed. The design, inspired by puzzles, takes advantage of the complex geometric shapes enabled by 3D printing technology. The puzzle blocks consist of 9

individual printed pieces, incorporating elements of 5 distinct shapes (Figure 7.15(a)(b)). Each piece is modified from the basic 300 mm × 300 mm × 50 mm (5 layers) shape to produce a variety of intricate geometric patterns. The pieces fit together using interlocking convex and concave shapes, with a concave arc radius of 85 mm, a convex radius of 45 mm. The width of a single filament is approximately 30 mm.

Printing utilized the CSA-ECC mixture proposed in this study, and the components were cured under 20 ± 3°C and 16 ± 5% RH. No shrinkage cracks were observed on the printed pieces, which were printed without any lubrication applied on the base plane (see Figure 7.15(c)). Even in areas with curved corners, which are typically prone to cracking due to print defects or drying shrinkage, no signs of cracking were observed.

7.8. Summary and conclusions

The present study developed a low-carbon, expansive ECC in the context of 3D printing. Through experimental investigation and analysis, the following conclusions can be drawn:

(1) LC3-ECC and CSA-ECC mixes have been designed to meet the printability requirements with a minimum open time of 1 hour.

(2) Cast LC3-ECC exhibited gradually stabilized shrinkage development during the 28-day air curing period, whereas CSA-ECC demonstrated expansion behavior instead of shrinkage under air curing and wet curing conditions. Furthermore, 3-day wet curing after demolding promoted consistent expansion of CSA-ECC.

(3) A non-contact measurement method was implemented for monitoring the length change of printed multi-layer ECC. The results indicated that compared with cast ECC of the same compositions and similar curing conditions, printed ECC showed a larger magnitude of free shrinkage or a reduced magnitude of expansion. This is attributed to 3D printing exposing the material to the external environment at an early stage, and the length change monitoring beginning right from the fresh state after printing.

(4) Wet curing or water spray within the first few hours after printing of CSA-ECC contributed to developing expansion behavior. Given the notable expansion seen in cast CSA-ECC, prolonging the wet curing time after printing has the potential to guarantee a more robust expansion.

(5) The designed LC3-ECC and CSA-ECC materials exhibited a substantially lower carbon footprint than concrete and lower embodied energy than classic M45 ECC. CSA-ECC, in particular, presents only 59% of the embodied carbon of concrete if CO_2 sequestration is taken into account. When the contribution of ECC's superior performance to structure size reduction and material consumption saving is further considered, the carbon and energy embodied in printed ECC structures will be significantly lower than that of concrete structures with the same functionality.

(6) The mechanical properties of printed ECC surpassed those of cast specimens, with printed CSA-ECC demonstrating comparable or superior mechanical properties to printed LC3-ECC. However, carbonation weakens the flexural performance of printed ECC. Therefore, care should be taken when carbonation curing is used to mitigate the material's carbon footprint.

Chapter 8. Concluding Remarks

8.1. Research finding

This dissertation presents studies of 3D printing engineered cementitious composites (3DP-ECC), which represent an efficient synergy between emerging construction technologies and advanced building materials. Material design and performance, process control, structural form and behavior at different life cycle stages are investigated. Major scientific findings from the research are drawn as follows:

- ECC has been validated as a promising ink for 3D printing. Through delicate tailoring of mix proportions, smooth extrusion of ECC and reasonable open time are guaranteed. The cohesive nature of ECC's matrix and the incorporation of fibers collectively yield exceptional post-extrusion buildability, thus endorsing its immense potential in construction. Despite the notable disparity between the extrusion process and the conventional casting approach, 3D printed ECC retains the remarkable properties inherent to ECC as an advanced building material, including its strain-hardening behavior and excellent ductility, and in some instances, even surpasses its cast counterpart. Owing to ECC's comprehensive knowledge base of micromechanics, printable ECC can be deliberately designed and adjusted to fulfill the diverse demands in various application scenarios.

- To establish the interaction between printing materials and process parameters, a time-evolving buildability analysis model was proposed to facilitate successful printing without premature material failure. This model encompasses a comprehensive assessment of material properties, time progression, and printing parameters, thus forging a quantifiable relationship between these variables and buildability. Additionally, the risk of structural self-buckling failure was evaluated in cases where structures experienced non-material-related collapse.

- Correlations between printing parameters and the resultant prints were established, shedding light on the influence of these parameters on the microstructure and macroscopic properties of printed materials. The study revealed that reducing the nozzle standoff distance within a specific range enhances the in-plane tensile strength and strain capacity of 3DP-ECC. Furthermore, a moderate printing speed also improves the material's tensile performance. Additionally, it was observed that the interfacial fiber bridging force increases as the nozzle standoff distance is increased for a circular nozzle.

- To alleviate the anisotropy present in 3D printed ECC (3DP-ECC), two innovative printing patterns, “knitting” and “tilting” filaments, were proposed, mimicking the natural crossed-lamellar structure of conch shells. Taking advantage of 3DP’s flexibility in enabling complex paths, 3D spatial paths were designed to allocate tensile/flexural resistance to multiple directions. Furthermore, the novel patterns created an interwoven interface system, converting the original weak links into a structural strengthening method. It was found that knitted and tilted filaments revealed superior or comparable bending performance to cast ECC in two favorable orientations in four-point bending tests. Furthermore, flexural performance in the weakest orientation was notably improved by knitting and tilting compared with that of parallel filaments, substantially alleviating anisotropy in 3DP-ECC.

- The structural-scale behaviors of 3DP-ECC walls under compression were investigated. The distinctive crack and failure patterns were attributed to the end effects of loading, the inherent material properties of ECC, the presence of multiple interfaces introduced by 3D printing, and the design of the printing path. It is noted that the ductile mechanical response and enhanced energy absorption capacity captured in 3DP-ECC walls highlight their promising resilience advantage in delaying failure, preserving functionality, and facilitating rapid post-event recovery.

- To address the shrinkage and high carbon footprint concerns, low-carbon, expansive, printable ECC with appropriate mechanical properties were designed and validated. LC3-based ECC combined with CSA was adopted to design printable mixes with a minimum open time of 60 min. The length deformation monitoring of cast and printed ECCs revealed that wet curing at an early age could effectively promote expansion. Regarding environmental sustainability, the CSA-ECC mix has a carbon footprint of merely 69% of

concrete. Considering ECC's ability to reduce element size and material consumption, the environmental friendliness of printable CSA-ECC can be further enhanced. In addition, mechanical tests confirmed that the proposed ECCs demonstrated comparable or superior performance to their cast counterparts.

8.2. Research impacts and highlights

As an emerging construction method, 3DP-ECC necessitates a strong fundamental knowledge base for its feasibility assessment. This thesis brings forth insights into the life-cycle knowledge system of 3DP-ECC, offering practical technical solutions and value propositions for real-world applications. Different stages of the life cycle present distinct challenges and specific demands. Accordingly, this thesis identifies and investigates the corresponding areas of focus, addressing various technical complexities and practical considerations. The following sections provide a detailed account of the key research highlights in each life phase:

Material production phase:

- For the material design and evaluation of buildability, the proposed models in Chapter 3 enable the quantification of buildability for freshly extruded structures. These models offer valuable guidance for optimizing material tailoring and process control in 3D printing, effectively reducing the costs associated with trial-and-error iterations and minimizing material waste. Moreover, the material-level model enables accurate predictions of structural deformation during the early stages of fabrication, thus improving construction precision and mitigating potential structural issues resulting from dimensional variations. Furthermore, the material testing and modeling approaches introduced in this study extend beyond the scope of printable ECC, encompassing a wide range of cementitious materials suitable for extrusion printing. As a result, this research holds significant promise for diverse applications in various fields.
- Low-carbon printable ECC formulations proposed and verified in Chapter 7 effectively reduce the environmental impact compared to traditional printable cementitious materials while retain the extraordinary mechanical performance of ECC materials. Additionally, the

exceptional material and structural properties of ECC warrant the reduction in structure and element size and in material consumption. These benefits are far from trivial when it comes to mitigating environmental stress.

Manufacturing phase:

- The correlation between the printing process and the performance of the printed products in Chapter 4 serves as the fundamental basis for optimizing printing procedures and enhancing product quality. This comprehension facilitates effective adjustments of printing parameters, leading to improved and optimized printed products. Furthermore, the properties manifested by the finished products can serve as valuable feedback, providing crucial information and guidance for the optimization of printing parameters, thereby enabling a closed-loop 3D printing process control.

- The anisotropy alleviation approach proposed in Chapter 5 serves as a catalyst for a novel concept in enhancing 3D printed structures as a whole: how to alleviate the inherent anisotropy issue of 3DP-ECC and 3DP cementitious materials without introducing external reinforcements and interrupting the automated construction process. Following this underlying logic, the structure forms do not need to be limited to "knitted" or "tilted" structures, which have been proven effective in this study. More advanced, architectured, and efficient structural forms can be designed and applied to structural components.

Use phase:

- The feasibility of adopting 3DP-ECC walls to bear compressive load was validated in Chapter 6. The significant resilience response is in line with the structural requirements for delayed failure and functional preservation, thereby bolstering the overall safety of the structure. Consequently, these findings provide additional validation for the application potential of 3DP-ECC as a safe and efficient construction approach.

- As elucidated in Chapter 7, the proposed expansive ECC's resistance to early-age shrinkage eliminates the latent risks associated with cracking. By diminishing shrinkage cracking, coupled with ECC’s material feature of inherent tight crack width, the structural integrity and durability of printed components will be enhanced in the use phase, thereby reducing the need for maintenance during their service life.

8.3. Recommendations for future research

This thesis has successfully established the knowledge framework of 3DP-ECC and accomplished foundational research. These endeavors aim to contribute to continued and future studies on 3DP-ECC and its practical applications. To further strengthen the knowledge base of 3DP-ECC, the following research priorities and recommendations have been identified:

- Considering the inherent flexibility of 3DP technology and its capability to handle intricate paths, taking advantage of delicate path design to enhance structural performance should be embraced as the fundamental approach to maximize the potential of 3DP technology. Promising directions for in-depth exploration encompass: (1) utilizing architectured structural design and the inherent material properties of ECC to mitigate anisotropy, as demonstrated in this study, and enhance structural performance; (2) employing topology design to optimize structures, reducing material consumption and promoting sustainable development, while meeting the requirements for load-bearing capacity and safety. Regarding the former, the architectured forms proposed in this study serve as an initial step and a source of inspiration. It is essential to delve into more possibilities to introduce efficient structural forms that can be readily applied in engineering practice. As for the latter, topology optimization allows for the efficient conversion of material properties into structural capacity. Usually, it poses challenges to traditional concrete casting due to custom formwork fabrication. Herein lies the potential of 3DP technology, as it can overcome this predicament. Given the multiple degrees of freedom offered by additive manufacturing technology, 3DP is well-suited for fabricating topology-optimized structures.

- To facilitate the engineering application of 3DP-ECC, it is imperative to extend the research scope to encompass structural-level research on structural elements and joints. The study carried out in Chapter 6 focused on investigating the compressive behavior of 3DP-ECC walls. Nonetheless, to validate the secure utilization of 3DP-ECC in structural contexts, extensive research on different structural elements is necessitated. These verifications should include comprehensive tests for columns, slabs, joints, and other components subjected to simple or complex loading conditions. By conducting such tests,

robust evidence regarding the structural performance and safety of 3DP-ECC can be gathered, thus fostering its confident implementation in practical applications.

- Significant progress has been made in advancing the sustainability of 3DP-ECC in Chapter 7. Reduced carbon emission and embedded energy are gained through the utilization of LC3, high-volume FA, and CSA. The outcomes are indeed noteworthy; however, there is still room for further enhancement to drive sustainable development. One promising avenue is the replacement or partial substitution of synthetic fibers, e.g., PVA fiber and PE fiber employed in this study, with low-carbon or natural alternatives. Materials like sisal fiber and hemp fiber offer viable options. By incorporating such fibers, green printable ECC can further unlock its potential in contributing to the carbon neutrality goal. This research endeavor presents an opportunity to advance the field and promote a more sustainable and greener future.

- The development of multi-functional printable ECC holds immense potential for integrating advanced manufacturing technology with smart building materials, resulting in substantial social benefits. In general, buildings and infrastructure can make a significant contribution to sustainability by incorporating smart building materials. Such materials have been designed for conventional casting to adapt and respond to the changing external environment. One notable example is thermal adaptive ECC, which can effectively reduce building energy consumption by dynamically adjusting its thermal capacity in response to temperature fluctuations. Additionally, photo-catalytic ECC possesses the remarkable ability to purify the surrounding air, contributing to improved air quality. It is anticipated that technology enabling simultaneous printing of bulk elements with ECC and facades with multifunctional ECC will substantially contribute to promoting the construction of smart cities and addressing global environmental degradation and resource shortages.

Bibliography

[1] G. De Schutter, K. Lesage, V. Mechtcherine, V.N. Nerella, G. Habert, I. Agusti-Juan, Vision of 3D printing with concrete — Technical, economic and environmental potentials, CEMENT CONCRETE RES, 112 (2018) 25-36.

[2] M.K. Mohan, A.V. Rahul, G. De Schutter, K. Van Tittelboom, Extrusion-based concrete 3D printing from a material perspective: A state-of-the-art review, Cement and Concrete Composites, 115 (2021) 103855.

[3] R.A. Buswell, W.R. Leal De Silva, S.Z. Jones, J. Dirrenberger, 3D printing using concrete extrusion: A roadmap for research, CEMENT CONCRETE RES, 112 (2018) 37-49.

[4] I. Agustí-Juan, F. Müller, N. Hack, T. Wangler, G. Habert, Potential benefits of digital fabrication for complex structures: Environmental assessment of a robotically fabricated concrete wall, J CLEAN PROD, 154 (2017) 330-340.

[5] I. Perkins, M. Skitmore, 3D printing in the Construction Industry: a review, Int. J. Constr. Manage, 15 (2015) 1-9.

[6] V.C. Li, F.P. Bos, K. Yu, W. McGee, T.Y. Ng, S.C. Figueiredo, K. Nefs, V. Mechtcherine, V.N. Nerella, J. Pan, G.P.A.G. van Zijl, P.J. Kruger, On the emergence of 3D printable Engineered, Strain Hardening Cementitious Composites (ECC/SHCC), CEMENT CONCRETE RES, 132 (2020) 106038.

[7] V.C. Li, Engineered Cementitious Composites (ECC), 1st ed., Springer, Berlin, Germany, 2019.

[8] B. Felekoglu, K. Tosun-Felekoglu, R. Ranade, Q. Zhang, V.C. Li, Influence of matrix flowability, fiber mixing procedure, and curing conditions on the mechanical performance of HTPP-ECC, Composites Part B: Engineering, 60 (2014) 359-370.

[9] N. Xu, Y. Qian, J. Yu, C.K.Y. Leung, Tensile performance of 3D-printed Strain-Hardening Cementitious Composites (SHCC) considering material parameters, nozzle size and printing pattern, Cement and Concrete Composites, 132 (2022) 104601.

[10] F. Aslani, R. Dale, F. Hamidi, A. Valizadeh, Mechanical and shrinkage performance of 3D-printed rubberised engineered cementitious composites, CONSTR BUILD MATER, 339 (2022) 127665.

[11] A.L. van Overmeir, S.C. Figueiredo, B. Šavija, F.P. Bos, E. Schlangen, Design and analyses of printable strain hardening cementitious composites with optimized particle size distribution, CONSTR BUILD MATER, 324 (2022) 126411.

[12] K. Yu, W. McGee, T.Y. Ng, H. Zhu, V.C. Li, 3D-printable engineered cementitious composites (3DP-ECC): Fresh and hardened properties, CEMENT CONCRETE RES, 143 (2021) 106388.

[13] B. Zhu, J. Pan, B. Nematollahi, Z. Zhou, Y. Zhang, J. Sanjayan, Development of 3D printable engineered cementitious composites with ultra-high tensile ductility for digital construction, MATER DESIGN, 181 (2019) 108088.

[14] S.C. Figueiredo, C.R. Rodríguez, Z.Y. Ahmed, D.H. Bos, Y. Xu, T.M. Salet, O. Çopuroğlu, E. Schlangen, F.P. Bos, An approach to develop printable strain hardening cementitious composites, MATER DESIGN, 169 (2019) 107651.

[15] H. Ogura, V. Nerella, V. Mechtcherine, Developing and Testing of Strain-Hardening Cement-Based Composites (SHCC) in the Context of 3D-Printing, MATERIALS, 11 (2018) 1375.

[16] E. Ivaniuk, M. Friedrich Eichenauer, Z. Tošić, S. Müller, D. Lordick, V. Mechtcherine, 3D printing and assembling of frame modules using printable strain-hardening cement-based composites (SHCC), MATER DESIGN, 219 (2022) 110757.

[17] D.G. Soltana, V.C. Li, A self-reinforced cementitious composite for building-scale 3D printing, Cement and Concrete Composites, 90 (2018) 1-13.

[18] J. Yu, C.K.Y. Leung, Impact of 3D Printing Direction on Mechanical Performance of Strain-Hardening Cementitious Composite (SHCC), RILEM International Conference on Concrete and Digital Fabrication, Zurich, Switzerland, 2018, pp. 255-265.

[19] S.C. Figueiredo, C.R. Rodríguez, Z.Y. Ahmed, D.H. Bos, Y. Xu, T.M. Salet, O.G.Ç. Glu, E. Schlangen, F.P. Bos, Mechanical Behavior of Printed Strain Hardening Cementitious Composites, MATERIALS, 13 (2020) 2253.

[20] B. Zhu, J. Pan, Z. Zhou, J. Cai, Mechanical properties of engineered cementitious composites beams fabricated by extrusion-based 3D printing, ENG STRUCT, 238 (2021) 112201.

[21] B. Khoshnevis, Automated construction by contour crafting—related robotics and information technologies, AUTOMAT CONSTR, 13 (2004) 5-19.

[22] T.T. Le, S.A. Austin, S. Lim, R.A. Buswell, A.G.F. Gibb, T. Thorpe, Mix design and fresh properties for high-performance printing concrete, MATER STRUCT, 45 (2012) 1221-1232.

[23] XtreeE, Krypton, a column in Aix-en-Provence, 2016.

[24] Totalkustom, 3D Concrete House Printer, 2016.

[25] N. Zhang, M. Xia, J. Sanjayan, Short-duration near-nozzle mixing for 3D concrete printing, Cement and Concrete Research, 151 (2022) 106616.

[26] S. Muthukrishnan, S. Ramakrishnan, J. Sanjayan, Set on demand geopolymer using print head mixing for 3D concrete printing, Cement and Concrete Composites, 128 (2022) 104451.

[27] A. Paolini, S. Kollmannsberger, E. Rank, Additive manufacturing in construction: A review on processes, applications, and digital planning methods, Additive Manufacturing, 30 (2019) 100894.

[28] S. Lim, R. Buswell, T. Le, Development of a Viable Concrete Printing Process, the 28th ISARC, Seoul, Korea, 2011, pp. 665-670.

[29] S. Lim, R.A. Buswell, T.T. Le, S.A. Austin, A.G.F. Gibb, T. Thorpe, Developments in construction-scale additive manufacturing processes, AUTOMAT CONSTR, 21 (2012) 262-268.

[30] V. Mechtcherine, V.N. Nerella, F. Will, M. Näther, J. Otto, M. Krause, Large-scale digital

concrete construction – CONPrint3D concept for on-site, monolithic 3D-printing, AUTOMAT CONSTR, 107 (2019) 102933.

[31] E. Lloret, A.R. Shahab, M. Linus, R.J. Flatt, F. Gramazio, M. Kohler, S. Langenberg, Complex concrete structures, COMPUT AIDED DESIGN, 60 (2015) 40-49.

[32] B. Lu, Y. Weng, M. Li, Y. Qian, K.F. Leong, M.J. Tan, S. Qian, A systematical review of 3D printable cementitious materials, CONSTR BUILD MATER, 207 (2019) 477-490.

[33] T. Wangler, N. Roussel, F.P. Bos, T.A.M. Salet, R.J. Flatt, Digital Concrete: A Review, CEMENT CONCRETE RES, 123 (2019) 105780.

[34] J. Assaad, K.H. Khayat, J. Daczko, Evaluation of Static Stability of Self-Consolidating Concrete, ACI Mater. J., (2004) 207–215.

[35] D. Jiao, C. Shi, Q. Yuan, X. An, Y. Liu, H. Li, Effect of constituents on rheological properties of fresh concrete-A review, Cement and Concrete Composites, (2017) 146-159.

[36] S.H. Lee, H.J. Kim, E. Sakai, M. Daimon, Effect of particle size distribution of fly ash–cement system on the fluidity of cement pastes, CEMENT CONCRETE RES, 33 (2003) 763-768.

[37] P.F.G. Banfill, Rheological methods for assessing the flow properties of mortar and related materials, CONSTR BUILD MATER, 8 (1994) 43-50.

[38] A.M. Neville, Properties of concrete. Vol. 4, London: Longman1995.

[39] C.K. Park, M.H. Noh, T.H. Park, Rheological properties of cementitious materials containing mineral admixtures, CEMENT CONCRETE RES, 35 (2005) 842-849.

[40] E. Güneyisi, M. Gesoglu, A. Al-Goody, S. İpek, Fresh and rheological behavior of nano-silica and fly ash blended self-compacting concrete, CONSTR BUILD MATER, 95 (2015) 29-44.

[41] R.S. Ahari, T.K. Erdem, K. Ramyar, Thixotropy and structural breakdown properties of self consolidating concrete containing various supplementary cementitious materials, Cement and Concrete Composites, 59 (2015) 26-37.

[42] X. Zhang, J. Han, The effect of ultra-fine admixture on the rheological property of cement paste, CEMENT CONCRETE RES, 30 (2000) 827-830.

[43] K. Vance, A. Kumar, G. Sant, N. Neithalath, The rheological properties of ternary binders containing Portland cement, limestone, and metakaolin or fly ash, CEMENT CONCRETE RES, 52 (2013) 196-207.

[44] C.F. Ferraris, K.H. Obla, R. Hill, The influence of mineral admixtures on the rheology of cement paste and concrete, CEMENT CONCRETE RES, 31 (2001) 245-255.

[45] A.I. Laskar, S. Talukdar, Rheological behavior of high performance concrete with mineral admixtures and their blending, CONSTR BUILD MATER, 22 (2008) 2345-2354.

[46] S. Grzeszczyk, G. Lipowski, Effect of content and particle size distribution of high-calcium fly ash on the rheological properties ofcement pastes, CEMENT CONCRETE RES, 27 (1997) 907-916.

[47] A. Beycioğlu, H. Yılmaz Aruntaş, Workability and mechanical properties of self-compacting concretes containing LLFA, GBFS and MC, CONSTR BUILD MATER, 73 (2014) 626-635.

[48] M.K. Rahman, M.H. Baluch, M.A. Malik, Thixotropic behavior of self compacting concrete

with different mineral admixtures, CONSTR BUILD MATER, 50 (2014) 710-717.

[49] R. Derabla, M.L. Benmalek, Characterization of heat-treated self-compacting concrete containing mineral admixtures at early age and in the long term, CONSTR BUILD MATER, 66 (2014) 787-794.

[50] O. Boukendakdji, E. Kadri, S. Kenai, Effects of granulated blast furnace slag and superplasticizer type on the fresh properties and compressive strength of self-compacting concrete, Cement and Concrete Composites, 34 (2012) 583-590.

[51] M. Mastali, A. Dalvand, Use of silica fume and recycled steel fibers in self-compacting concrete (SCC), CONSTR BUILD MATER, 125 (2016) 196-209.

[52] M. Benaicha, X. Roguiez, O. Jalbaud, Y. Burtschell, A.H. Alaoui, Influence of silica fume and viscosity modifying agent on the mechanical and rheological behavior of self compacting concrete, CONSTR BUILD MATER, 84 (2015) 103-110.

[53] H. Zhu, K. Yu, V.C. Li, Influence of citric acid on fresh and hardened properties of sprayable CSA-ECC, submitted to ACI Materials, (2021) Under review.

[54] M. Dedenis, M. Sonebi, S. Amziane, A. Perrot, G. Amato, Effect of Metakaolin, Fly Ash and Polypropylene Fibres on Fresh and Rheological Properties of 3D Printing Based Cement Materials, Second RILEM International Conference on Concrete and Digital Fabrication, 2020, pp. 206-215.

[55] K. Yun, S. Choi, J.H. Yeon, Effects of admixtures on the rheological properties of high-performance wet-mix shotcrete mixtures, CONSTR BUILD MATER, 78 (2015) 194-202.

[56] H. Kong, S.G. Bike, V.C. Li, Development of a self-consolidating engineered cementitious composite employing electrosteric dispersion/stabilization, CEMENT CONCRETE COMP, 25 (2003) 301-309.

[57] A. Leemann, F. Winnefeld, The effect of viscosity modifying agents on mortar and concrete, Cement and Concrete Composites, 29 (2007) 341-349.

[58] M. Lachemi, K.M.A. Hossain, V. Lambros, P.C. Nkinamubanzi, N. Bouzoubaâ, Performance of new viscosity modifying admixtures in enhancing the rheological properties of cement paste, CEMENT CONCRETE RES, 34 (2004) 185-193.

[59] K.H. Khayat, Viscosity-enhancing admixtures for cement-based materials — An overview, Cement and Concrete Composites, 20 (1998) 171-188.

[60] G. Ma, L. Wang, A critical review of preparation design and workability measurement of concrete material for largescale 3D printing, FRONT STRUCT CIV ENG, 12 (2018) 382-400.

[61] G. Zhang, G. Li, Y. Li, Effects of superplasticizers and retarders on the fluidity and strength of sulphoaluminate cement, CONSTR BUILD MATER, 126 (2016) 44-54.

[62] G. Li, T. He, D. Hu, C. Shi, Effects of two retarders on the fluidity of pastes plasticized with aminosulfonic acid-based superplasticizers, CONSTR BUILD MATER, (2011).

[63] Y. Zhu, Y. Yang, Y. Yao, Use of slag to improve mechanical properties of engineered cementitious composites (ECCs) with high volumes of fly ash, CONSTR BUILD MATER, 36 (2012) 1076-1081.

[64] W. McGee, T. Ng, K. Yu, V.C. Li, Extrusion nozzle shaping as an approach for improved 3DP of engineered cementitious composites, Digital Concrete 2020, 2020.

[65] M. Şahmaran, Z. Bilici, E. Ozbay, T.K. Erdem, H.E. Yucel, M. Lachemi, Improving the workability and rheological properties of Engineered Cementitious Composites using factorial experimental design, Composites Part B: Engineering, 45 (2013) 356-368.

[66] E. Yang, M. Sahmaran, Y. Yang, V.C. Li, Rheological Control in Production of Engineered Cementitious Composites, ACI MATER J, 106 (2009) 357.

[67] M. Li, V.C. Li, Rheology, fiber dispersion, and robust properties of Engineered Cementitious Composites, MATER STRUCT, 46 (2013) 405-420.

[68] H. Kong, S.G. Bike, V.C. Li, Constitutive rheological control to develop a self-consolidating engineered cementitious composite reinforced with hydrophilic poly(vinyl alcohol) fibers, CEMENT CONCRETE COMP, 25 (2003) 333-341.

[69] S. Jacobsen, L. Haugan, T.A. Hammer, E. Kalogiannidis, Flow conditions of fresh mortar and concrete in different pipes, CEMENT CONCRETE RES, 39 (2009) 997-1006.

[70] G. Lu, K. Wang, T.J. Rudolphi, Modeling rheological behavior of highly flowable mortar using concepts of particle and fluid mechanics, Cement and Concrete Composites, 30 (2008) 1-12.

[71] J.R. Abbott, N. Tetlow, A.L. Graham, S.A. Altobelli, E. Fukushima, L.A. Mondy, T.S. Stephens, Experimental observations of particle migration in concentrated suspensions: Couette flow, J RHEOL, 35 (1991) 773-795.

[72] N. Roussel, Rheological requirements for printable concretes, CEMENT CONCRETE RES, 112 (2018) 76-85.

[73] E. Secrieru, V. Mechtcherine, C. Schröfl, D. Borin, Rheological characterisation and prediction of pumpability of strain-hardening cement-based-composites (SHCC) with and without addition of superabsorbent polymers (SAP) at various temperatures, CONSTR BUILD MATER, 112 (2016) 581-594.

[74] E. Secrieru, D. Cotardo, V. Mechtcherine, L. Lohaus, C. Schröfl, C. Begemann, Changes in concrete properties during pumping and formation of lubricating material under pressure, CEMENT CONCRETE RES, 108 (2018) 129-139.

[75] R.J.M. Wolfs, F.P. Bos, T.A.M. Salet, Early age mechanical behaviour of 3D printed concrete: Numerical

modelling and experimental testing, CEMENT CONCRETE RES, 106 (2018) 103-116.

[76] A. Kazemian, X. Yuan, E. Cochran, B. Khoshnevis, Cementitious materials for construction-scale 3D printing: Laboratory testing of fresh printing mixture, CONSTR BUILD MATER, 145 (2017) 639-647.

[77] C. Gosselin, R. Duballet, P. Roux, N. Gaudillière, J. Dirrenberger, P. Morel, Large-scale 3D printing of ultra-high performance concrete – a new processing route for architects and builders, Materials and Design, 100 (2016) 102-109.

[78] Z. Malaeb, H. Hachem, A. Tourbah, T. Maalouf, N.E. Zarwi, F. Hamzeh, 3D Concrete Printing: Machine and Mix Design, International Journal of Civil Engineering and Technology, 6 (2015) 14-22.

[79] V.N. Nerellaa, M. Nätherb, A. Iqbala, M. Butlera, V. Mechtcherinea, Inline quantification of extrudability of cementitious materials for digital construction, Cement and Concrete Composites,

95 (2019) 260-270.

[80] M. Hambach, D. Volkmer, Properties of 3D-printed fiber-reinforced Portland cement paste, Cement and Concrete Composites, 79 (2017) 62-70.

[81] N. Roussel, A thixotropy model for fresh fluid concretes: Theory, validation and applications, CEMENT CONCRETE RES, 36 (2006) 1797-1806.

[82] T. Wangler, E. Lloret, L. Reiter, N. Hack, F. Gramazio, M. Kohler, M. Bernhard, B. Dillenburger, J. Buchli, N. Roussel, R. Flatt, Digital Concrete: Opportunities and Challenges, RILEM Technical Letters, 1 (2016) 67-75.

[83] A. Perrot, D. Rangeard, A. Pierre, Structural built-up of cement-based materials used for 3D-printing extrusion techniques, MATER STRUCT, 49 (2016) 1213-1220.

[84] A.S.J. Suiker, Mechanical performance of wall structures in 3D printing processes: Theory, design tools and experiments, INT J MECH SCI, 137 (2018) 145-170.

[85] T.T. Le, S.A. Austin, S. Lim, R.A. Buswell, R. Law, A.G.F. Gibb, T. Thorpe, Hardened properties of high-performance printing concrete, CEMENT CONCRETE RES, 42 (2012) 558-566.

[86] N. Roussel, F. Cussigh, Distinct-layer casting of SCC: The mechanical consequences of thixotropy, CEMENT CONCRETE RES, 38 (2008) 624-632.

[87] L. Josserand, O. Coussy, F. de Larrard, Bleeding of concrete as an ageing consolidation process, CEMENT CONCRETE RES, 36 (2006) 1603-1608.

[88] H. Jeong, S. Han, S. Choi, Y. Lee, S. Yi, K. Kim, Rheological Property Criteria for Buildable 3D Printing Concrete, MATERIALS, 12 (2019) 657.

[89] Q. Yuan, Z. Li, D. Zhou, T. Huang, H. Huang, D. Jiao, C. Shi, A feasible method for measuring the buildability of fresh 3D printing mortar, CONSTR BUILD MATER, 227 (2019) 116600.

[90] R.J.M. Wolfs, F.P. Bos, T.A.M. Salet, Hardened properties of 3D printed concrete: The influence of process parameters on interlayer adhesion, CEMENT CONCRETE RES, 119 (2019) 132-140.

[91] B. Panda, S.C. Paul, N.A.N. Mohamed, Y.W.D. Tay, M.J. Tan, Measurement of tensile bond strength of 3D printed geopolymer mortar, MEASUREMENT, 113 (2018) 108-116.

[92] B. Zareiyan, B. Khoshnevis, Effects of interlocking on interlayer adhesion and strength of structures in 3D printing of concrete, AUTOMAT CONSTR, 83 (2017) 212-221.

[93] B. Panda, N.A. Noor Mohamed, S.C. Paul, G. Bhagath Singh, M.J. Tan, B. Šavija, The Effect of Material Fresh Properties and Process Parameters on Buildability and Interlayer Adhesion of 3D Printed Concrete, MATERIALS, 12 (2019) 2149.

[94] E. Keita, H. Bessaies-Bey, W. Zuo, P. Belin, N. Roussel, Weak bond strength between successive layers in extrusion-based additive manufacturing: measurement and physical origin, CEMENT CONCRETE RES, 123 (2019) 105787.

[95] J.G. Sanjayan, B. Nematollahi, M. Xia, T. Marchment, Effect of surface moisture on inter-layer strength of 3D printed concrete, CONSTR BUILD MATER, 172 (2018) 468-475.

[96] J. Van Der Putten, M. Deprez, V. Cnudde, G. De Schutter, K. Van Tittelboom, Microstructural Characterization of 3D Printed Cementitious Materials, MATERIALS, 12 (2019) 2993.

[97] V.N. Nerella, S. Hempel, V. Mechtcherine, Effects of layer-interface properties on mechanical performance of concrete elements produced by extrusion-based 3D-printing, CONSTR BUILD MATER, 205 (2019) 586-601.

[98] E. Keita, H. Bessaies-Bey, W. Zuo, P. Belin, N. Roussel, Weak bond strength between successive layers in extrusion-based additive manufacturing: measurement and physical origin, CEMENT CONCRETE RES, 123 (2019) 105787.

[99] I. Dressler, N. Freund, D. Lowke, The Effect of Accelerator Dosage on Fresh Concrete Properties and on Interlayer Strength in Shotcrete 3D Printing, MATERIALS, 13 (2020) 374.

[100] B. Panda, N.A.N. Mohamed, Y.W.D. Tay, M.J. Tan, Bond Strength in 3D Printed Geopolymer Mortar, RILEM International Conference on Concrete and Digital Fabrication, Zurich, Switzerland, 2018, pp. 200-206.

[101] T. Ding, J. Xiao, S. Zou, X. Zhou, Anisotropic behavior in bending of 3D printed concrete reinforced with fibers, COMPOS STRUCT, 254 (2020) 112808.

[102] B. Nematollahi, M. Xia, P. Vijay, J.G. Sanjayan, Chapter 18 - Properties of Extrusion-Based 3D Printable Geopolymers for Digital Construction Applications, 3D Concrete Printing Technology, Butterworth-Heinemann2019. pp. 371-388.

[103] B. Nematollahi, M. Xia, J. Sanjayan, P. Vijay, Effect of Type of Fiber on Inter-Layer Bond and Flexural Strengths of Extrusion-Based 3D Printed Geopolymer, Materials Science Forum, 939 (2018) 155-162.

[104] T. Marchment, J. Sanjayan, M. Xia, Method of enhancing interlayer bond strength in construction scale 3D printing with mortar by effective bond area amplification, MATER DESIGN, 169 (2019) 107684.

[105] E. Hosseini, M. Zakertabrizi, A.H. Korayem, G. Xu, A novel method to enhance the interlayer bonding of 3D printing concrete: An experimental and computational investigation, Cement and Concrete Composites, 99 (2019) 112-119.

[106] G. Ma, N.M. Salman, L. Wang, F. Wang, A novel additive mortar leveraging internal curing for enhancing interlayer bonding of cementitious composite for 3D printing, CONSTR BUILD MATER, 244 (2020) 118305.

[107] J.V.D. Putten, G.D. Schutter, K.V. Tittelboom, Surface modification as a technique to improve inter-layer bonding strength in 3D printed cementitious materials, RILEM Technical Letters, 4 (2019) 33-38.

[108] G. Ma, Z. Li, L. Wang, F. Wang, J. Sanjayan, Mechanical anisotropy of aligned fiber reinforced composite for extrusion-based 3D printing, CONSTR BUILD MATER, 202 (2019) 770-783.

[109] B. Panda, S.C. Paul, M.J. Tan, Anisotropic mechanical performance of 3D printed fiber reinforced sustainable construction material, MATER LETT, 209 (2017) 146-149.

[110] K. Yu, W. McGee, T.Y. Ng, H. Zhu, V.C. Li, 3D-printable engineered cementitious

composites (3DP-ECC): Fresh and hardened properties, CEMENT CONCRETE RES, (2021) Accepted, Feb. 2021.

[111] F.P. Bos, E. Bosco, T.A.M. Salet, Ductility of 3D printed concrete reinforced with short straight steel fibers, Virtual and physical prototyping, 14 (2018) 160-174.

[112] B. Nematollahi, P. Vijay, J. Sanjayan, A. Nazari, M. Xia, V. Naidu Nerella, V. Mechtcherine, Effect of Polypropylene Fibre Addition on Properties of Geopolymers Made by 3D Printing for Digital Construction, MATERIALS, 11 (2018) 2352.

[113] G.M. Moelich, J. Kruger, R. Combrinck, Plastic shrinkage cracking in 3D printed concrete, Composites Part B: Engineering, 200 (2020) 108313.

[114] G.M. Moelich, P.J. Kruger, R. Combrinck, A plastic shrinkage cracking risk model for 3D printed concrete exposed to different environments, Cement and Concrete Composites, 130 (2022) 104516.

[115] F.P. Bos, C. Menna, M. Pradena, E. Kreiger, W.R.L. Da Silva, A.U. Rehman, D. Weger, R.J.M. Wolfs, Y. Zhang, L. Ferrara, V. Mechtcherine, The realities of additively manufactured concrete structures in practice, CEMENT CONCRETE RES, 156 (2022) 106746.

[116] A.V. Rahul, M.K. Mohan, G. De Schutter, K. Van Tittelboom, 3D printable concrete with natural and recycled coarse aggregates: Rheological, mechanical and shrinkage behaviour, Cement and Concrete Composites, 125 (2022) 104311.

[117] L. Ma, Q. Zhang, H. Lombois-Burger, Z. Jia, Z. Zhang, G. Niu, Y. Zhang, Pore structure, internal relative humidity, and fiber orientation of 3D printed concrete with polypropylene fiber and their relation with shrinkage, Journal of Building Engineering, 61 (2022) 105250.

[118] F. Aslani, R. Dale, F. Hamidi, A. Valizadeh, Mechanical and shrinkage performance of 3D-printed rubberised engineered cementitious composites, CONSTR BUILD MATER, 339 (2022) 127665.

[119] K. Federowicz, M. Kaszyńska, A. Zieliński, M. Hoffmann, Effect of Curing Methods on Shrinkage Development in 3D-Printed Concrete, MATERIALS, 13 (2020) 2590.

[120] G.M. Moelich, P.J. Kruger, R. Combrinck, The effect of restrained early age shrinkage on the interlayer bond and durability of 3D printed concrete, Journal of Building Engineering, 43 (2021) 102857.

[121] I.M.G. Bertelsen, C. Kragh, G. Cardinaud, L.M. Ottosen, G. Fischer, Quantification of plastic shrinkage cracking in mortars using digital image correlation, CEMENT CONCRETE RES, 123 (2019) 105761.

[122] J. Van Der Putten, D. Snoeck, R. De Coensel, G. De Schutter, K. Van Tittelboom, Early age shrinkage phenomena of 3D printed cementitious materials with superabsorbent polymers, Journal of Building Engineering, 35 (2021) 102059.

[123] H. Zhang, J. Xiao, Plastic shrinkage and cracking of 3D printed mortar with recycled sand, CONSTR BUILD MATER, 302 (2021) 124405.

[124] G.M. Moelich, P.J. Kruger, R. Combrinck, Mitigating early age cracking in 3D printed concrete using fibres, superabsorbent polymers, shrinkage reducing admixtures, B-CSA cement and curing measures, CEMENT CONCRETE RES, 159 (2022) 106862.

[125] I. Serpukhov, V. Mechtcherine, Early-Age Shrinkage of Ordinary Concrete and a Strain-Hardening Cement-Based Composite (SHCC) in the Conditions of Hot Weather Casting, 10th International Conference on Mechanics and Physics of Creep, Shrinkage, and Durability of Concrete and Concrete Structures, Vienna, Austria, 2015, pp. 1504–1513.

[126] M.V. Tran, Y.T.H. Cu, C.V.H. Le, Rheology and shrinkage of concrete using polypropylene fiber for 3D concrete printing, Journal of Building Engineering, 44 (2021) 103400.

[127] R.G. Nemkumar Banthia, Influence of polypropylene fiber geometry on plastic shrinkage cracking in concrete, CEMENT CONCRETE RES, 36 (2006) 1263-1267.

[128] W.P. Boshoff, R. Combrinck, Modelling the severity of plastic shrinkage cracking in concrete, CEMENT CONCRETE RES, 48 (2013) 34-39.

[129] P. Zhan, Z. He, Application of shrinkage reducing admixture in concrete: A review, CONSTR BUILD MATER, 201 (2019) 676-690.

[130] D. Snoeck, L. Pel, N. De Belie, Superabsorbent polymers to mitigate plastic drying shrinkage in a cement paste as studied by NMR, Cement and Concrete Composites, 93 (2018) 54-62.

[131] D. Snoeck, O.M. Jensen, N. De Belie, The influence of superabsorbent polymers on the autogenous shrinkage properties of cement pastes with supplementary cementitious materials, CEMENT CONCRETE RES, 74 (2015) 59-67.

[132] W. Boshoff, V. Mechtcherine, D. Snoeck, C. Schröfl, N. De Belie, A.B. Ribeiro, D. Cusson, M. Wyrzykowski, N. Toropovs, P. Lura, The effect of superabsorbent polymers on the mitigation of plastic shrinkage cracking of conventional concrete, results of an inter-laboratory test by RILEM TC 260-RSC, MATER STRUCT, 53 (2020).

[133] A.K.F. Cheung, C.K.Y. Leung, Shrinkage reduction of high strength fiber reinforced cementitious composites (HSFRCC) with various water-to-binder ratios, Cement and Concrete Composites, 33 (2011) 661-667.

[134] I. Mehdipour, K.H. Khayat, Enhancing the performance of calcium sulfoaluminate blended cements with shrinkage reducing admixture or lightweight sand, Cement and Concrete Composites, 87 (2018) 29-43.

[135] Y. Chen, M. Liang, Y. Zhang, Z. Li, B. Šavija, E. Schlangen, O. Çopuroğlu, Can superabsorbent polymers be used as rheology modifiers for cementitious materials in the context of 3D concrete printing? CONSTR BUILD MATER, 371 (2023) 130777.

[136] G.M. Moelich, J. Kruger, R. Combrinck, Modelling the interlayer bond strength of 3D printed concrete with surface moisture, CEMENT CONCRETE RES, 150 (2021) 106559.

[137] I.A. Chen, C.W. Hargis, M.C.G. Juenger, Understanding expansion in calcium sulfoaluminate–belite cements, CEMENT CONCRETE RES, 42 (2012) 51-60.

[138] J. Bizzozero, C. Gosselin, K.L. Scrivener, Expansion mechanisms in calcium aluminate and sulfoaluminate systems with calcium sulfate, CEMENT CONCRETE RES, 56 (2014) 190-202.

[139] G.A. Keoleian, A. Kendall, J.E. Dettling, V.M. Smith, R.F. Chandler, M.D. Lepech, V.C. Li, Life Cycle Modeling of Concrete Bridge Design: Comparison of Engineered Cementitious Composite Link Slabs and Conventional Steel Expansion Joints, J INFRASTRUCT SYST, 11 (2005) 51-60.

[140] S.Z. Qian, V.C. Li, H. Zhang, G.A. Keoleian, Life cycle analysis of pavement overlays made with Engineered Cementitious Composites, Cement and Concrete Composites, 35 (2013) 78-88.

[141] M.D. Lepech, V.C. Li, Sustainable Pavement Overlays Using Engineered Cementitious Composites, International Journal of Pavement Research and Technology, 3 (2010) 241-250.

[142] H. Zhang, M.D. Lepech, G.A. Keoleian, S. Qian, V.C. Li, Dynamic Life-Cycle Modeling of Pavement Overlay Systems: Capturing the Impacts of Users, Construction, and Roadway Deterioration, J INFRASTRUCT SYST, 16 (2010) 227-354.

[143] Shanghai Lengguang Industrial Co., Ltd, The 10th Flower Expo Garden- the Bamboo and Rattan Pavilion, 2021.

[144] Japan Society Of Civil Engineers, Recommendations for Design and Construction of High Performance Fiber Reinforced Cement Composites with Multiple Fine Cracks (HPFRCC), Concrete Engineereing Series, vol. Concrete L., 2008.

[145] K. Rokugo, T. Kanda, Strain Hardening Cement Composites: Structural Design and Performance, Springer2013.

[146] Ministry of Industry and Information Technology of P.R. China, JC/T 2461–2018, standard test method for the mechanical properties of ductile fiber reinforced cementitious composites, 2017.

[147] China Association for Engineering Construction Standardization, T/CECS 1212-2022, Technical Specification for Strain-Hardening Cementitious Composites Structures, 2022.

[148] X. Han, J. Yan, M. Liu, L. Huo, J. Li, Experimental study on large-scale 3D printed concrete walls under axial compression, AUTOMAT CONSTR, 133 (2022) 103993.

[149] T. Daungwilailuk, P. Pheinsusom, W. Pansuk, Uniaxial load testing of large-scale 3D-printed concrete wall and finite-element model analysis, CONSTR BUILD MATER, 275 (2021) 122039.

[150] M. Amran, H.S. Abdelgader, A.M. Onaizi, R. Fediuk, T. Ozbakkaloglu, R.S.M. Rashid, G. Muralih, 3D-printable alkali-activated concretes for building applications: A critical review, CONSTR BUILD MATER, 319 (2022) 126126.

[151] Y. Zhang, Y. Zhang, G. Liu, Y. Yang, M. Wu, B. Pang, Fresh properties of a novel 3D printing concrete ink, CONSTR BUILD MATER, 174 (2018) 263-271.

[152] S. Muthukrishnan, S. Ramakrishnan, J. Sanjayan, Technologies for improving buildability in 3D concrete printing, Cement and Concrete Composites, 122 (2021) 104144.

[153] V.N. Nerella, M. Krause, V. Mechtcherine, Direct printing test for buildability of 3D-printable concrete considering economic viability, AUTOMAT CONSTR, 109 (2020) 102986.

[154] B. Panda, M.J. Tan, Rheological behavior of high volume fly ash mixtures containing micro silica for digital construction application, MATER LETT, 237 (2019) 348-351.

[155] Y. Weng, M. Li, M.J. Tan, S. Qian, Design 3D printing cementitious materials via Fuller Thompson theory and Marson-Percy model, CONSTR BUILD MATER, 163 (2018) 600-610.

[156] C. Joh, J. Lee, T.Q. Bui, J. Park, I. Yang, Buildability and Mechanical Properties of 3D Printed Concrete, MATERIALS, 13 (2020) 4919.

[157] S. Ahmed, S. Yehia, Evaluation of Workability and Structuration Rate of Locally Developed

3D Printing Concrete Using Conventional Methods, MATERIALS, 15 (2022) 1243.

[158] Y. Chen, S. Chaves Figueiredo, Z. Li, Z. Chang, K. Jansen, O. Çopuroğlu, E. Schlangen, Improving printability of limestone-calcined clay-based cementitious materials by using viscosity-modifying admixture, CEMENT CONCRETE RES, 132 (2020) 106040.

[159] Q. Liu, Q. Jiang, M. Huang, J. Xin, P. Chen, S. Wu, Modifying effect of anionic polyacrylamide dose for cement-based 3DP materials: Printability and mechanical performance tests, CONSTR BUILD MATER, 330 (2022) 127156.

[160] L. Casagrande, L. Esposito, C. Menna, D. Asprone, F. Auricchio, Effect of testing procedures on buildability properties of 3D-printable concrete, CONSTR BUILD MATER, 245 (2020) 118286.

[161] R.J.M. Wolfs, F.P. Bos, T.A.M. Salet, Triaxial compression testing on early age concrete for numerical analysis of 3D concrete printing, Cement and Concrete Composites, 104 (2019) 103344.

[162] B. Panda, J.H. Lim, M.J. Tan, Mechanical properties and deformation behaviour of early age concrete in the context of digital construction, Composites Part B: Engineering, 165 (2019) 563-571.

[163] Y. Wang, Y. Jiang, T. Pan, K. Yin, The Synergistic Effect of Ester-Ether Copolymerization Thixo-Tropic Superplasticizer and Nano-Clay on the Buildability of 3D Printable Cementitious Materials, MATERIALS, 14 (2021) 4622.

[164] A. Tripathi, S.A.O. Nair, N. Neithalath, A comprehensive analysis of buildability of 3D-printed concrete and the use of bi-linear stress-strain criterion-based failure curves towards their prediction, Cement and Concrete Composites, 128 (2022) 104424.

[165] B. Zhu, B. Nematollahi, J. Pan, Y. Zhang, Z. Zhou, Y. Zhang, 3D concrete printing of permanent formwork for concrete column construction, Cement and Concrete Composites, 121 (2021) 104039.

[166] R. Jayathilakage, P. Rajeev, J.G. Sanjayan, Yield stress criteria to assess the buildability of 3D concrete printing, CONSTR BUILD MATER, 240 (2020) 117989.

[167] J. Kruger, S. Zeranka, G. van Zijl, 3D concrete printing: A lower bound analytical model for buildability performance quantification, AUTOMAT CONSTR, 106 (2019) 102904.

[168] I. Ivanova, E. Ivaniuk, S. Bisetti, V.N. Nerella, V. Mechtcherine, Comparison between methods for indirect assessment of buildability in fresh 3D printed mortar and concrete, CEMENT CONCRETE RES, 156 (2022) 106764.

[169] M. Tramontin Souza, I. Maia Ferreira, E. Guzi De Moraes, L. Senff, S. Arcaro, J.R. Castro Pessôa, M. J. Ribeiro, A.P. Novaes De Oliveira, Role of chemical admixtures on 3D printed Portland cement: Assessing rheology and buildability, CONSTR BUILD MATER, 314 (2022) 125666.

[170] G. Ma, Z. Li, L. Wang, Printable properties of cementitious material containing copper tailings for extrusion based 3D printing, CONSTR BUILD MATER, 162 (2018) 613-627.

[171] H. Zhu, K. Yu, W. McGee, T.Y. Ng, V.C. Li, Limestone Calcined Clay Cement for Three-Dimensional- Printed Engineered Cementitious Composites, ACI MATER J, 118 (2021).

[172] C. Matthäus, D. Back, D. Weger, T. Kränkel, J. Scheydt, C. Gehlen, Effect of Cement Type and Limestone Powder Content on Extrudability of Lightweight Concrete, Second RILEM International Conference on Concrete and Digital Fabrication. DC 2020, 2020, pp. 312-322.

[173] A.S. El-Dieb, M.M.R. Taha, Flow characteristics and acceptance criteria of fiber-reinforced self-compacted concrete (FR-SCC), CONSTR BUILD MATER, 27 (2012) 585-596.

[174] P.F.G. Banfill, G. Starrs, G. Derruau, W.J. McCarter, T.M. Chrisp, Rheology of low carbon fibre content reinforced cement mortar, Cement and Concrete Composites, 28 (2006) 773-780.

[175] W. Wang, A. Shen, Z. Lyu, Z. He, K.T.Q. Nguyen, Fresh and rheological characteristics of fiber reinforced concrete——A review, CONSTR BUILD MATER, 296 (2021) 123734.

[176] L. Martinie, P. Rossi, N. Roussel, Rheology of fiber reinforced cementitious materials: classification and prediction, CEMENT CONCRETE RES, 40 (2010) 226-234.

[177] M. Cao, L. Xu, C. Zhang, Rheology, fiber distribution and mechanical properties of calcium carbonate (CaCO3) whisker reinforced cement mortar, Composites Part A: Applied Science and Manufacturing, 90 (2016) 662-669.

[178] S. Jiang, B. Shan, J. Ouyang, W. Zhang, X. Yu, P. Li, B. Han, Rheological properties of cementitious composites with nano/fiber fillers, CONSTR BUILD MATER, 158 (2018) 786-800.

[179] ASTM C469/C469M, Standard Test Method for Static Modulus of Elasticity and Poisson's Ratio of Concrete in Compression, ASTM International, 2014.

[180] F. Bos, R. Wolfs, Z. Ahmed, T. Salet, Additive manufacturing of concrete in construction: potentials and challenges of 3D concrete printing, Virtual and physical prototyping, 11 (2016) 209-225.

[181] R.J.M. Wolfs, F.P. Bos, E.C.F. van Strien, T.A.M. Salet, A Real-Time Height Measurement and Feedback System for 3D Concrete Printing, Springer International Publishing, Cham, 2017. pp. 2474-2483.

[182] J. Zhou, S. Qian, G. Ye, O. Copuroglu, K. van Breugel, V.C. Li, Improved fiber distribution and mechanical properties of engineered cementitious composites by adjusting the mixing sequence, Cement and Concrete Composites, 34 (2012) 342-348.

[183] ASTM C1437, Standard test method for flow of hydraulic cement mortar.

[184] JSCE, Recommendations for Design and Construction of High Performance Fiber Reinforced Cement Composites with Multiple Fine Cracks, Japan Society of Civil Engineers, Tokyo, Japan, pp. 1–16.

[185] S.P. Shah, Determination of fracture parameters (K Ic s and CTODc) of plain concrete using three-point bend tests, MATER STRUCT, 23 (1990) 457-460.

[186] T. Ding, J. Xiao, S. Zou, Y. Wang, Hardened properties of layered 3D printed concrete with recycled sand, Cement and Concrete Composites, 113 (2020) 103724.

[187] Y. Yang, C. Wu, Z. Liu, H. Wang, Q. Ren, Mechanical anisotropy of ultra-high performance fibre-reinforced concrete for 3D printing, Cement and Concrete Composites, 125 (2022) 104310.

[188] X. Sun, J. Zhou, Q. Wang, J. Shi, H. Wang, PVA fibre reinforced high-strength cementitious composite for 3D printing: Mechanical properties and durability, Additive Manufacturing, 49 (2022) 102500.

[189] T. Marchment, J. Sanjayan, Mesh reinforcing method for 3D Concrete Printing, AUTOMAT CONSTR, 109 (2020) 102992.

[190] T. Marchment, J. Sanjayan, Penetration reinforcing method for 3D concrete printing, Second RILEM International Conference on Concrete and Digital Fabrication, Springer International Publishing, Cham, 2020, pp. 680-690.

[191] J. Kruger, A. Cicione, F. Bester, M. van den Heever, S. Cho, R. Walls, G. van Zijl, Facilitating ductile failure of 3D printed concrete elements in fire, Second RILEM International Conference on Concrete and Digital Fabrication, Springer International Publishing, Cham, 2020, pp. 449-458.

[192] O. Geneidy, S. Kumarji, A. Dubor, A. Sollazzo, Simultaneous reinforcement of concrete while 3D printing, Second RILEM International Conference on Concrete and Digital Fabrication, Springer International Publishing, Cham, 2020, pp. 895-905.

[193] L. Wang, G. Ma, T. Liu, R. Buswell, Z. Li, Interlayer reinforcement of 3D printed concrete by the in-process deposition of U-nails, CEMENT CONCRETE RES, 148 (2021) 106535.

[194] L.T. Kuhn-Spearing, H. Kessler, E. Chateau, R. Ballarini, A.H. Heuer, S.M. Spearing, Fracture mechanisms of the Strombus gigas conch shell: implications for the design of brittle laminates, J MATER SCI, 31 (1996) 6583–6594.

[195] J. Ye, C. Cui, J. Yu, K. Yu, J. Xiao, Fresh and anisotropic-mechanical properties of 3D printable ultra-high ductile concrete with crumb rubber, Composites Part B: Engineering, 211 (2021) 108639.

[196] T. Ding, J. Xiao, S. Zou, J. Yu, Flexural properties of 3D printed fibre-reinforced concrete with recycled sand, CONSTR BUILD MATER, 288 (2021) 123077.

[197] P.M. Pohl, F. Kümmel, C. Schunk, I. Serrano-Munoz, H. Markötter, M. Göken, H.W. Höppel, About the Role of Interfaces on the Fatigue Crack Propagation in Laminated Metallic Composites, Materials (Basel), 14 (2021) 2564.

[198] Y.M. Lim, V.C. Li, Durable repair of aged infrastructures using trapping mechanism of engineered cementitious composites, Cement and Concrete Composites, 19 (1997) 373-385.

[199] F. Bos, Z. Ahmed, C. Romero Rodriguez, S. Chaves Figueiredo, 3D Concrete Printing for Structural Applications, SPOOL, 2 (2019) 5-10.

[200] D. Asprone, F. Auricchio, C. Menna, V. Mercuri, 3D printing of reinforced concrete elements: Technology and design approach, CONSTR BUILD MATER, 165 (2018) 218-231.

[201] T.A.M. Salet, Z.Y. Ahmed, F.P. Bos, H.L.M. Laagland, Design of a 3D printed concrete bridge by testing, Virtual and Physical Prototyping, 13 (2018) 222-236.

[202] F. Bos, R. Wolfs, Z. Ahmed, T. Salet, Large Scale Testing of Digitally Fabricated Concrete (DFC) Elements. In: Wangler, T., Flatt, R. (eds) First RILEM International Conference on Concrete and Digital Fabrication – Digital Concrete 2018. DC 2018. RILEM Bookseries, vol 19. Springer, Cham.,2019.

[203] Z. Ahmed, R. Wolfs, F. Bos, T. Salet, A Framework for Large-Scale Structural Applications of 3D Printed Concrete: the Case of a 29 m Bridge in the Netherlands, Open Conference Proceedings, 1 (2022) 5-19.

[204] V.C. Li, A Simplified Micromechanical Model of Compressive Strength of Fiber-Reinforced Cementitious Composites, Cement and Concrete Composites, 14 (1992) 131-141.

[205] J. Zhang, C. Gong, Z. Guo, M. Zhang, Engineered cementitious composite with characteristic of low drying shrinkage, CEMENT CONCRETE RES, 39 (2009) 303-312.

[206] M.B. Weimann, V.C. Li, DRYING SHRINKAGE AND CRACK WIDTH OF ENGINEERED CEMENTITIOUS COMPOSITES (ECC), Brittle Matrix Composites 7, (2003) 37-46.

[207] V.C. Li, H. Stang, Elevating FRC material ductility to infrastructure durability, 6th RILEM Symposium on Fiber-Reinforced Concretes (FRC) - BEFIB 2004, Varenna, Italy, 2004, pp. 171-186.

[208] ASTM C1437-20, Standard Test Method for Flow of Hydraulic Cement Mortar, ASTM International, West Conshohocken, PA, 2020.

[209] ASTM C403/C403M-16, Standard Test Method for Time of Setting of Concrete Mixtures by Penetration Resistance, ASTM International, West Conshohocken, PA, 2017.

[210] C490/C490M-21, Standard Practice for Use of Apparatus for the Determination of Length Change of Hardened Cement Paste, Mortar, and Concrete, ASTM International, West Conshohocken, PA, 2021.

[211] H. Zhu, E.G. Ftwi, W.H. Hu, Z. Li, G. Zapsas, W. Nasser, V.C. Li, Theory and Strategies for Developing Full Service Life Self-stressing ECC Enabling the Jointless Pavement, submitted to Cement and Concrete Research, (2023).

[212] M.K. Mohan, A.V. Rahul, G. De Schutter, K. Van Tittelboom, Early age hydration, rheology and pumping characteristics of CSA cement-based 3D printable concrete, CONSTR BUILD MATER, 275 (2021) 122136.

[213] M.K. Mohan, A.V. Rahul, Y. Tao, G. De Schutter, K. Van Tittelboom, Hydration re-initiation of borated CSA systems with a two-stage mixing process: An application in extrusion-based concrete 3D printing, CEMENT CONCRETE RES, 159 (2022) 106870.

[214] P. Sukontasukkul, K. Panklum, B. Maho, N. Banthia, P. Jongvivatsakul, T. Imjai, V. Sata, S. Limkatanyu, P. Chindaprasirt, Effect of synthetic microfiber and viscosity modifier agent on layer deformation, viscosity, and open time of cement mortar for 3D printing application, CONSTR BUILD MATER, 319 (2022) 126111.

[215] W. Zhou, W. McGee, H. Zhu, H.S. Gökçe, V.C. Li, Time-dependent fresh properties characterization of 3D printing engineered cementitious composites (3DP-ECC): On the evaluation of buildability, Cement and Concrete Composites, 133 (2022) 104704.

[216] H. Zhu, D. Zhang, T. Wang, M. McBain, V.C. Li, Intrinsic self-stressing and low carbon Engineered Cementitious Composites (ECC) for improved sustainability, CEMENT CONCRETE RES, 149 (2021) 106580.

[217] L. Wang, N. Ur Rehman, I. Curosu, Z. Zhu, M.A.B. Beigh, M. Liebscher, L. Chen, D.C.W. Tsang, S. Hempel, V. Mechtcherine, On the use of limestone calcined clay cement (LC3) in high-strength strain-hardening cement-based composites (HS-SHCC), CEMENT CONCRETE RES, 144 (2021) 106421.

[218] Y. Dhandapani, T. Sakthivel, M. Santhanam, R. Gettu, R.G. Pillai, Mechanical properties and durability performance of concretes with Limestone Calcined Clay Cement (LC3), CEMENT CONCRETE RES, 107 (2018) 136-151.

[219] H. Du, S.D. Pang, High-performance concrete incorporating calcined kaolin clay and limestone as cement substitute, CONSTR BUILD MATER, 264 (2020) 120152.

[220] J. Ston, A. Hilaire, K. Scrivener, Autogenous Shrinkage and Creep of Limestone and Calcined Clay Based Binders. In: Martirena, F., Favier, A., Scrivener, K. (eds) Calcined Clays for Sustainable Concrete. RILEM Bookseries, vol 16. Springer, Dordrecht., 2018, pp. 447–454.

[221] F. Winnefeld, B. Lothenbach, Hydration of calcium sulfoaluminate cements — Experimental findings and thermodynamic modelling, CEMENT CONCRETE RES, 40 (2010) 1239-1247.

[222] Y. Tao, A.V. Rahul, M.K. Mohan, G. De Schutter, K. Van Tittelboom, Recent progress and technical challenges in using calcium sulfoaluminate (CSA) cement, Cement and Concrete Composites, 137 (2023) 104908.

[223] F.P. Glasser, L. Zhang, High-performance cement matrices based on calcium sulfoaluminate–belite compositions, CEMENT CONCRETE RES, 31 (2001) 1881-1886.

[224] L. Zhang, F.P. Glasser, Hydration of calcium sulfoaluminate cement at less than 24 h, Advances in cement research., 14 (2002) 141 - 155.

[225] X. Cai, D. Yang, D. Zhang, J. Cui, W. Wang, L. Liu, Development of high-early-strength low-carbon engineered cementitious composites with calcium sulfoaluminate cement incorporating high-volume fly ash, Case Studies in Construction Materials, 18 (2023) e01959.

[226] B. Zhu, J. Pan, J. Li, P. Wang, M. Zhang, Relationship between microstructure and strain-hardening behaviour of 3D printed engineered cementitious composites, Cement and Concrete Composites, 133 (2022) 104677.

[227] Y.M. Lim, V.C. Li, Durable repair of aged infrastructures using trapping mechanism of engineered cementitious composites, Cement and Concrete Composites, 19 (1997) 373-385.

[228] T. Nishikawa, K. Suzuki, S. Ito, K. Sato, T. Takebe, Decomposition of synthesized ettringite by carbonation, CEMENT CONCRETE RES, 22 (1992) 6 - 14.

[229] B. Chen, M. Horgnies, B. Huet, V. Morin, K. Johannes, F. Kuznik, Comparative kinetics study on carbonation of ettringite and meta-ettringite based materials, CEMENT CONCRETE RES, 137 (2020) 106209.

[230] L. Kan, H. Shi, Investigation of self-healing behavior of Engineered Cementitious Composites (ECC) materials, CONSTR BUILD MATER, 29 (2012) 348-356.

[231] J. Yu, C.K.Y. Leung, Strength Improvement of Strain-Hardening Cementitious Composites with Ultrahigh-Volume Fly Ash, J MATER CIVIL ENG, 29 (2017).

[232] H. Zhu, D. Zhang, T. Wang, H. Wu, V.C. Li, Mechanical and self-healing behavior of low carbon engineered cementitious composites reinforced with PP-fibers, CONSTR BUILD MATER, 259 (2020) 119805.

[233] L.E. Burris, K.E. Kurtis, Influence of set retarding admixtures on calcium sulfoaluminate cement hydration and property development, CEMENT CONCRETE RES, 104 (2018) 105-113.

[234] M. Abdellatief, S.M. AL-Tam, W.E. Elemam, H. Alanazi, G.M. Elgendy, A.M. Tahwia, Development of ultra-high-performance concrete with low environmental impact integrated with metakaolin and industrial wastes, Case Studies in Construction Materials, 18 (2023) e01724.

[235] M.S. Meddah, M.A. Ismail, S. El-Gamal, H. Fitriani, Performances evaluation of binary concrete designed with silica fume and metakaolin, CONSTR BUILD MATER, 166 (2018) 400-412.

[236] H. Zhu, W. Chen, S. Cheng, L. Yang, S. Wang, J. Xiong, Low carbon and high efficiency limestone-calcined clay as supplementary cementitious materials (SCMs): Multi-indicator comparison with conventional SCMs, CONSTR BUILD MATER, 341 (2022) 127748.

[237] S. Sánchez Berriel, A. Favier, E. Rosa Domínguez, I.R. Sánchez Machado, U. Heierli, K. Scrivener, F. Martirena Hernández, G. Habert, Assessing the environmental and economic potential of Limestone Calcined Clay Cement in Cuba, J CLEAN PROD, 124 (2016) 361-369.

[238] D. Shoji, Z. He, D. Zhang, V.C. Li, The greening of engineered cementitious composites (ECC): A review, CONSTR BUILD MATER, 327 (2022) 126701.

[239] K. Toshiyuki, P. Kabele, H. Fukuyama, Y. Uchida, H. Suwada, V. Slowik, Strain Hardening Cement Composites: Structural Design and Performance, vol. 6. RILEM (2013),2013.

[240] M. Hou, D. Zhang, V.C. Li, Material processing, microstructure, and composite properties of low carbon Engineered Cementitious Composites (ECC), Cement and Concrete Composites, 134 (2022) 104790.